Effect of Nozzle Guide Vane Shaping on High Pressure Turbine Stage Performance



Amir Rahim

Department of Engineering Science
University of Oxford

A thesis submitted in partial fulfillment of the requirements for the degree of
Doctor of Philosophy

University College Hilary 2017

Acknowledgements

I wish to express my gratitude to my research supervisor, Dr. Bidur Khanal, for his technical support for the duration of my D.Phil. His insights, advice and candour helped to further my knowledge of computational, turbomachinery and industry nuances. I am particularly grateful for his generosity with time to explain the fundamentals of HYDRA which would form the basis for the rest of my research.

I would like to thank Prof. Li He for his advice and contributions to various aspects of this research.

I am thankful to Rolls-Royce for their financial assistance, and namely Dr. Ed Romero and Dr. Haidong Li for their useful input and comments relating to the NGV design work.

I would like to acknowledge and thank Advanced Research Computing (ARC) for providing the computational resources and support that enabled me to obtain the CFD results required for the optimisation procedure in a timely manner.

To my parents, I wish to thank them for their love, guidance and support unconditionally given throughout my life, and without whom I would never have enjoyed so many opportunities.

Finally and foremost, to my wife, for her love, patience and support during the final stages of writing and completion, and for being the catalyst that has enabled me to successfully finish this endeavour.

Abstract

Effect of Nozzle Guide Vane Shaping on High Pressure Turbine Stage Performance

Amir Rahim, University College

A thesis submitted in partial fulfillment of the requirements for the degree of Doctor of Philosophy, University of Oxford, Hilary Term, 2017.

This thesis presents a computational fluid dynamic (CFD) study of high pressure gas turbine blade design with different realistic inlet temperature and velocity boundary conditions. The effects of blade shaping and inlet conditions can only be fully understood by considering the aerodynamics and heat transfer concurrently; this is in contrast to the sequential method of blade design for aerodynamics followed by cooling. The inlet boundary conditions to the NGV simulations are governed by the existence of discrete fuel injectors in the combustion chamber. An appreciation of NGV shaping design under engine realistic inflow conditions will allow for an identification of the correct three dimensional shaping parameters that should be considered for design optimisation.

The Rolls-Royce efficient Navier-Stokes solver, HYDRA, was employed in all computational results for a transonic turbine stage. The single passage unsteady method based on the Fourier Shape Correction is adopted. The solver is validated under both rich burn (hot steak only) and the case with swirl inlet profiles for aerothermal characteristics; good agreement is noted with the validation data. Post processing methods were used in order to obtain time-averaged results and blade visualisations. Subsequently, a surrogate design optimisation methodology using machine learning combined with a Genetic Algorithm is implemented and validated.

A study of the effect of NGV compound lean on stage performance is carried out and contrasted for uniform and rich burn inlets, and subsequently for lean burn. Compound lean is shown to produce a tip uploading at the rotor inlet, which is beneficial for rich burn, but detrimental for lean burn. It is also found that for rich burn, fluid driving temperature is more dominant than HTC in determining rotor blade heat transfer, the opposite sense to the uniform inlet. Also, for a lean burn inlet, there is another role reversal, with HTC dominating fluid driving temperature in determining heat transfer.

A novel NGV design methodology is proposed that seeks to mitigate the combined effects of inlet hot streak and swirling flow. In essence, the concept two NGVs in a pair are shaped independently of each other, thus allowing the inlet flow non uniformity to be suitably accommodated.

Finally, two numerical NGV optimisation studies are undertaken for the combined hot streak and swirl inlet for two clocking positions; vane impinging and passage aligned. Due to the prohibitive cost of unsteady CFD simulations for an optimisation strategy, a suitable objective function at the NGV exit plane is used to minimise rotor tip heat flux. The optimised shape for the passage case resulted in the lowest tip heat flux distribution, however the optimum shape for the impinging case led to the highest gain in stage efficiency. This therefore suggests that NGV lean and clocking position should be a consideration for future optimisation and design of the HP stage.

Table of contents

List of figures **xi**

List of tables **xvii**

Nomenclature **xix**

1 Introduction **1**

1.1 Background 1
1.2 Rich Burn and Lean Burn Combustion Concepts 3
1.3 High Pressure Turbine 5
1.4 Thermodynamic Efficiency 7
1.5 Motivation 9
1.6 Thesis Outline 11
1.7 Accomplishments 12

2 Literature Review **13**

2.1 Introduction 13
2.2 HPT Stage Aerodynamic Design and Analysis 14
2.2.1 HPT Stage Aerodynamics 14
2.2.2 Effect of Vane Shaping on Aerodynamics 16
2.3 Effect of Hot Streaks on HPT Stage Aerodynamics and Heat Transfer . . . 19
2.4 Effect of Swirling Flow on HPT Stage Aerodynamics and Heat Transfer . . 23
2.5 Effect of Combined Hot Streak and Swirling Flow on HPT Stage Aerodynamics and Heat Transfer 26
2.6 Effect of Heat Transfer on Aerodynamics 27
2.7 Blade Shape Optimisation With and Without Turbine Inlet Non-Uniformities 28
2.7.1 Advances in Surrogate Modelling for HP Turbine Optimisation . . 31
2.7.2 Optimisation of HP Turbine Stage with Non-Uniform Inlet Profiles 33
2.8 Summary of Chapter 34

3 Computational Methodology **37**
3.1 Introduction . . . 37
3.2 CFD Solver . . . 38
3.3 Turbulence Modelling . . . 40
3.3.1 Spalart-Allmaras One Equation Model . . . 40
3.3.2 K - ω SST Turbulence Model . . . 41
3.4 Discretisation . . . 42
3.4.1 Discretisation in Space . . . 43
3.4.2 Discretisation in Time . . . 46
3.4.3 Temporal Discretisation for Unsteady Flows . . . 48
3.5 Single Passage Method . . . 49
3.6 Modelling the Interface between Stator and Rotor Row . . . 51
3.6.1 Mixing Plane Interface . . . 52
3.6.2 Sliding Mesh Interface . . . 53
3.7 Rolls-Royce CFD Suite . . . 53
3.7.1 PADRAM . . . 54
3.7.2 HYDRA . . . 55
3.8 Mesh Independency and Solver Validation . . . 55
3.8.1 Hot Streak Mesh Independency and Validation . . . 58
3.8.2 Inlet Swirl Mesh Independency and Validation . . . 69
3.9 Summary of Chapter . . . 75

4 Optimisation and Predictive Modelling **77**
4.1 Introduction . . . 77
4.2 Optimisation Strategies . . . 78
4.2.1 Evolution Algorithms (EA) . . . 79
4.3 Design of Experiments (DOE) . . . 82
4.3.1 Classical Designs . . . 82
4.3.2 Space-Filling Designs . . . 84
4.4 Surrogate Modelling . . . 85
4.4.1 Support Vector Regression (SVR) . . . 86
4.4.2 Random Forests for Regression . . . 88
4.4.3 Cross Validation (CV) for Predictive Models . . . 91
4.5 Optimisation Validation . . . 93
4.5.1 Test Case 1: Rosenbrock's Function . . . 93
4.5.2 Test Case 2: Ackley's Function . . . 95
4.6 Summary of Chapter . . . 97

5 NGV Shaping under a Rich Burn Combustor Exit Profile 101
5.1 Introduction . . . 101
5.2 Method and Computational Setup . . . 104
5.2.1 Time-Averaging Procedure . . . 104
5.2.2 Computation of Stage Aerothermal Efficiency . . . 105
5.2.3 Leaned NGV Grid Dependency Study for Hot Streak Inlet . . . 106
5.3 NGV Passage Analysis . . . 112
5.3.1 Effect of Compound Lean on HP Vane Aerodynamics . . . 112
5.3.2 Radial Mass Flow Redistribution in NGV passage . . . 118
5.4 Rotor Passage Analysis . . . 121
5.4.1 Influence of NGV Lean and Hot streak on Rotor Inlet . . . 121
5.4.2 Rotor Aerothermal Results . . . 127
5.5 Overall Heat Transfer and Stage Performance . . . 133
5.5.1 Stage Heat Transfer Results . . . 133
5.5.2 Stage Efficacy Results . . . 134
5.6 Summary of Chapter . . . 135

6 Effect of NGV Shaping Under Combined Hot Streak and Swirling Flow 137
6.1 Introduction . . . 137
6.2 Computational Setup . . . 138
6.2.1 CFD Solver . . . 138
6.2.2 Geometry and mesh . . . 139
6.2.3 Mesh sensitivity analysis . . . 140
6.2.4 Inflow temperature and velocity profile . . . 146
6.3 NGV Passage Analysis . . . 147
6.4 Rotor Blade and Tip Analysis . . . 152
6.4.1 Uniform inlet versus hot-streak only inlet . . . 152
6.4.2 Rotor tip heat transfer for combined hot streak and swirl . . . 159
6.5 Heat Transfer and Stage Efficacy . . . 164
6.6 Summary of Chapter . . . 167

7 NGV Design Optimisation for Lean Burn Combustion 169
7.1 Introduction . . . 169
7.2 NGV Design Concept . . . 170
7.2.1 Current State of Art . . . 170
7.2.2 Proposed Design Methodology and Analysis . . . 171
7.3 Design Optimisation Problem and Setup . . . 178

7.3.1 Problem Definition . . . 178
7.3.2 Steady Versus Unsteady CFD . . . 178
7.3.3 Objective Function . . . 180
7.3.4 Design Variable Definition . . . 181
7.3.5 DOE Sampling for CFD Simulations . . . 183
7.3.6 Model Setup . . . 185
7.4 Case 1: Design Optimisation with Impinging Hot Streak and Swirl . . . 186
7.4.1 Model Performance . . . 186
7.4.2 Feature Importance . . . 189
7.4.3 Optimised NGV Geometry . . . 190
7.5 Case 1: Analysis and Discussion . . . 192
7.5.1 NGV Analysis . . . 193
7.5.2 Rotor Analysis . . . 198
7.5.3 Integrated Results and Stage Efficacy . . . 203
7.6 Case 2: Design Optimisation with Passage Hot Streak and Swirl . . . 204
7.6.1 Model Performance . . . 204
7.6.2 Feature Importance . . . 206
7.6.3 Optimised NGV Geometry . . . 207
7.7 Case 2: Analysis and Discussion . . . 209
7.7.1 NGV Analysis . . . 210
7.7.2 Rotor Analysis . . . 214
7.7.3 Integrated Results and Stage Efficacy . . . 219
7.8 Summary of Chapter . . . 220

8 Conclusions and Future Work **223**
8.1 Introduction . . . 223
8.2 Conclusions . . . 223
8.3 Recommendations for Future Work . . . 225

References **227**

List of figures

1.1 Rolls Royce Trent 900 engine. Taken from Rolls-Royce (2005) 2
1.2 Combustor primary zone. Taken from Rolls-Royce (2005) 3
1.3 High pressure turbine stage 6
1.4 Progression of Turbine Entry Temperature in recent decades 8
1.5 Example block diagram of sequential blade design 10

2.1 Vortex structures present at endwall in a turbine blade passage 16
2.2 Positive compound leaned vane 18
2.3 Positive and negative jetting effects due to hot streak 21

3.1 Single passage domain 49
3.2 Upper and lower periodic boundaries for a single passage domain 51
3.3 Mixing plane interface 52
3.4 PADRAM parametric Capabilities 54
3.5 H-O-H Mesh Schematic 55
3.6 Computational mesh for a vane passage 57
3.7 Isentropic Mach number plots for varying cells in NGV boundary layer at 10%, 50% and 90% spanwise locations 60
3.8 Isentropic Mach number plots for varying radial grid points on NGV at 10%, 50% and 90% spanwise locations 61
3.9 Nusselt number plots for varying cells in NGV boundary layer at 10%, 50% and 90% spanwise locations 62
3.10 Nusselt number plots for varying radial grid points on NGV at 10%, 50% and 90% spanwise locations 63
3.11 Non-dimensionalised static pressure plots for varying cells in rotor blade boundary layer at 10%, 50% and 90% spanwise locations 65
3.12 Non-dimensionalised static pressure plots for varying radial grid points on rotor blade at 10%, 50% and 90% spanwise locations 66

3.13 Nusselt number plots for varying cells in rotor blade boundary layer at 10%, 50% and 90% spanwise locations 67
3.14 Nusselt number plots for varying radial grid points on rotor blade at 10%, 50% and 90% spanwise locations 68
3.15 Spanwise pitch angle variation (combustor-NGV count ratio of 1:2) 69
3.16 Spanwise yaw angle variation (combustor-NGV count ratio of 1:2) 70
3.17 Isentropic Mach number plots for swirl impinged and unimpinged NGV at 10%, 50% and 90% spanwise locations 72
3.18 Nusselt number plots for swirl impinged and unimpinged NGV at 10%, 50% and 90% spanwise locations 73
3.19 Nusselt number plots for rotor blade at 10%, 50% and 90% spanwise locations for inlet swirl 74

4.1 Tournament selection operator and a crossover procedure for the creation of a new EA generation 80
4.2 CCD example (consisting of two levels and three factors). Taken from Simpson (1998) 84
4.3 CCD example (Latin Hypercube Design) 85
4.4 Support Vector Regression modelling approach 88
4.5 Illustration of a decision tree in two dimensions 90
4.6 An example of k-fold cross validation 92
4.7 Matlab plot of Rosenbrock's function 94
4.8 Optimisation history for Rosenbrock's function 95
4.9 Plot of Ackley's function 96
4.10 Optimisation history for Ackley's function 97
4.11 Flow chart of optimisation procedure 99

5.1 Radial variation of pitch-averaged total temperature (K) at NGV inlet . . . 102
5.2 Inlet hot streak total temperature (K) profile 102
5.3 h-s diagram for a turbine stage 106
5.4 Isentropic Mach number distribution on NGV surface, with boundary layer grid variation 108
5.5 Nusselt number distribution on NGV surface, with boundary layer grid variation 109
5.6 Isentropic Mach number distribution on NGV surface, with radial point grid variation 110
5.7 Nusselt number distribution on NGV surface, with radial point grid variation 111
5.8 Blade-to-blade static pressure (Pa) distribution 112

5.9 NGV surface isentropic Mach numbers at 50% and 90% span sections for straight and leaned cases 113
5.10 Vane suction surface streamline movement and corner circulation 114
5.11 Vane pressure surface streamline pattern 114
5.12 Blade-to-blade flow on hub casing 115
5.13 Total pressure loss coefficient at NGV exit 116
5.14 Radial plot of pressure loss at vane exit 117
5.15 Radial plot of absolute yaw angle (deg) at vane exit 118
5.16 Mass flux (kg m^{-2} s^{-1}) contours on NGV exit plane 119
5.17 Streamline traces on mesh plane close to pressure surface and mass flux (kg m^{-2} s^{-1}) contours on the NGV exit plane 120
5.18 Radial plot of pitch-average mass flux (kg m^{-2} s^{-1}) at vane exit 121
5.19 Axial velocity (m s^{-1}) contours at NGV exit (uniform inlet) 123
5.20 Axial velocity (m s^{-1}) contours at NGV exit (hot streak) 123
5.21 Density (kg m^{-3}) contours at NGV exit for a uniform and hot streak inlet (leaned NGV configuration) 123
5.22 Radial plot of relative yaw angle (deg) at rotor inlet 124
5.23 Velocity diagrams at rotor inlet near to the tip 125
5.24 Radial plot of relative total pressure (Pa) at rotor inlet 127
5.25 Heat flux (W m^{-2}) contours on rotor pressure surface 128
5.26 Heat flux (W m^{-2}) contours on rotor suction surface 129
5.27 Local pressure differences on rotor pressure surface 130
5.28 Heat flux (W m^{-2}) on rotor tip (uniform inlet) 130
5.29 Heat flux (W m^{-2}) on rotor tip (hot streak inlet) 131
5.30 HTC (W m^{-2} K^{-1}) and T_{aw} (K) (time-averaged) on rotor pressure surface . . 132
5.31 Radial variations of pitch-averaged relative total temperature (K) at the rotor inlet 132

6.1 Computational mesh for different vane arrangements 140
6.2 Mesh dependency check for different NGV radial mesh points for isentropic Mach number at 10%, 50%, and 90% span 142
6.3 Mesh dependency check for different NGV radial mesh points for Nusselt number at 10%, 50%, and 90% span 143
6.4 Isentropic Mach number on rotor tip surface for varying number of grid points in the tip gap 144
6.5 Isentropic Mach number (pitch-averaged across tip surface) versus axial position on rotor tip surface for varying number of grid points in the tip gap 145

6.6 Heat flux on rotor tip surface for varying number of grid points in the tip gap 145
6.7 Heat flux (W m^{-2}) (pitch-averaged across tip surface) versus axial position on rotor tip surface for varying number of grid points in the tip gap 146
6.8 Combined hot streak and swirl profiles at turbine inlet (T_0 units: K) 147
6.9 Hot streak iso-surface visualisation (T_0 = 495 K) with and without swirl through NGV passage as viewed from upstream 148
6.10 Absolute total temperature (K) at vane exit for straight vane arrangement for positive and negative swirl directions, as well as a reference inlet hot streak case 150
6.11 Absolute total temperature (K) at vane exit (hot streak and positive swirl) . 151
6.12 Absolute total temperature (K) at vane exit (hot streak and negative swirl) . 152
6.13 Tip heat flux (W m^{-2}), HTC (W m^{-2} K^{-1}) and T_{aw} (K) for straight and compound lean vanes *(uniform inflow)* 153
6.14 Tip heat flux (W m^{-2}), HTC (W m^{-2} K^{-1}) and T_{aw} (K) for straight and compound lean vanes *(hot streak only)* 154
6.15 Heat flux (W m^{-2}), HTC (W m^{-2} K^{-1}) and T_{aw} (K) on rotor pressure surface for different vane shapes *(hot streak and positive swirl)* 155
6.16 δHTC and δT_{aw} plots on rotor pressure surface *(hot streak and positive swirl)* 157
6.17 Heat flux (W m^{-2}), HTC (W m^{-2} K^{-1}) and T_{aw} (K) on rotor pressure surface for different vane shapes *(hot streak and negative swirl)* 158
6.18 δHTC and δT_{aw} plots on rotor pressure surface *(hot streak and negative swirl)* 159
6.19 Tip heat flux (W m^{-2}), HTC (W m^{-2} K^{-1}) and T_{aw} (K) for straight, CL and RCL shapes *(hot streak and positive swirl)* 160
6.20 Tip pitch-averaged heat flux (W m^{-2}) for the three NGV shapes *(hot streak and positive swirl)* 161
6.21 δHTC and δT_{aw} plots on rotor tip surface for the three NGV shapes *(hot streak and positive swirl)* 161
6.22 Tip heat flux (W m^{-2}), HTC (W m^{-2} K^{-1}) and T_{aw} (K) for straight, CL and RCL shapes *(hot streak and negative swirl)* 162
6.23 Tip pitch-averaged heat flux (W m^{-2}) for the three NGV shapes *(hot streak and negative swirl)* 163
6.24 δHTC and δT_{aw} plots on rotor tip surface for the three NGV shapes *(hot streak and negative swirl)* 163

7.1 Portion of an annular NGV cascade, with a conventional periodic blading arrangement 172
7.2 A pair of unequally designed NGVs within a vane row 173

7.3 Comparison between baseline (straight) and unequal cases at NGV exit for absolute total temperature (K) and pressure loss coefficient (pitch averaged) 175
7.4 Rotor heat flux (W m^{-2}) on (left to right) on pressure and suction surfaces, as well as tip (straight vane case) 176
7.5 Rotor heat flux (W m^{-2}) on (left to right) on pressure and suction surfaces, as well as tip (unequal vane case) 176
7.6 Total temperature distribution at NGV exit and effect on rotor tip heat flux . 181
7.7 Design variable specification on nozzle guide vanes 183
7.8 t-SNE two dimensional representation of feature design space 187
7.9 Residual plot for SVR linear model 188
7.10 Lasso coefficients versus regularization parameter 190
7.11 Optimisation history using GA, indicating best and mean fitness per generation 191
7.12 Optimum and baseline NGV geometry comparison 192
7.13 NGV static pressure distributions on impinged vane at (a) 10%, (b) 50% and (c) 90% spanwise sections 194
7.14 NGV static pressure distributions on unimpinged vane at (a) 10%, (b) 50% and (c) 90% spanwise sections 195
7.15 Pitch averaged axial (left) and tangential (right) velocities (m s^{-1}) at the NGV exit plane for baseline and optimum case 196
7.16 Axial velocity (m s^{-1}) contours near NGV hub for baseline and optimum cases 197
7.17 Pressure loss coefficient difference (optimum - baseline) 198
7.18 Radial distribution of total temperature (K) at NGV exit plane 199
7.19 Rotor surface heat flux (W m^{-2}) distributions for baseline geometry on pressure surface (left) and suction surface (right) 200
7.20 Rotor surface heat flux (W m^{-2}) distributions for optimum geometry on pressure surface (left) and suction surface (right) 201
7.21 Rotor tip heat flux (W m^{-2}) distributions for the baseline (left) and optimised (right) NGV geometries 201
7.22 Rotor static pressure (Pa) distributions at (a) 10%, (b) 50% and (c) 90% spanwise sections for the baseline and optimum NGV configurations 202
7.23 t-SNE two dimensional representation of feature design space 204
7.24 Residual plot for SVR linear model 206
7.25 Lasso coefficients versus regularization parameter 207
7.26 Optimum and baseline NGV geometry comparison 209
7.27 NGV static pressure distributions on impinged vane at (a) 10%, (b) 50% and (c) 90% spanwise sections 211

7.28 NGV static pressure distributions on unimpinged vane at (a) 10%, (b) 50% and (c) 90% spanwise sections 212
7.29 Pitch averaged axial (left) and tangential (right) velocities (m s^{-1}) at the NGV exit plane for baseline and optimum case 213
7.30 Axial velocity (m s^{-1}) contours near NGV hub for baseline and optimum cases 214
7.31 Pressure loss coefficient difference (optimum - baseline) 214
7.32 Radial distribution of total temperature (K) at NGV exit plane 215
7.33 Rotor surface heat flux (W m^{-2}) distributions for baseline geometry on pressure surface (left) and suction surface (right) 216
7.34 Rotor surface heat flux (W m^{-2}) distributions for optimum geometry on pressure surface (left) and suction surface (right) 217
7.35 Rotor tip heat flux (W m^{-2}) distributions for the baseline (left) and optimised (right) NGV geometries 217
7.36 Rotor static pressure (Pa) distributions at (a) 10%, (b) 50% and (c) 90% spanwise sections for the baseline and optimum NGV configurations 218

List of tables

4.1 User specified values for GA parameters 93

5.1 Integrated Heat Flux (NGV) 133
5.2 Integrated Heat Flux (Rotor) 134
5.3 Non-adiabatic efficacy calculations 134

6.1 NGV heat flux breakdown for the three vane shapes (hot streak and positive swirl) 164
6.2 NGV heat flux breakdown for the three vane shapes (hot streak and negative swirl) 164
6.3 Rotor heat flux breakdown for the three vane shapes (hot streak and positive swirl) 165
6.4 Rotor heat flux breakdown for the three vane shapes (hot streak and negative swirl) 166
6.5 Stage performance calculations for all six cases 166

7.1 Percentage changes in heat load and efficacy relative to baseline (straight NGVs, positive swirl) 177
7.2 Steady versus unsteady CFD for non-adiabatic efficacy 179
7.3 Steady versus unsteady CFD for rotor heat load 180
7.4 Steady versus unsteady CFD adiabatic efficacy 180
7.5 Design variable specification 182
7.6 Prediction models to be investigated, with hyperparameters to be tuned . . . 185
7.7 Hyperparameter values specified for grid search 186
7.8 Performance metrics for the best model 188
7.9 Objective function for Linear SVR (predicted and actual CFD) 191
7.10 Objective function comparison for baseline and optimised geometries . . . 191
7.11 NGV optimum design variables 192
7.12 NGV heat flux component breakdown for baseline and optimum NGV cases 203

7.13 Rotor heat flux component breakdown for baseline and optimum NGV cases 203
7.14 Performance metrics for the best model 205
7.15 Objective function for Linear SVR (predicted and actual CFD) 208
7.16 Objective function comparison for baseline and optimised geometries . . . 208
7.17 NGV optimum design variables 209
7.18 NGV heat flux component breakdown for baseline and optimum NGV cases 219
7.19 Rotor heat flux component breakdown for baseline and optimum NGV cases 219

Nomenclature

Roman Symbols

$\dot{m}$	Mass flow rate
$\hat{f}$	Prediction function
$\hat{y}$	Predicted response value
$\mathbf{k}$	k^{th} fold in k-fold cross validation
$\mathbf{w}$	Weight vector
$\mathbf{x}_i$	Feature/input vector for the i^{th} sample
B	Total number of bootstrapped samples
b	Bias value
C	Chord length; blade chord
C	DOE centrepoint
D	Training dataset
d	Polynomial degree
h	Static enthalpy
k	Number of design variables
$K(\mathbf{x}_i, \mathbf{x})$	Kernel function
M	Mach number
m	Total number of samples in training set

Nu Nusselt number

p Total number of predictors/inputs

P_0 Stagnation pressure

q Heat transfer per unit area

R Universal gas constant

s Decision tree splitting value or cutpoint

T Static temperature

t time

V_x Velocity component in axial direction

x, y, z Components in the x, y and z directions, respectively

y Response/target value for the i^{th} sample

Greek Symbols

α, $\hat{\alpha}$ Lagrange multipliers for SVR

ε Insensitivity loss parameter

η_{non-ad} Non-adiabatic efficacy

γ RBF kernel parameter

γ Ratio of specific heats of a gas

ξ, ξ^* Slack variables for SVR model

Subscripts

0 Stagnation condition; initial condition

aw Adiabatic wall

axial Quantity in axial direction

bag Average prediction over all bagged samples

baseline Quantity representing the baseline/control case

$isentropic$ Isentropic

l Design variable lower bound

$local$ Local

$R1$ Region 1 for decision tree split

$R2$ Region 2 for decision tree split

rel Quantities in relative frame of reference

u Design variable upper bound

w Values at the wall

* Optimal point

b b^{th} bootstrapped sample

Acronyms / Abbreviations

CFD Computational Fluid Dynamics

GPU Graphics Processing Unit

LES Large Eddy Simulation

CCD Central Composite Design

CFD Computational Fluid Dynamics

CL Compound Lean

CV Cross Validation

DOE Design of Experiments

EA Evolution Algorithm

GA Genetic Algorithm

HP High Pressure

HPT High Pressure Turbine

HTC Heat Transfer Coefficient

LHS Latin Hypercube Sampling

MSE Mean Squared Error

NGV Nozzle Guide Vane

NGV Nozzle Guide Vane

RBF Radial Basis Function

RCL Reverse Compound Lean

RFR Random Forest Regression

RSS Residual Sum of Squares

RVE Representative Elemental Volume

SVM Support Vector Machine

SVR Support Vector Regression

SH Savage Hutter

Chapter 1

Introduction

1.1 Background

The advent of the gas turbine to the aviation industry over eighty years ago provided a catalyst in the development of aircraft engines with unimaginable success. Although the concept of the gas turbine had been around for at least a century earlier (patent filed by John Barber in 1791), the discovery of the application of the gas turbine to jet propulsion can be credited to efforts by Sir Frank Whittle in England and Hans van Ohain in Germany during the early 1930s.

The potential for the jet engine concept was extremely promising, as was demonstrated by the first experiment turbo-jet flight by the Heinkel He-178 in 1939, which produced impressive power output that was comparable with the most powerful piston engines at the time, whilst also dealing with the speed limitations posed by propeller propulsion (Barnard and Philpot (2004)). Additionally, flying at higher altitudes could partly manage the extremely high temperatures that were limiting efficiency; this also provided an added benefit for military applications. Furthermore, through the advancement in material development, blade design and cooling, the thermodynamic efficiency continued to see significant gains in the early life of the jet engine.

All modern high-bypass turbofan engines comprise of four main components, as is shown pictorially in Figure 1.1.

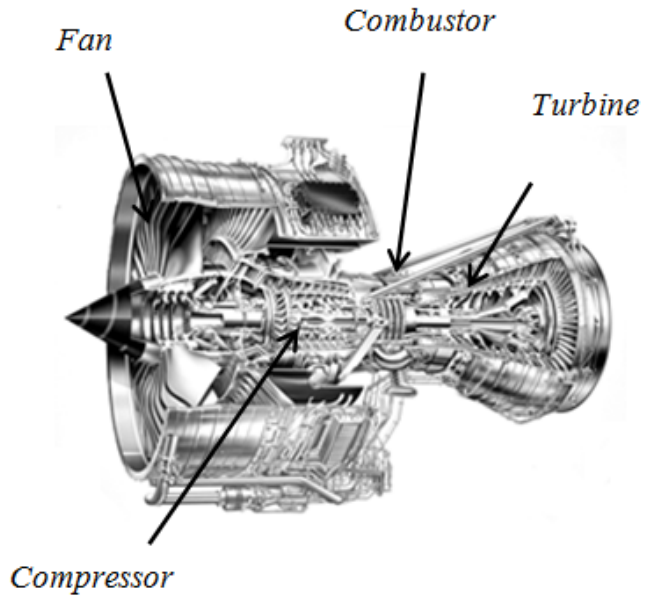


Fig. 1.1 Rolls Royce Trent 900 engine. Taken from Rolls-Royce (2005)

1. Fan. A large volume of incoming air from the engine inlet is essentially sucked into the fan blades where it is accelerated. A small proportion of the air passes through the core of the engine (the precise components are detailed next) in order to produce shaft work and some thrust. A majority of the high velocity air bypasses the engine core to produce forward thrust.

2. Compressor. Incoming air from the fan is compressed over several stages in order to increase the pressure and temperature of the air. The ideas of Whittle and von Ohain were based on a centrifugal compressor, which had drawbacks in terms of size and efficiency. The axial compressor, which is used in most modern large engines, was successfully implemented in the turbo- jet by Anselm Franz in 1942, and was able to increase the overall pressure ratio and efficiency.

3. Combustor. A fine spray of fuel is added to the pressurised air and burned which provides a further temperature rise (see Section 1.2).

4. Turbine. The primary function of the turbine is to convert kinetic energy (at the stator row exit) into mechanical energy (in the rotor blade row) in order to produce shaft work; this is used to drive the compressor and fan.

   This thesis is primarily concerned with the interactions between the combustor and turbine, which will now be discussed in more detail.

1.2 Rich Burn and Lean Burn Combustion Concepts

Within the combustion chamber, air from the compressor is mixed with fuel and burnt in order to further increase the temperature of the gas. Since the incoming compressor air is travelling at very high velocities, it is decelerated in order to ensure that the flame within the 'primary zone' (see Figure 1.2) remains alight.

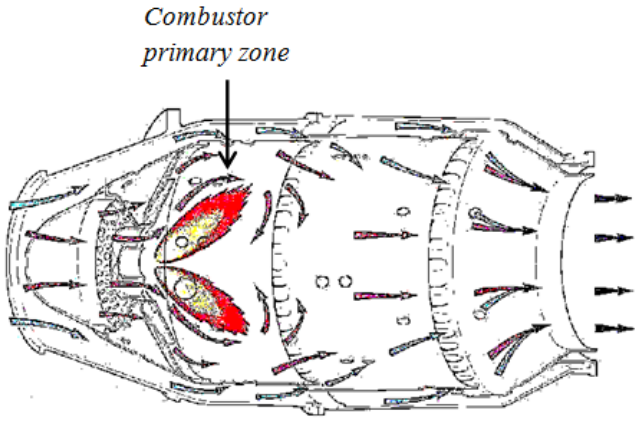


Fig. 1.2 Combustor primary zone. Taken from Rolls-Royce (2005)

In the primary zone, the air-to-fuel ratio is relatively low, and so air is gradually added and burnt. Since the air content is less than the stoichiometric ratio, the mixture

is fuel rich. For these 'rich burn' combustors, regions of excessively high temperatures exist which can result in high NO_x production rates in the secondary combustor zone.

Due to a discrete number of combustors placed around the annulus, there are regions of hotter and cooler gas flow present at the combustor exit with temperature differences of a considerable magnitude. This results in the creation of a combustor exit temperature profile which is commonly referred to as a 'hot streak.' A typical combustor-to-NGV count ratio is 1:2. For rich burn combustors, the exit variations are largely dominated by these temperature non-uniformities, which can affect the heat load on the vane (largely steady manner) and corresponding rotor blade row (unsteady manner).

Civil aviation is a growth industry, with some long-term forecasts suggesting approximately 30,000 new planes over the next twenty years. This growth, however, also leads to new challenges being faced by the industry. Aviation companies have received a large amount of attention in respect to greenhouse gas emissions, and will face pressure from governments globally to reduce their emissions. Rich burn combustors cannot meet the stringent NO_x regulations set out, and this has led to other options being considered. One effective alternative is the implementation of lean burn combustors. These combustors benefit from a higher air-to-fuel ratio which emits fewer unburned greenhouse gases, whilst also being less fuel intensive. This latter point is one to be noted, as it is well known that the price of fuel will increase over the next few decades. The excess air associated with this method results in lower temperatures and hence lower levels of NOx being produced (due to a reduction in oxidation of the nitrogen). The lean burn combustion concept does add extra complexities to combustor design; with excess air present, ignition will not be straightforward. A way of solving this problem is through the use of air swirlers that are capable of providing flame stabilisation and rapid mixing (McGuirk (2014)). They achieve this through creating

recirculation zones that form low velocity regions, in which ignition can occur. It is important to note that swirlers are used for rich burn combustion but are weak in comparison to those used for lean burn, which can be aggressive in order to deal with the excess air.

Therefore, for lean burn combustion the hot streak will be coupled with a highly distorted velocity field that arises from the swirling flow produced by the air swirlers. This poses new challenges for HPT design as they are positioned immediately downstream of these highly non-uniform combustor exit conditions (see next section).

1.3 High Pressure Turbine

The high pressure turbine (Figure 1.3) is responsible for driving the high pressure compressor through an extraction of work from the incoming hot gas. The high pressure turbine (HPT) stage experiences some of the harshest conditions within the jet engine. The NGV and rotor blades operate in an extremely pressure and temperature intensive environment, as a result of the exit conditions produced by the combustor. After combustion, the resulting gas passes through to the stationary NGV row, which accelerates the flow due to its convergent shape (Rolls-Royce (2005)). Once exiting the NGVs, the gas impinges the rotor blades, causing them to rotate. This kinetic energy is converted to mechanical energy, which drives the turbine shaft and high pressure compressor. However, due to losses within the system, efficiencies of just over 90 per cent are deemed acceptable by designers. Designers thus aim to minimise losses to increase the work done by the rotor and improve engine performance. Some of the most common types of losses will now be briefly discussed.

Profile losses are associated with the blade surfaces themselves, due to boundary layer formation, separation and other detrimental flow phenomena. It is known that the

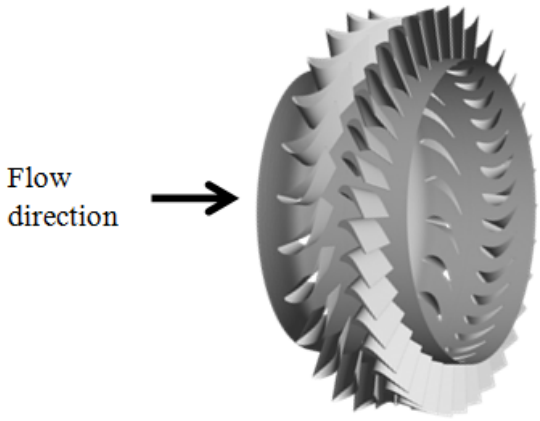


Fig. 1.3 High pressure turbine stage

rate of entropy generation per unit wetted area within a turbulent boundary layer (and hence loss) is proportional to the free stream velocity cubed (Denton (1993)). This implies that the loss generation is greater on the suction surface, where the highest velocities develop.

Leakage losses refer to losses that occur in the rotor tip region as flow leaks from the pressure surface to the suction surface. Since the angle at which leakage is occurring differs from the bulk main flow, there are mixing losses created that lead to vortex formation. Shrouded blades can minimise the tip leakage in the radial direction, but are heavy; removing the shroud would increase the rotor blade speed leading to a higher efficiency (see next section) but may result in higher leakage effects. Research efforts into reducing over tip leakage for unshrouded blades are ongoing.

The final loss to be mentioned is endwall and secondary flow loss (used interchangeably in this thesis), which is caused by the interaction between the endwall boundary layer and the blade leading edge. Due to the higher stagnation pressure at the leading edge, the boundary layer separates before reaching the blade, resulting in the formation of various vortex structures (see Chapter 2 for further details), that have implications on loss downstream of the NGV passage. This loss is especially important

for low aspect ratio blades (such as those found in turbines) and can account for up to half of the losses of the HPT. One way of dealing with the endwall and secondary losses is through contoured endwall design (for example, Harvey et al. (2000)) although gains in efficiency using this method are minimal. Another option is to exploit NGV geometrical design parameters to deal with these highly three dimensional flows. Amongst others, this includes blade lean, which is investigated in this thesis.

1.4 Thermodynamic Efficiency

For the HPT stage, a small incremental increase in efficiency can equate to large savings of fuel. One option to increase the work output would be to increase the mean blade speed (the turbine pressure drop is proportional to the square of the blade speed), as described in Rolls-Royce (2005). However, this has the adverse effect of increasing the stress in the turbine disc; rotor blades rotate at speeds in excess of 10,000 revolutions per minute experiencing very high centrifugal loads. A trade-off must therefore be sought.

An alternative (and more favourable) way of increasing specific thrust and thermal efficiency is through raising the turbine entry temperature (TET). The relationship between specific thrust and TET can be derived through consideration of the gas turbine engine cycle, as described in Lakshminarayana (1996).

Having increasingly higher TETs, however, can be problematic, since the incoming gas temperature exceeds the metal melting temperature of the NGV and rotor blades. These thermal loads add to a host of other stresses experienced by the HPT stage, including centrifugal loads associated with the rotor, fatigue and corrosion. There are two main ways in which turbine designers seek to address this issue. The first is through advances in material research, which has enabled the development of

nickel base superalloys, which demonstrate highly favourable mechanical strength characteristics at high temperatures (even increasing in strength with high temperatures up to a point). Second, since these materials are still unable to withstand the high temperatures experienced by the HPT, the blade surfaces must be cooled. The coolant for the turbine blades is fed in from the compressor (known as 'bleed' air), where compressed air is diverted away from the combustor. This results in a penalty to efficiency, as potential thrust is being lost through this process. Therefore, extensive cooling research studies have been carried out in order to minimise loss through effective cooling systems. Broadly speaking, there are internal and external cooling techniques. Internal cooling includes impingement cooling, where high speed air impacts with the inner surfaces of the vanes and blades, reducing the temperature. Another more efficient technique is external full coverage film cooling, which feeds through a thin layer of cool air (through closely spaced holes) to insulate the blade surface. Figure 1.4 illustrates how the development of cooling systems and techniques since the 1960s has resulted in significant increases in TET, and how in conjunction with material advances will aim to continue this upward trend.

Moving forward, it is important to know the thermal distribution on the HPT stage and understand and reduce the thermal loads that the blades are subjected to (through potential blade design), so that effective cooling systems may be designed. Heat transfer considerations are thus becoming increasingly more significant.

1.5 Motivation

Fuel savings can be achieved through an improvement in engine efficiency and power output, which has positive implications in monetary and environmental terms. As has been discussed, one of the most prominent ways of seeking an improvement (increase)

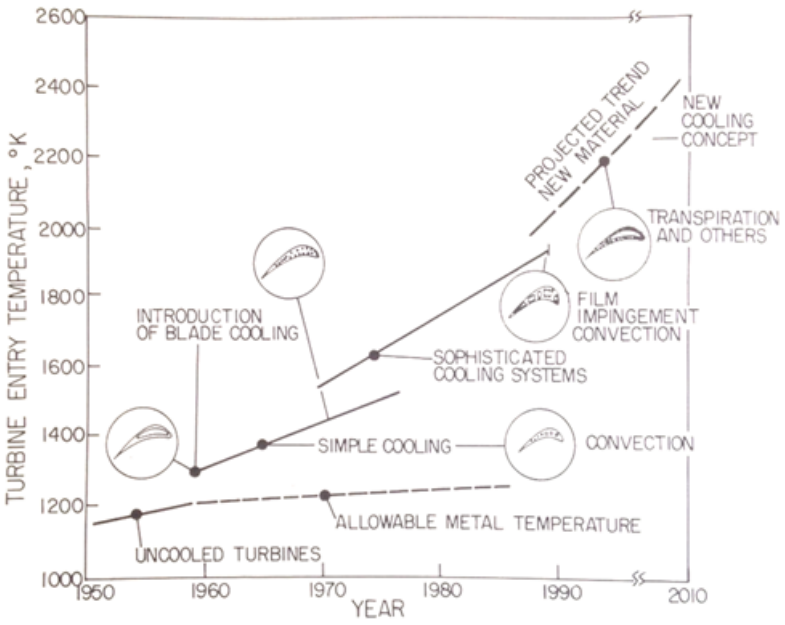


Fig. 1.4 Progression of TET in recent decades, taken from Lakshminarayana (1996)

in thermodynamic efficiency is through an increase in turbine entry gas temperatures. Higher TETs, however, lead to challenges in the design of NGVs and rotor blades, and one way of managing these issues has been through the development of superalloys, which are capable of coping with the extremely hot temperatures experienced and ensuring an adequate lifespan for the components. Furthermore, an effective cooling system can aid in reducing the adverse temperature effects, which can lead to higher operation temperatures being reached. This continuing trend of increasing the TET highlights the significance of heat transfer effects on the HP turbine stage.

The current practice for the design of turbine blades is largely sequential; blades are designed for aerodynamic performance in the first instance, followed by heat transfer and cooling, with little or no feedback in the design process, as exemplified by Figure 1.5. This design methodology fails to effectively account for heat transfer as it is now a discipline that must be considered on a similar level to the aerodynamics in order to obtain a favourable blade shape. Thus, the primary objective of this thesis is

to adopt a multi-disciplinary approach in order to assess the aerothermal (combined aerodynamics and heat transfer) performance on the HPT stage. This outcome will only be fully recognised when there is a clearer understanding of the flow and thermal mechanisms simulated with realistic turbine inlet conditions.

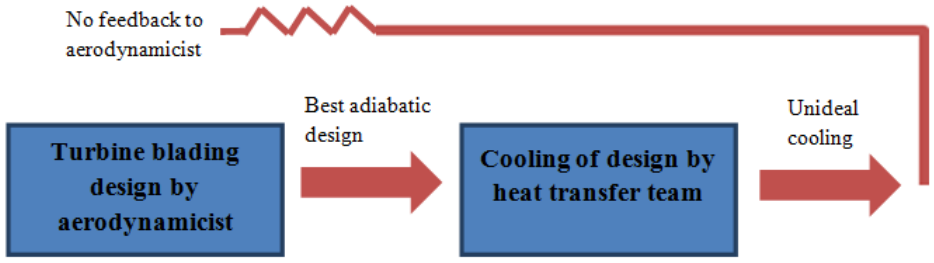


Fig. 1.5 Example block diagram of sequential blade design

With respect to previous studies relating to HPT blade design, there is a lack of exploration of the NGV design space that accounts for the non-uniform inlet profiles that the HP turbine stage experiences from the combustors (see Chapter 2). To simply translate the current understanding of vane shaping under uniform turbine inlet temperature conditions to those with current industry practice of rich burn combustion (i.e. hot streaks) may not be accurate in predicting the aerothermal stage performance.

The case for understanding the effect of NGV shaping on the rotor and overall stage under the correct turbine inflow conditions is even more crucial for modern lean burn combustors, which produce highly distorted velocity fields in addition to hot streaks. Since research into lean burn combustion is relatively new, there is a need to further the fundamental understanding of the aerodynamic and heat transfer characteristics yielded by such temperature and velocity profiles on the rotor and overall stage. This is particularly relevant for aircraft engines, as land based ones are more robust and heavy, and so suffer less combustion instability problems associated with lean burn. The transport of combined hot streaks and the swirling flow through the NGV and rotor passages and related interactions are far more complex than for the

rich burn scenario, where hot streaks are largely convected passively through the NGV row and affect the rotor mainly through changing the rotor relative inflow conditions only.

The motivation for the current work can be most appreciated and fully realised through an optimisation of the NGV row for HPT stage aerothermal performance. This is predicted to result in different optimum shapes depending on whether rich burn or lean burn combustion is being considered. Finally, the validity of any results is dependent on the fidelity of the CFD solver being used, thus any work carried out must not compromise on the accuracy purely to benefit from time savings. Ensuring the correct fidelity where necessary is paramount.

1.6 Thesis Outline

Chapter 2 provides a literature review of works relating to the understanding and effect of turbine inlet non-uniformities (temperature and/or velocity) and NGV shaping on the HPT stage from an aerodynamics and heat transfer perspective. Previous optimisation efforts on the stage are also explored. Chapter 3 provides a cogent explanation of the computational setup, including geometry and mesh creation, and the unsteady computational fluid dynamics (CFD) method. Validation of the CFD solver and mesh dependency studies are also presented in this chapter. The optimisation methodology follows in Chapter 4, with multi-fidelity strategies being discussed. Chapter 5 presents the first results chapter, analysing the aerothermal impact of NGV shaping under realistic hot streak (rich burn) conditions compared with conventional uniform temperature inlet studies. This is followed in Chapter 6 by an investigation of the effect of a combined hot streak and swirling flow (lean burn) profiles on rotor blade heat transfer. Additionally, NGV shaping is implemented in order to assess its impact

on rotor heat transfer and overall performance. After highlighting and understanding the influential design variables and objective function suitability, Chapter 7 presents an optimisation of the NGVs for the HPT stage performance with a lean burn combustor exit profile for two different inlet clocking (circumferential) positions. The chapter also introduces a novel NGV design method, which seeks to mitigate the adverse swirling flow effects brought about by a lean burn combustor exit profile. Finally, Chapter 8 presents conclusions based on the work in this thesis.

1.7 Accomplishments

This research thesis has culminated in the following:

- Publications
  (a) Rahim, A., He, L., 2014, "Rotor blade heat transfer of high pressure turbine stage under inlet hot-streak and swirl," ASME J. Eng. Gas Turbines Power., Vol. 137, pp. 062601 (also ASME conference paper GT2014-26832).
  (b) Rahim, A., Khanal, B., He. L., and Romero, E., 2013, "Effect of NGV lean under influence of inlet temperature traverse," ASME J. Turbomachinery., Vol. 136, pp. 071002 (also ASME conference paper GT2013-94686).
- Patents
  (a) He, L., Rahim, A., Khanal, B., Romero, E., 2014, "Stator Vane Row," Publication number: US20140245741 A1, Filing date: Feb 27 2014.

Chapter 2

Literature Review

2.1 Introduction

This chapter provides a background of past literature concerned with the turbine aerodynamics and heat transfer effects on high pressure stator and rotor blades. An emphasis is placed on understanding these effects from a design perspective and when subjected to inlet non-uniformities. Section 2.2 introduces the current understanding of secondary flow and its effect on performance, together with design techniques that may be used to mitigate the associated losses. Sections 2.3 and 2.4 provide a review of aerodynamic and heat transfer studies carried out with inlet hot streak and swirling flow conditions respectively (low speed and high speed experimental work, as well as computational RANS/URANS studies). Section 2.5 explores literature concerned with the combined hot streak and swirl turbine inlet case based on numerical studies, since experimental rigs capable of generating the required inlet are yet to be operational. Section 2.6 addresses the concept of HTC and its dependence on thermal boundaries, leading to the broader question as to what effect heat transfer may have on aerodynamics. Finally, Section 2.7 reviews various optimisation methodologies,

with a focus on optimiser development and the implementation of surrogate modelling techniques to turbine blade optimisation.

2.2 HPT Stage Aerodynamic Design and Analysis

Previous discourse concerning the design and understanding of axial flow turbines has mostly been considered from an aerodynamic perspective. This design orientation can also be found in an industry environment, in which conventional high pressure turbines are designed in a sequential manner; a design is sought for the adiabatic case by the aerodynamicist, which is then cooled by the heat transfer designer. This, however, results in little or no feedback of heat transfer in the design process.

The lack of emphasis on treating heat transfer in a more concurrent manner should not detract from the importance of the understanding of turbine aerodynamics on performance. To this extent, the discussion begins with a review of literature concerned with turbine aerodynamic design.

2.2.1 HPT Stage Aerodynamics

One of the biggest factors affecting the performance of axial flow turbines is the loss due to secondary flow formation. This aerodynamic loss, which is caused by viscous effects within the hub endwall boundary layer leading to the formation of vortices, can represent a significant proportion of the overall aerodynamic loss within a turbine blade row, with Sharma and Butler (1987) noting that this figure can be as high as 30-50%.

Some of the earliest works relating to secondary flow were conducted by Squire and Winter (1951) and Hawthorne (1955-a), in which the secondary flow generation

was explained mathematically in terms of the vorticity component perpendicular to the primary flow direction upstream of a blade row. This component interacts and causes the inlet boundary layer to roll up on the endwall. The loss in turbine work and increase in aerodynamic loss associated with secondary flows was shown experimentally by Langston et al. (1977) in which static pressure distributions on the surface of the aerofoil show a decrease in lift (and hence turbine work) close to the endwall compared with a midspan section (as illustrated through a decrease in the area between the suction and pressure surface points for the endwall section).

The general understanding of secondary flow features at the turbine endwalls is well established, as developed by Langston (1980) and Sharma and Butler (1987), and confirmed by Hodson and Dominy (1987) and Yamamoto (1989), amongst others. Sieverding and den Bossche (1983) employ a smoke visualization technique in a turbine cascade in order to assess the progression of the horseshoe vortex through a blade passage (as discussed below).

The three dimensional flow field illustrating secondary flow features is shown in Figure 2.1 (taken from Sharma and Butler (1987)). As the inlet boundary layer interacts with the vane leading edge, it separates at a saddle point, forming a horseshoe vortex. The pressure side leg of the vortex, known as the passage vortex, is drawn into the passage, and grows as it accumulates new lossy endwall boundary layer fluid that is forming beneath it, as travels towards the suction side. The suction side leg of the horseshoe vortex forms a second vortex, which is referred to as a counter vortex (since it rotates in the opposite sense to the passage vortex). Once the passage vortex reaches the suction side, it interacts with the counter vortex. Sharma and Butler (1987) note that the counter vortex wraps around the passage vortex, which was contrary to that observed by Langston et al. (1977). Harvey et al. (2000) comment on the counter vortex remaining above the passage vortex, causing it to move upwards as the passage

vortex grows. Through cascade measurements, Gregory-Smith et al. (1988) noted that for cases with high flow turning, the secondary flow loss can not only be attributed to the passage vortex formation close to the endwall, but a significant loss presence is also found in the spanwise direction.

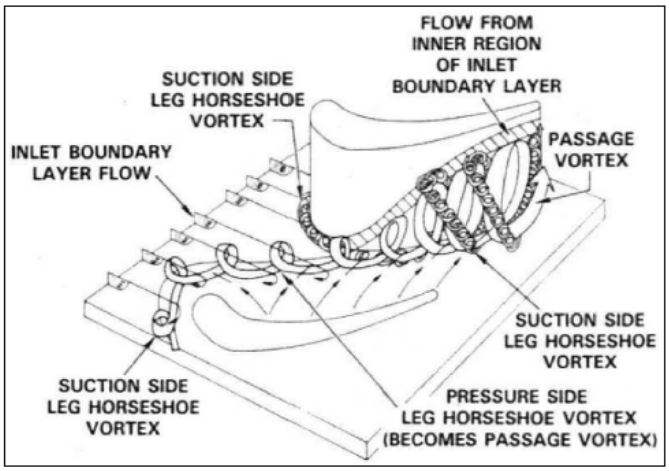


Fig. 2.1 Illustration of vortex structures present in a turbine blade passage. Image taken from Sharma and Butler (1987)

Langston (2001) builds on a review carried out by Sieverding (1985) and provides an update of developments in the understanding of secondary flow, with endwall vortex structures described, as well as potential methods of reducing and predicting secondary flow.

More recently, Pullan (2006) investigates secondary flow interactions between the stator and rotor passages using a low speed experimental setup as well as a numerical study. He notes that in the presence of the stator exit flowfield, additional vortex structures are observed in the rotor passage away from the hub endwall. In addition, due to the sensitivity and relevance of the stator exit pitchwise pressure gradient, steady simulations were not capable of predicting the loss correctly.

2.2.2 Effect of Vane Shaping on Aerodynamics

Studies into the effect of three dimensional geometric design parameters to manipulate flow control and blade loading as well as downstream processes have been conducted for many years. Perhaps the most well-known design parameter is the concept of blade lean i.e. non-radial stacking. A positive compound lean, which will be referred to as 'compound lean' hereafter, is a circumferential bend that is applied to the near casing and hub sections from the pressure surface to the suction surface of the blade. This is shown in Figure 2.2. Conversely, a reverse compound lean is defined in this study as a bend that is applied to the near casing and hub sections from the suction surface to the pressure surface. Some of the earliest experimental studies into the effect of NGV lean on turbine aerodynamics were presented by Houmouziadis and Hubner (1985), Huber et al. (1985), Walker (1987) and Harrison (1992), in which the lean was shown to affect (and hence could be used to control) the loading distribution and secondary flow features in the vane passage. Specifically, Huber et al. (1985) showed that compound lean increased the blade loading at the midspan whilst reducing the loading at the endwalls, resulting in a lower hub endwall loss. This was also observed by Wang et al. (1987), explaining the reduction in hub loss through a migration of low energy boundary layer fluid towards the midspan due to the pressure gradient. Harrison (1992) noted that the exit yaw angle associated with blade lean is non-uniform which may lead to extra mixing losses downstream. Denton and Xu (1999) provide one of the earliest computational reviews of blade lean and sweep (airfoil sections displaced in an axial manner) in a fully three dimensional flow field for turbine and compressor blades. It is noted that for low aspect ratio blades the radial pressure term dominates. This is due to the blade to blade pressure gradient being much greater than hub to casing pressure gradient, resulting in radial lines of constant pressure. More recently, numerical and computational investigations have been conducted by Sharma et al. (2003), Tan et al.

(2003) and Bagshaw et al. (2005), which have confirmed these previous studies i.e. a redistribution of loss that is dependent on the direction of lean. In particular, Bagshaw et al. (2005) show that in the case of reverse compound lean, the endwalls experience a higher secondary flow loss compared with the midspan, which is due to a radial force in the blade passage that reduces the pressure at the hub and casing. Gregory-Smith et al. (2008) explain and show that this feature can be utilised in conjunction with contoured endwalls, in order to reduce secondary flow and overall loss. More recently, Rosic and Xu (2012) have shown agreement with previous work in relation to the change in spanwise pressure (and loading) distribution due to lean, but also highlighted that this may not result in a reduction in total loss. Generally speaking, there appears to be no conclusive findings on blade lean in relation to loss reduction due to blade lean. Furthermore, the literature discussed above follows the conventional wisdom adopted for turbine blade design (for NGV and rotor), in which aerodynamics is designed for, which determines the subsequent cooling, with little feedback or interaction in order to understand the role of heat transfer combined with aerodynamics.

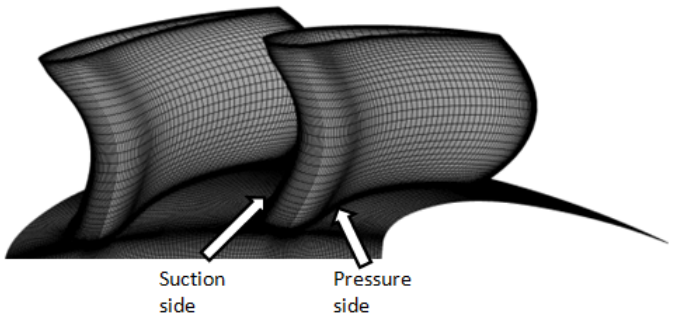


Fig. 2.2 Positive compound lean (CL) vanes

It is noted that most of the previous CFD analyses for blade lean studies are based on steady flow simulations (either in a single blade row or multi-rows linked by a mixing-plane for passing the mixed out information from one row to another). Although the steady flow solution may capture some basic flow features during the design

process, particularly for those configurations/conditions where the radial (rather than circumferential) aerodynamic and thermal variations dominate, any steady assumption must be treated with caution. Turbomachinery flows are naturally unsteady mainly due to the relative motion of rotors and stators. The stator/rotor interaction especially is a 3D unsteady phenomenon driven by the wake/shock/rotor interactions. In fact, the works of Takahashi et al. (1996) already indicated that unsteady flow simulations would be needed to capture the correct physics of hot-streak migration. Recent work by the authors group (Khanal et al. (2012), Khanal et al. (2013)) also highlighted the need for unsteady CFD while investigating the effect of inlet non-uniformities for HP turbines.

2.3 Effect of Hot Streaks on HPT Stage Aerodynamics and Heat Transfer

This section looks at past studies concerned with understanding the effect of hot streaks produced by 'rich burn' combustion as discussed in Chapter 1, on the HPT stage. The impact on the stage performance is discussed in a multidisciplinary sense, with aerodynamics, heat transfer and mechanical considerations accounted for. Research into hot streak effects on the turbine stage has spanned well over 20 years, with early experimental efforts occurring in the late 1980's. Perhaps one of the most basic aerodynamic concepts relating to hot streaks can be attributed to Munk and Prim (1947), which showed theoretically that for a stationary blade row (such as the NGV row of a HPT), a stagnation temperature gradient could not generate secondary flows within the passage provided that the stagnation pressure gradient was unchanged, and this was shown by Horlock (1977) to be due to the preservation of the dynamic pressure. In contrast, additional secondary flows are generated in the rotor blade row, due to the

relative motion, as the stagnation temperature gradients cause gradients in the 'reduced stagnation pressure'. A fundamental understanding of hot streak migration through the rotor passage was based on an unsteady wake transport compressor study by Kerrebrock and Mikolajczak (1970). It was seen that rotor pressure surfaces experience higher heat loads compared with the suction surface. This 'preferential heating' was a result of an enhanced cross passage fluid movement from the suction side to the pressure side due to an increased incidence of the hot gas; this is often referred to as positive jetting. The progression of hot streak studies through the past couple of decades will now be discussed with consideration given to both experimental (measured) and computational (predicted) works. The remainder of this section is divided into sub headings that the author feels reflects the development of the understanding of hot streaks.

- Early rotor heat load findings. In one of the early experimental works relating to hot streaks, Butler et al. (1989) simulated a streak of hot air seeded with carbon dioxide through an axial turbine stage. A redistribution, or segregation, of the hot and cold gas (to the pressure and suction rotor surfaces respectively) was observed in a similar manner to what was noted by Kerrebrock and Mikolajczak (1970) for compressors. This preferential migration was confirmed computationally by Dorney et al. (1992) using a three-dimensional Navier-Stokes solver. This was also confirmed by Sharma et al. (1988), Rai and Dring (1990), and Krouthen and Giles (1990). In addition, Dorney et al. (1992) found the blade count ratio to have had a 'substantial' effect on unsteady flow characteristics (discussed further in the next sub section). Realistic rotor blade hot streak measurements within a transonic turbine were first conducted by Shang (1995), where it was observed that the hot gas was radially transported towards the hub endwall. Furthermore, this was confirmed by CFD simulations by Shang and Epstein (1997) and the endwall migration was attributed partly to a buoyancy effect.

- Effect of blade count. Shang and Epstein (1997) and Sondak et al. (2002) identified the heating effect to be partially dependent on the stator-rotor blade interaction, thus heating may be reduced by an appropriate choice of vane/blade count ratio. Further, it was found that the total blade heat load showed an increase by as much as 30 per cent when exposed to a hot streak, which may be attributed in part to the turbine geometry (Shang and Epstein (1997)).
- Effect of hot streak clocking. One of the earliest reports on the effect of circumferential positioning or clocking of the hot streak was performed experimentally by Roback and Dring (1993). In this study, the hot spot was aligned with the NGV leading edge and transported along the vane suction surface and interacts with the wake at the vane exit. This high-loss fluid is then convected from the pressure surface to the suction surface and is termed as a negative jet. The negative jet mechanism acts in the opposite sense to the segregation effect due to the incidence. The opposing effects of the positive and negative jets are shown in Figure 2.3. This results in a more uniform temperature field. The numerical works of Dorney and Gundy-Burlet (1996) and Takahashi et al. (1996) confirmed this finding by also noting that hot streak clocking can minimise blade heating.

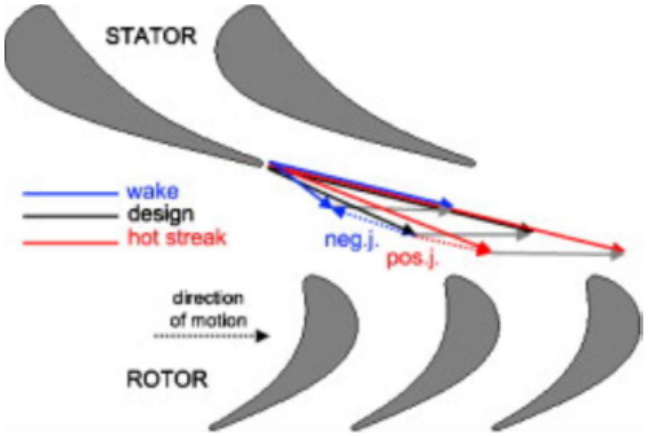


Fig. 2.3 Positive and negative jetting effects due to hot streak inlet. Image taken from Salvadori et al. (2012)

- Aeromechanical understanding. There have been fewer works relating to vibration responses caused by hot streaks. One of the earlier works by Manwaring and Kirkengr (1997) found that even the low pressure turbine experienced unsteady forcing, showing that the inlet temperature distortion has importance throughout the turbine stages from an aeromechanical perspective.
- Effect of hot streak-to-NGV count ratio. He et al. (2007) investigated the influence of the clocking position and combustor hot streak-to-NGV count ratio for hot streak profiles on aerothermal performance. With a hot streak count matching the number of NGVs, it was (again) confirmed that preferential heating occurs; strong suction-to-pressure surface heat load convection. It was found that a hot streak impinging the vane leading edge resulted in a lower rotor pressure side heat load compared with a passage clocking position. However, with a reduced hot streak count (as is the case for realistic engine configurations), the clocking effect was minimal on rotor surface temperature distribution, but did result in an overall lower temperature in comparison to the initial case.

A more recent experimental study using a non-uniform inlet temperature generator was performed at QinetiQ UK by Chana et al. (2003). It was found that NGV heat transfer was higher on the suction side with little change on the pressure side in comparison to a uniform temperature inlet. Chana and Jones (2002) also took heat transfer measurements on the rotor tip and casing. They found a reduction in overall heat load with the inlet non-uniformity. Povey and Qureshi (2009) reviewed different existing combustor simulators and hot streak profiles, leading to the development of a new, more realistic simulated profile with radial and circumferential variations. Using this profile, and impinging the hot streak on the vane leading edge, Qureshi et al. (2010) found that the vane endwalls experienced a significant reduction in heat load compared to the uniform case, which was attributed to the local gas driving temperature. A

subsequent study by Qureshi et al. (2011-a) showed that changes in heat transfer on the rotor blade and casing were driven by the adiabatic wall temperature (driving temperature) with little change in heat transfer coefficient. Additionally, Salvadori et al. (2012) noted that the radial temperature profile for the hot streak case was not fully mixed out at the vane exit and this resulted, contrary to previous literature, in a cooler rotor casing.

It is noted that these efforts used a combustor-to-NGV count ratio of 1:1, as opposed to a more realistic 1:2, and it has already been seen by He et al. (2007) that this can lead to altered temperature distributions on the rotor blade.

To conclude this section, a special mention on the importance of correct flow conditioning is necessary. Wheeler et al. (2011) carried out a study of blade tip heat transfer for low speed and high speed flows. It was shown that the heat transfer was a strong function of Mach number, resulting in significant differences in tip heat load and flow structure. Additionally, high speed flows were seen to be less sensitive to the choice of turbulence model. Furthermore, recent work by He and Oldfield (2011) showed that unsteady hot streaks could lead to a noticeable time-averaged heat transfer reduction compared to a steady equivalent cases with the same mean inlet temperature. These studies highlight the need for turbine investigations to be carried out under correct flow conditions, and also indicating the need to adopt unsteady simulations for heat transfer analysis for HPT design, particularly under hot streak conditions.

2.4 Effect of Swirling Flow on HPT Stage Aerodynamics and Heat Transfer

The concept and purpose of swirling flow for lean burn combustion was explained in Chapter 1. There have been considerable research efforts looking at the effect of swirling flow on combustion and emission characteristics. Lilley (1977) provided a review of swirling flow effects for general combustor practical applications. This was followed by studies focussing specifically on gas turbine combustors from, amongst others, Datta and Som (1999) (effect on combustion efficiency) and Gupta et al. (2001) (flame thermal characteristics).

For the HPT stage, it is expected that swirling flow would most certainly affect the inlet total pressure gradient, free-stream turbulence levels, inlet flow incidence angle and secondary flow patterns. Previous works relating to these topics will now be mentioned in order to gain an appreciation of the possible effects of swirl on aerodynamic and heat transfer characteristics within the turbine stage:

- Total pressure gradients. A study by Hawthorne (1955-a) showed that for inviscid, compressible flows, stagnation pressure gradients (found in swirling flows) would give rise to secondary vorticities for three-dimensional flows; this could potentially reduce the adiabatic efficiency for the HPT stage.
- Combustor turbulence. Early experimental measurements by Goldstein et al. (1983) showed that the gas turbine combustor exit (for different types of combustors) turbulence intensity could range from approximately 8% to 40%. An investigation by Hodson (1985) found that the free-stream turbulence affected the boundary layer transition location close to the leading edge of a high speed blade. Radomsky and Thole (2002) found that at higher free-stream turbulence levels the suction side boundary layer transition position moved further upstream

compared with lower levels. This was confirmed by Ames et al. (2003) in a low speed linear cascade, who also observed an augmentation of heat transfer with higher turbulence. More recently, large scale high free-stream turbulence measurements were taken in a high speed linear cascade by Nasir et al. (2009). Higher augmentation of heat transfer was observed especially on the pressure surface, and on the suction side (except for a Mach number of unity) as the exit Reynolds number was increased. The earliest boundary layer transition on the suction side was seen for the highest Reynolds number.

- Incidence angle and loading distribution. Jouini et al. (2001) investigated the effect of incidence on loading and observed major changes in the loading distribution near the vane leading edge. Higher losses were observed at off-design incidence angles. Benner et al. (1997) found that the loading distribution was more influential than leading edge geometry in determining the secondary flow field and losses. Further, Corriveau and Sjolander (2004) studied the influence of loading on the performance of HPT blades, and found that an aft loaded airfoil yielded a significant reduction in loss for design incidence and Mach number.

The first known experimental studies assessing the impact of swirling flow on the HPT stage were conducted by Qureshi et al. (2011-b) using the Oxford Turbine Research Facility (OTRF). A combustor swirl simulator, capable of generating an 'aggressive' swirl (yaw and pitch angles of over +/- 40 degrees) was implemented, and the swirler-to-vane count ratio was 1:2. These experimental investigations (together with computational results presented in the papers) highlighted the impact of swirl on the NGV passage. It was observed that an increase in incidence at the hub relative to casing at the turbine inlet (caused by the swirl) resulted in changes to aerodynamic loading (higher at hub) and secondary flow structures through the NGV passage. Additional loss cores attributed to the swirl were observed close to the hub at the

vane exit caused by a redistribution of boundary layer fluid to the region due to the higher loading and surface velocities. The vane heat transfer results on the surface and endwalls revealed altered Nusselt number distributions due to loading and secondary flow field considerations.

In a subsequent study by Qureshi et al. (2011-c), the effect of swirl on the rotor passage (blade and casing) was carried out using the same experimental arrangement. It was noted that the effect of clocking position (circumferential positioning) of the swirl relative to the vanes (vane impinging or passage aligned) on rotor heat transfer was minimal. An increase in heat transfer was observed on both the casing (approximately 20%) and rotor blade surface with the introduction of swirl. The general increase in heat transfer on the blade itself was attributed to an enhancement in turbulence intensity and secondary flow. For a swirl inlet, Beard (2010) measured a mean turbulence intensity of 11.2%, and for a uniform inlet, Chana (1992) measured a turbulence intensity of 6.5%. Therefore, the free stream turbulence intensity is almost doubled due to the introduction of swirl.

More recently, Beard et al. (2014) carried out an experimental (using the OTRF rig) and numerical study to assess the impact of swirl on the HPT stage efficiency. The measured and predicted results showed a decrease in shaft and turbine power, and an overall drop in efficiency of approximately 1% with swirl present, with the additional loss being linked to the vane passage altered flow characteristics, and reaffirming the views of Qureshi et al. (2011-c) that the swirl is more influential in the vane passage compared with the rotor passage.

Schmid et al. (2014) investigated the impact of swirl on a 1.5 stage axial turbine whilst varying the swirl orientation (where positive swirl is defined as being in the direction of rotor blade rotation) and clocking position. It was found that the swirl orientation made a significant difference with negative swirl being more favourable

(1.5% higher than positive counterpart) and leading edge clocking provided some benefit over passage aligned.

The current section together with Section 2.3 has assessed the previous understanding of the isolated effects of swirl and hot streaks respectively on the HPT stage. It is known that in practice, for a lean burn combustor arrangement, both of these phenomena occur simultaneously within a jet engine. The next section assesses past relevant literature that considers both effects concurrently, as the conventional wisdom of unsteady hot streak migration through the rotor passage may be influenced by the swirling flow, resulting in altered rotor heat transfer characteristics. Indeed, this was exemplified in a recent study by Khanal et al. (2012) where the superposition of a hot streak only and swirl only inlet solution did not equate to the direct solution of a combined inlet hot streak and swirl for the heat flux on a rotor blade.

2.5 Effect of Combined Hot Streak and Swirling Flow on HPT Stage Aerodynamics and Heat Transfer

The computational works by Khanal (Khanal et al. (2012), Khanal et al. (2013)) appear to be the only known studies in open literature that investigate the effect of combined hot streak and swirl on the HP turbine aerothermal behaviour. In the paper, Khanal et al. (2012) uses an unsteady single passage CFD solver (HYDRA, developed by Rolls-Royce) and investigates four different inlet conditions, arising from two clocking positions, vane impinging and passage aligned, and two swirl directions, positive swirl and negative swirl. It was seen how the hot fluid stretching towards the tip and/or hub endwall through the vane passage may be explained through a splitting of the swirl vortex, with the resulting fluid migration dependent on the swirl direction and partially on the clocking position. In the rotor passage, the rotor surface streamlines

were strongly influenced by the swirl direction, caused by the local surface pressure difference, with significant radial flow patterns being observed. Furthermore, the rotor heat transfer showed sensitivity to swirl direction and clocking, with the combined hot streak and negative swirl cases yielding the highest efficiency gain.

This latter result was confirmed in Khanal et al. (2013) in which unsteady heat load time traces revealed smaller peak to peak heat load fluctuations for negative swirl compared with the positive swirl combined case. However, this was not the case in terms of unsteady tangential blade forcing, where negative swirl was less favourable than its positive counterpart. In an unsteady analysis through a spectral breakdown, the location or passing frequency of the dominant heat load amplitude was again seen to be dependent on swirl direction and clocking position, reinforcing that they represent two important considerations in the design of the HP turbine stage.

2.6 Effect of Heat Transfer on Aerodynamics

One of the main aims of this thesis is to assess the aerothermal behaviour within the HP turbine stage environment; it is therefore important to ensure that all methods and parameters used to measure these interactions are valid. In a recent paper by Mafulli and He (2014-a), the effect of wall temperature on the heat transfer coefficient is examined. The study assesses whether aerodynamics fully determines heat transfer and is thus independent of the imposed thermal boundary condition. Essentially, this follows the conventional thinking that there is a one way interaction from the fluid to the metal (at a blade surface for example) and that the solid to fluid interaction is negligible. Furthermore, this suggests that the linear relationship between heat flux and wall temperature is a misrepresentation, and a non-linear approach must be taken, in which the HTC must be corrected locally for a given wall temperature.

A two dimensional study by Mafulli and He (2014-b) measuring local HTC for a range of temperature ratios (wall-to-inlet ratio) at the trailing edge of a transonic aerofoil indicates significant variation in HTC. The wall temperature is seen to affect the external aerodynamic flow structure and alter the boundary layer which in turn affects the external HTC. A follow up study by Mafulli and He (2014-b) reinforced this concept with an application to a three dimensional turbine passage. The results reinforced the concept of strong HTC dependency on temperature ratio, with HTC variations of up to 40% being observed. Secondary flow patterns were also sensitive to the wall temperature, with a cooled case showing a reduction in loss. To address this non-linear, dependency issue, a new three-point correction method is proposed by the authors in order to calculate the HTC on a local basis, allowing a significant reduction in error when compared with the standard two-point method. The correction method was also applied to the case of a transonic rotor blade flat and winglet tip by Zhang and He (2013) to address HTC variations of up to 30% that were obtained from the conventional two point method. Again, the method was seen to provide more accurate results.

2.7 Blade Shape Optimisation With and Without Turbine Inlet Non-Uniformities

The application of numerical optimisation to turbomachinery in a variety of contexts is well established in the open literature, but includes (relatively fewer) studies that explore the concept of optimisation for the high pressure turbine blades and overall stage. To this extent, this section will not only include a review of results from turbine blade optimisation, but also optimisation methodologies applied to compressor blades and NGV passage profiled endwalls.

In general terms, optimisers are combined with a CFD or other high fidelity solver in order to search a design space, with defined shaping parameters and possibly constraints, and to locate the optimum (as a maximum or minimum) solution for a specified objective function. An optimisation algorithm may be of a deterministic or stochastic nature. Deterministic methods include gradient based optimisers which search along the direction of steepest descent (through gradient computations) in order to find an optimum. There have been instances when a gradient based optimizer has been implemented for blade optimisation, for example, Chen et al. (2009). Chen et al. (2009) applied a simple gradient based optimization method to a rotor compressor blade, with an approximate three per cent increase in adiabatic efficiency. Although the gradient method can be easily programmed and implemented, it also poses several difficulties, primarily the expensive task of computing the gradient of the objective function, especially if the number of design parameters is large (Periaux and Verstraete (2010)). To some extent, this problem has been addressed by Wang and He (2010-a) in which the gradients are obtained efficiently using a continuous adjoint method, which was then implemented in an optimization methodology and subsequently validated by Wang et al. (2010-b).

A stochastic optimisation approach introduces an element of randomness to achieve a solution for a given problem. The rationale for this concept is to ensure that the optimisation algorithm does not get trapped in a local optimum region, thereby not resulting in a correct solution. There are a number of different stochastic methods that are continuously being explored and developed. Evolution algorithms (EAs) have been used extensively for blade optimization. The most common type of EAs are known as genetic algorithms (GAs), the theory of which will be discussed in Chapter 4.

Milli and Shahpar (2008) used an adaptive range multi-objective genetic algorithm (ARMOGA) to redesign the hub endwalls for a HP turbine stage for aerodynamic stage

efficiency. The ARMOGA code focusses on the highest fitness individuals and narrows the design space in this manner. In the paper, 800 partially converged CFD solutions (initialised from a high fidelity baseline case) successfully achieved an improvement in stage efficiency through the minimisation of secondary flow effects.

Oksuz and Akmandor (2010) note that although GAs can converge to the global optimum, they require a large number of function evaluations. They propose a modified GA using coarse and fine meshes (to represent low/high fidelity) in order to cope with the dynamic optimization environment and achieve a slight improvement in torque over a standard GA.

Multiobjective optimisation procedures have become a useful tool in achieving a compromise between conflicting objectives for application in real world situations. Puente et al. (2011) applied a multi objective differential evolutionary (DE) algorithm (developed by Storn and Price (1997)) combined with full CFD analysis to a three dimensional transonic vane row in order to improve efficiency whilst reducing rotor forcing. This study served as a continuation of the work of Joly et al. (2010), who investigated the objectives in a two dimensional set up. Similar to the genetic algorithm, the DE is iterative in allowing individuals to evolve over successive generations. The method or function applied for the evolution is where it differs from the conventional GA strategy. A difference vector between two points selected randomly from the design space is used to evolve a third random point. In this manner, the design space is exhausted in order to locate a global optimum. The optimised result showed that rotor forcing could be reduced by smoothing the static pressure field.

Boselli and Zangeneh (2011) use an inverse design approach to optimize a low pressure turbine rotor. This method computes the optimum blade geometry based on a prescribed blade loading distribution. A non-dominated sorting genetic algorithm

(NSGA) is used in an attempt to reduce the maximum stress whilst preserving the rotor performance.

2.7.1 Advances in Surrogate Modelling for HP Turbine Optimisation

Through experience, designers have realised that coupling an optimization tool with a CFD solver alone would result in hundreds of hours being expended, since each new geometry alteration in the design process would have to be evaluated by the flow solver; a highly infeasible option given the computational cost associated with this method. This has led to the development of surrogate or metamodels that can be used to provide an approximation (the fidelity is dependent on the designers requirements) for objective functions and constraints. This is discussed further in Chapter 4. If a metamodel is to be selected, it requires what is known as a training period in which high fidelity CFD simulations are implemented in order for the numerical model to provide reasonable approximations for the objective functions. The method that is used to select the initial geometry cases to train the metamodel is known as Design of Experiments (DOE). There is a requirement that the DOE must contain sufficient data, enough to locate the optimal regions, but not an excessive amount that time is wasted on poor, sub optimal regions. Forrester et al. (2006) assessed the accuracy of the approximate objective function values generated from metamodels by comparing with the actual values. It showed that an increase in DOE points resulted in a higher accuracy metamodel, up to a point, after which any further increase in the number of DOE points would return minimal increase.

The number of surrogate model studies relating to blade optimisation is limited. Arabnia and Ghaly (2010) investigated the effect of blade stagger and lean through

a stage optimization, using a GA coupled with an Artificial Neural Network (ANN) metamodel. A weighted sum of individual objectives (namely, the total to total efficiency and the streamwise vorticity) was used as the objective function, which included a penalty term to account for any constraints. An efficiency improvement of almost 2 per cent was attained, with the optimized stator being leaned towards the pressure surface, and for the rotor towards the suction surface and having an increased stagger angle distribution.

Mengistu et al. (2007) used a genetic algorithm (GA) coupled with an ANN to aerodynamically optimize the shape of a rotor turbine blade. Several design parameters are investigated, with results showing that the tangential chord and throat area are important for improving overall efficiency.

Keskin et al. (2008) implements a multi objective EA coupled with a Kriging meta-model in order to optimize a compressor blade. Although a performance improvement was achieved (lower pressure loss at design and off-design incidence), the Kriging approach initially caused convergence problems due to the poor approximation quality of the model.

Aside from Kriging and ANN modelling methods, a study by Modgil et al. (2013) provides an optimisation of a HP turbine rotor blade for aerodynamic performance. In this case, a generalised polynomial chaos surrogate method is implemented, which is capable of sampling and constructing polynomial functions using stochastic collocation techniques as opposed to response surface methods based on CFD simulations in order to achieve an approximate function evaluation. The resultant design yielded increased turning and high rotor blade Mach numbers compared with the baseline.

As has been discussed previously, rotor blade tips represent a significant portion of secondary flow loss in the high pressure turbine stage. Therefore, there is significant interest in blade tip design, particularly in obtaining optimum configurations in order

to potentially understand underlying geometrical implications. A recent paper by Schabowski et al. (2014) investigated tip design in a multidisciplinary sense, with an aeromechanical optimisation using a radial basis function metamodel and ARMOGA optimiser. Coarse (reduced density) meshes were employed during the optimisation process, and verified with standard meshes once a solution had been obtained. The resultant tip geometry showed a reduction in loss through reduced pressure differences and splitting of the loading due to geometrical design parameters. Maesschalck et al. (2013) also performed a tip optimisation for aerothermal performance. A separate heat load and aerodynamic loss parameter were defined to be used in a multi objective approach, which coupled a differential evolution optimiser with an ANN. The tip geometry is modified on a two dimensional local profile basis, with the authors noting that the shaping in this manner can reduce aerodynamic loss by up to 20% and heat load loss by 40%.

2.7.2 Optimisation of HP Turbine Stage with Non-Uniform Inlet Profiles

To the author's knowledge, there appears to be no literature concerned with NGV or rotor blade optimisation of the high pressure turbine stage in the presence of only an inlet temperature distortion from the combustor exit. Furthermore, there is just one known paper that relates to an aerodynamic design optimisation in the presence of lean burn conditions (temperature and moderate yaw and pitch angles), although the centre of the hot streak is not aligned with the swirling core. This was conducted by Shahpar and Caloni (2012) in which an NGV and rotor blade are both subject to modification, with shaping parameters including lean, skew, sweep and leading edge aerofoil recambering. The optimisation methodology was based on a Multipoint Approximation Method (MAM), in which high resolution and low resolution regions

are obtained in parallel using response surface models in order to construct accurate trust regions at a lower computational cost. The procedure yielded an optimum shape with a 1% improvement in stage efficiency. The optimised NGVs, with changes in recambering and skew, reveal an offloading at the endwalls (hence reduction in secondary flow) compared to the baseline, and a reduction in boundary layer thickness due to an increase in axial velocity. The optimised rotor blade had a lean applied towards the tip, and exhibited a lower pressure difference at the tip, leading to a reduction in the leakage vortex.

2.8 Summary of Chapter

The chapter commenced with the progression in understanding of secondary flow losses in the high pressure turbine. There has been significant interest relating to geometrical parameters that may be used to control the secondary flow, in order to reduce this loss. A review of NGV lean design studies (spanning several decades) was presented, with experimental and computational work being considered. Despite the many publications related to this topic, the author highlighted the lack of understanding regarding its effect on HPT aerodynamic performance for a transonic turbine. Furthermore, these previous efforts have been carried out based on an adiabatic set up; there has yet to be a study assessing the impact of NGV lean on heat transfer and aerodynamics in a concurrent manner. Moreover, the studies considered assume a uniform temperature at the turbine inlet; this provides a useful basis but may not be representative of the effects of lean once inlet non-uniformities (temperature and/or velocity) are introduced.

Past hot streak and swirl studies have studied their effects in isolation on NGV and rotor aerodynamics and heat transfer. However, the vast majority of these studies

have been conducted using a straight vane configuration; little attempt has been made to explore the effect of three dimensional design parameters.

The author wishes to conclude this chapter by drawing some observations and remarks relating to the past studies discussed in Section 2.7 relating to HP turbine optimisation. One of the motivations for the present work is to bridge the gap in understanding relating to all of the aspects mentioned below:

- From the discussion above, it becomes apparent that a significant proportion of studies relating to HP turbine blade optimisation have been designed with only an aerodynamic objective function or goal. This has been reflected in an adiabatic efficiency objective, pressure loss or other parameters relating to secondary flow. Designing in a single objective, single disciplinary sense may be restricting the potential or validity of the results. It is unclear in these studies as to what the effect is on the heat transfer, and vice versa. Indeed the recent findings by Mafulli and He (2014-a) and Mafulli and He (2014-b) indicate an aerodynamic-heat transfer interaction/dependence that should not perhaps be neglected. This is further supported by the findings of Khanal et al. (2013). Therefore, the true optimum shape in a multidisciplinary environment subjected to high pressures and high temperatures has not fully been explored to date.
- Another fundamental element that has not been included in HP design optimisation studies is the correct modelling or flow conditioning at the turbine inlet (most papers implement a uniform temperature). It has been noted in previous sections of this review (Sections 2.3 to 2.5) that inlet non-uniformities can significantly affect heat transfer and aerodynamics with the NGV and rotor passages, which would most certainly alter the optimum shape and possibly the design parameters to be considered.

- Following on from implementing the correct inflow conditions, the modelling of hot streaks and swirling flow would most certainly affect NGV-rotor aerothermal interactions, and points to the use of a higher fidelity CFD solver, i.e. unsteady methods. This has potentially not been an issue with past literature, since a uniform turbine inlet temperature would be less likely to qualitatively affect the accuracy of mixing plane results as adopted in all previous HPT design optimisation studies in open literature.

Chapter 3

Computational Methodology

3.1 Introduction

The work underpinning this thesis is based on computational fluid dynamics, CFD, which uses a Navier-Stokes based solver to solve the flow around a chosen geometry using a computational grid. The computational approach adopted for the current work will first be described, commencing with the Navier-Stokes governing equations, followed by turbulence modelling, spatial and temporal discretisation. The periodic flow unsteadiness related to stator-rotor row interactions is discussed, with the Fourier Shape Correction method enabling a smaller three dimensional computational domain to be considered (and therefore reduction in CFD time cost). The remainder of the chapter will focus on grid independence studies and validation cases for the HYDRA solver against known experimental data specific to an isolated hot streak and isolated swirl combustor exit conditions that will be implemented in this thesis.

3.2 CFD Solver

In this research, the CFD solver HYDRA was used to simulate the three dimensional geometry cases. In HYDRA, the governing Navier-Stokes equations are solved in integral form. The integral form for a control volume V with a differential surface area S can be expressed as follows:

$$\frac{\partial}{\partial t}\int_V \mathbf{Q}dV + \int_S [\mathbf{E}+\mathbf{F}+\mathbf{G}-\mathbf{S}_V]\cdot dS = \int_V \mathbf{H}dV \tag{3.1}$$

Where **H** represents all source terms such as body forces and energy sources. The vector **H** is zero in absence of external forcing and heat sources. The conservative variables and the inviscid flux variables are represented as:

$$\mathbf{Q}=\begin{bmatrix}\rho\\ \rho u\\ \rho v\\ \rho w\\ \rho e_t\end{bmatrix},\quad \mathbf{E}=\begin{bmatrix}\rho u\\ \rho u^2+p\\ \rho uv\\ \rho uw\\ (\rho e_t+p)u\end{bmatrix},\quad \mathbf{F}=\begin{bmatrix}\rho v\\ \rho uv\\ \rho v^2+p\\ \rho vw\\ (\rho e_t+p)v\end{bmatrix},\quad \mathbf{G}=\begin{bmatrix}\rho w\\ \rho uw\\ \rho vw\\ \rho w^2+p\\ (\rho e_t+p)w\end{bmatrix}$$

For air as an ideal gas, the total energy term is given by $\rho e_t = \frac{p}{\gamma-1}+\frac{1}{2}\rho(u^2+v^2+w^2)$.

where $\gamma = c_p/c_v$ is the ratio of specific heat coefficients under constant pressure and constant volume.

The term $\mathbf{S}_v$ is the source term containing the viscous flux derivatives and is represented as:

$$\mathbf{S}_v = \frac{\partial \mathbf{E}_v}{\partial x} + \frac{\partial \mathbf{F}_v}{\partial y} + \frac{\partial \mathbf{G}_v}{\partial z}.$$

$$\text{where } \mathbf{E}_v = \begin{bmatrix} 0 \\ \tau_{xx} \\ \tau_{xy} \\ \tau_{xz} \\ u\tau_{xx} + v\tau_{xy} + w\tau_{xz} + q_x \end{bmatrix}, \quad \mathbf{F}_v = \begin{bmatrix} 0 \\ \tau_{yx} \\ \tau_{yy} \\ \tau_{yz} \\ u\tau_{yx} + v\tau_{yy} + w\tau_{yz} + q_y \end{bmatrix}$$

$$\text{and } \mathbf{G}_v = \begin{bmatrix} 0 \\ \tau_{zx} \\ \tau_{zy} \\ \tau_{zz} \\ u\tau_{zx} + v\tau_{zy} + w\tau_{zz} + q_z \end{bmatrix}$$

The viscous stress tensor components are related to the Cartesian velocity components by the following equations:

$$\begin{aligned}
\tau_{xx} &= \frac{1}{\mathrm{Re}_\infty}\left(2\mu\frac{\partial u}{\partial x} + \lambda\nabla.\mathbf{v}\right), \quad \tau_{xy} = \tau_{yx} = \frac{\mu}{\mathrm{Re}_\infty}\left(\frac{\partial u}{\partial y} + \frac{\partial v}{\partial x}\right) \\
\tau_{yy} &= \frac{1}{\mathrm{Re}_\infty}\left(2\mu\frac{\partial v}{\partial y} + \lambda\nabla.\mathbf{v}\right), \quad \tau_{yz} = \tau_{zy} = \frac{\mu}{\mathrm{Re}_\infty}\left(\frac{\partial v}{\partial z} + \frac{\partial w}{\partial y}\right) \\
\tau_{zz} &= \frac{1}{\mathrm{Re}_\infty}\left(2\mu\frac{\partial w}{\partial z} + \lambda\nabla.\mathbf{v}\right), \quad \tau_{xz} = \tau_{zx} = \frac{\mu}{\mathrm{Re}_\infty}\left(\frac{\partial w}{\partial x} + \frac{\partial u}{\partial z}\right)
\end{aligned} \tag{3.2}$$

where μ is molecular viscosity and λ and μ are related by Stokes' hypothesis :$\lambda + 2\mu/3 = 0$.

The heat flux terms are evaluated as:

$$q_x = \frac{\mu}{(\gamma-1)\,\mathrm{Pr}\,\mathrm{Re}_\infty M_\infty^2}\frac{\partial T}{\partial x} \quad , \quad q_y = \frac{\mu}{(\gamma-1)\,\mathrm{Pr}\,\mathrm{Re}_\infty M_\infty^2}\frac{\partial T}{\partial y} \quad , \quad q_z = \frac{\mu}{(\gamma-1)\,\mathrm{Pr}\,\mathrm{Re}_\infty M_\infty^2}\frac{\partial T}{\partial z} \tag{3.3}$$

3.3 Turbulence Modelling

Turbulence is a state of fluid motion characterised by random and chaotic three-dimensional vorticity. Turbulence results in increased energy dissipation, mixing, and heat transfer in the flow. Turbulence is of great technological importance because of the large effects it has on the flows in which it occurs. The prediction of these effects in a flow of interest is one of the primary concerns of applied fluid dynamicists, and it is often the case that the uncertainties in a fluid dynamic calculation are dominated by uncertainties in the turbulence model. Therefore, one can argue that for researchers of fluid dynamics, turbulence models, their approximations and limitations are extremely important. Turbulence research is continuously evolving and several turbulence modelling strategies are available today.The choice of turbulence model depends on several factors such as the physics encompassed in the flow, the established practice for a specific class of problem, the level of accuracy required, the available computational resources, and the amount of time available for the simulation.

3.3.1 Spalart-Allmaras One Equation Model

The Spalart-Allmaras, or SA, turbulence model (Spalart and Allmaras (1992)) has been designed specifically for applications that concern wall bounded flows. The model has provided good predictions for boundary layers that experience adverse pressure

gradients. The model is defined as a low Reynolds number model, which relies on the viscous affected regions of the boundary layer to be properly resolved. The turbulent transport equation solved in this case is given by,

$$\frac{\partial}{\partial t}(\rho\tilde{\nu}) + \frac{\partial}{\partial x_j}(\rho\tilde{\nu}u_j) = G_\nu + \frac{1}{\sigma_\nu}\left[\frac{\partial}{\partial x_j}\left((\mu+\rho\tilde{\nu})\frac{\partial\tilde{\nu}}{\partial x_j}\right) + C_{b2}\rho\left(\frac{\partial\tilde{\nu}}{\partial x_j}\right)^2\right] - Y_\nu \tag{3.4}$$

where G_ν is the production term of turbulent viscosity and Y_ν is the turbulent viscosity destruction term. σ_ν and C_{b2} are constant. Additional details of the turbulence model can be found in Spalart and Allmaras (1992). The system of partial differential equations above is solved for the transport variable $\tilde{\nu}$ to calculate μ_t using the relation, $\mu_t = \rho\tilde{\nu}f_{\nu 1}$. The turbulent viscosity term (μ_t) is required to close the system of equations in Equation 3.1 (in order to model the Reynolds stress terms). $f_{\nu 1}$ is the viscous damping function. The standard RANS SA turbulence model uses the distance to the nearest wall to define a length scale d that is used to calculate the production and the dissipation terms of turbulent viscosity.

3.3.2 K - ω SST Turbulence Model

The two equation SST model is based on the calculations of the turbulence kinetic energy, K, and the rate of dissipation of the eddies, ω, as expressed below:

$$\frac{\partial(\rho K)}{\partial t} + \frac{\partial(\rho u_j K)}{\partial x_j} = \rho P - \beta^*\rho\omega K + \frac{\partial}{\partial x_j}\left[(\mu+\sigma_K\mu_t)\frac{\partial K}{\partial x_j}\right] \tag{3.5}$$

$$\frac{\partial(\rho\omega)}{\partial t} + \frac{\partial(\rho u_j\omega)}{\partial x_j} = \frac{\gamma}{\nu_t}P - \beta\rho\omega^2 + \frac{\partial}{\partial x_j}\left[(\mu+\sigma_\omega\mu_t)\frac{\partial\omega}{\partial x_j}\right] + 2(1-F_1)\frac{\rho\sigma_{\omega 2}}{\omega}\frac{\partial K}{\partial x_j}\frac{\partial\omega}{\partial x_j} \tag{3.6}$$

The terms on the right hand side represent the eddy-viscosity production, dissipation and conservative diffusion respectively. The additional term in the ω equation describes the cross diffusion. The turbulent viscosity is computed through the equation:

$$\mu_t = \frac{\rho a_1 K}{max(a_1\omega, \Omega F_2)} \tag{3.7}$$

Where Ω is the vorticity magnitude. The variable definitions and constants relating to the SST equations above can be found in Blazek (2001). The boundary conditions for the kinetic turbulent energy and the specific dissipation at solid walls are:

$$K = 0, \; and \; \omega = 10 \cdot \frac{6\mu_L}{\rho\beta 1 (d_1)^2} \tag{3.8}$$

Where d_1 is the distance of the first cell centroid from the wall. For the inflow boundaries, the following freestream values are implemented:

$$\omega_\infty = C_1 \frac{\|\mathbf{v}_\infty\|_2}{L}, \; (\mu_T)_\infty = (\mu_L)_\infty 10^{-C_2}, \; K_\infty = \frac{(\mu_T)_\infty}{\rho_\infty}\omega_\infty \tag{3.9}$$

Where L is the length of the computational domain, C_1 takes a value between 1 and 10, and C_2 is specified between 2 and 5.

3.4 Discretisation

This chapter has thus far presented a derivation of the governing equations to describe the dynamics of a fluid in three dimensions, and has accounted for the effects of turbulence on the flow variables to be determined. The methodology used to obtain a solution to the equations is described in this section. The equations in their current integral form provide a continuous range of values throughout the domain for the different

flow variables (e.g. density, velocity, energy) but cannot be solved analytically; instead an approximation is required in which the flow variables are solved using numerical methods at discrete points in the domain. This discretisation process is applied in both a spatial and temporal sense. In a spatial sense, the physical space is sub divided into a number of elements, a process that is known as grid generation. Following this, the flow variables are assigned a location within this grid. The methods implemented in this thesis will be discussed in section 3.4.1. The temporal discretisation is necessary in both the steady and unsteady flow equations. In a steady sense, it is used as pseudo time in order to 'march' the iterative solution towards convergence. In an unsteady context, the time represents a physical term. This will be detailed in Section 3.4.2.

3.4.1 Discretisation in Space

The entire physical space is divided into smaller elements to create a grid or mesh. There are different ways in which this may be achieved. A structured grid is used in the current work, which implements quadrilateral shaped elements in two dimensions and hexahedra elements in three dimensions. It is noted that there is no overlapping or gaps between any two elements. One of the main benefits of a structured approach is due to the arrangement of the grid points (where the quantities of the flow variables are stored). Since they are ordered in a uniform, structured manner, it allows for fast access to neighbouring grid points, resulting in an efficient use of computer memory storage and leading to a quicker computation time.

Once a grid has been generated, control volumes are constructed on the grid to evaluate the integrals of the convective and viscous fluxes, and the source terms (Equation 3.1), enabling the solution vector to be determined. By assuming that each control volume does not change in time, and that the surface integrals may be

approximated by the sum of fluxes crossing the faces of the volume, Equation 3.1 can be rewritten for a certain control volume, with location XYZ, as:

$$\frac{d\mathbf{Q}_{XYZ}}{dt} = -\frac{1}{V_{XYZ}}\left[\sum_{n=1}^{N_F}(\mathbf{E}+\mathbf{F}+\mathbf{G}-\mathbf{S}_V)_n \Delta S_n\right] \tag{3.10}$$

The bracketed term in Equation 3.10 is known as the residual, which will be denoted as $\mathbf{R}$. In Equation 3.10, ΔS_n is the area of the n^{th} control volume face, and N_F is the total number of faces for a particular volume, which is six in three dimensions. The positioning of each of the control volumes does not necessarily have to coincide with the physical computational grid. In this thesis, a cell vertex scheme with dual control volumes is implemented; this means that the flow quantities to be determined are located at the grid nodes, with the control volume surrounding it. In two dimensions, this is achieved by joining the centroids of four cells that have the node in common. In three dimensions, the centroids of eight cells have to be connected in order to create the six faces of the control volume.

The computation of the face area of a control volume and the volume of a hexahedron can be found in full in Blazek (2001). In essence, an area expression for the face vector S_n in three dimensions can be computed using the area of a quadrilateral (extended to three dimensions) derived by the formula of Gauss. The face area of the n^{th} control volume is then:

$$\Delta S_n = \sqrt{(S_{x,n}^2 + S_{y,n}^2 + S_{z,n}^2)} \tag{3.11}$$

This operation is required for three of the six faces of a given hexahedron control volume. The other three faces are obtained from the relevant neighbouring control volumes in order to reduce memory storage and number of computations. The volume

of the control volume V_{XYZ} is obtained as a third of the summation of the midpoint of each control volume face multiplied by its face area vector.

The convective and viscous fluxes at each face of the control volume are required in order to compute the solution variable. For the convective flux, an interpolation of the flow variables or fluxes from the grid points to the control volume face is required. For a given control volume face, a separate, non-symmetric, interpolation procedure, referred to as an upwind scheme, is carried out on the left and right side of the face. This procedure is followed by a computation of the fluxes through the face using the difference between the left and right state via a specified function. In this thesis, a flux difference splitting scheme is chosen to solve for the convective fluxes. This scheme is inbuilt in the Rolls-Royce CFD code, HYDRA. Specifically, a modification proposed by Moinier (1999) to Roe's approximate Riemann solver is used. The original Roe solver (Roe (1981)) can be expressed as:

$$\mathbf{F}_C = \frac{1}{2}(\mathbf{F}_R + \mathbf{F}_L) - \frac{1}{2}A_{Roe}(\mathbf{W}_R - \mathbf{W}_L) \tag{3.12}$$

Where $\mathbf{F}_R$ and $\mathbf{F}_L$ are computed using the reconstructed solution vectors $\mathbf{W}_R$ and $\mathbf{W}_L$ on the right and left side of the face. A_{Roe} is the Roe matrix which is equivalent to the convective flux Jacobian, $\frac{\partial \mathbf{F}}{\partial \mathbf{W}}$, with the flow variables replaced by the Roe averaged variables, as defined in Blazek (2001). One of Moinier's alterations to the Roe solver is through an approximation of the (expensive) calculation of convective flux terms for the left and right states. This is achieved through the use of nodal values, called N1 to the left of the volume interface, and N2 to the right, as opposed to an interpolation. Another modification arises through defining a four point scheme in order to reduce the computational cost of the second term on the right and side of Equation 3.12. This leads to:

$$\mathbf{F}_C = \frac{1}{2}(\mathbf{F}_{N1} + \mathbf{F}_{N2}) - \frac{1}{2}(1-\kappa) - A_{Roe}(\mathbf{L}_{N2} - \mathbf{L}_{N1}) \tag{3.13}$$

Where $\kappa = [0,1]$ and represents a one-parameter family of second order schemes. This work adopts a value of $\kappa = \frac{1}{2}$ as recommended in Moinier (1999). $\mathbf{L}$ represents a pseudo-Laplacian, which is evaluated in Moinier (1999).

For non-derivative quantities in the viscous flux term, it is possible to average the flow variable at nodes N1 and N2 (located either side of the interface in question) in order to obtain the variable at the control volume face. However, in the treatment of gradient terms, an auxiliary or secondary control volume is required and constructed using the edges of adjacent grid cells. Subsequently, the gradient may be computed through the use of Green's theorem, in which the first derivative may be expressed in terms of the surface integral of a particular flow variable. For example, the derivative in the x-direction for flow variable U is:

$$\frac{\partial U}{\partial x} \approx \frac{1}{\Omega_{aux}} \sum_{n=1}^{N_{faces}} U_n S_{x,n}^{aux} \tag{3.14}$$

Where $S_{x,n}^{aux}$ represents the x component of the face vector for the auxiliary control volume. The flow variable for each face may be calculated through the use of an averaging technique. The computation of the convective and viscous flux terms across the control volume faces has been presented. The following section discusses how the equations may now be discretised in a temporal sense.

3.4.2 Discretisation in Time

The approach that is undertaken in order to achieve temporal discretisation and convergence is dependent on whether the problem is one of a steady or unsteady nature.

For the steady flow case, the time derivative is discretised using an explicit m-stage Runge-Kutta scheme, which is given by:

$$W^0 = W^n$$
$$\Delta W^i = -\alpha_i \Delta t \Gamma^{-1} R^{i-1}$$
$$W^{n+1} = W^m$$

Where W represents the primitive variables, $\Delta W^i = W^i - W^n$ and $i = 1, 2, ..., m$ is the stage counter for the m-stage scheme. α_i is the multi-stage coefficient for the i^{th} stage. Γ represents the preconditioning matrix, and R^i is the residual term. The time step Δt is computed from the CFL (Courant-Friedrichs-Lewy) condition:

$$\Delta t = \frac{2 \cdot CFL \cdot V}{\Sigma_f \lambda_f^{max} A_f} \tag{3.15}$$

Where V is the cell volume, A_f is the face area, and λ_f^{max} is the maximum of the local eigenvalues of the preconditioned system. In the current work, the CFL was set as 2.

Convergence acceleration for the explicit formulation above can be achieved with the use of local time stepping, in which the solution at each control volume is advanced in time with respect to the cell time step; the CFL number is close to the local stability limit.

A multigrid approach developed by Fedorenko (1962) and Bakhvalov (1966) is also adopted for convergence acceleration. The underlying motivations for the use of this method results from the fact that point explicit (iterative) solvers are efficient in removing the local, high frequency (oscillatory) errors in the solution on a given mesh. However, they are far less effective in reducing the global, low frequency errors on a

specified mesh. The multigrid method can assist in solving this problem through the implementation of fine and coarser meshes, in which global errors on the finer meshes become local errors on the coarser meshes which are easier to eliminate.

3.4.3 Temporal Discretisation for Unsteady Flows

The importance of unsteadiness in the analysis of high pressure turbine performance has been discussed in Chapter 2, particularly due to the stator-rotor interactions that occur. Therefore, a formulation for the temporal discretisation that accurately accounts for the physical time scales is required. In this thesis, a dual time (implicit) stepping approach is implemented. The time dependent Navier-Stokes equations can be written as:

$$\frac{dQ}{dt} + R(Q) = 0 \tag{3.16}$$

Using the θ-method weighted time discretisation gives

$$\frac{1}{\Delta t}(Q^{n+1} - Q^n) + \theta R(Q^{n+1}) + (1-\theta)R(Q^n) = 0 \tag{3.17}$$

With Backward Euler corresponding to $\theta = 1$, and Crank-Nicholson corresponding to $\theta = 0.5$. This can be rearranged to give

$$\frac{1}{\Delta t}(Q^{n+1} - Q^n) + \theta(R(Q^{n+1}) - R(Q^n)) = -R(Q^n) \tag{3.18}$$

Using a second order discretisation for the right hand side, and first order discretisation for the left hand side yields:

$$\frac{1}{\Delta t}(Q^{n+1} - Q^n) + \theta(R_1(Q^{n+1}) - R_1(Q^n)) = -R_2(Q^n) \tag{3.19}$$

This can be rearranged to give:

$$\left(\frac{1}{\theta\Delta t}Q^{n+1} + R_1(Q^{n+1})\right) = \left(\frac{1}{\theta\Delta t}Q^n + R_1(Q^n)\right) - \frac{1}{\theta}R_2(Q^n) \tag{3.20}$$

3.5 Single Passage Method

The application of CFD to three dimensional turbomachinery related flows can potentially prove to be very computationally expensive. This is because simulating a full annulus for one or even many blade rows would not be feasible due to central processing costs. In order to address this issue, there are two approximation methods that are widely used. The first method involves altering the blade count and modelling a fraction of the annulus whilst maintaining blade-count periodicity. The second method is based on the assumption that a given blade passage experiences the same flow patterns as their neighbouring identical passage. This periodicity in space enables a truncation of the complete annulus (360 degrees) domain to a single passage, as shown in Figure 3.1; in computational time terms, 92 blade passage (32 NGVs + 60 rotor blade passages) may be reduced to a total of three blade passages (2 NGVs + 1 rotor), which is a factor of 30 in time savings.

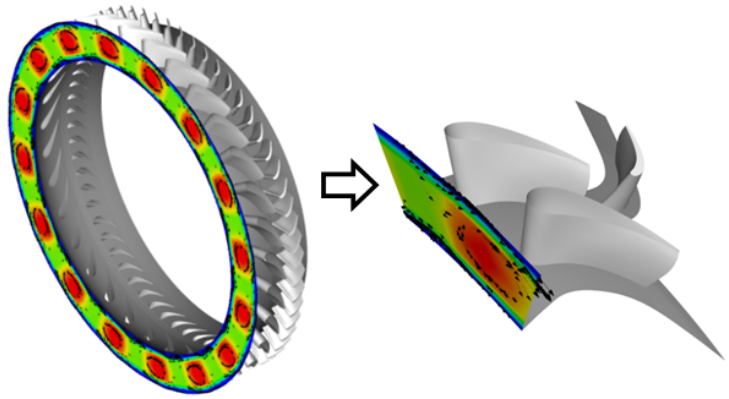


Fig. 3.1 Reduction in computational cost through the use of a single-passage domain with phase shift condition

The steady and unsteady CFD methodologies used in this thesis are based on the single passage method. In order to treat unsteady flows, it is necessary to define a phase shift temporal condition (in addition to the spatial condition), or phase-shift periodicity, in which adjacent blade passages see the disturbances of the same amplitude but with a constant temporal phase angle shift (He (2010)). In order to address this time domain issue, a Fourier shape correction method is proposed by He (1990), using a temporal Fourier series applied at the upper and lower boundaries of the single passage domain, as shown in Figure 3.2. At the boundaries, He (1990) showed that this Fourier series may be written as:

$$U^L(x,t) = \overline{U}(x)^L + \int_{n=1}^{N_f} A_n^L \cos(n\omega t) + B_n^L \sin(n\omega t) \tag{3.21}$$

$$U^U(x,t) = \overline{U}(x)^U + \int_{n=1}^{N_f} A_n^U \cos(n\omega t) + B_n^U \sin(n\omega t) \tag{3.22}$$

Where the superscripts L and U represent the lower and upper boundaries respectively. The number of harmonics, N_f, is usually very small. The Fourier harmonics A_n and B_n are obtained by a temporal summation over the number of time steps and

used to determine the harmonics at the upper boundary using the values from the lower boundary, and vice versa. This correction is continued until the phase shift periodicity boundary condition is satisfied. During this procedure, the solution flow variables at the boundaries through the corrections are obtained. A full description of the method can be found in He (2010).

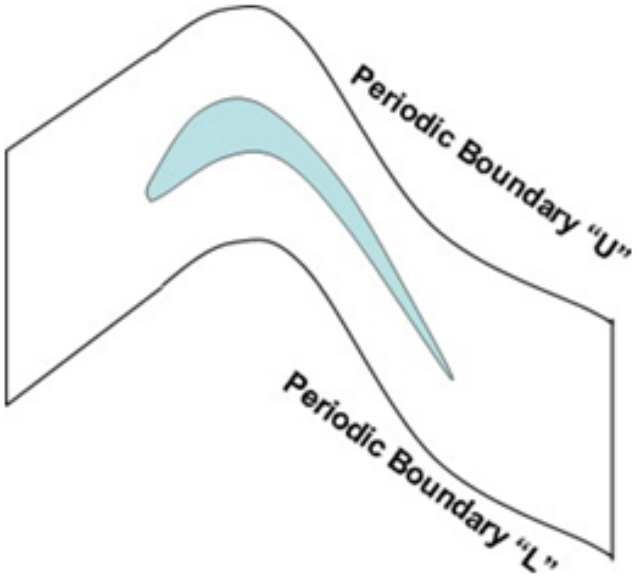


Fig. 3.2 Illustration of upper and lower periodic boundaries for a single passage domain, taken from He (2010)

3.6 Modelling the Interface between Stator and Rotor Row

The inherent nature of the stationary and rotating parts of the high pressure turbine stage (or any stage) means that an interface is required at the boundary between the stator and rotor zones, which allows the flow to be solved using the appropriate equations in the correct frame of reference or fluid zone. The type of interface that is required is dependent on whether a steady state or transient solution is being sought.

Since both flow characteristics are of interest in this thesis, a mixing plane interface is used for the steady state solutions and a sliding mesh for the transient ones. These concepts will now be discussed.

3.6.1 Mixing Plane Interface

The mixing plane concept was devised and implemented by Denton and Singh (1979) and allows a steady state solution to be computed for each zone with an exchange of flow variable information occurring at the interface boundary (Figure 3.3). Since the radial flow variations are of first order importance in a rotating blade passage (He (2010)), the flow variables are pitchwise averaged ('mixed out') across the interface. Thus circumferential variations are removed but radial disturbances are captured. A mass averaged method is implemented, which is defined, for a given flow variable f, as:

$$\overline{f} = \frac{1}{\dot{m}} \int_A f \rho \mathbf{v} \cdot \mathbf{n} dA \tag{3.23}$$

Where $\dot{m} = \int_A \rho \mathbf{v} \cdot \mathbf{n} dA$.

At each iteration, the flow field solution is updated in the stator and rotor domains. The flow properties are averaged at the stator exit and rotor inlet boundaries in order to obtain profiles for use in updating the boundary conditions. The stator exit profiles are passed as the boundary condition input for the rotor inlet and vice versa.

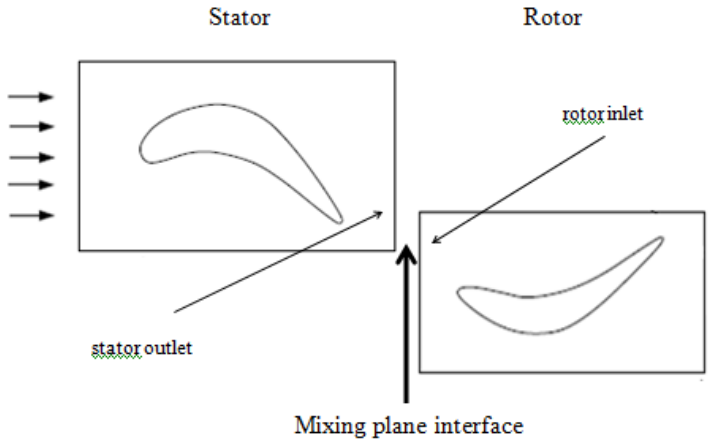


Fig. 3.3 Mixing plane at the stator-rotor interface, taken from ANSYS (2010)

3.6.2 Sliding Mesh Interface

As has been observed, the mixing plane concept removes any spatial non-uniformities and physical flow phenomena that would usually be associated with the rotor inlet flow, such as stator exit wakes, shock waves and separation. To account for these transient characteristics, the sliding mesh technique is implemented. The independent mesh zones for the stator and rotor are merged to form an interface, along which the rotor mesh will slide with respect to the stator. The shape of the control volume is not altered over time, since the grid nodes move rigidly in a given dynamic mesh zone (ANSYS (2010)). Therefore, within the conservation equations, for a given scalar flow quantity, the velocity vector $\mathbf{v}$ (within the convective flux terms) must account for the mesh velocity of the moving mesh, $\mathbf{v}_m$, hence becoming $(\mathbf{v} - \mathbf{v}_m)$. Finally, the mesh conservation law requires that the volume time derivative of the control volume (zero in the case of sliding meshes) is expressed as:

$$\frac{dV}{dt} = \sum_{n=1}^{N_F} \mathbf{v}_m A_n \tag{3.24}$$

3.7 Rolls-Royce CFD Suite

The numerical results presented in this thesis are carried out using the Rolls-Royce CFD suite, consisting of two software packages. The pre-processing is carried out using PADRAM, which can create the geometries required and generate the mesh for a given case. The numerical solver HYDRA is next used to solve for the three dimensional flow field.

3.7.1 PADRAM

PADRAM (PArametric Design and RApid Meshing) is a software capable of parametrically modifying two or three dimensional blade geometries, as well as being a rapid mesh generator for single passage and multi-passage cases for viscous and inviscid CFD calculations. With regards to blade parameterisation, there are five engineering design variables available that are commonly used to alter the blade geometry; skew (twisting of the blade about a spanwise location, Figure 3.4, left), lean (tangential displacement, Figure 3.4, centre), sweep (axial displacement, Figure 3.4, right), and leading edge and trailing edge recambering.



Fig. 3.4 Parametric capabilities of PADRAM with (from left to right) a skewed, leaned and swept blade

PADRAM allows for structured and unstructured meshes to be generated depending on the complexity as required by the user. In this case, the computational grid consisted of a multi-block structured mesh, which creates an O mesh for the immediate

region around the turbine blades that may capture the physical flow effects in this vicinity. The rest of the passage domain is joined to the O mesh by an H mesh, which is located upstream and downstream of the blade. The grid distribution is smooth, with orthogonality of grid lines being maintained in most regions. A schematic of an 'H-O-H' mesh is illustrated in Figure 3.5.

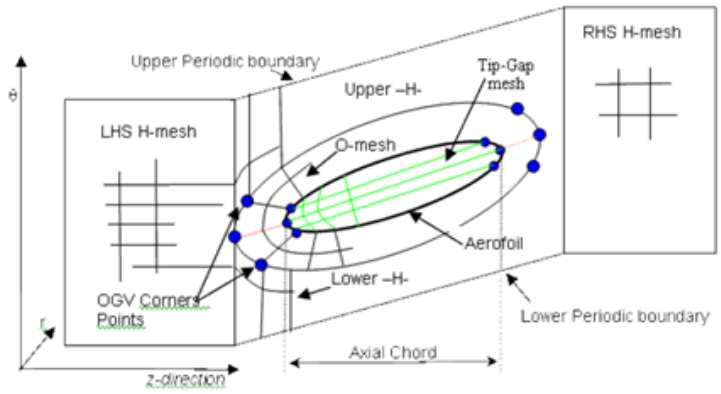


Fig. 3.5 Schematic of a single passage 'H-O-H' mesh, taken from Rolls-Royce (2006)

3.7.2 HYDRA

The numerical solver HYDRA is employed in all the computational results presented in this thesis. The solver is based on a preconditioned time marching of the Reynolds-averaged Navier-Stokes equations (RANS). The equations are discretised in space using a 2nd order edge based finite volume scheme and integrated in time using a multi-stage Runge-Kutta scheme (Moinier (1999)). The time marching integration is accelerated by the multi-grid and local time stepping techniques. Further details of the method have been presented earlier in the Chapter.

3.8 Mesh Independency and Solver Validation

This section investigates mesh sensitivity to ensure correct predictions of aerodynamics and heat transfer, and validates HYDRA against available experimental data and, in some cases, against other numerical codes. A mesh independency analysis is carried out by running several simulations with different mesh sizes in order to achieve a refinement in the mesh beyond which there are no appreciable differences in the results. It is known that a coarse mesh solution will result in a reduction in the computational effort expended; hence the current exercise will allow a compromise to be reached in which a desired fidelity will be sought after whilst keeping the CPU time to a minimum.

Mesh independency has been investigated for two different mesh variables. First, the number of nodes within the boundary layer is varied by changing the cell density of the NGV and rotor O-meshes (see Figure 3.5). The mesh was tested for 5, 10, 15 and 20 cells normal to the wall. The corresponding y+ values are 45, 24, 6 and 4 respectively for the NGV and 48, 28, 16 and 10 for the rotor. Secondly, using the optimum number of boundary layer cells, the number of spanwise grid points on the NGV and rotor is tested for 40, 50, 70 and 120 radial points.

The results are presented to assess the predictions of aerodynamics and heat transfer at three spanwise locations; 10%, 50% and 90%. The aerodynamics are assessed through isentropic Mach number or static pressure plots along the axial chord, whilst the heat transfer is presented as the Nusselt number, Nu based on inlet total conditions and blade axial chord, in the same manner as that described in Chana et al. (2001):

$$Nu = \frac{\dot{q}C}{(T_0 - T_{wall})k} \tag{3.25}$$

$\dot{q}$ represents the blade surface heat flux. The specifics of the HYDRA solver have been mentioned in Section 3.7.2. For the present work, steady (mixing plane) RANS calculations were performed initially which were then used for initialising the unsteady (sliding plane) simulations. Turbulence modelling was achieved by using the one equation Spalart-Allmaras turbulence model for the hot streak inlet, and the $k-\omega$ two equation model for inlet swirl. A uniform turbulence intensity of 12% was applied at the stage inlet.

For the unsteady solutions, the dual-time stepping method (Jameson (1991)) is used and the unsteady converged solutions were obtained after computing for 10 hot-streak periods. Given a hot-streak/NGV count of 1:2, each hot-streak period corresponds to two NGV blade passing periods as seen in the rotor frame of reference. Each hot-streak period is resolved by 240 physical time steps with 30 sub-iterations per time step. The single-passage unsteady method discussed earlier has been implemented in HYDRA by P. Adami (Rolls-Royce). For the present studies, the computational domain contains two NGV passages (to accommodate the hot-streak and/or swirl profile) and one rotor passage.

The geometry used in the current study is the MT1 HP stage (the NGV geometry can be seen in Figure 3.6); an unshrouded, high pressure research turbine as used in the previous hot-streak studies (see Chana and Jones (2002), Chana et al. (2003), and Qureshi et al. (2011-a)). The MT1 stage has 32 NGVs and 60 rotor blades with a tip clearance gap of 1.2%. The rotational speed is 9500 RPM, with a uniform inlet total pressure of 4.6 bar and the exit static pressure is 1.4 bar. All the solid surfaces are treated as isothermal walls (288 K) with a no-slip condition.

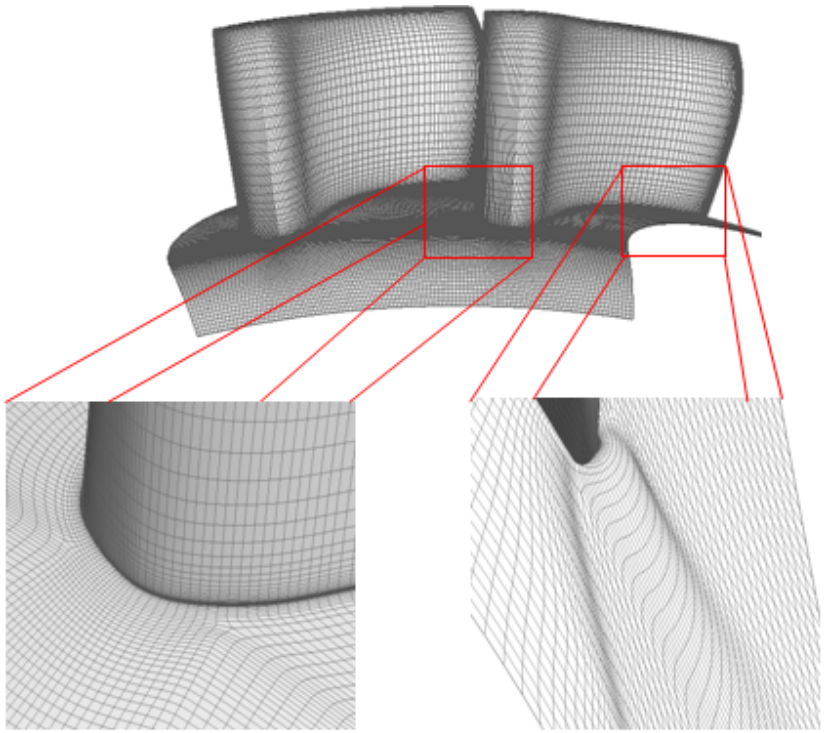


Fig. 3.6 Computational mesh for a vane passage

3.8.1 Hot Streak Mesh Independency and Validation

To validate the solver for a rich burn environment, a non-uniform temperature profile is applied at the turbine inlet; a spanwise plot and visualisation can be found in Chapter 5. The hot-streak profile is based on a practical combustor-NGV count ratio of 16:32 i.e. one hot-streak for every two NGV passages. The mass averaged temperature of the profile is 432 K, which is kept the same for both the profile and the uniform inlet. The hot-streak profile had a peak of 525 K, which was located at the blade mid-height, with the minimum of 290 K near the endwalls. The max-to-min temperature ratio was approximately 1.81, and the max-to-mean temperature ratio was around 1.22.

NGV Results

The isentropic Mach number distributions for the NGV are plotted in Figure 3.7 (varying boundary layer mesh) and Figure 3.8 (varying radial grid points) for 10%, 50% and 90% of the vane span. The isentropic Mach number is defined as:

$$M_{isentropic} = \sqrt{\left(\left(\frac{p_{0,inlet}}{p}\right)^{\frac{\gamma-1}{\gamma}} - 1\right) \cdot \frac{2}{\gamma - 1}} \tag{3.26}$$

Where $p_{0,inlet}$ represents the inlet total pressure. For the boundary layer densities, there are slight discrepancies for 5 cells and 10 cells mesh towards the trailing edge for all spanwise locations, thus grid independency is achieved for 15 cells and above. With respect to radial grid variation (Figure 3.8), grid independency is achieved for 50 radial points and above (some small differences can be observed compared with 40 radial points). Furthermore, HYDRA agrees well with the experimental data.

Nusselt number distributions are plotted in Figure 3.9 and Figure 3.10 for boundary layer and radial grid variations respectively. One observation from the plots is the significant discrepancy in heat transfer on the suction side at all spanwise locations. The over-prediction of heat transfer from the numerical simulations is due to the front portion of the NGV being modelled as fully turbulent, whereas in reality, a laminar region exists, as reflected by the experimental data. From Figure 3.9, large differences in heat transfer are observed for 5 cells and 10 cells (mostly over predictions) compared with 15 cells and above for all spanwise locations. In terms of radial grid, the changes in mesh density do not have a noticeable impact on Nusselt number. On the pressure side, HYDRA shows fair agreement with the experimental data.

Based on the discussion above, 70 radial points and 20 cells in the boundary layer was decided upon for the NGV mesh to ensure grid independency for the

aerothermal computations. The computational mesh as generated by PADRAM is shown in Figure 3.6.

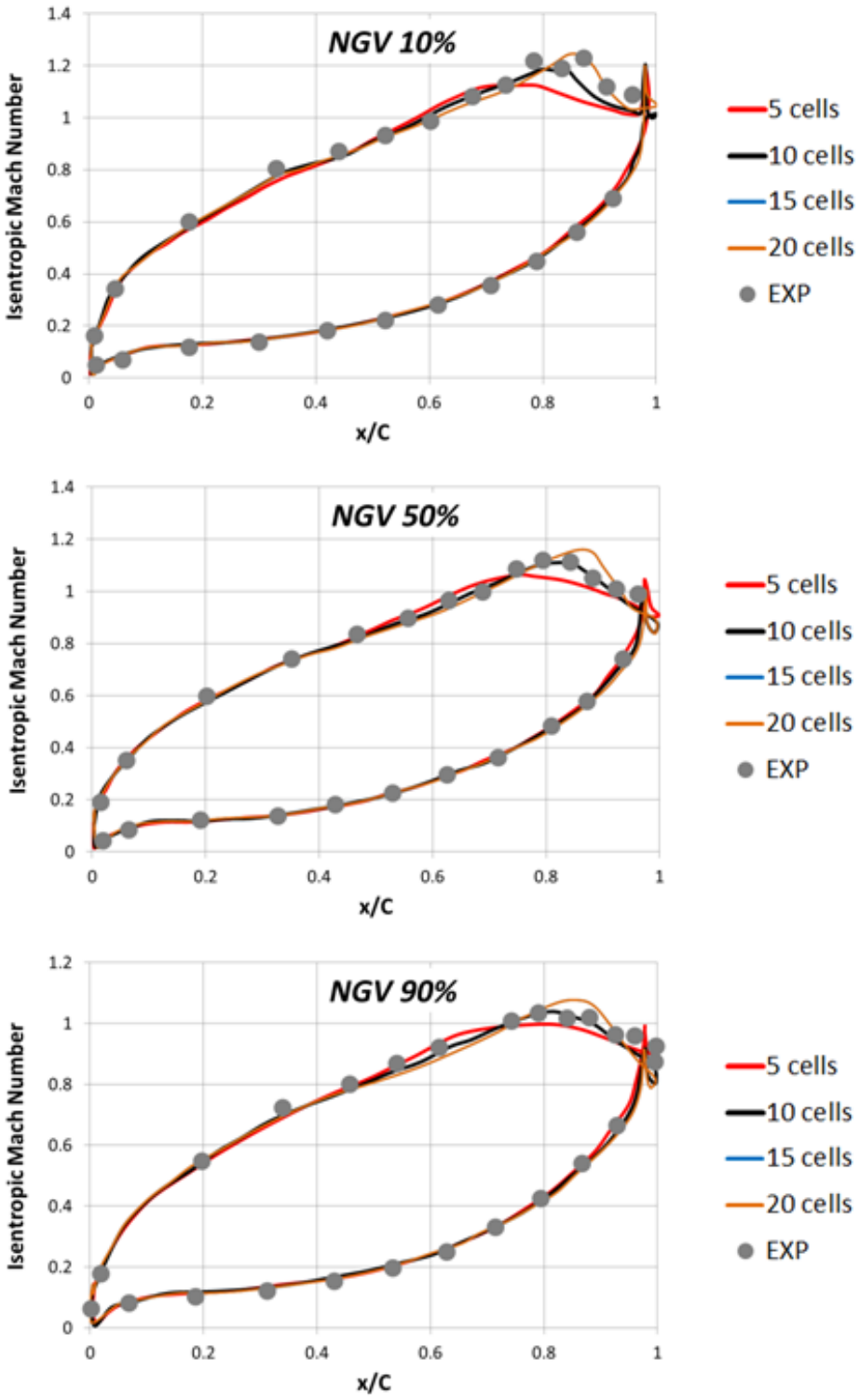


Fig. 3.7 Isentropic Mach number plots for varying cells in NGV boundary layer at 10%, 50% and 90% spanwise locations. The 15 cells line (blue) overlaps with the 20 cells line (orange)

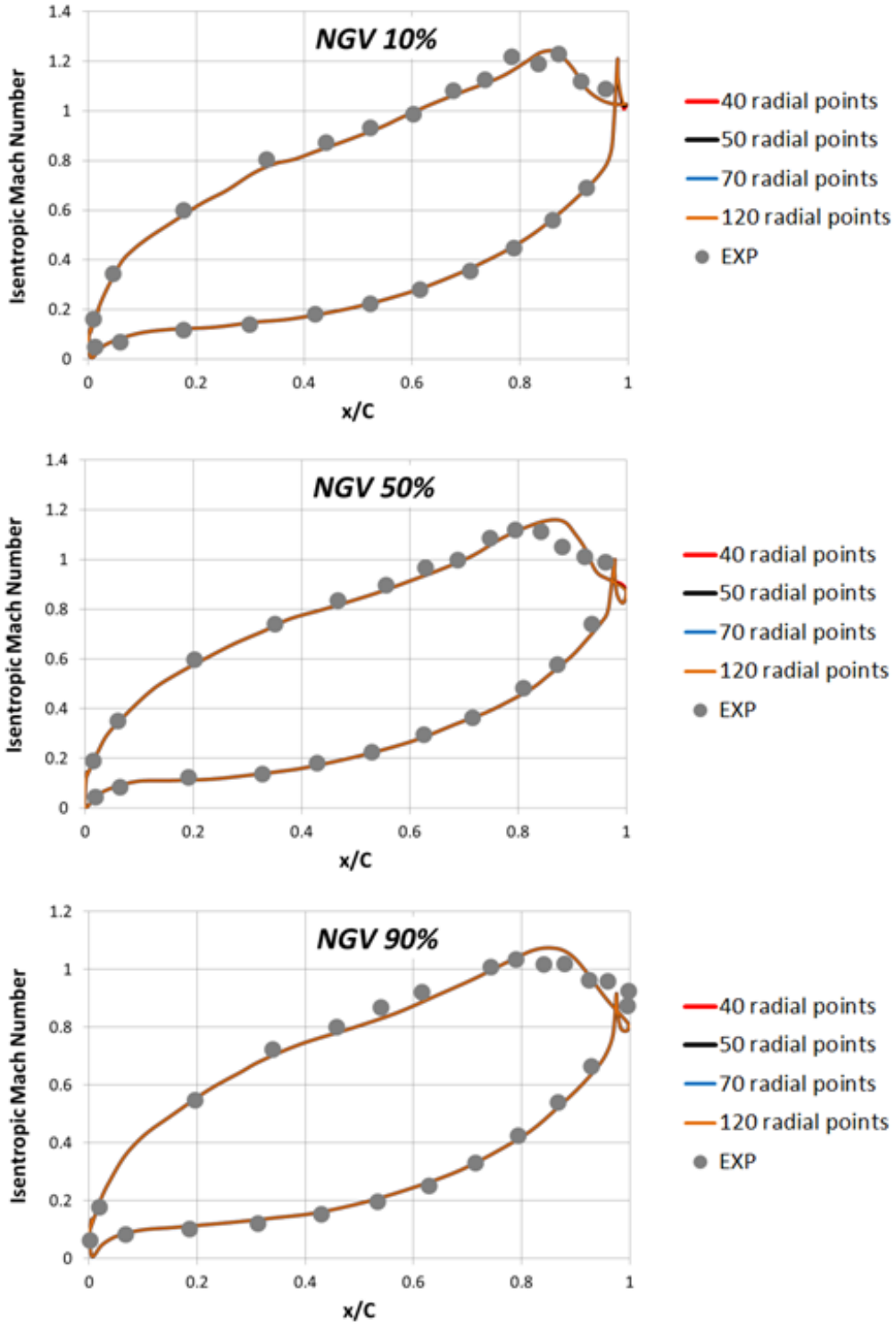


Fig. 3.8 Isentropic Mach number plots for varying radial grid points on NGV at 10%, 50% and 90% spanwise locations. Where there appears to be only a single line, it reflects all radial point cases overlapping

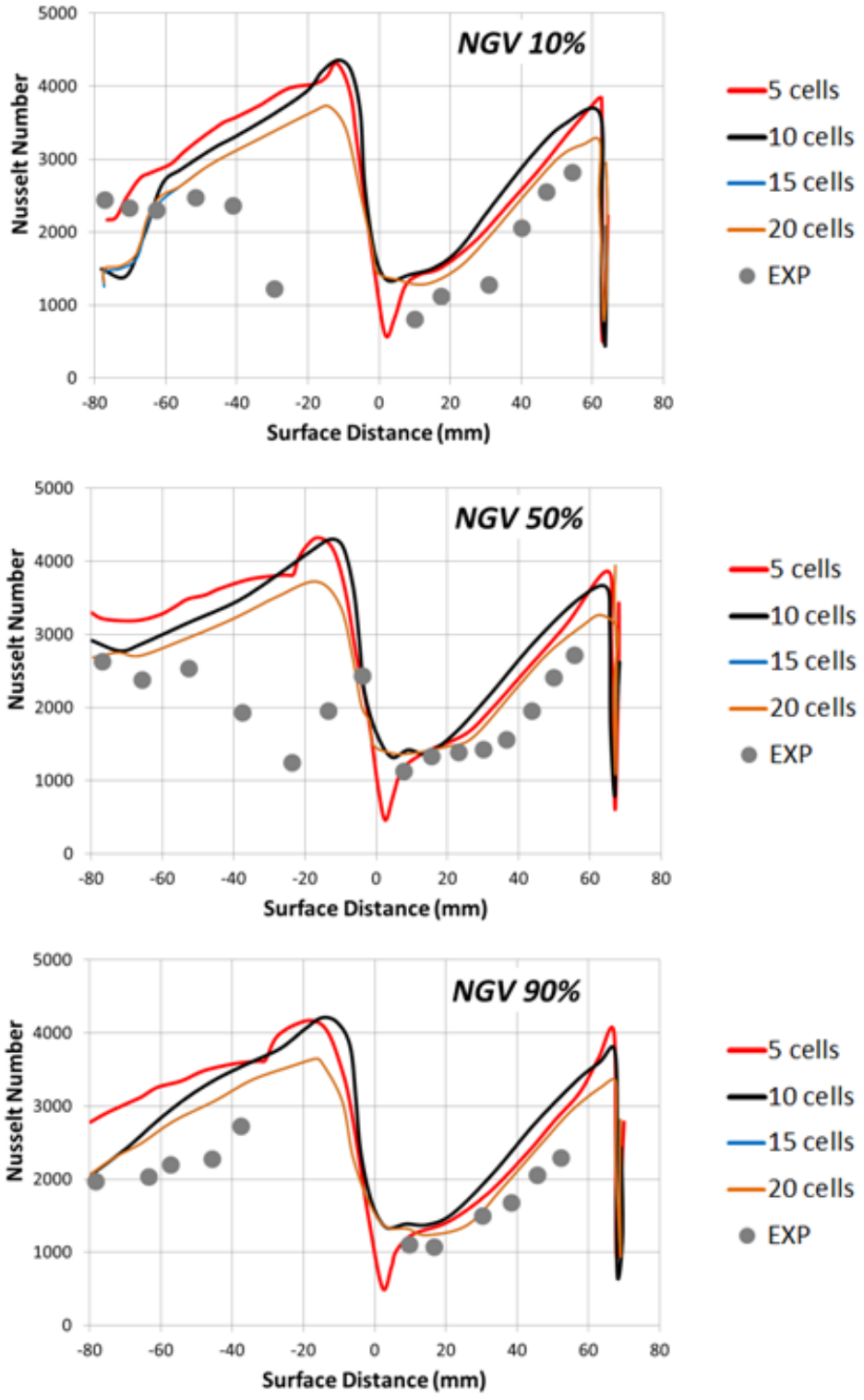


Fig. 3.9 Nusselt number plots for varying cells in NGV boundary layer at 10%, 50% and 90% spanwise locations. Negative surface distances represents the vane suction surface. The 15 cells line (blue) overlaps with the 20 cells line (orange)

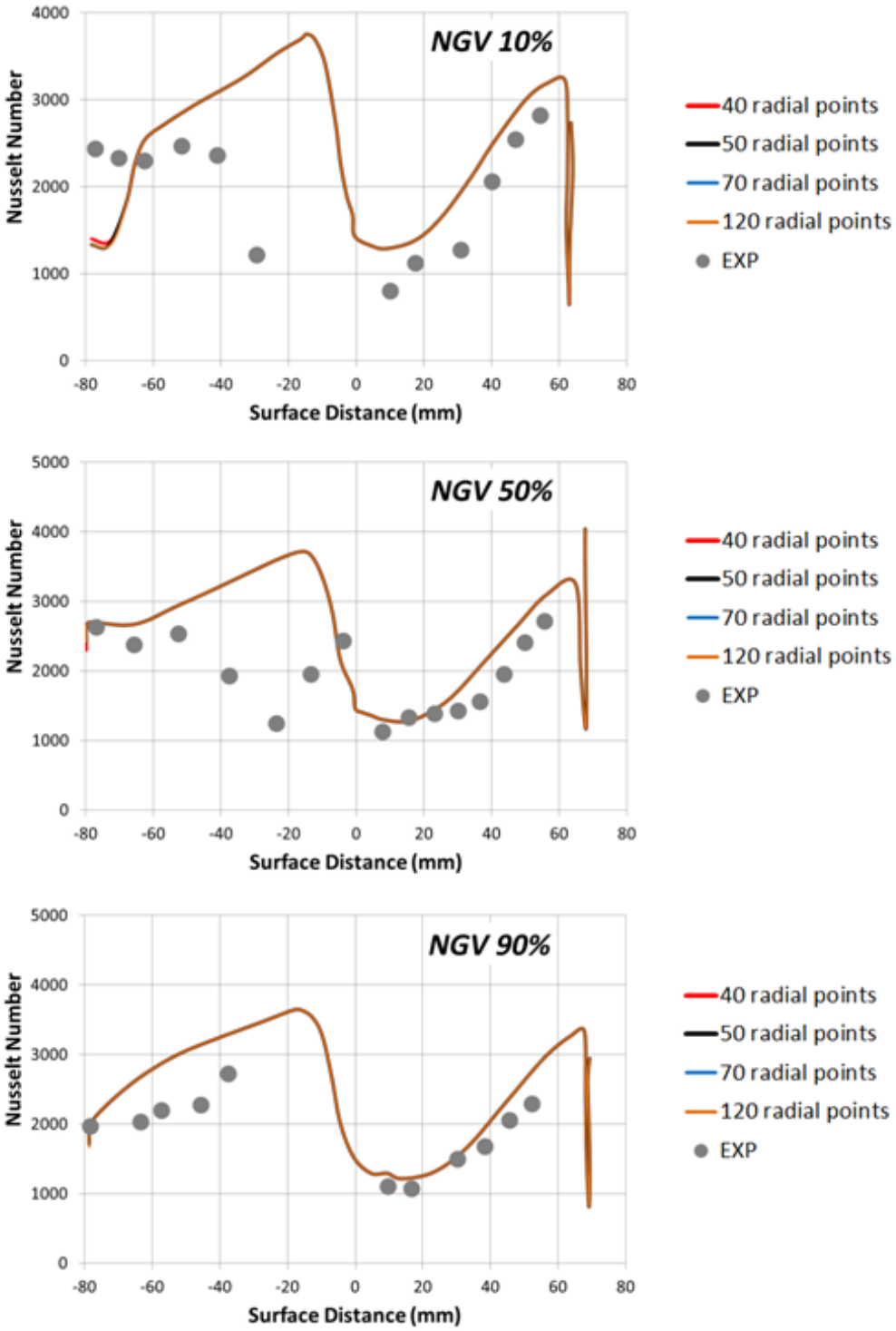


Fig. 3.10 Nusselt number plots for varying radial grid points on NGV at 10%, 50% and 90% spanwise locations. Negative surface distances represents the vane suction surface. For NGV 10%, the 50, 70 and 120 radial point cases overlap at around -75mm

Rotor Results

Static pressure plots (non-dimensionalised by stage inlet total pressure) for the rotor blade are plotted in Figure 3.11 and Figure 3.12 for boundary layer and radial grid mesh variations respectively. In terms of cell layers, variations result in little difference on the suction surface, but result in changes on the pressure surface. For 5 cells and 10 cells, differences are present towards the leading edge and trailing edge of the blade, with the most noticeable change occurring towards the rotor hub (10% span). Mesh independency is achieved for 15 cell layers and above. For spanwise mesh variations, little change is observed for the different meshes, and grid independency is obtained for 50 radial points and above. Experimental data is only available for 50% span, and HYDRA shows fair agreement with this, with a slight over prediction on the pressure side.

Figure 3.13 and Figure 3.14 shows the Nusselt number distributions for the boundary cells and radial grid respectively. In addition, results from the CFD software elsA (Cambier and Gazaix (2002)), which has been developed at ONERA, were used for a direct comparison to the HYDRA results. The results of the elsA code used in the present work can be found in Martelli et al. (2008). Figure 3.13 does not seem to indicate any specific trend between the cell layer mesh variations. However, generally speaking, as the mesh becomes finer, the difference between the plots reduces. Additionally, over the three spanwise locations, the 20 cells in the boundary layer appears to show the best fit with the experimental data, particularly at 90% span. From Figure 3.14 it can be seen that a radial grid of 50 points is sufficient to capture the heat transfer effects (some slight changes seen on the pressure surface at 10% rotor span). When compared with the ELSA numerical code, HYDRA shows promising results on the rotor blade, with good consistency at 90% blade span.

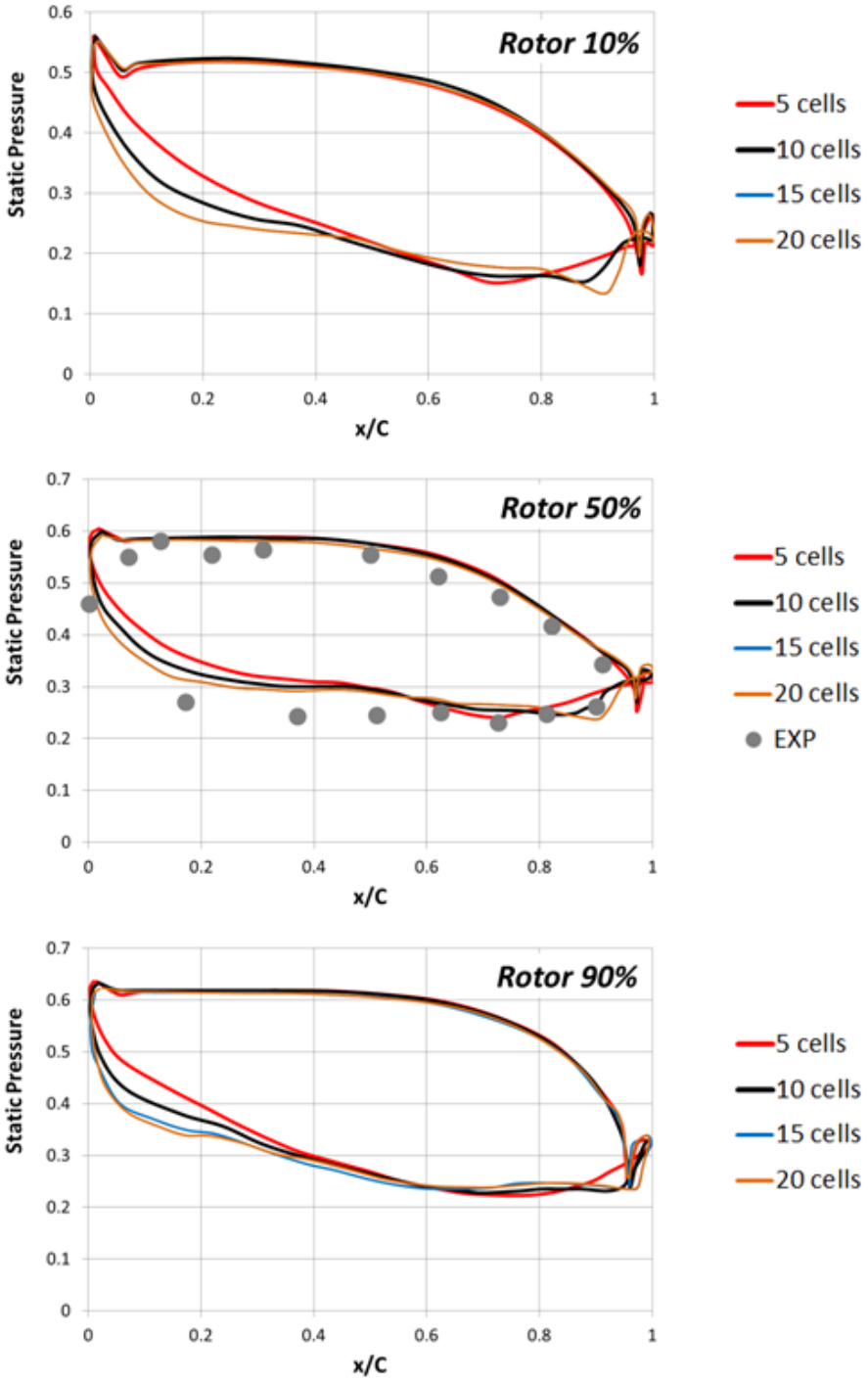


Fig. 3.11 Static pressure plots for varying cells in rotor blade boundary layer at 10%, 50% and 90% spanwise locations. Where it appears missing, the 15 cells line (blue) overlaps with the 20 cells line (orange)

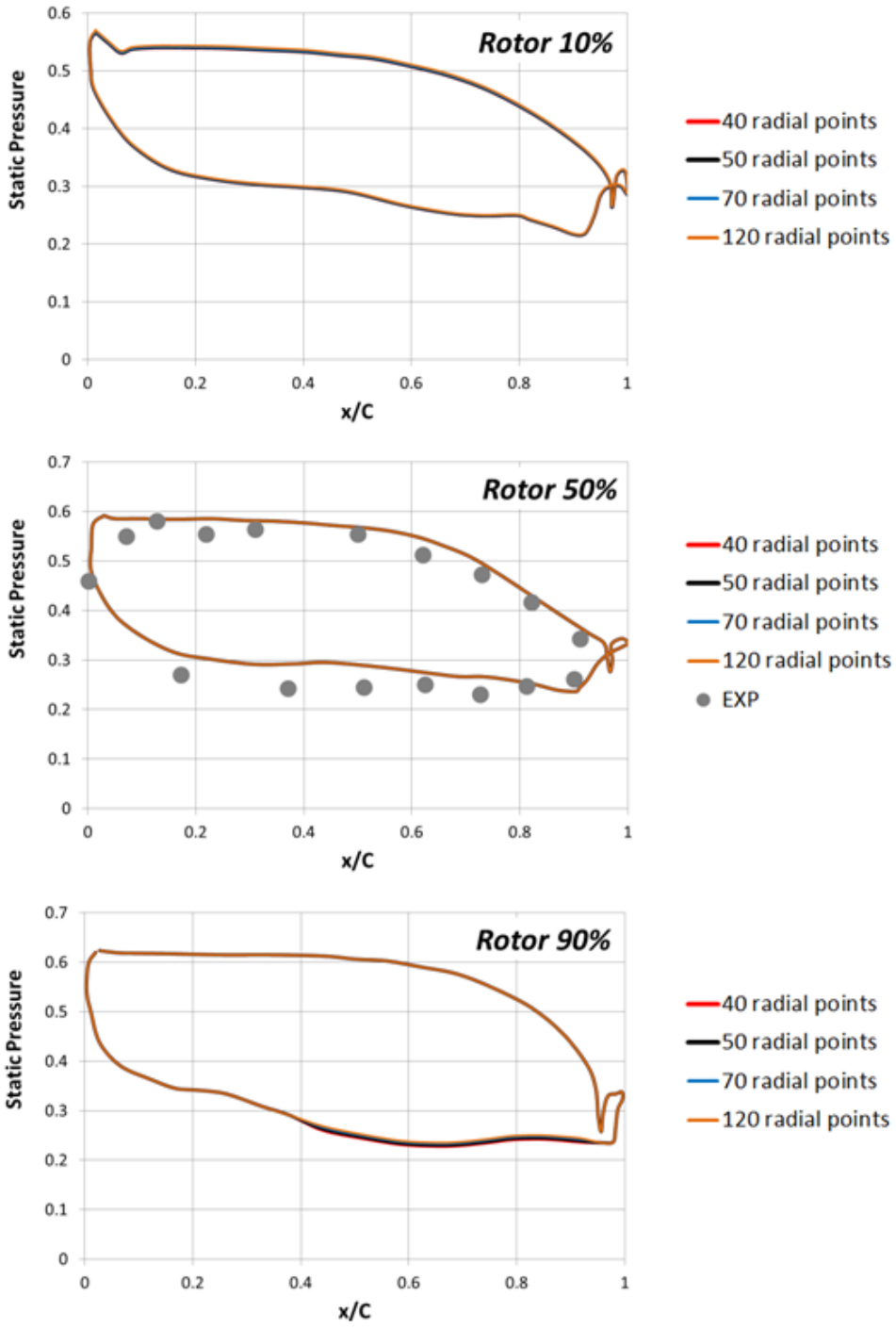


Fig. 3.12 Static pressure plots for varying radial grid points on rotor blade at 10%, 50% and 90% spanwise locations. Where there appears to be only a single line, it reflects all radial point cases overlapping

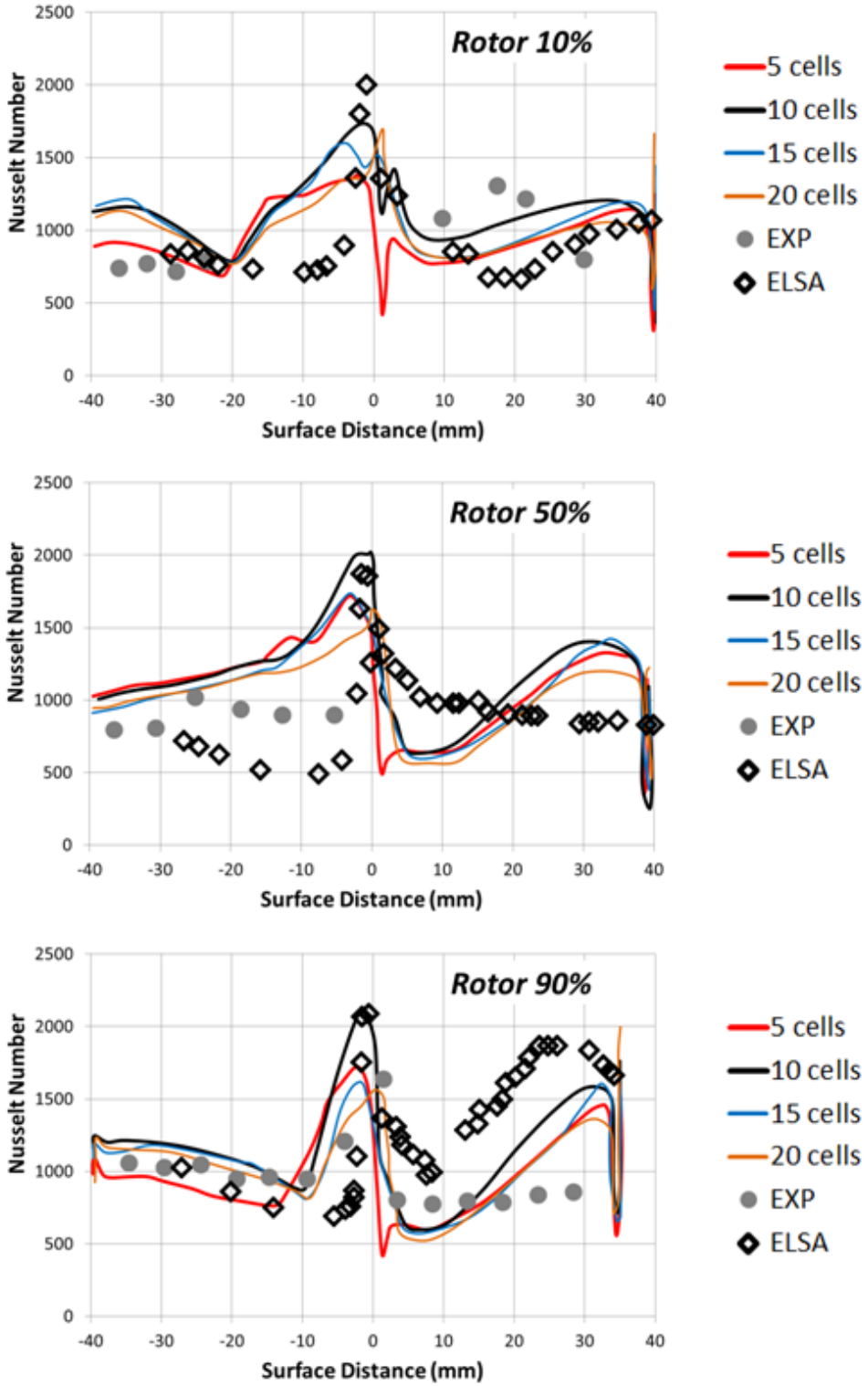


Fig. 3.13 Nusselt number plots for varying cells in rotor blade boundary layer at 10%, 50% and 90% spanwise locations. Negative surface distances represents the vane suction surface.

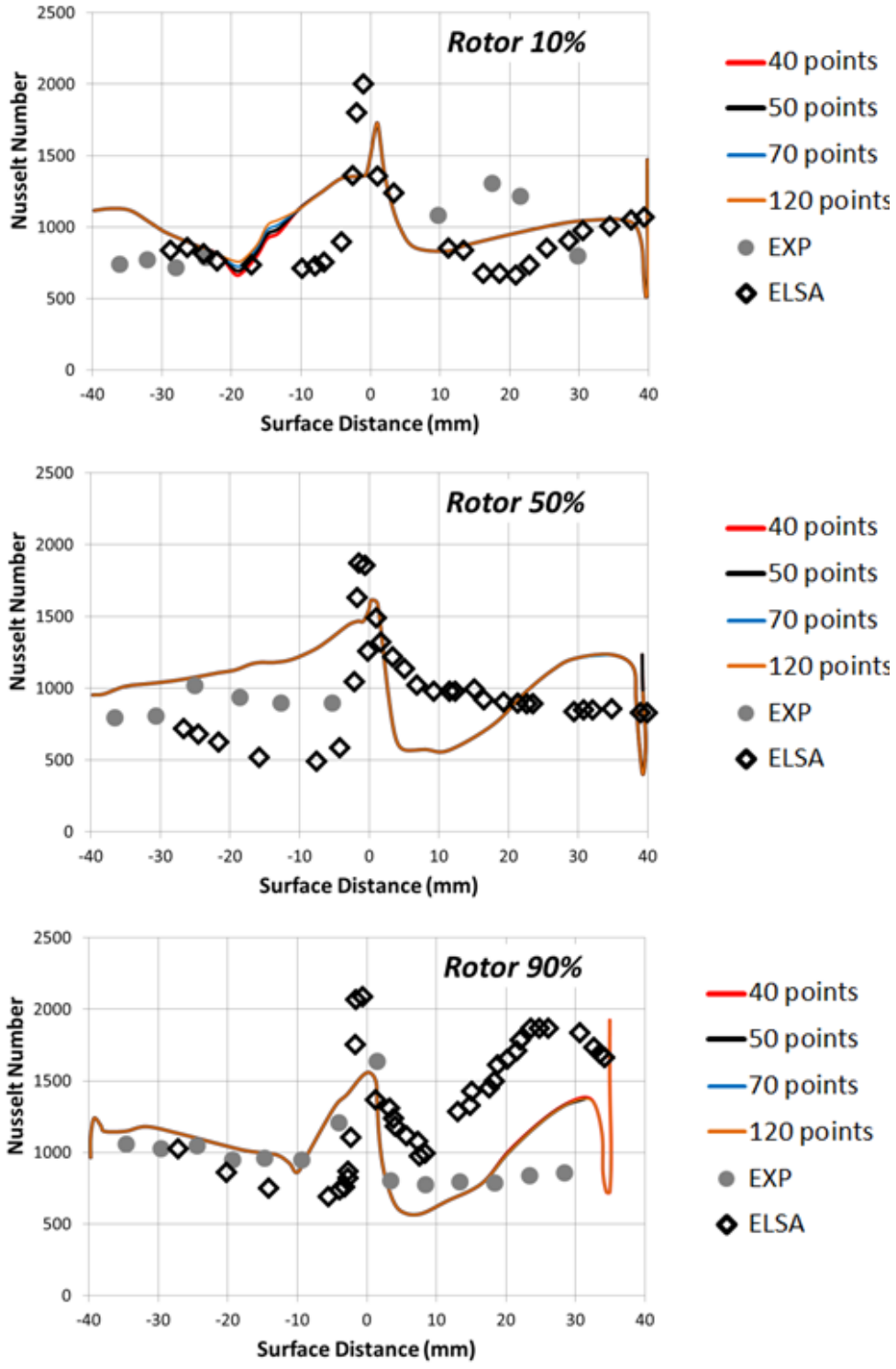


Fig. 3.14 Nusselt number plots for varying radial grid points on rotor blade at 10%, 50% and 90% spanwise locations. Negative surface distances represents the vane suction surface. Where there appears to be only a single line, it reflects all radial point cases overlapping

3.8.2 Inlet Swirl Mesh Independency and Validation

In this section, the unsteady single passage method is validated against experimental data for the presence of inlet swirl found in lean burn combustion. The swirl profile is based on the combustion swirl simulator implemented in a transonic turbine facility by Qureshi et al. (2011-b). The pitch and yaw angles are varied between +/- 40 degrees as shown in Figure 3.15 and Figure 3.16 respectively, and the total temperature (mass averaged) at the turbine inlet was set to 444 K (for consistency with the data from Qureshi et al. (2011-b). A positive swirl direction is defined as being in the direction of rotor blade rotation; a visualisation of the velocity vectors for both positive and negative swirl can be found in the computational setup section in Chapter 6. The validation is carried out with positive swirl, as data is only available for this scenario. As has been mentioned earlier, a realistic combustor to NGV count is 1:2, and in line with this, the centre of the swirl profile is clocked (circumferentially aligned) with the leading edge of one of the two vanes, which will be referred to as the 'impinged vane.'

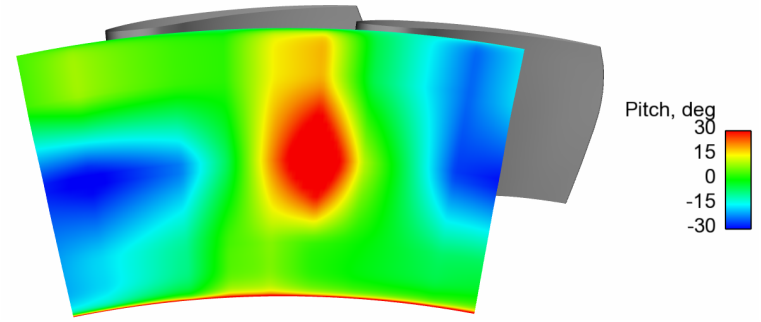


Fig. 3.15 Spanwise pitch angle variation (combustor-NGV count ratio of 1:2)

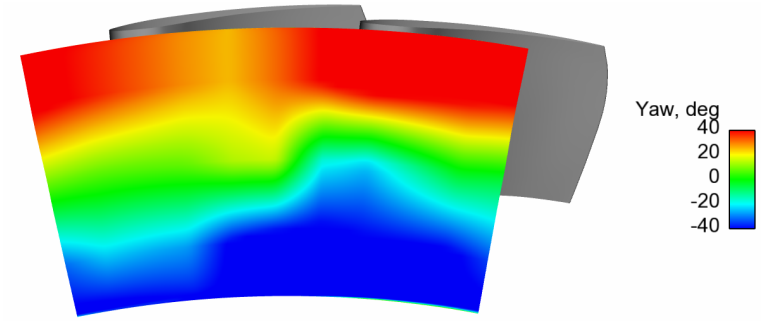


Fig. 3.16 Spanwise yaw angle variation (combustor-NGV count ratio of 1:2)

Aerodynamic Validation

The isentropic Mach number distributions on the NGV surface are plotted in Figure 3.17, for 10%, 50% and 90% spanwise locations. At 10% span, the observed increase in Mach number for the impinged vane relative to the unimpinged vane is correctly predicted by the numerical solver, and agrees well with the experimental data. This increase is due to a shift in the stagnation point towards the pressure surface (caused by the inlet swirl), resulting in higher hub loading; this has been reported in past literature (Khanal et al. (2013)). At 50% span, there is good agreement between the numerical and experimental data on the suction side. However, on the pressure side, it can be seen that there is a discrepancy between the CFD and experimental plots for the impinged vane. The reduction in loading observed is higher for the experimental case compared with the CFD. This has been explained by Qureshi et al. (2011-b) to be potentially caused by a non-uniform pressure variation at the inlet during the experiment, resulting in lower pressure (and thus higher Mach number) at the midspan. This is in contrast to the numerical computational setup, in which a uniform total pressure was imposed at the turbine inlet. At 90% span, there is again good agreement between HYDRA and the experimental data, with the expected reduction in loading compared with the midspan (corresponding to the negative incidence towards the tip) being observed.

Heat Transfer Validation

The Nusselt number plots on the NGV surface at 10%, 50% and 90% spanwise locations are shown in Figure 3.18. Good agreement is generally observed on the pressure surface, especially for 90% span. However, there are significant discrepancies on the suction surface towards the leading edge, with over predictions by HYDRA compared with the experimental data. This is due to the front portion of the vane being solved as fully turbulent, whereas a laminar region exists in reality, which is reflected in the experimental lines.

The Nusselt number distributions on the rotor surface at the three spanwise locations are plotted in Figure 3.19. The HYDRA solver provides satisfactory agreement compared with the experimental data within the uncertainty range of +/- 10%. Some of the over predictions on the suction surface leading edge (noticeable at 50% span) can be attributable to the transitional nature of the flow for the MT1 geometry.

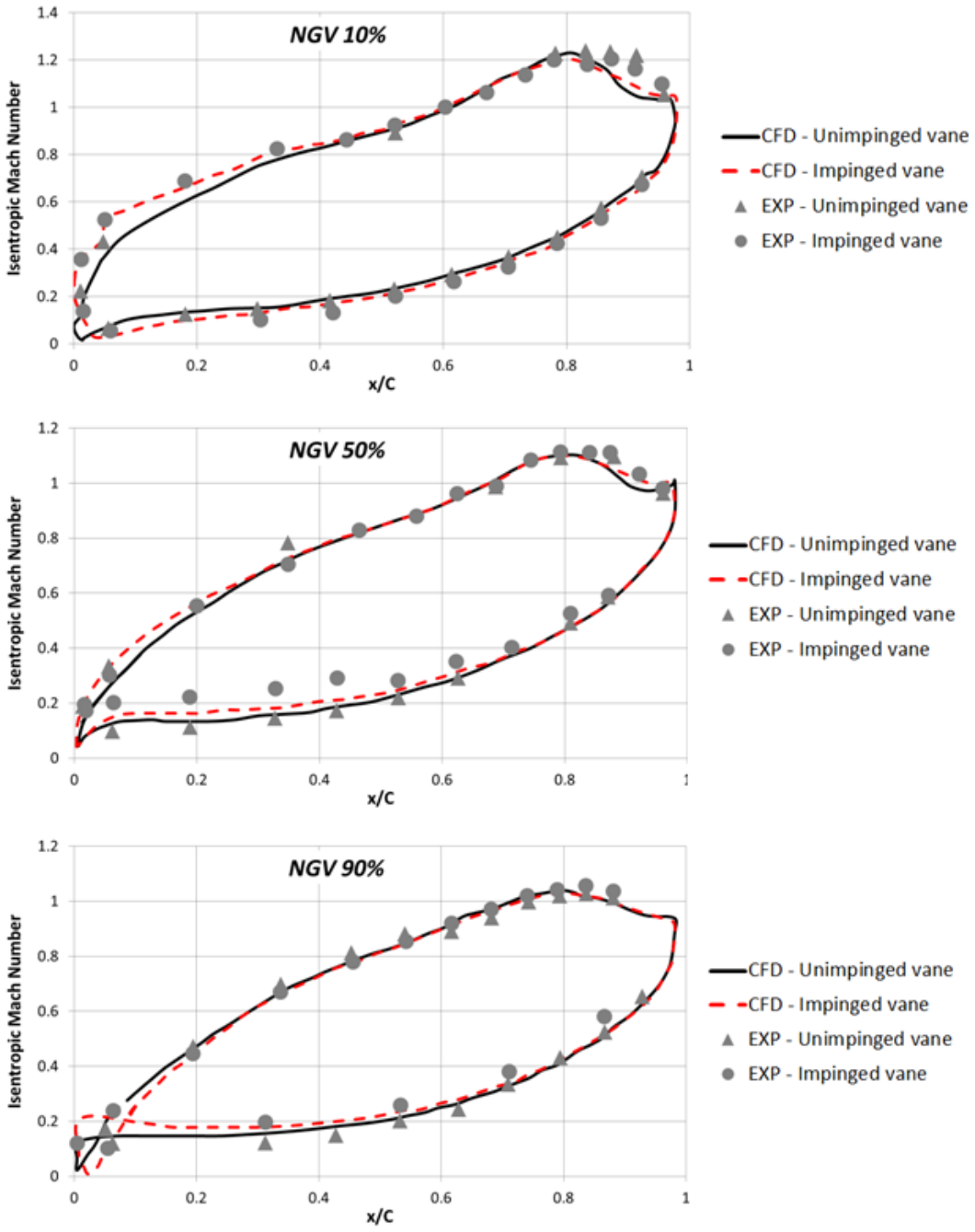


Fig. 3.17 Isentropic Mach number plots for swirl impinged and unimpinged NGV at 10%, 50% and 90% spanwise locations

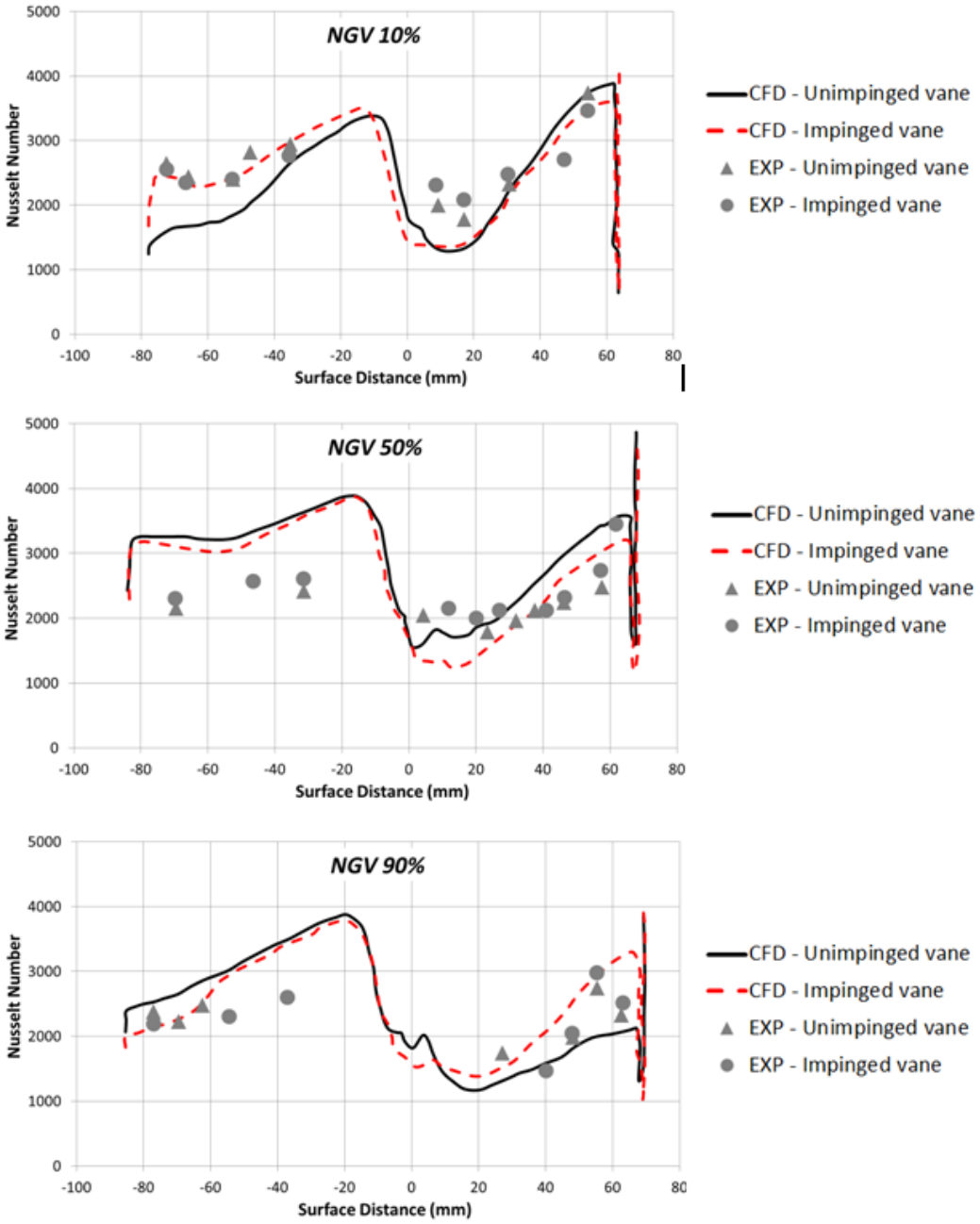


Fig. 3.18 Nusselt number plots for swirl impinged and unimpinged NGV at 10%, 50% and 90% spanwise locations. Negative surface distances represents the vane suction surface.

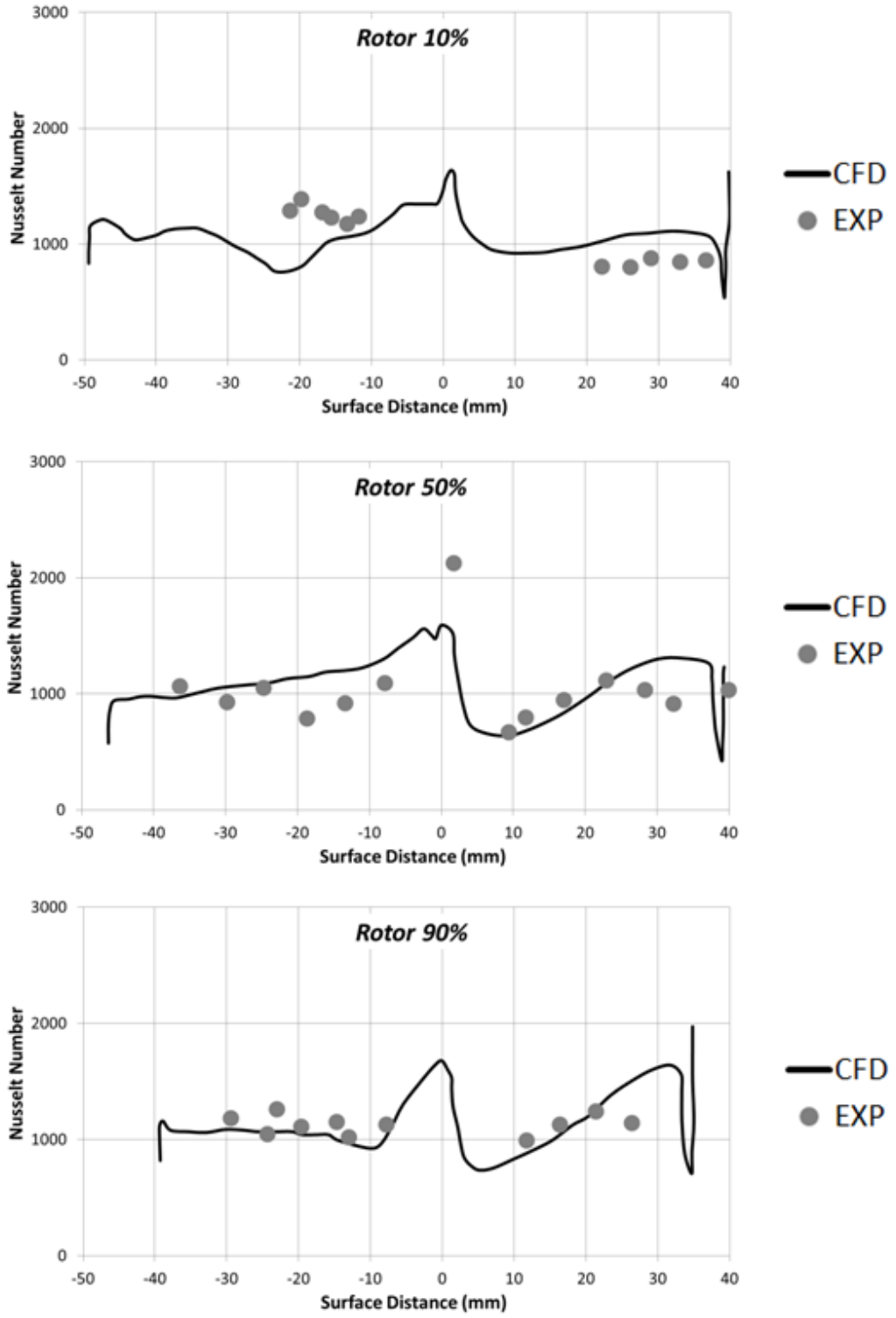


Fig. 3.19 Nusselt number plots for rotor blade at 10%, 50% and 90% spanwise locations for inlet swirl. Negative surface distances represents the vane suction surface.

3.9 Summary of Chapter

The first half of the chapter has described the CFD theory underpinning the basis of the research and subsequent results. The Navier-Stokes equations were given in three dimensions and modified to account for turbulence which yielded the RANS equations. Two turbulence models (Spalart-Allmaras and $k-\omega$) were defined that solve for the eddy viscosity, allowing the Reynolds stresses to be determined via the Boussinesq approach. The discretisation of the equations in both space and time was next discussed, allowing for the fluxes to be determined for each control volume and progressed iteratively in time. The single passage unsteady method which has been implemented for this work shows the significant cost benefits over complete annulus runs.

The latter half of the chapter introduces the Rolls-Royce CFD suite HYDRA, which was successfully validated against available experimental data for rich burn and lean burn non-uniformities using the MT1 stage geometry. Mesh independency studies were also conducted to ensure that the computational mesh on the NGV and rotor provide a grid that used the minimum number of nodes possible without affecting aerothermal predictions.

Chapter 4 will provide optimisation theory and code validation, leading to the development of an approach that will implement data produced from the CFD simulations. Together, Chapter 3 and Chapter 4 will provide the basis for three-dimensional optimisation of NGVs for stage performance.

Chapter 4

Optimisation and Predictive Modelling

4.1 Introduction

In this chapter, the concept of design optimisation is introduced and developed to be integrated with cost beneficial methods by approximating deterministic computer experiments. Section 4.2 provides general mathematical expressions for the optimisation problem and considers cases with a single goal or objective. Section 4.2.1 outlines the theory for the evolution algorithm optimisation technique that is widely used in an engineering context and implemented in the design methodology. A multi fidelity optimisation strategy using surrogate modelling techniques (namely, support vector machines and random forests for regression) is described in Section 4.4 (with Section 4.3 outlining various sampling methods for constructing the model), thus completing the discussion of the entire optimisation procedure. Section 4.5 presents a validation of the implemented code with two test cases using well known functions. Finally, a flow chart for the different steps in the methodology approach applicable to the current

work is provided at the end of the chapter. This algorithm will be integrated and tested in Chapter 7 i.e. a multi fidelity, multi-disciplinary optimisation of HPT NGVs under realistic turbine inlet conditions.

4.2 Optimisation Strategies

The purpose of design optimization is to enable an automated deterministic system to operate in which a favourable characteristic or objective function is improved upon whilst satisfying a number of constraints. The approach implemented to achieve this desired improvement is through the manipulation of a vector consisting of known design variables. Starting from an initial guess, the algorithm perturbs their values to produce successively improved design variables which progress in the direction of the desired global optimum within the design space. The area encompassed by the design space is specified by the user, and is an important consideration in order to keep computational costs to a minimum.

It is assumed without loss of generality that the given problem is one of minimization, and can be expressed mathematically as:

$$\begin{gathered} \text{minimise f(x)} \\ \text{subject to } g_i(x) \geq 0 \; for \; i = 1, ..., p \\ \text{for } x_l \leq x \leq x_u \end{gathered} \tag{4.1}$$

Where x_l and x_u represent the lower and upper bounds respectively for the design variable (either scalar or vector). If an optimal solution exists, then the design variables that achieve this, x^*, will satisfy:

$$f(x)^* \leq f(x) \; \forall \; x$$

$g_i(x)$ represents inequality constraints that are present for a given problem, and are constraints that are required to be satisfied to achieve a physically feasible solution. These types of problems may be translated into unconstrained optimization problems in which a penalty function may be applied to the objective function that accounts for any constraints that do not meet the criteria specified.

4.2.1 Evolution Algorithms (EA)

Evolution algorithms (EAs) are stochastic search methods that operate on a population of potential solutions applying the principle of survival of the fittest to produce better approximations to a solution. At each generation, a new set of approximations is generated by identifying those individuals in the previous generations that have a suitable level of fitness in the problem domain, and selecting them for breeding. In this way, the population of individuals evolves and becomes more suited to their environment. A commonly used type of EA is the genetic algorithm (GA).

Standard GAs are binary coded, meaning that the geometry defined design variables are represented by a binary string. The length of the string will determine the accuracy and computational cost associated with the optimization process. If the value of the string and hence resolution is very low, it may not allow the GA to accurately locate the minimum. There are three fundamental stages to the GA algorithm:

i Selection. The choice of the potential parents is of high importance to ensure the algorithm is successful in creating new generations (of future children and subsequent parents) that will eventually converge to a global minimum. A common selection method, known as tournament selection, randomly chooses a specified number of individuals (tournament size) and the individual with the highest fitness (lowest numerical value) represents the first parent. The second parent is selected

in a similar manner, as shown in Figure 4.1 (a). A large or small value of the tournament size determines whether the selection is diverse or elitist respectively (Periaux and Verstraete (2010)).

ii Crossover. Upon selection of the parents, a form of reproduction must take place in order to create offspring to represent the new generation; a crossover procedure is applied, in which the binary string for both parents at a randomly selected position is recombined (Figure 4.1(b)). Two children are therefore produced, and in this manner a new generation is formed. It is possible that a parent may not undergo the crossover operation, as a probability is attached to the procedure occurring.

iii Mutation. Immediately after the crossover, a further modification to the binary string may occur, in which a bit in the sequence is altered from a 0 to 1, or a 1 to 0. This mutation prevents the algorithm from getting caught in a local minimum, and hence encourages global convergence through a more diverse exploration of the design space.

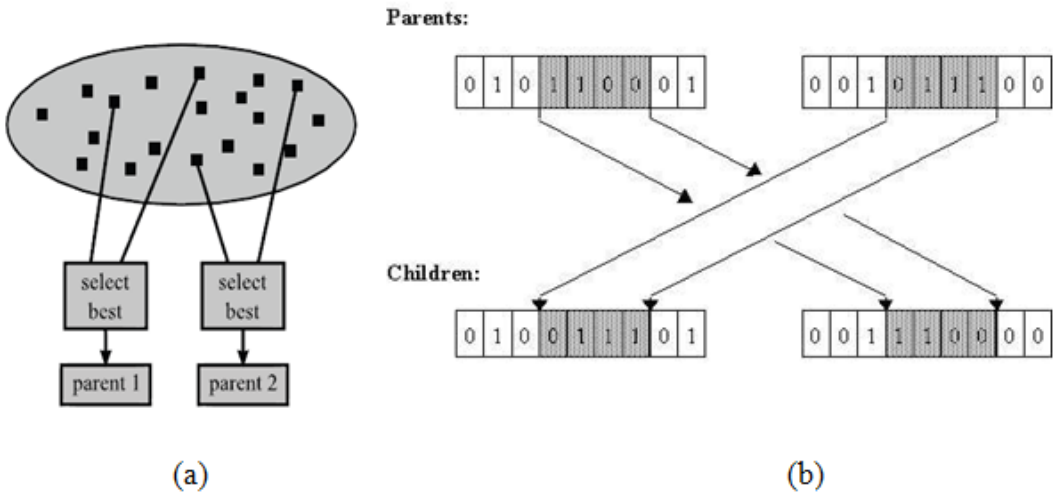


Fig. 4.1 Tournament selection operator (a) and a crossover procedure (b) for the creation of a new generation

The simplicity, speed and accuracy of the GA method make it a very attractive prospect. Unlike other optimisation techniques, it does not search from a single point, but operates on a whole population of points, which reduces the chances of becoming trapped in a local minimum point (Sivanandam and Deepa (2007)). Its inclusion of a small number of recessive samples in each generation ensures that a beneficial evolutionary possibility is not missed. Furthermore, provided the problem can be written in a binary string, it can solve any optimization case. However, one main drawback to the algorithm is the large number of objective function evaluations that must be performed in order to achieve convergence. For the optimization problem intended in this project (i.e. NGV optimization), accurate performance evaluations require a high-fidelity, computationally expensive, three dimensional RANS solver (which may involve both steady and unsteady RANS simulations). Hence it would not be feasible to couple the GA optimisers with the CFD solver, and the unsustainable progression of computational power means that alternative methods must be sought in order to reduce the computational effort currently being expended. One such method explores the idea of adopting a multi fidelity approach, in which a faster approximate model, or surrogate model, is used to find a solution close to the optimum geometry, which is then confirmed by a high fidelity, sophisticated CFD solver. An initial database of points is required to be analysed by the expensive CFD solver, in order to 'train' or enable the surrogate model to compute a relationship between the design variable inputs and the performance outputs, which is then permitted to replace the role of the CFD solver and be coupled with the GA, to solve and predict the optimum at a quicker rate. Since these predictions may not always be entirely accurate, the CFD simulations will be needed to confirm the most promising solutions.

There are two factors that influence the effective implementation of this procedure. First, a good initial database of points must be selected for the training of the model,

the more complete the information, the more accurate a relationship will be established between the inputs and outputs by the surrogate model. Second, the surrogate model itself must be accurate such that the number of additional performance evaluations is kept to a minimum. These two aspects will now be discussed in the following two sections.

4.3 Design of Experiments (DOE)

The end of Section 4.2 highlighted the importance of building surrogate models (a reduced fidelity strategy) in order to develop an optimisation procedure capable of producing accurate results within an acceptable timeframe. The surrogate model is constructed or 'trained' using a predetermined number of samples or 'experiments' to produce high fidelity, known outputs. In most cases, the fidelity of such models would increase as the numbers of experiments are increased but this would also result in an additional time cost; an efficient experiment-selection strategy is thus required. Design of Experiments (DOE) generally refers to any formal methods for setting input or parameter values in a set of experiments. The concept was first introduced by R.A. Fisher in the 1920s and 1930s in an agricultural context and later investigated in depth in the 1940s by Taguchi, with other DOE approaches emerging in the 1980s. DOE sampling can be categorised as either classical or space filling experimental designs; these will now be discussed in sections 4.3.1 and 4.3.2 respectively.

4.3.1 Classical Designs

The classical design approach accounts for random variation by spreading the data points out in the design space and taking multiple samples (replicates) at each of these

locations. This method has traditionally been used for the analysis of physical experiments, where replication and blocking are used to control noise, and randomisation is used to control bias. However, computer experiments (such as those executed in the present research) are deterministic; the output value is independent of the number of times that the simulation is run. Therefore, replication and blocking requirements are no longer true (i.e. only one output is required for a given set of inputs). Rather, for these computer experiments, the aim is to fit a cheaper predictor of the output (i.e. surrogate model) to a given data set; this is because the experiments, in this case steady and unsteady CFD runs, are computationally expensive. In order to achieve this, experimental designs should be spread evenly throughout the entire design space i.e. space filling designs.

One of the most common (and least complicated) classical designs to implement is called the central composite design (CCD); this has been used for comparative purposes in a validation test case presented later in this chapter. Hence, a brief treatment of the CCD will now be given.

A central composite design (CCD) is comprised of three types of runs or points; factorial points (determined according to the number of levels and factors specified), star or axial points (positioned below and above the median of the factorial levels) and a centre point. A CCD design with three design variables and 2 factorial levels is illustrated in Figure 4.2. This can be written mathematically as:

$$N = 2^k \left(factorial points\right) + 2k \left(star points\right) + C \left(centre point\right) \tag{4.2}$$

Where k represents the number of design variables. Variations of the CCD exist depending on the distance of the star points from the centre of the design space. For example, an ordinary CCD would have the star points placed at a distance of $\pm\alpha$

(where $\alpha > 1$) from the centre with the cube points being positioned at ± 1 from the centre. In the current work, a face centred central composite design (CCD) is employed, in which the star points are positioned on the faces of the cube.

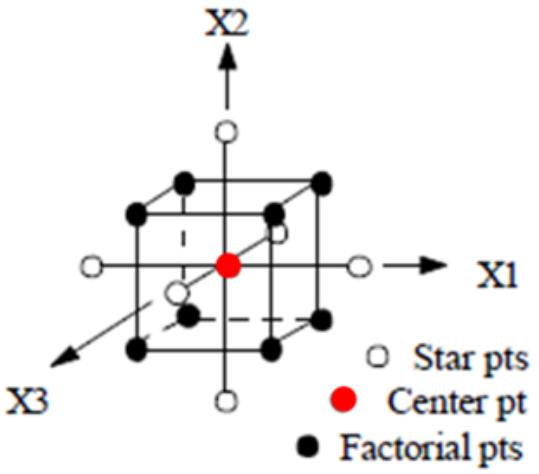


Fig. 4.2 CCD example (consisting of two levels and three factors). Taken from Simpson (1998)

4.3.2 Space-Filling Designs

There have been several investigations into space filling designs for computer based experiments in the past few decades. Koehler and Owen (1996) investigates different (random approach) experimental designs including the Latin hypercube sampling (LHS). LHS was introduced by McKay et al. (1979) and was applied on computer experiments. In the study, LHS was compared against random sampling and stratified sampling (Simpson (1998)). Random sampling can be seen as the least preferred as there is no guaranteed coverage over the entire design space. Stratified sampling partitions the design space into various strata, from which random samples are selected. LHS applies the same reasoning as stratified sampling, by dividing the design variable range into a set number of strata (that will have the same probability of being chosen) and taking a random sample from each stratum (McKay et al. (1979)).

Expressing this more explicitly, a domain may be split into n intervals for each k input. A matrix can then be constructed with dimensions n x k; each column contains the levels $1,\ldots,n$ (placed randomly) with the k columns being matched at random to form the Latin square (i.e. exactly one sample in a each row and each column). An example of a LHS design is shown in Figure 4.3 for a two variable case. In the case of space filling designs, there is no restriction or limit to the number of samples that can be selected; it is purely a user specified value, which is a significant benefit. The advantageous space filling properties, combined with the low computational cost makes the LHS method the most suitable choice for implementation in the current research.

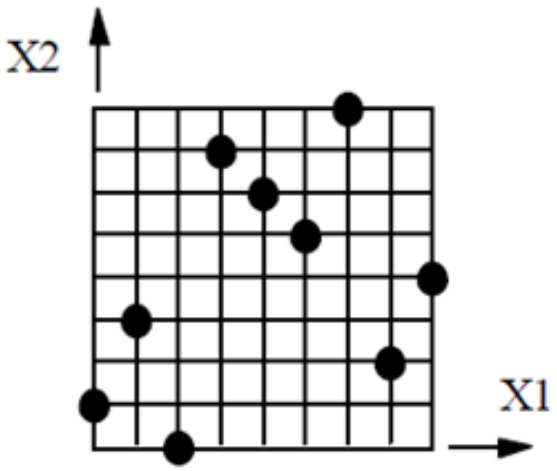


Fig. 4.3 Latin Hypercube Design (image taken from Simpson, 1998)

4.4 Surrogate Modelling

A surrogate model is designed to replace the expensive CFD code with a less expensive approximate model in determining a given output or response based on the inputs or design variables. Once the lower fidelity surrogate is constructed (using a design of experiments sampling plan), the optimiser is able to search the design space and

compute the objective for a given design variable combination in a shorter time period and hence obtain the global optimum (maximum or minimum) more quickly than the optimiser-CFD procedure. The solution from the surrogate model would then be validated using the CFD solver and further improvement or iterations would be run accordingly.

Two modelling approaches are considered in this thesis; support vector regression (SVR) and random forests.

4.4.1 Support Vector Regression (SVR)

Support Vector Regression is a class of supervised learning algorithms known as Support Vector Machines (SVMs), which are based on the principle of identifying a maximum margin hyperplane that aims to minimise the error between the prediction and actual output. In SVR, the inputs are first mapped or projected to a higher dimensional feature space through a linear or non-linear transformation, from which a linear model may be constructed (James et al. (2015)). Consider a training set, with m samples, that may be expressed as:

$$D = (\mathbf{x}_1, y_1), (\mathbf{x}_2, y_2), ..., (\mathbf{x}_m, y_m) \tag{4.3}$$

Where $\mathbf{x}_i$ is a n-dimensional vector for the i^{th} sample, y_i is the real number for each $\mathbf{x}_i$. The training set may be approximated by a linear function, taking the form:

$$f(x) = \mathbf{w} \cdot \mathbf{x} - b \tag{4.4}$$

Where $\mathbf{w}$ is a weight vector and b is the bias. The goal is to estimate the weights and bias of the function that gives the best fit of the data. The SVR may then be

expressed by the following optimisation problem, using an ε-insensitive loss function (shown in Figure 4.4(b)):

$$\begin{aligned} \underset{w}{\text{minimize}} \quad & \frac{1}{2}\|w\|^2 + C\sum_{i=1}^{m}(\xi_i + \xi_i^*) \\ \text{subject to} \quad & y_i - \mathbf{w}\cdot\mathbf{x}_i - b \leq \varepsilon + \xi_i, i = 1,2,...,m \\ & \mathbf{w}\cdot\mathbf{x}_i + b - y_i \leq \varepsilon + \xi_i^*, i = 1,2,...,m \\ & \xi_i, \xi_i^* \geq 0, i = 1,2,...,m \end{aligned} \tag{4.5}$$

The regularization constant, C, determines the complexity of the model. The slack variables, ξ_i and ξ_i^* imposes a penalty to deviations that are larger than ε. The deviations are penalised in a linear manner. Figure 4.4(b) illustrates how points outside the ε tube contribute to the loss. The optimisation problem above with inequality constraints can be transformed into a dual optimisation problem, and a kernel function is now added for the non-linear mapping case. This yields:

$$f(x) = \sum_i (\hat{\alpha}_i - \alpha_i) K(\mathbf{x}_i, \mathbf{x}) \tag{4.6}$$

Where α_i and $\hat{\alpha}_i$ are Lagrange multipliers. The kernel function has a significant computational cost saving by allowing just the inner products of the observations to be calculated. This is in contrast to transforming the inputs using a mapping function and calculating the inner product between pairs of vectors in a potentially very high dimensional feature space (Gunn (1998)). A polynomial kernel function of degree d for two sample inputs, for example, $\mathbf{x}_i$ and $\mathbf{x}_j$ may be expressed as:

$$K(\mathbf{x}_i, \mathbf{x}_j) = (1 + \mathbf{x}_i \cdot \mathbf{x}_j)^d \tag{4.7}$$

Where d is to be optimised. Another popular kernel function is the Gaussian Radial Basis Function:

$$K(\mathbf{x}_i, \mathbf{x}_j) = \exp(-\gamma \|\mathbf{x}_i - \mathbf{x}_j\|) \tag{4.8}$$

Where γ is a positive constant to be optimised. The radial basis kernel has very local behaviour; only nearby training inputs and associated response are taken into consideration when predicting on a test input.

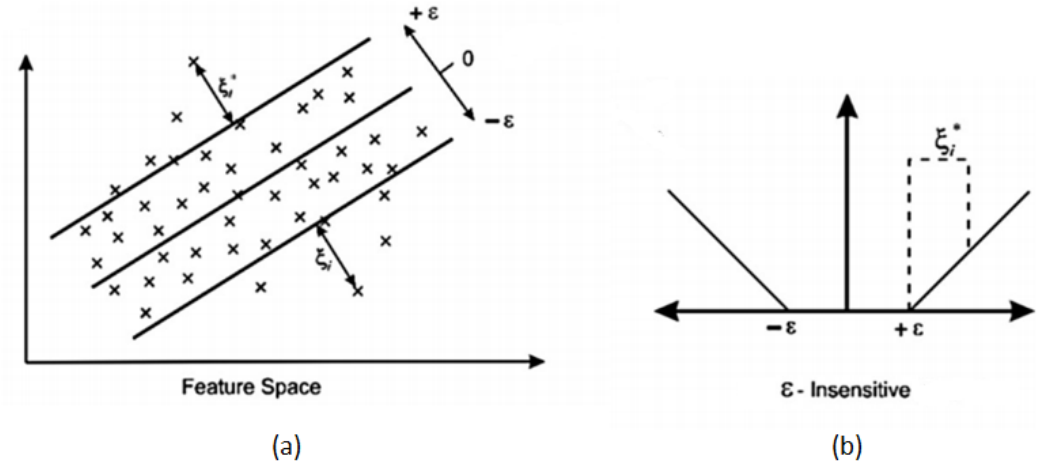


Fig. 4.4 Support Vector Regression; modelling approach shown in (a), ε insensitive loss function shown in (b). Taken from Zhong and Carr (2016)

4.4.2 Random Forests for Regression

Decision Trees

Random Forests is a method that is based on decision tree theory. Decision trees involve segmenting the predictor design space into a number of smaller regions. In order to make a prediction, the test response is equal to the mean response of the training points for the region to which it belongs. For regression based problems (as

is the case in this thesis), a recursive binary splitting approach is adopted. In order to perform this, a predictor j (also referred to as design variable or feature) and cutpoint s are selected such that splitting the design space using these values will lead to the greatest possible reduction in the residual sum of squares (RSS) (James et al. (2015)). The RSS is generally defined as the total sum residuals (difference between actual and predicted response). The two regions created through the splitting process can be denoted as R_1 and R_2 and can be defined as:

$$R_1(j,s) = \{X|X_j < s\} \; and \; R_2(j,s) = \{X|X_j > s\} \tag{4.9}$$

Hence, a minimisation is sought to the following expression:

$$\sum_{i:x_i \in R_1(j,s)} (y_i - \hat{y}_{R1}) + \sum_{i:x_i \in R_2(j,s)} (y_i - \hat{y}_{R2}) \tag{4.10}$$

Where $\hat{y}_{R1}$ is the mean response for training observations in $R_1(j,s)$, and $\hat{y}_{R2}$ is the mean response for training observations in $R_2(j,s)$. This process has resulted in the creation of two regions. For the next tree split, one of these regions is selected and another split is performed using the above process. This process is continued until a stopping criterion is reached, for example, when the number of training observations within a region falls below a specified value. The recursive binary splitting method is referred to as a greedy approach, since at each step of the tree building process, the best split is chosen without any consideration of future splits. An example of a decision tree that has been split into 3 regions in a two dimensional space can be seen in Figure 4.5.

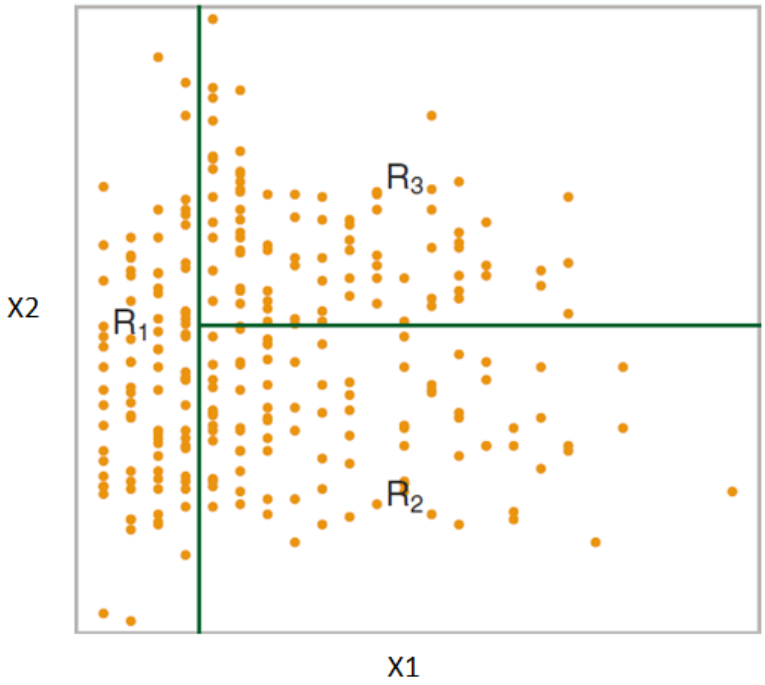


Fig. 4.5 Decision tree in two dimensions. Taken from James et al. (2015)

Bootstrap Aggregating

One disadvantage of decision trees is that they do not generally have the same level of predictive accuracy compared with other predictive modelling techniques. This is due to the method overfitting on the training data. One method to reduce the variance (whilst keeping the low bias associated with decision trees) is to apply bootstrap aggregating, or 'bagging.' This involves taking B repeated samples from the same training set, and building a decision tree for the b^{th} bootstrapped training set in order to get a prediction $\hat{f}^b(x)$, and finally average the predictions over all B trees:

$$\hat{f}_{bag}(x) = \frac{1}{B}\sum_{b=1}^{B}\hat{f}^b(x) \tag{4.11}$$

Random Forests

As has already been discussed, decision trees are built using a greedy approach. Therefore, even when adopting the bagging approach, a strong predictor may dominate all bagged trees, resulting in highly correlated trees. Random Forests aim to decorrelate trees. A bagging approach is again taken, however, for each tree, and for each split in a tree, a random sample of m predictors are chosen as split candidates from the full set of p predictors. Typically, the sample number is $m \approx \sqrt{p}$.

4.4.3 Cross Validation (CV) for Predictive Models

One of the key steps in building a predictive model is to estimate its performance on unseen data. By training a model on a given dataset, and using the same data to estimate how well it performs can lead to overfitting, associated with high variance. In order to address this potential problem, cross validation techniques can be applied, whereby the training dataset is split and a portion of observations are held out from the training process. This will now be discussed.

k-fold cross validation involves randomly dividing the training observations into k folds of approximately equal size. The model is trained on $k-1$ folds, and the unused fold is treated as the validation (or 'test') set. The mean squared error (MSE) is then calculated on the test fold. The MSE, which is the averaged difference between the actual and predicted responses (y and $\hat{y}$ respectively) of the test set (containing n data points), is defined as:

$$MSE = \frac{1}{n}\sum_{i=1}^{n}(y^{(i)} - \hat{y}^{(i)}) \tag{4.12}$$

This procedure is repeated k times; each time, a different fold is treated as the validation set. At the end of this procedure, k models are obtained with k estimates of the test error, $MSE_1, MSE_2, ..., MSE_k$. This is depicted in Figure 4.6. The k-fold CV estimate is then computed by averaging these values:

$$CV_{(k)} = \frac{1}{k} \sum_{i=1}^{k} MSE_i \tag{4.13}$$

An advantage of the k-fold CV method is that the sampling technique is without replacement, which means that for each training iteration, each sample point will be a part of the training and test datasets exactly once, resulting in a low variance. For the present work, the k-fold CV method will be used for model tuning, in order to find the optimal hyperparameter values for the models discussed in sections 4.4.1 and 4.4.2. Once these optimum values have been computed, the model will be retrained on the entire training set, and a final performance estimate will be obtained on the independent test set.

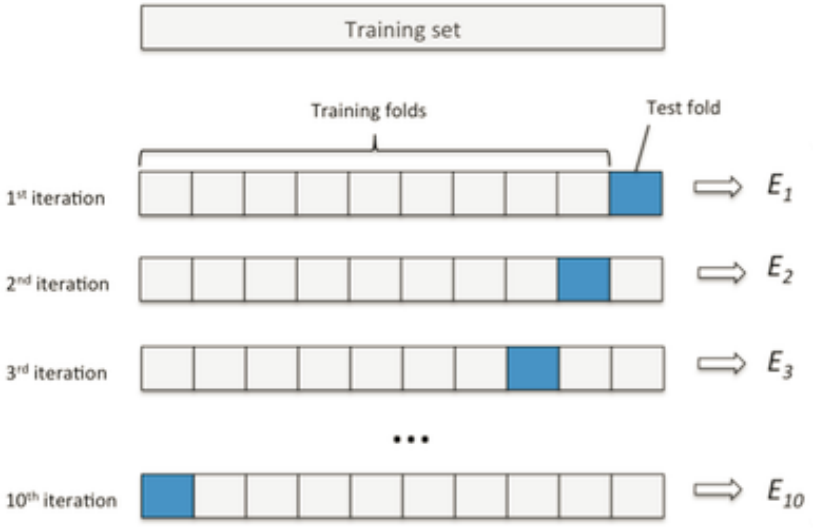


Fig. 4.6 An example of k-fold cross validation with 10 folds (image taken from Raschka (2015))

4.5 Optimisation Validation

This section presents a validation for the optimisation code and surrogate models implemented in the optimisation of NGVs for stage aerothermal performance. As described earlier in the chapter, the Genetic Algorithm (GA) method, specifically, the GA code within the Global Optimization Toolbox in MATLAB will be used for the optimisation. Two analytical test case functions are presented. The set up for the GA code in order to progress over a number of generations till convergence is given in Table 4.1. These defined parameters are used for both validation test cases.

Table 4.1 User specified values for GA parameters

GA Parameter	**Value**
Population size (per generation)	100 individuals.
Initial population	Randomly generated; uniformly distributed.
Parent selection (for next generation)	Tournament; tournament size set to 4.
Mutation	Adaptive feasible; based on success of previous generation.
Crossover	Random binary vector used to select genes from parent 1 and parent 2 to create child.
Stopping criteria	Specified function tolerance ($1x10^6$) or maximum number of iterations as defined by 100*number of design variables. Algorithm stops based on whichever criterion is met first

4.5.1 Test Case 1: Rosenbrock's Function

Rosenbrock's function can be expressed generally as:

$$F(X,Y) = (a-X)^2 + b\,(Y-X^2)^2 \tag{4.14}$$

Where a and b represent user specified constants, and the global minimum is located at (a,a^2). In this case,

$$a = 1\ ,\ b = 100;\ F_{min}(1,1)\ =\ 0$$

And the range was chosen between:

$$-1.5\ <\ X\ <1.5;\ -1\ <\ Y\ <\ 1.5$$

The exact function, as plotted in Figure 4.7, illustrates a parabolic shaped valley, containing the global minimum.

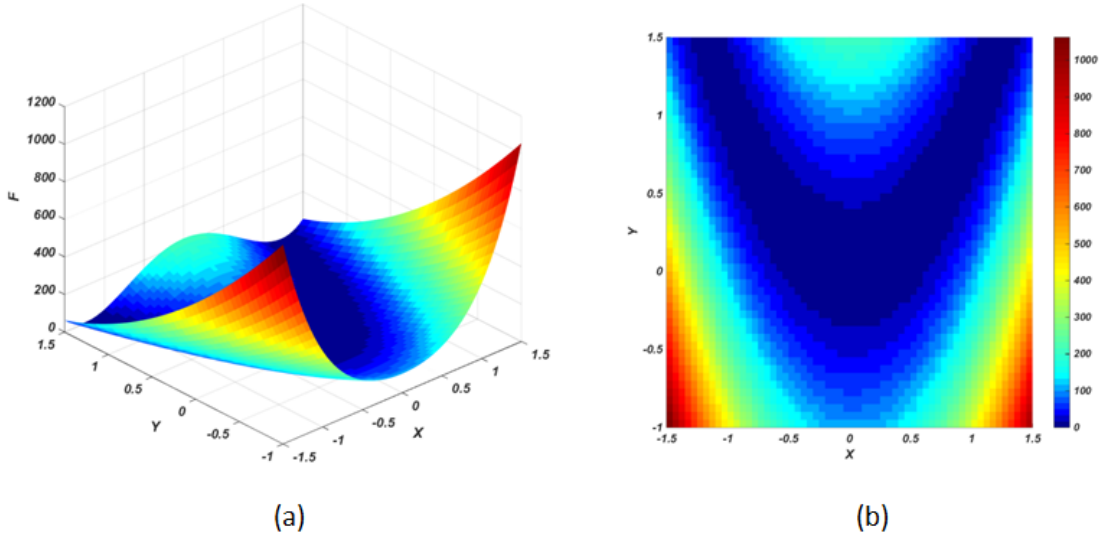


Fig. 4.7 Rosenbrock's function, plotted in Matlab as illustrated in three dimensions (a), and as viewed from above (b))

Given the defined constraints and constants, the GA optimiser was implemented in order to search the analytical function for the global minimum point. The optimisation history is displayed below in Figure 4.8; Figure 4.8 (a) shows the best and mean fitness values for each generation, and Figure 4.8 (b) shows the best, mean and worst fitness value per generation. It can be seen that the GA optimiser successfully locates the minimum value of 0, at the correct xy position of (1,1). The minimum fitness value is found from the first generation, and the mean fitness within a population reaches 0 by the twelfth generation.

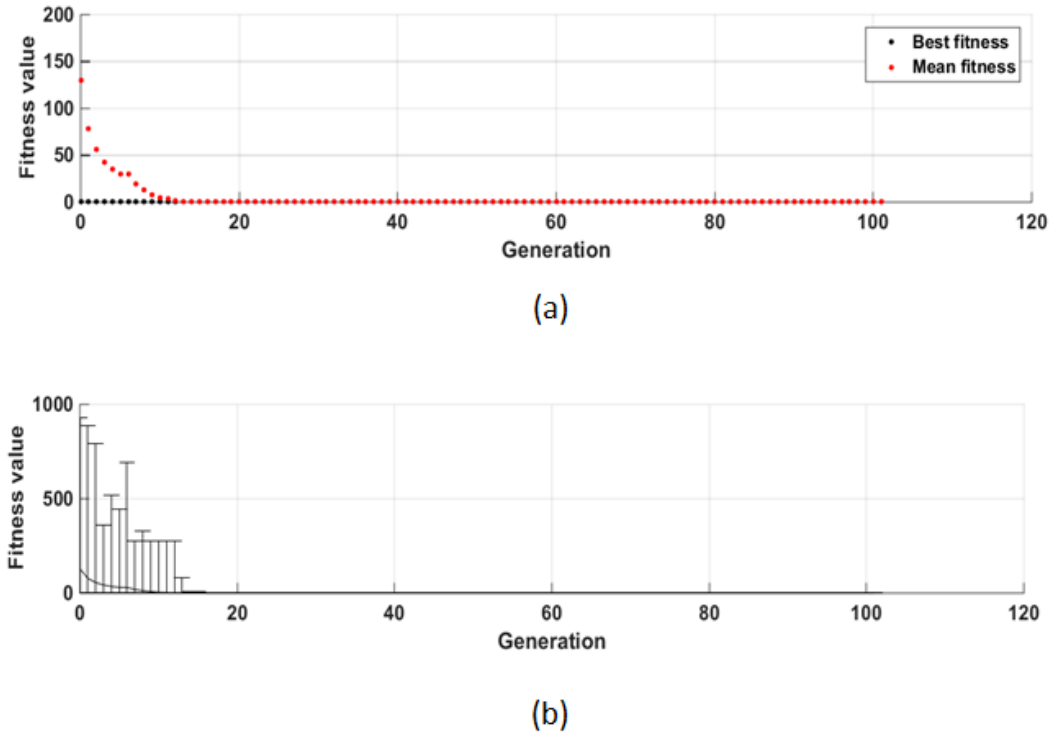


Fig. 4.8 Optimisation history for Rosenbrock's function. Graph (a) shows the best and mean fitness values per generation, (b) shows the best, mean and worst per generation

4.5.2 Test Case 2: Ackley's Function

Ackley's function can be expressed as:

$$F(X,Y) = -20\exp\left(-0.2\sqrt{0.5(X^2+Y^2)}\right) - \exp\left(0.5(\cos(2\pi X)+\cos(2\pi Y))\right) + 20 + \exp(1) \tag{4.15}$$

The two design variables X and Y lie in the range:

$$-5 < X\ ,\ Y < 5$$

And the minimum occurring at:

$$F_{min}(0,0) = 0$$

The exact solution is plotted in Figure 4.9 below. It is observed that the function takes its maximum values at the boundaries, whilst the dips are located around the centre, which represents the global optimum point. The function is used to test optimisation algorithms to ensure that they do not get caught in any local minima (i.e. troughs) surrounding the centre (i.e. midpoint).

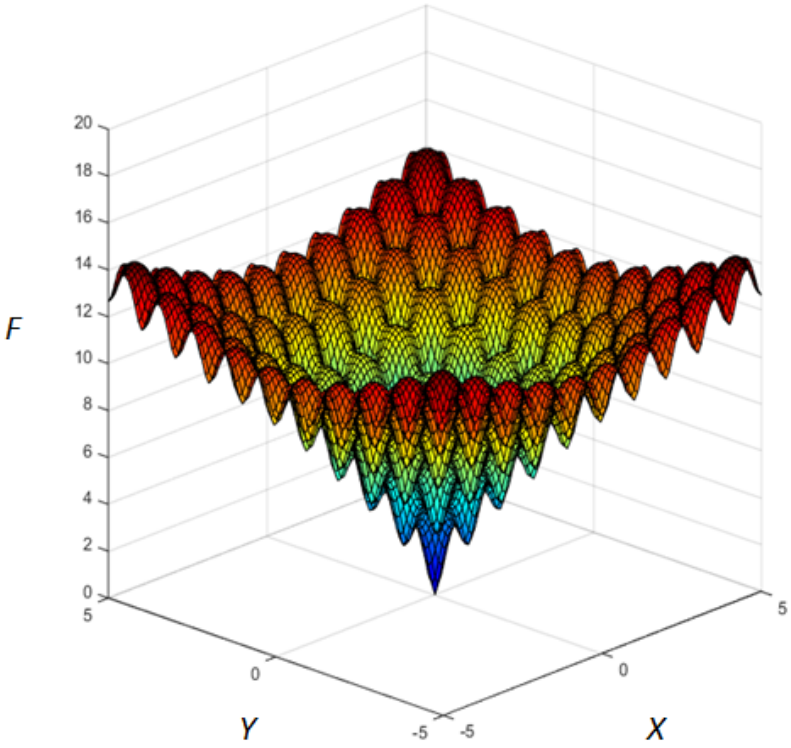


Fig. 4.9 Ackley's function (analytical solution), with $F_{min}(0,0) = 0$

Following a similar approach to that of test case 1 (Rosenbrock's function), the GA code is to be validated. Following the parameter setup as described in Table 4.1, the optimisation was carried out, with the history being displayed in Figure 4.10. The optimiser successfully locates the global minimum at the correct (midpoint) position. The best fitness value (i.e. zero) is found by the eleventh generation, and by the fifteenth generation the range of values and mean fitness are at the optimum value.

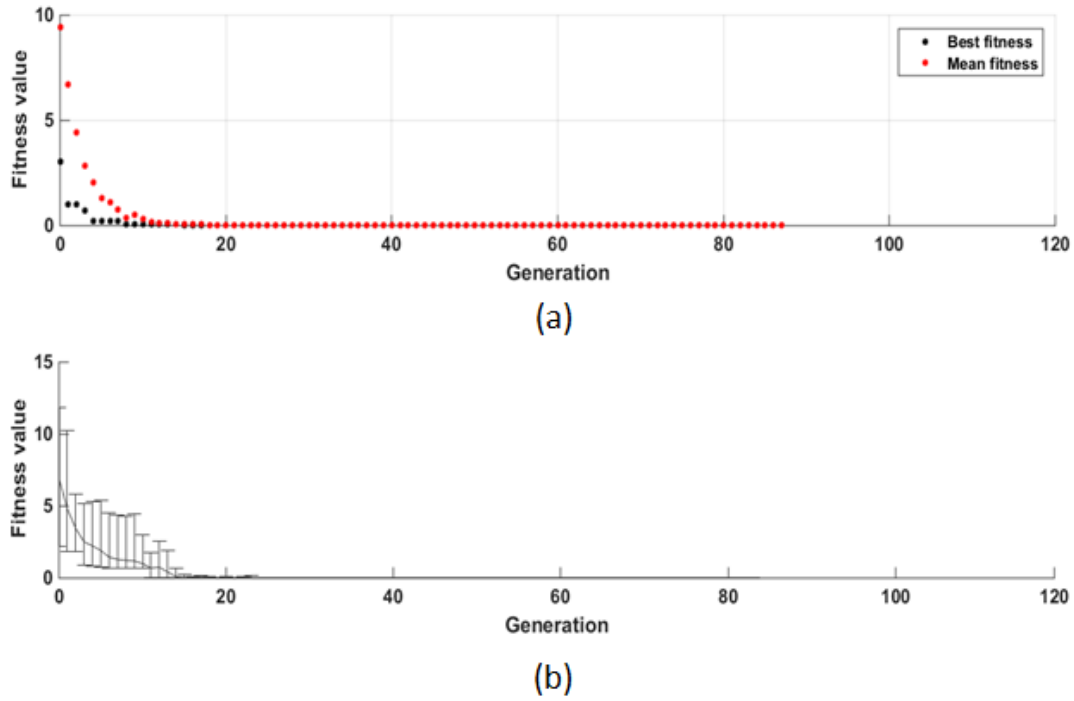


Fig. 4.10 Optimisation history for Ackley's function. Graph (a) shows the best and mean fitness values per generation, (b) shows the best, mean and worst per generation

4.6 Summary of Chapter

The chapter commenced with a discussion of the principles of design optimisation in both a single and multi-objective context. The Genetic Algorithm (GA) optimisation method was presented, with the search capability and applicability (despite the potentially large number of function evaluations) to a range of cases appear to make it a more suitable choice. Opting to run high fidelity CFD simulations in order to search the whole design space for a global optimum was seen to be infeasible (time intensive); a multi fidelity approach was discussed that implements a surrogate model which is constructed using relatively few accurate CFD runs. These sample (or 'experimental') points should fill the design space as evenly as possible, in order for an accurate surrogate model to be achieved; the Latin hypercube sampling method

was seen to fulfil this requirement. Predictive modelling techniques were presented (SVR and RFR), and both will be implemented for comparison purposes in the results chapters. Validation of the optimisation code has been successfully shown. The effect of potentially high variance in a model was discussed, with a cross validation method to be used in order to mitigate this. A flow chart showing the optimisation procedure is illustrated in Figure 4.11. This procedure will be applied to optimise NGVs in a computationally efficient and methodical manner.

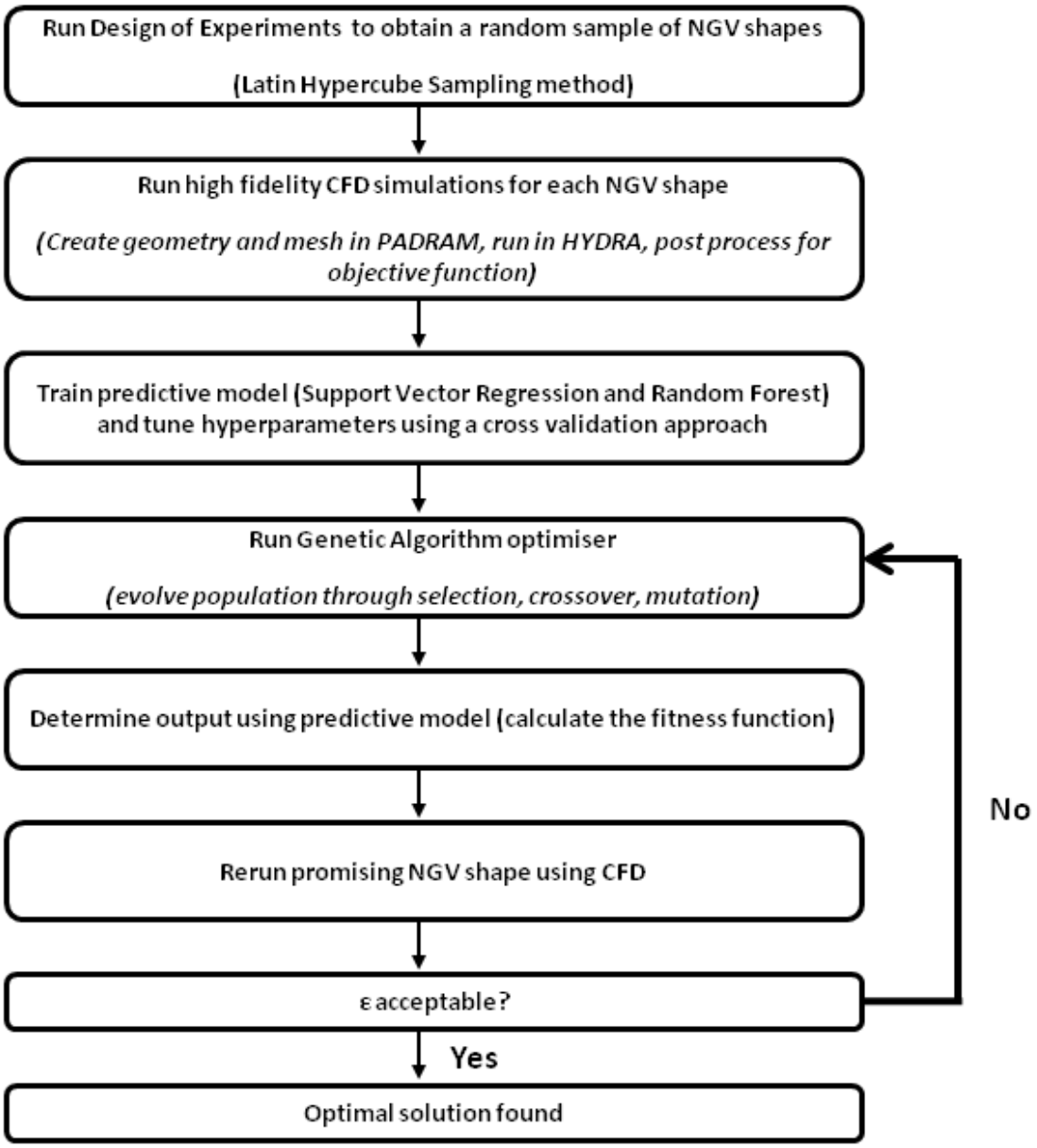


Fig. 4.11 Flow chart of optimisation procedure

Chapter 5

NGV Shaping under a Rich Burn Combustor Exit Profile

5.1 Introduction

In this chapter, the effect of a compound lean (CL) NGV arrangement on the downstream rotor row and stage aerothermal performance is presented. Two inlet conditions are investigated; a uniform temperature inlet (T_0 = 432 K) and an engine representative hot streak profile, with an overall mass averaged total temperature to match the uniform inlet case (i.e. T_0 of 432 K). As a reminder, the hot streak only boundary condition is representative of rich burn combustion. A radial distribution of the pitchwise averaged total temperature is plotted in Figure 5.1 for comparison purposes. It is noted that Figure 5.1 is computed from the CFD solution, hence there are some temperature deviations near the wall.

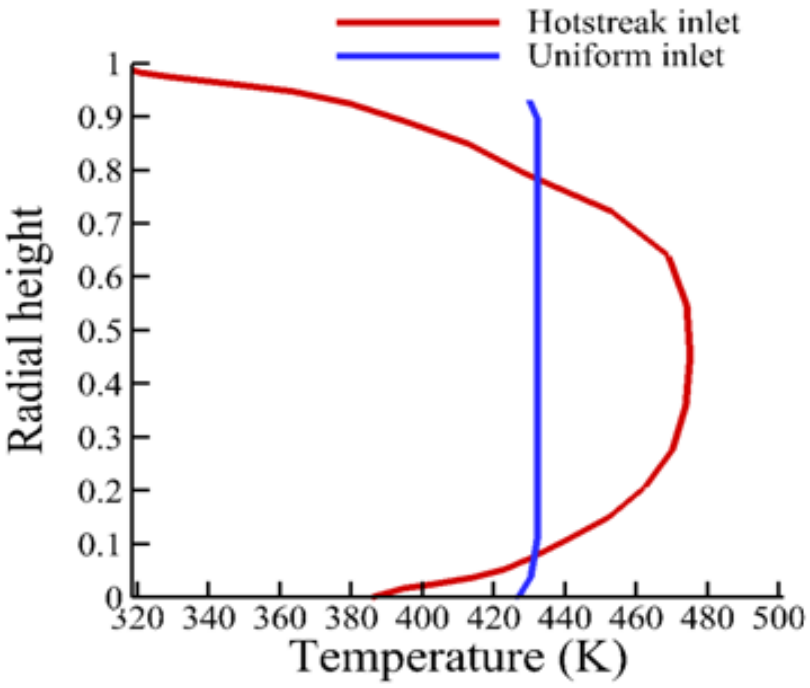


Fig. 5.1 Radial variation of pitch-averaged total temperature (K) at NGV inlet

The hot streak is clocked (circumferentially positioned) to align with the vane leading edge and this is shown pictorially in Figure 5.2. This clocking position is commonly considered as more suited for controlling the preferential heating on the rotor pressure surface (see Chapter 2 for further details).

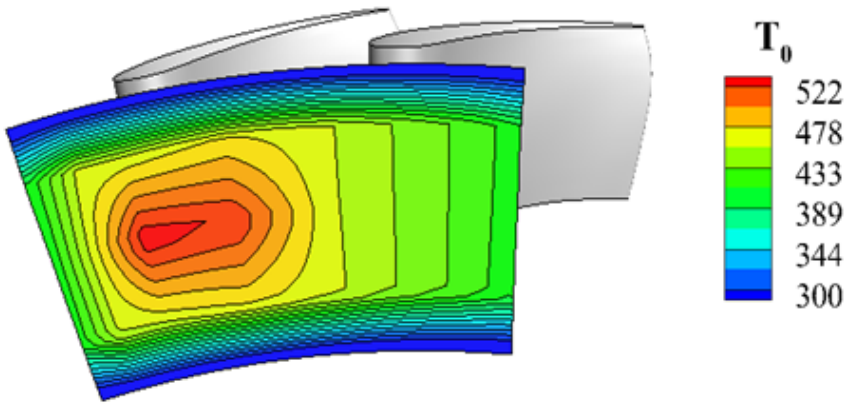


Fig. 5.2 Inlet hot streak total temperature (K) profile

The broad motivation for the present chapter and the following chapter is to understand how NGV lean can affect combined aerodynamics and heat transfer (aerothermal) performance of the HP turbine stage under realistic inflow conditions. Ensuring that geometrical parameters are vetted will allow the correct selection of the most suitable design variables to be implemented in an optimisation routine, resulting in a more efficient and accurate process. For the current chapter, two particular areas of interest are:

(a) Whether (and how) the effect of the NGV lean is dependent on the inflow temperature profile,

(b) Whether (and how) the changes in aerodynamics within the NGV passage due to lean affect the rotor aerodynamics and heat transfer (independent of the inlet temperature conditions).

Results and a discussion of the results are subsequently presented, by first analysing the vane aerodynamics before the rotor passage is investigated to assess the impact on heat transfer and aerodynamics. Finally the overall stage aerothermal performance and component heat load values are shown. The results presented in this chapter (and Chapter 6) are time-averaged from unsteady solutions. The unsteady behaviour associated with hot streaks, in terms of heat transfer, was shown by Khanal et al. (2012) to be only a small percentage of the time-averaged value. The analysis of detailed unsteady behaviour is relevant, but it is seen as more important in the current work to identify and analyse the time-averaged unsteady results. The procedure used to time average the data can be found in Section 5.2.1.

Before discussing the results, the computational setup implemented for this study will now be presented, including a grid dependency study for the compound lean vane configuration under rich burn conditions.

5.2 Method and Computational Setup

The MT1 geometry and inlet boundary conditions for the uniform and hot streak only cases are the same as those stated in the solver validation section in Chapter 3 (Section 3.8). Turbulence modelling was achieved by using the standard one equation turbulence model of Spalart-Allmaras (see Section 3.3 for details) and a realistic uniform turbulence intensity of 12% was applied at the stage inlet. The current chapter now considers leaned vanes in addition to straight vanes. As defined in Chapter 2, a compound lean is a circumferential bend that is applied to the near casing and hub sections from the pressure surface to the suction surface of the vane (shown pictorially in Figure 5.8). For the current leaned configuration, the displacement of the NGV midspan section is approximately 17% of the radial height. A grid dependency study is presented in Section 5.2.3 for the compound leaned NGV to ensure that the simulations are run with the fewest number of grid points, whilst still providing valid results.

5.2.1 Time-Averaging Procedure

The time-averaged HTC and T_{aw} parameters are calculated using the unsteady HYDRA simulation. The time-averaged HTC for the rotor blade is computed by first considering the unsteady heat flux (with n instantaneous snapshots per hot-streak period) from two isothermal runs with different specified wall temperatures ($T_{w,1}$, $T_{w,2}$) as a function of both space and time:

$$q_1(x,t^n) \, and \, q_2(x,t^n)$$

The unsteady HTC of position x at time instant n is then computed using the established definition, noting that it is still a function of time:

$$HTC(x,t^n) = \frac{q_2 - q_1}{T_{w,1} - T_{w,2}} \tag{5.1}$$

Similarly, for the unsteady T_{aw}:

$$T_{aw}(x,t^n) = \frac{q_2 T_{w,1} - q_1 T_{w,2}}{q_2 - q_1} \tag{5.2}$$

The n snapshots of HTC and T_{aw} are then averaged, which results in the time-averaged HTC at position x, $\overline{HTC}(x)$ and $\overline{T_{aw}}(x)$.

5.2.2 Computation of Stage Aerothermal Efficiency

The HP turbine stage efficiency which is implemented in the analysis section of this chapter is measured by a performance parameter, which accounts for aerodynamic and heat transfer effects. The parameter was proposed and applied in Khanal et al. (2013). As shown in Figure 5.3, the real process is represented as outputting work whilst rejecting heat (dashed line). This non-adiabatic efficacy, applicable for an uncooled or internally cooled blade, is defined as (see Figure 5.3):

$$\eta_{non-ad} = \frac{net\,useful\,work\,out}{ideal\,work} = \frac{\Delta h - \Delta Q}{\Delta h_{isentropic}} \tag{5.3}$$

Where

ΔQ = Total stage heat loss (calculated as the total integrated heat flux on all NGV and rotor components for all passages) per unit mass flow,

Δh = Actual enthalpy change,

$\Delta h_{isentropic}$ = Ideal enthalpy change (adiabatic and reversible, for an expansion to the same exit pressure).

This definition is useful as it allows the stage aerodynamic and heat transfer performance to be evaluated simultaneously in just one CFD run.

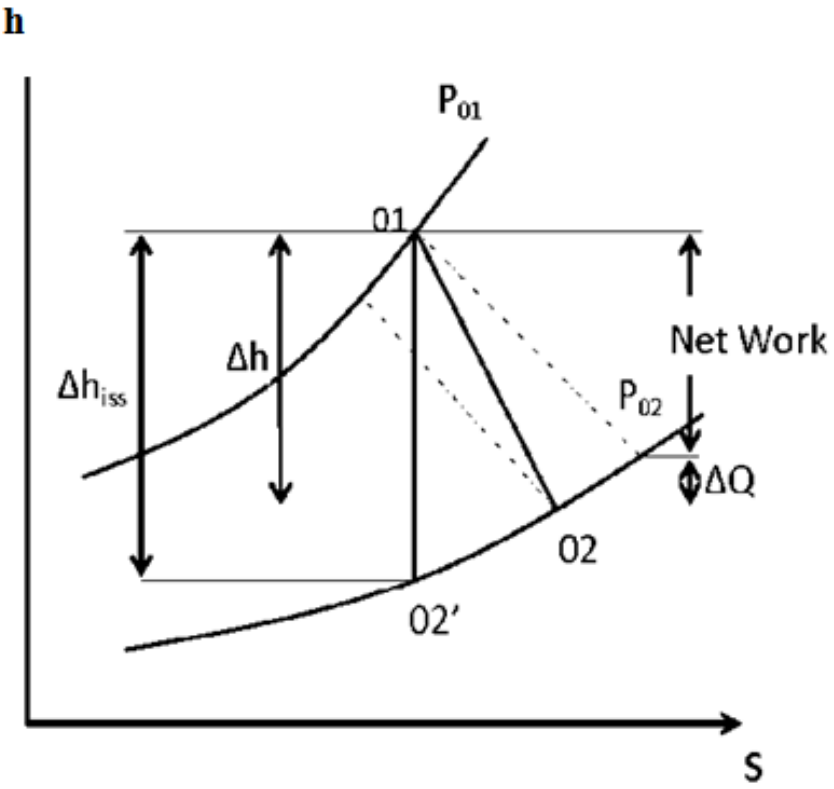


Fig. 5.3 Computation of stage efficacy from h-s diagram

5.2.3 Leaned NGV Grid Dependency Study for Hot Streak Inlet

A mesh sensitivity study for aerodynamics and heat transfer is provided in this section to ensure that sufficient grid points are used for the case with the leaned vanes. First, the O-mesh density in the boundary layer, normal to the NGV surface, was varied at 5, 10, 15 and 20 nodes normal to the wall, with the resulting isentropic Mach number and Nusselt number (Nu) distributions plotted in Figure 5.4 and Figure 5.5 respectively, at

three spanwise locations; 10%, 50% and 90%. It is noted that where three lines are visible, it implies that the 15 and 20 cell meshes overlap. Considering the Mach number (Figure 5.4), the cell density with 5 cells and 10 cells in the mesh shows considerable differences when compared with the finer meshes. This is apparent towards the trailing edge on the pressure side, and from 50% axial chord onwards for the suction side. Similarly, for the Nu distributions (Figure 5.5) the coarser meshes of 5 cells and 10 cells significantly overpredict the heat transfer on the pressure and suction surfaces. For meshes over 15 cells in the boundary, there is good agreement and hence grid independency is achieved.

For the finest O-mesh density, radial mesh independency was investigated by varying the number of grid points in the radial direction, with 30, 50, 70 and 100 points selected for the study. As can be seen in Figure 5.6 and Figure 5.7, there is very little discrepancy between the cases for any spanwise location. In order to ensure that complex flow structures are accounted for, a mesh of 20 cells in the boundary layer and 70 radial grid points is deemed sufficient for the aerothermal computations.

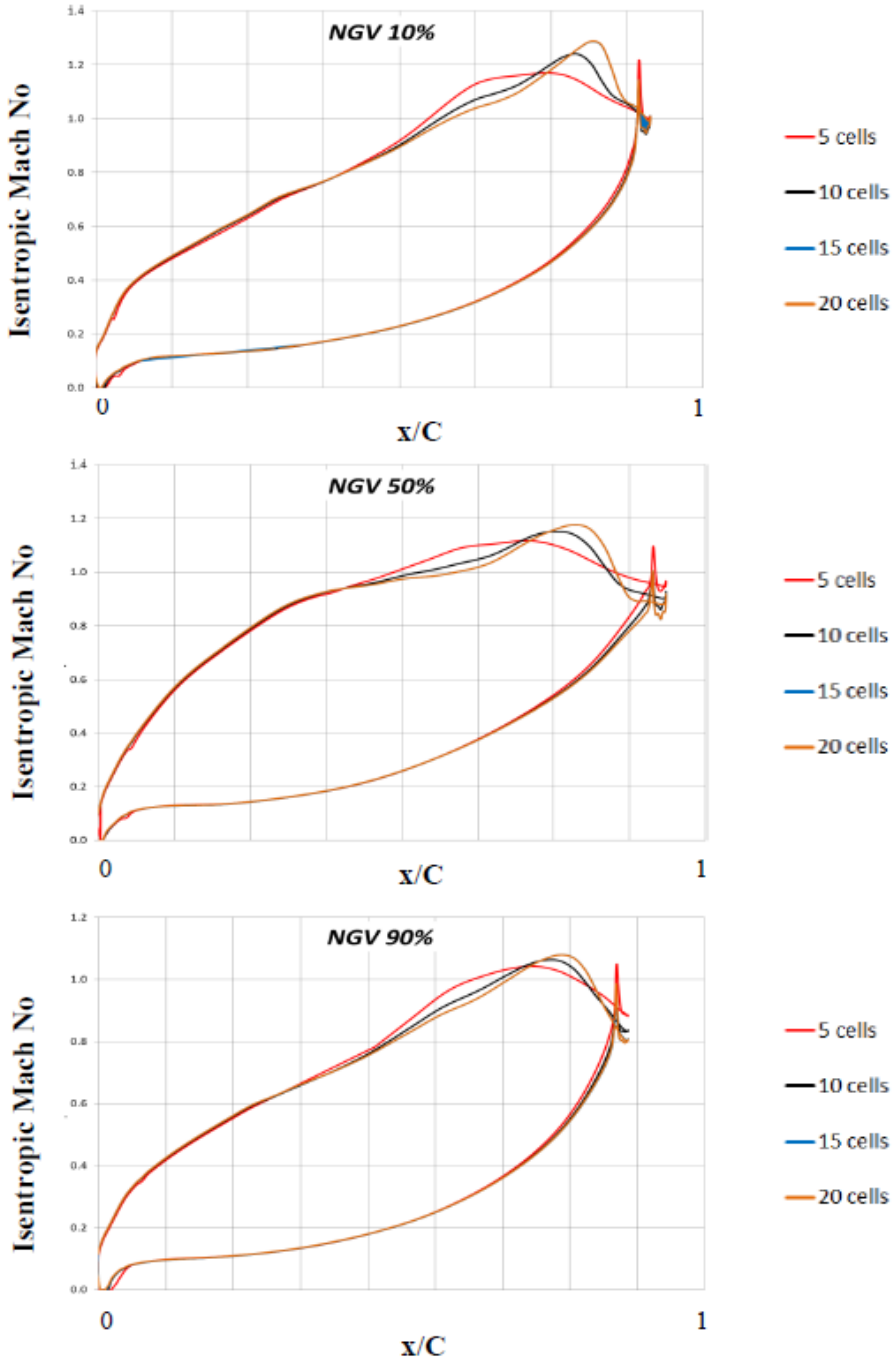


Fig. 5.4 Isentropic Mach number distribution on NGV surface with boundary layer grid variation

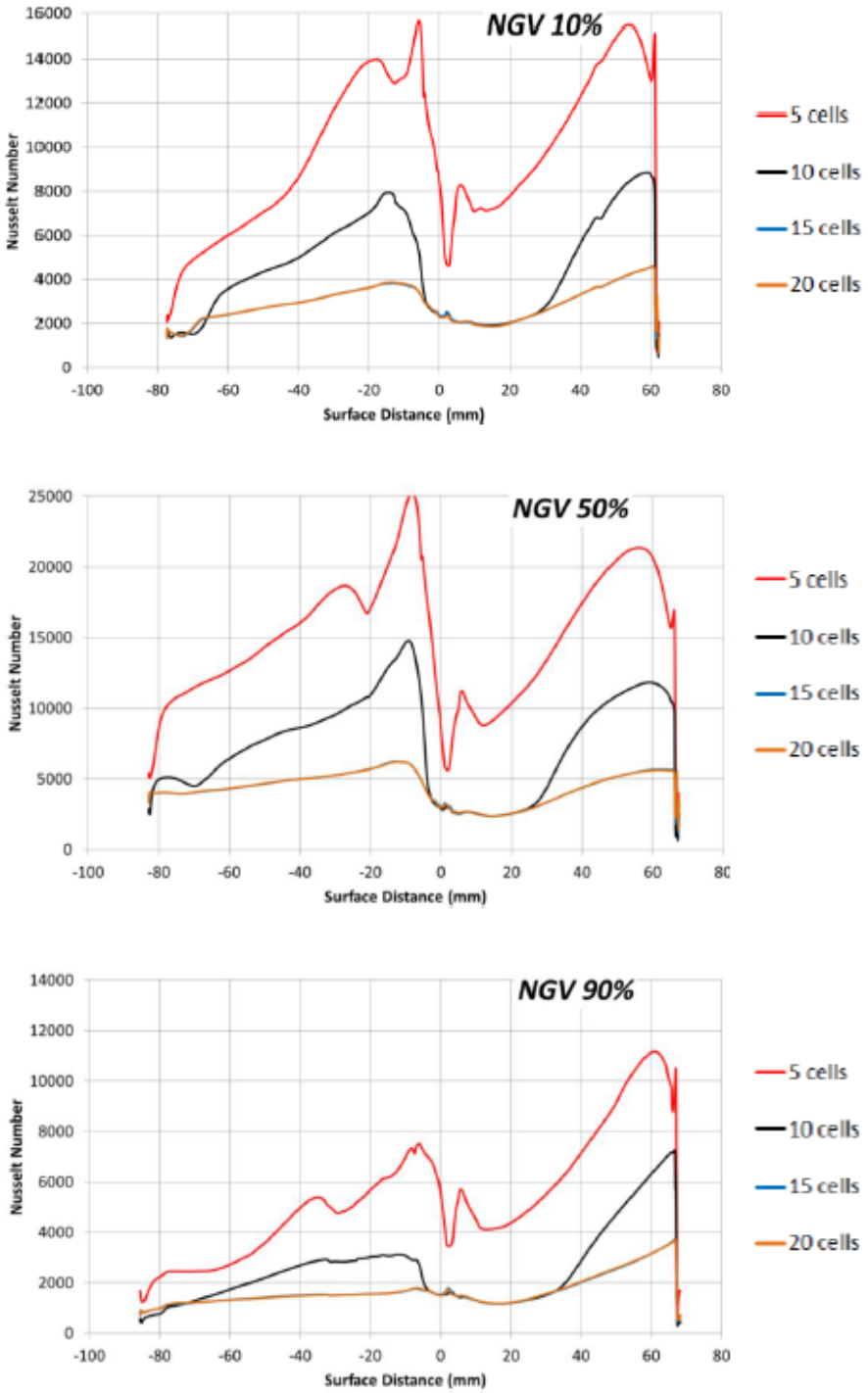


Fig. 5.5 Nusselt number distribution on NGV surface with boundary layer grid variation. Negative surface distances represents the vane suction surface.

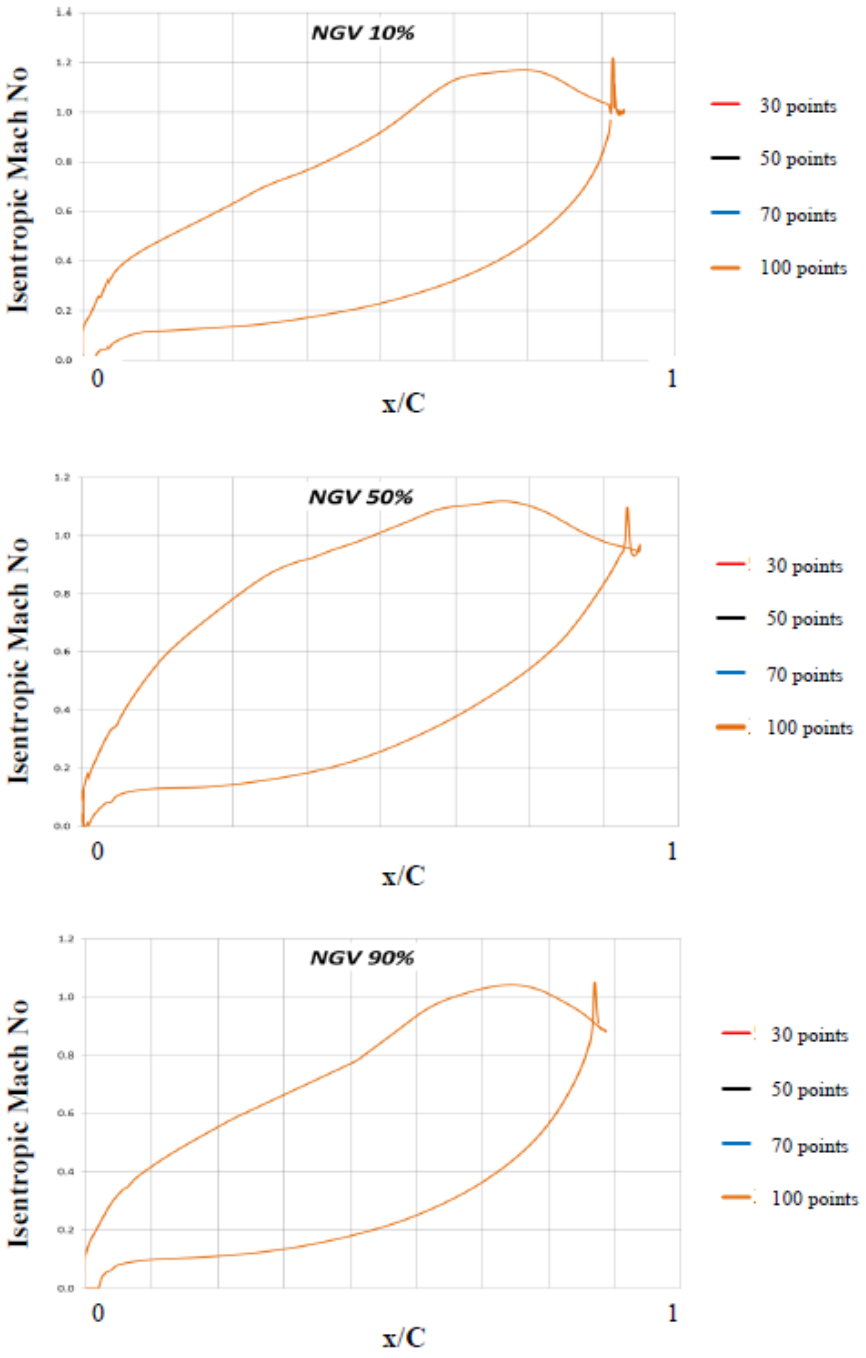


Fig. 5.6 Isentropic Mach number distribution on NGV surface with radial point grid variation

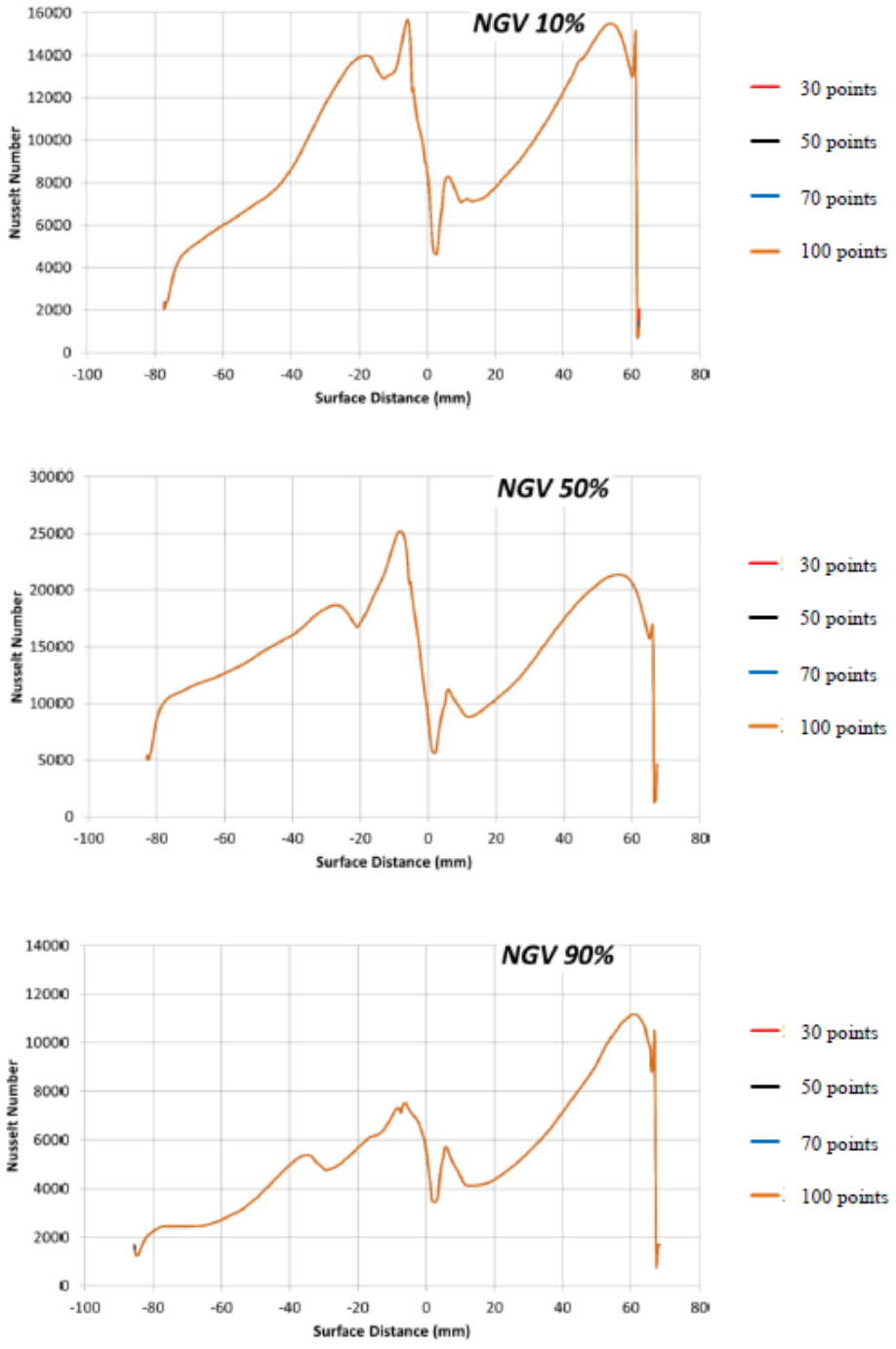


Fig. 5.7 Nusselt number distribution on NGV surface with radial point grid variation. Negative surface distances represents the vane suction surface.

5.3 NGV Passage Analysis

5.3.1 Effect of Compound Lean on HP Vane Aerodynamics

The aerodynamic results presented in this section agree with the current understanding from previous literature; there is a redistribution of loading with a decrease in secondary flow at the endwalls that is compensated for by an increase in profile loss at the midspan. This was explained in Chapter 2 (Denton and Xu (1999), Rosic and Xu (2012)) by the fact that the contour lines remain radial, since the pressure gradient in the radial direction is small in comparison with the blade-to-blade pressure gradient. The resulting 'frozen pressure field,' is independent of detailed blade shaping, as shown in Figure 5.8, which results in the midspan leaned sections being immersed in a region of lower pressure (compared with the straight vane configuration), thus increasing the loading. In contrast, the sections close to the endwalls experience a reduction in loading; this is confirmed by the isentropic Mach number plot in Figure 5.9, with a significant drop in Mach number near the casing for the leaned configuration on the suction side.

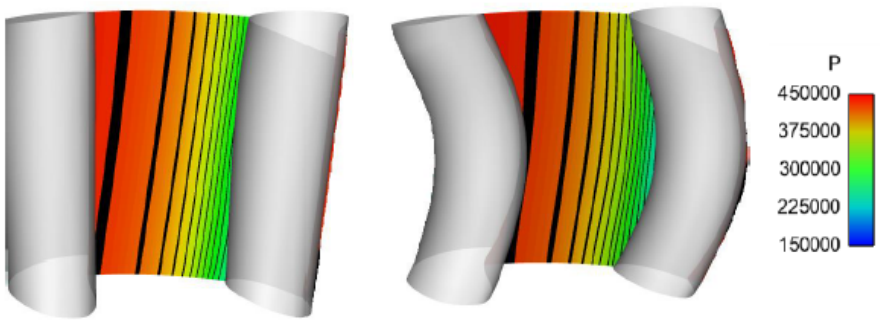


Fig. 5.8 Blade-to-blade static pressure (Pa) distribution

Noting the marked pressure difference between the endwall and the midspan, particularly on the suction surface (Figure 5.9), a radial flow movement from the

endwall to the midspan is expected. The convergent nature of the streamlines on the suction surface of the vane appears to confirm this movement in line with the increased loading at the midspan, as shown in Figure 5.10.

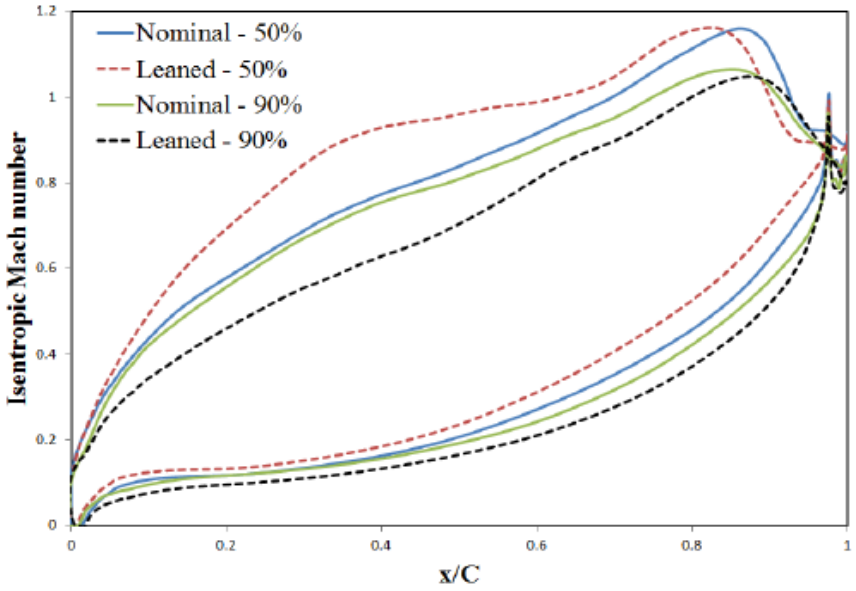


Fig. 5.9 NGV surface isentropic Mach numbers at 50% and 90% span sections for straight and leaned cases

At the hub suction surface corner, a region of circulation is present for both cases towards the trailing edge, as shown in Figure 5.10. It can be seen that the size of the circulation bubble is reduced with the introduction of compound lean. This is due to the pressure redistribution due to compound lean, which reduces the adverse pressure gradient effect towards the endwalls. The streamline pattern on the vane pressure side can also be seen in Figure 5.11, with slight divergence being observed towards the endwalls.

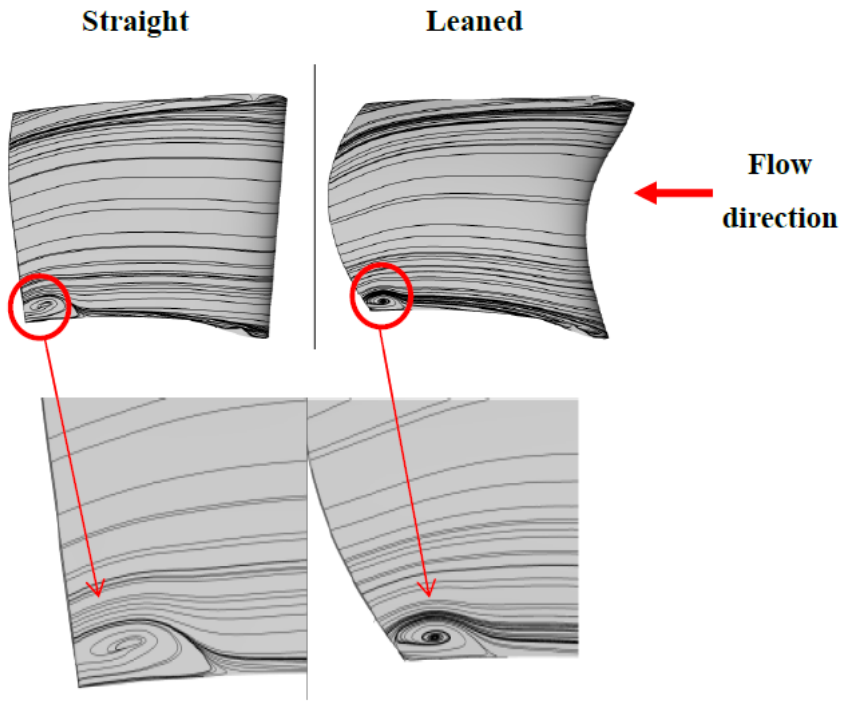


Fig. 5.10 Vane suction surface streamline movement and corner circulation

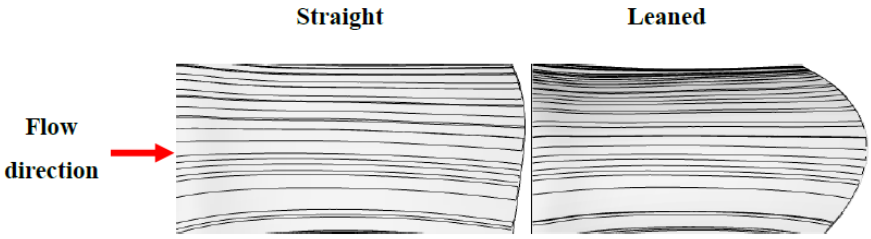


Fig. 5.11 Vane pressure surface streamline pattern

Figure 5.12 shows the blade-to-blade flow on the hub plane. It can be seen that there is less turning for the leaned case compared with the straight case. As mentioned earlier, this is caused by the cross-passage flow, which is created in the endwall regions and is a result of the imbalance between the near-wall low momentum and the pitchwise pressure gradient. In the endwall boundary layer, the flow velocity decreases and the force due to the pitchwise pressure gradient is now greater than the acceleration force in the main direction leading to crossflow. Since for the leaned case, the loading causes

a migration of low momentum fluid to the midspan, the pitchwise pressure gradient also decreases leading to a smaller amount of crossflow and hence less turning.

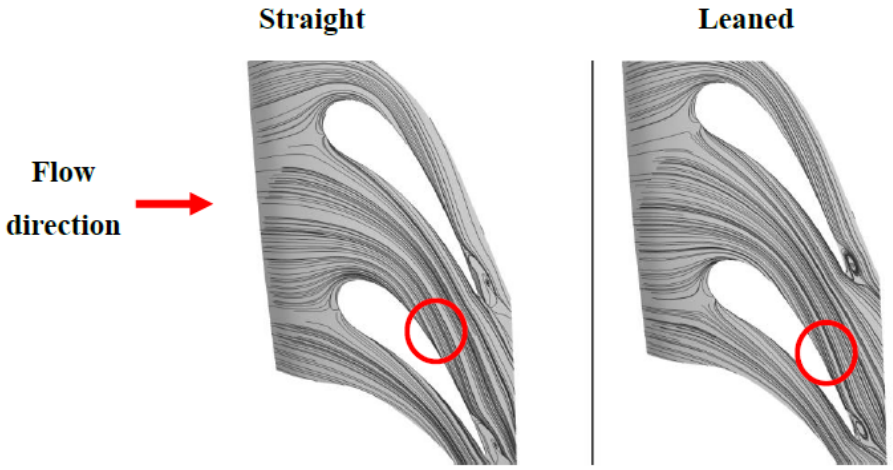


Fig. 5.12 Blade-to-blade flow on hub casing (indicating a reduced cross-passage flow for leaned NGV)

The total pressure loss coefficient distributions at the NGV exit plane are shown in Figure 5.13. The pressure loss coefficient is calculated using the following relation:

$$C_{p,loss} = \frac{P_{01} - P_{02}}{P_{ref}} \tag{5.4}$$

where P_{01} is the turbine inlet total pressure, P_{02} is the NGV exit total pressure (calculated using the isentropic pressure relation) and P_{ref} was taken to be the average dynamic pressure at the mid span of the exit plane in the uniform inlet case. A larger endwall hub loss core is observed for the straight case; the leaned case shows the endwalls being unloaded, with an increased load (and loss) near the midspan; this can be explained by considering the new locations of the midspan and endwall sections respectively in the 'frozen' passage pressure field with clustering constant pressure lines from the pressure surface to the suction surface (Figure 5.8). By considering the pressure coefficient variation in the radial direction, it is observed that the loading

is indeed redistributed for the leaned cases but does not necessarily result in a lower overall value; this is confirmed by the radial distribution of the pitchwise averaged total pressure plot in Figure 5.14, and in line with the observation made by Harrison (1992). In other words, the secondary pressure loss reduction near the endwalls is largely compensated by the increased profile loss near the midspan.

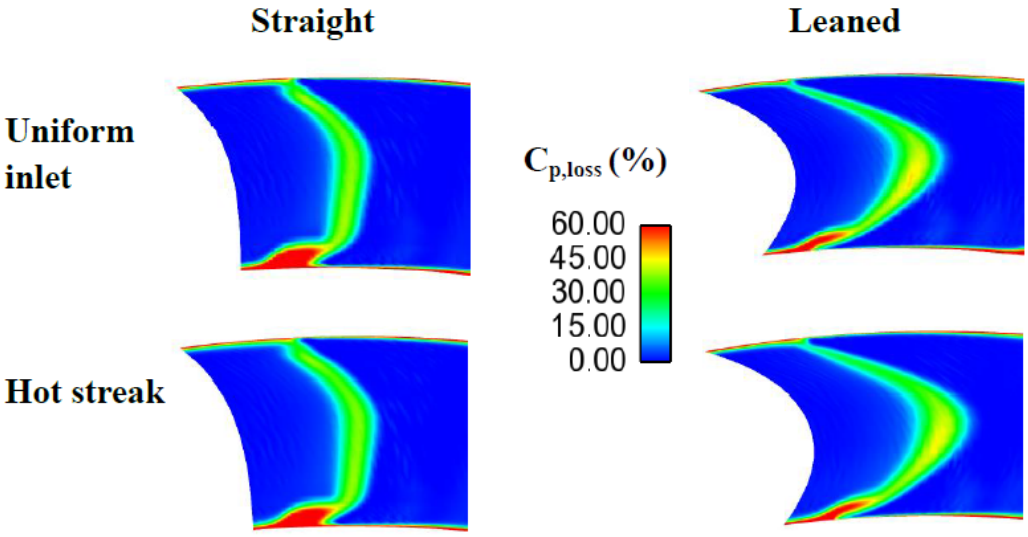


Fig. 5.13 Total pressure loss coefficient at NGV exit

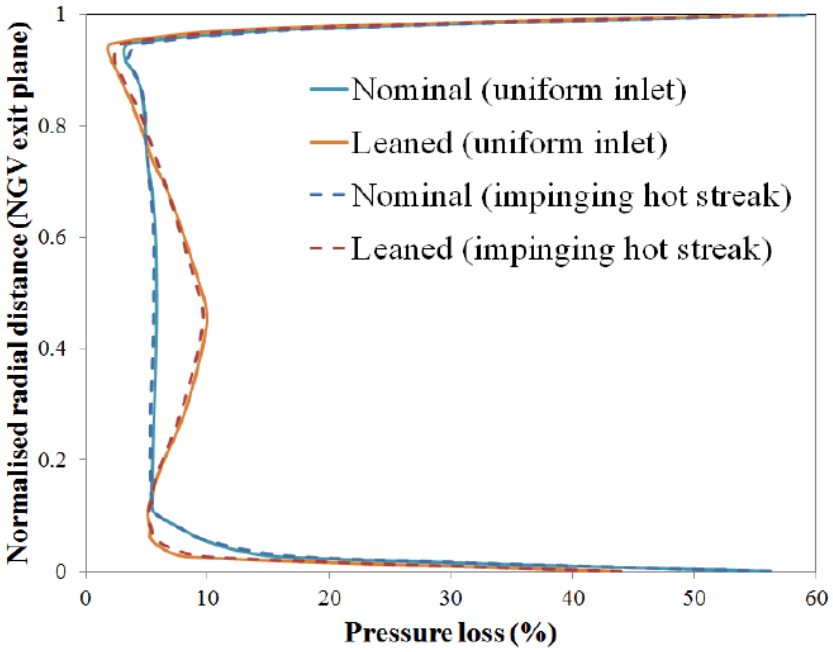


Fig. 5.14 Radial plot of pressure loss at vane exit

The absolute NGV exit flow angles are shown in Figure 5.14 for both inlet conditions. As expected, the blade lean increases the midspan turning while reducing the endwall turnings. It is also very clear from Figure 5.14 and Figure 5.15 that the introduction of a hot streak makes little difference to the NGV aerodynamic load and loss, in line with the Munk-Prim principle (Munk and Prim (1947)).

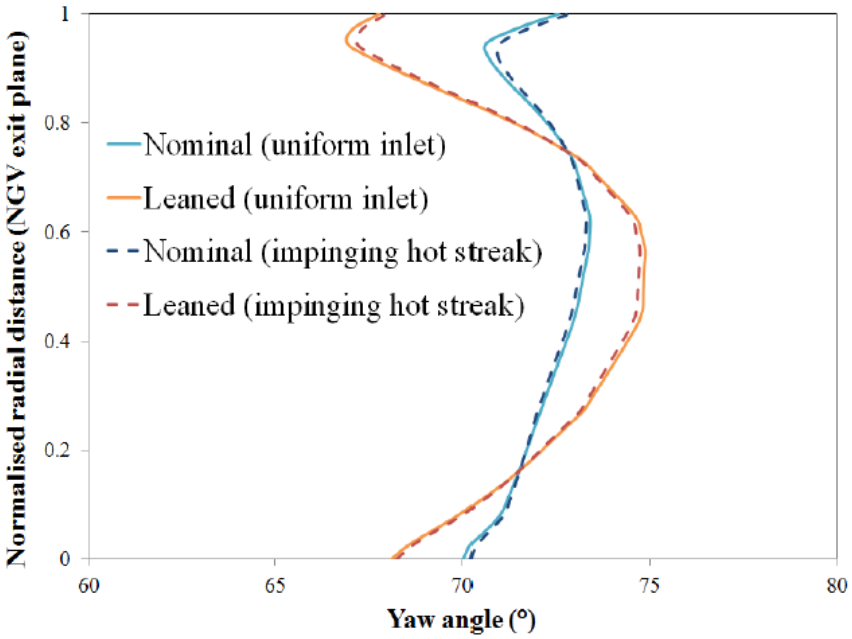


Fig. 5.15 Radial plot of absolute yaw angle (deg) at vane exit

5.3.2 Radial Mass Flow Redistribution in NGV passage

The discussion thus far has been concerned with the influence of compound lean on the aerodynamic loading redistribution, with the midspan tangentially displaced into a region of low pressure, resulting in a higher loading at midspan, and a lower loading at the endwalls. The results presented so far are completely in line with previous findings. An approach to the NGV radial redistribution mechanism is now made from a different perspective. The focus is directed to the potential impact of the radial redistribution on the downstream rotor; specifically, whether an offloading of the leaned vane endwall regions would result in an offloading of the rotor hub and tip regions.

First, a closer look is taken at the radial mass flow migration. Figure 5.16 shows the mass flux plotted on the NGV exit plane, with the approximate positions of the vane wake sketched onto the diagrams. Although there is a seemingly clear radial migration from endwalls towards the midspan, as seen in Figure 5.10, the NGV passage as whole

does not appear to behave in the same manner. From Figure 5.16, two observations can be made:

- For both inlet conditions, the compound lean appears to redistribute the passage mass flow significantly from the midspan to the endwalls.
- The hot streak also contributes to shifting mass from the central region to the endwalls; this effect seems to be largely independent of the vane configuration.

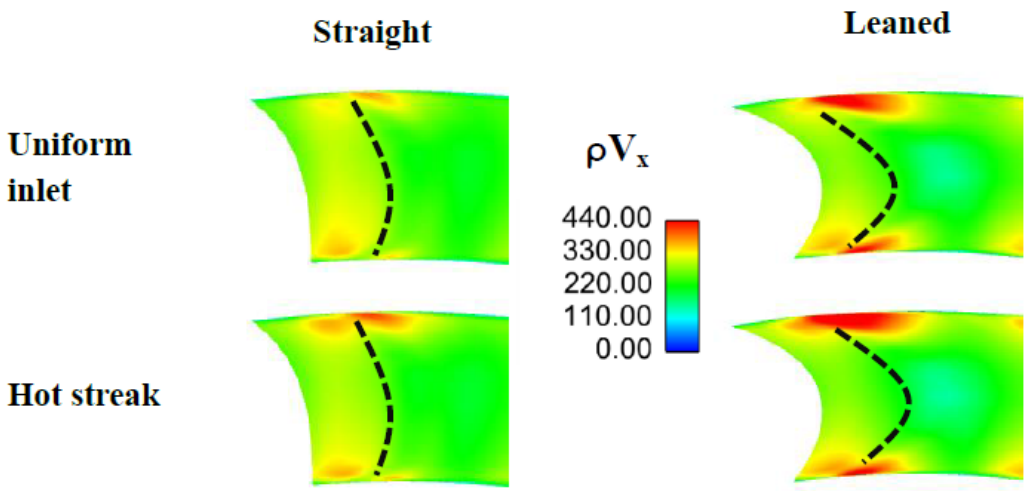


Fig. 5.16 Mass flux (kg m^{-2} s^{-1}) contours on NGV exit plane (dashed line indicates wake)

The first point appears to suggest that the lean redistribution towards the midspan described earlier may only be a localised feature close to the suction surface. Figure 5.17 shows the streamlines in the vane passage on a plane close to the pressure surface. A divergence of streamlines away from the midspan towards the endwalls is evident for the leaned configuration, an effect that is more visible near the casing. This suggests that the dominant influence in the vane passage is driven by the pressure surface diverting flow away from the midspan.

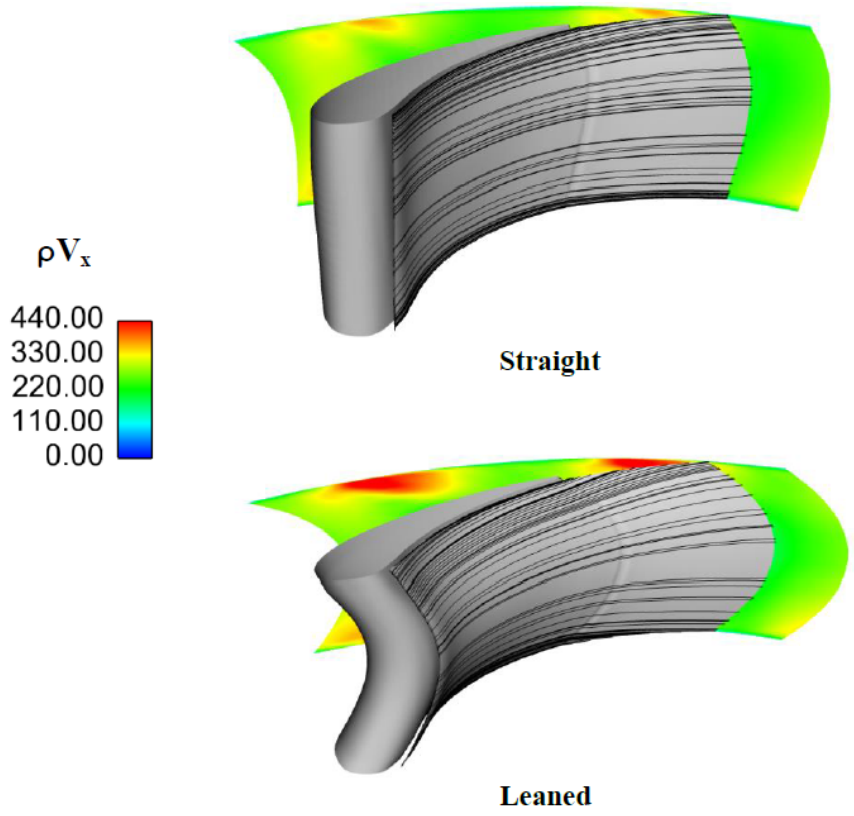


Fig. 5.17 Streamline traces on mesh plane close to pressure surface and mass flux (kg m^{-2} s^{-1}) contours on the NGV exit plane

With the introduction of the hot streak, the mass flux at the endwalls is further increased (as shown in Figure 5.16), as well as in the spanwise distributions of the pitch-averaged mass flux at the vane exit in Figure 5.18. An increase of between 10%-15% is seen for the configurations under hot streak conditions when compared with the equivalent uniform cases. This can be explained by considering the mass flow, which is directly proportional to the stagnation pressure and inversely proportional to the square root of the stagnation temperature (valid for choked flow),

$$\dot{m} \propto \frac{P_0}{\sqrt{T_0}} f(M) \tag{5.5}$$

For the hot streak profile, there is a reduction in the total temperature at the endwalls, which, based on the relationship above, results in a higher mass flow at the hub and casing. When this hot streak effect is combined with geometrical lean it results in the hot fluid at the turbine inlet being driven by the passage divergence mechanism towards the endwalls, resulting in the case with the highest mass accumulation.

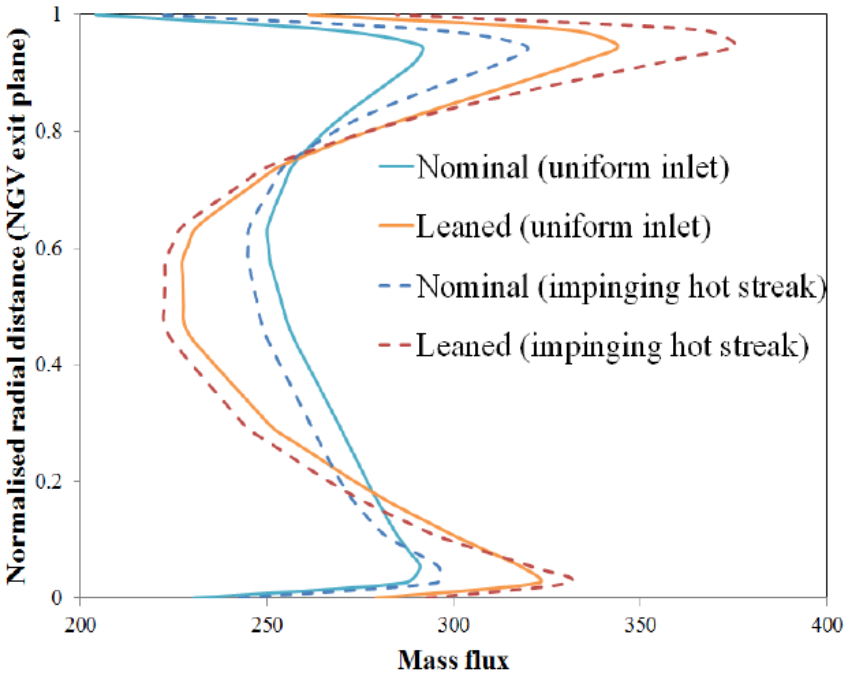


Fig. 5.18 Radial plot of pitch-average mass flux (kg m^{-2} s^{-1}) at vane exit

5.4 Rotor Passage Analysis

5.4.1 Influence of NGV Lean and Hot streak on Rotor Inlet

With such significant increases in the tip mass flow due to the NGV lean as well as the hot streak, it is useful to assess whether this is attributed to a change in density or axial velocity, or both. A velocity change would affect the rotor inflow angle, whilst a density change will affect the rotor relative dynamic head.

The axial velocity contours at the NGV exit are given for the two NGV configurations, for the uniform inlet (Figure 5.19) and the hot streak inlet (Figure 5.20). It is clear that the tip mass flow increase by the NGV lean is achieved through a local increase in the axial velocity (Figure 5.19 (b)). This concentrated high velocity region is likely to be a source of extra mixing losses in the rotor row. Interestingly, once the hot streak is introduced, the local high velocity region is considerably moderated (Figure 5.19 (b)), resulting in a more uniform velocity distribution; this is a desirable effect. According to Munk and Prim (1947), the Mach number remains unchanged through the vane passage even with a hot streak profile present at the inlet:

$$V_x = M_{axial}\sqrt{\gamma RT} \tag{5.6}$$

The static temperature change is proportional to the total temperature change. Given the same overall mean inlet temperature, the hot streak case will correspond to a cooler tip compared to the uniform inlet (Figure 5.1). Thus the local axial velocity for a hot streak case must also reduce accordingly for the Mach number to remain constant. Consequently, for a leaned NGV, the further increase of local mass flux near the tip when subject to a hot streak will be attributed solely to a local increase in density to compensate for this reduction in axial velocity near the tip. This is supported by the density contours plotted in Figure 5.21 for the uniform and hot streak inlets.

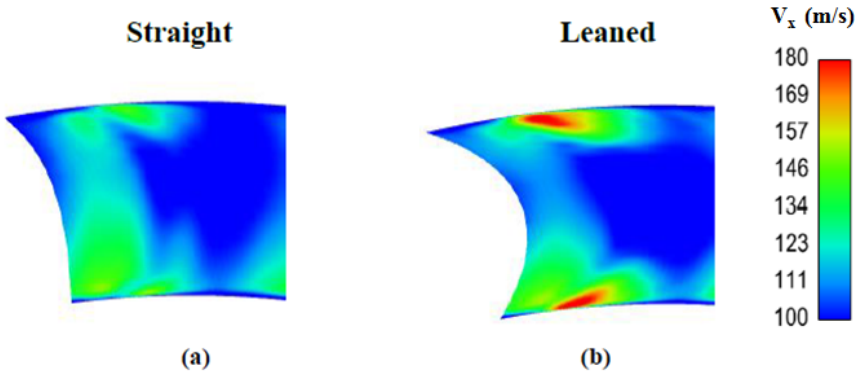


Fig. 5.19 Axial velocity (m s^{-1}) contours at NGV exit (uniform inlet)

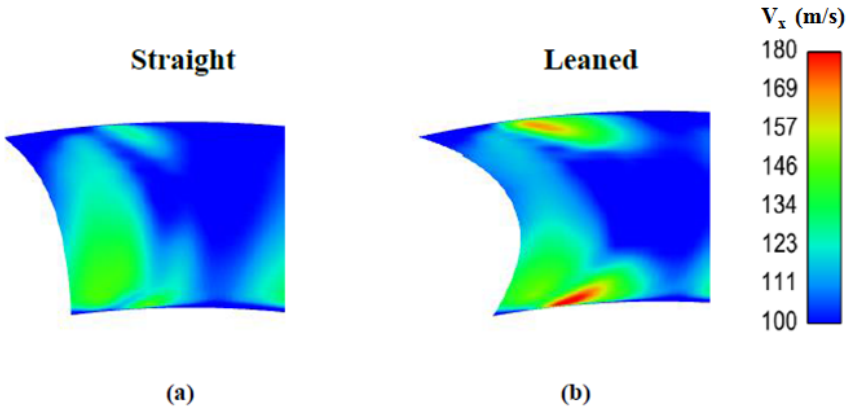


Fig. 5.20 Axial velocity (m s^{-1}) contours at NGV exit (hot streak)

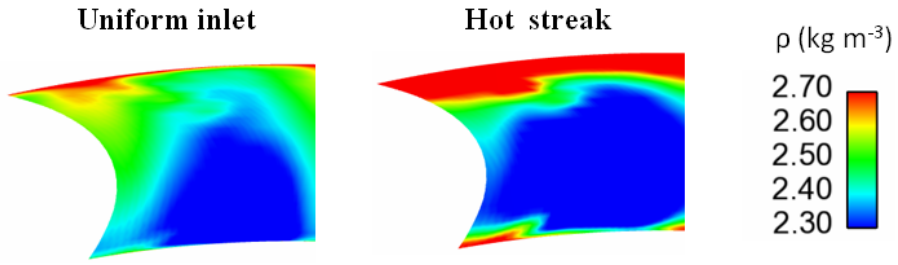


Fig. 5.21 Density (kg m^{-3}) contours at NGV exit for a uniform and hot streak inlet (leaned NGV configuration)

The relative yaw angle at the rotor inlet is plotted in Figure 5.22. Generally speaking, it can be see that there is an offloading at the endwalls and uploading at the

midspan when the lean is introduced; this is largely in line with what was observed at the vane exit (Figure 5.15). The hot streak effect is seen to reduce the rotor yaw angle at the endwall. An interesting point to note is that for the hot streak inlet, the local relative yaw angles for the leaned and straight NGV are approximately the same, from 75% span to the tip. This is in clear contrast to the uniform inlet cases, where there is a significant offloading due to the blade lean.

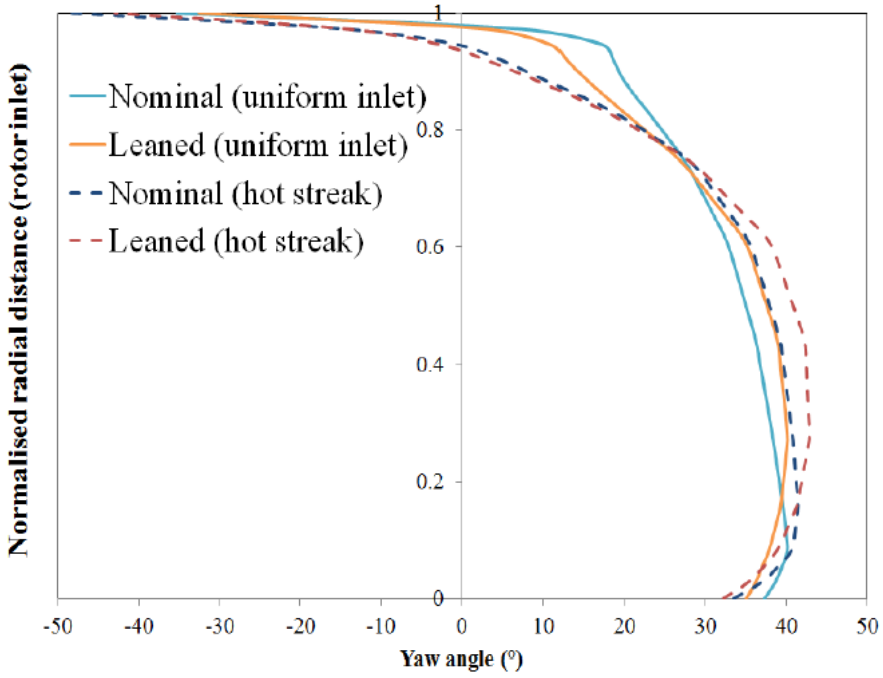


Fig. 5.22 Radial plot of relative yaw angle (deg) at rotor inlet

These contrasting characteristics may be understood by considering the rotor inlet velocity diagrams for the straight and lean configurations, as shown in Figure 5.23. The baseline (uniform inlet) velocity triangles are represented by *ABC* and *abc* for the straight and leaned cases respectively. The leaned vane has a lower absolute yaw angle (Figure 5.15), and a higher axial velocity, compared to the straight vane arrangement, as seen in Figure 5.19 and Figure 5.20. When the hot streak is introduced, the NGV exit yaw angle remains largely the same due to the Munk and Prim similarity rule, and

the local axial velocity is reduced – this reduction can be seen in the contrast between Figure 5.19 and Figure 5.20. The velocity triangles are hence reduced to $AB'C'$ and $ab'c'$ (Figure 5.23).

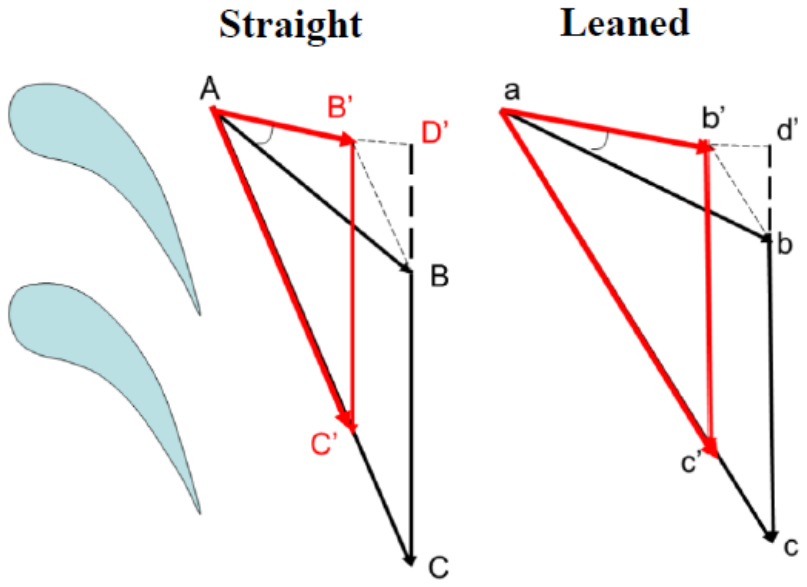


Fig. 5.23 Velocity diagrams at rotor inlet near to the tip (red velocity triangles indicate hot streak cases)

The offloading effects due to the hot streak are measured by the angle $\angle BAB'$ and $\angle bab'$ respectively. Given the same inlet temperature profile, it is reasonable to assume that the reduction in axial velocity is comparable (i.e. $B'D' \approx b'd'$). Consider the angle changes of interest are small enough, and the rotor relative velocities are roughly the same ($AB \approx ab$) when working out angles. This results in:

$$\angle BAB' \approx \frac{BD'}{AB} \tag{5.7}$$

$$\angle bab' \approx \frac{bd'}{ab} = \frac{bd'}{AB} \tag{5.8}$$

The difference between the relative velocities for the straight and the leaned NGV leads to $\angle bab'$ being smaller than $\angle BAB'$. This means that the reduction in the rotor inlet yaw due to the hot streak is smaller for a leaned NGV than that for a straight NGV. This difference results in a much closer rotor yaw angle in the tip region for the two configurations as observed in Figure 5.22.

The radial loading distribution in terms of the rotor relative total pressure (pitch-averaged) is shown in Figure 5.24. The distributions in terms of the inlet head for the leaned cases show the opposite trend to what is observed at the vane exit in terms of the NGV loading. The endwalls are now loaded up, whilst the midspan is offloaded. The loading distribution seemingly shows a higher non-uniformity once the vane lean is introduced.

For a leaned NGV, the rotor tip is subjected to two opposing influences; offloading in terms of the relative inflow angle (Figure 5.22), and an uploading due to the local high head (Figure 5.24). As will be seen in Section 5.4.2, the combined effect of these two factors seems to produce a beneficial radial pressure gradient to control the hot fluid migration without causing an extra cross-passage pressure difference, and hence additional secondary flows.

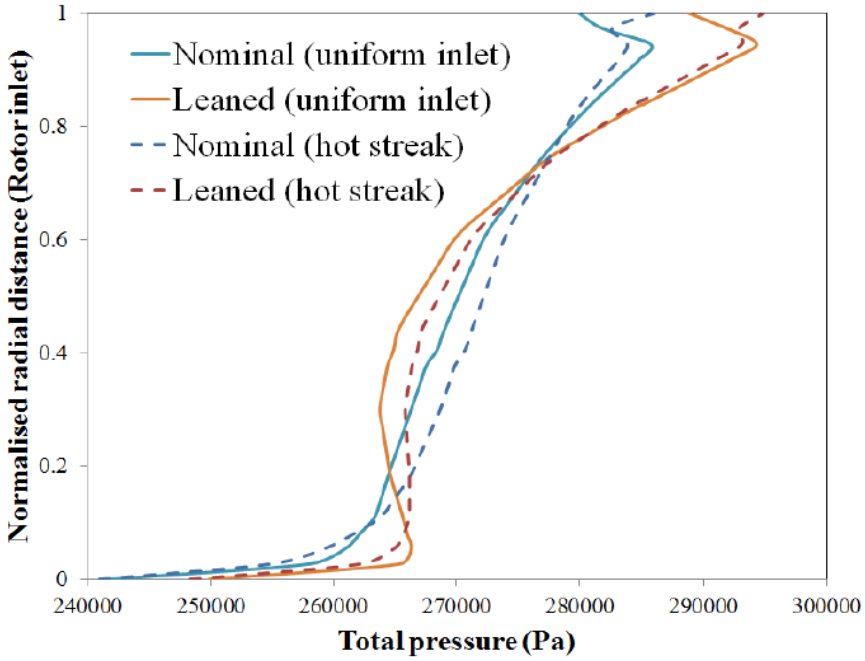


Fig. 5.24 Radial plot of relative total pressure (Pa) at rotor inlet

5.4.2 Rotor Aerothermal Results

Figure 5.25 shows the heat flux distributions on the rotor pressure surface, superimposed with the streamtraces. The impact on the distributions due to the lean with and without the hot streak will now be analysed. For the uniform inlet, the straight case shows positive characteristics over the leaned configuration, with a cooler leading edge extending radially over a larger portion of the span while the leaned case has clearly unfavourable heating towards the rotor tip. However, once the hot streak profile is introduced, the leaned case produces promising results, with a cooler tip region and a reduced trailing edge hot spot located close to the hub. Furthermore, there is a noticeable convergence of streamlines for the leaned NGV case in the midspan region, as they progress towards the trailing edge. For the straight NGV, however, the pressure surface streamtraces clearly diverge, particularly towards the tip.

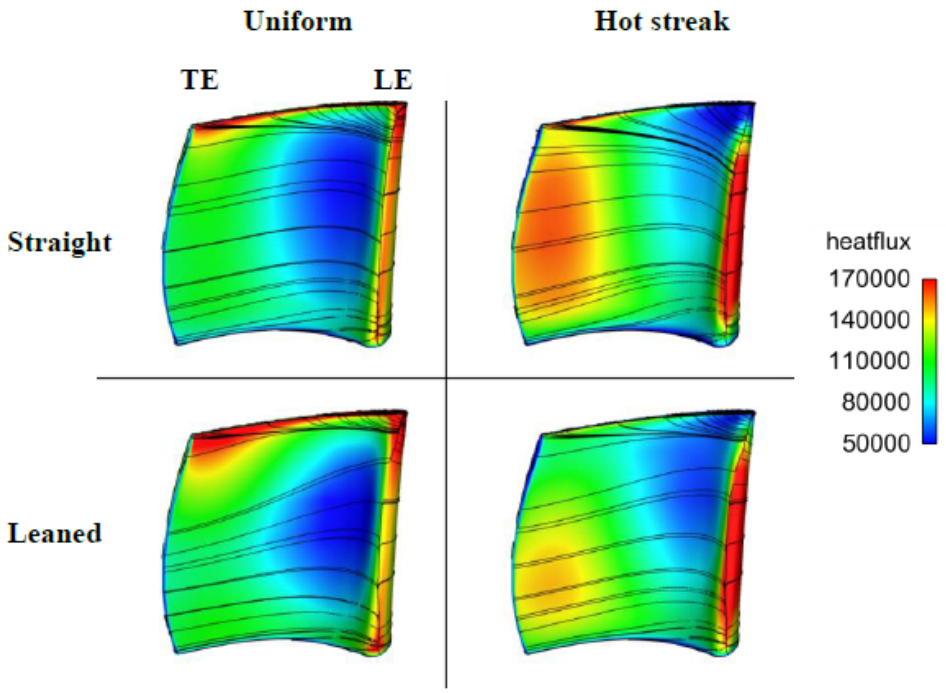


Fig. 5.25 Heat flux (W m^{-2}) contours on rotor pressure surface

The associated radial migration toward the tip for the straight NGV configurations indicates two undesirable consequences:

(a) A feeding secondary flow (tip leakage) from the pressure side tip corner.

(b) Migration of hot fluid from the midspan to the pressure surface tip (and further onto the tip gap), for a hot streak case.

Figure 5.26 shows the corresponding rotor suction surface heat flux and the stream-traces. The cooler hub and casing regions are noted for the hot streak cases, due to the nature of the temperature inlet profile. Whilst the lean has a significant effect on the rotor pressure side, no noticeable difference is seen on the suction surface.

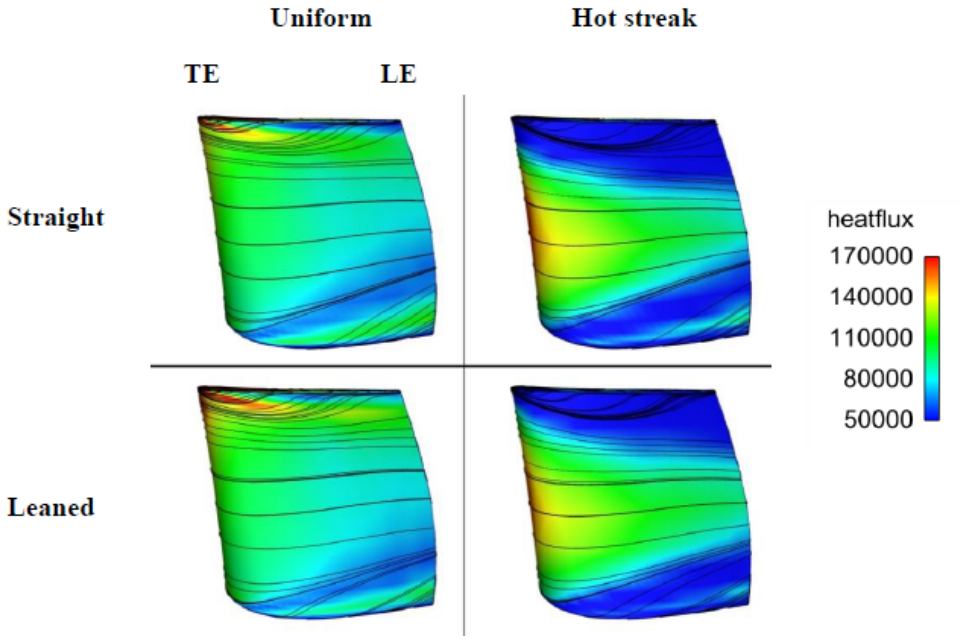


Fig. 5.26 Heat flux (W m^{-2}) contours on rotor suction surface

The different streamline patterns between the suction and pressure surfaces may be explained through a consideration of the local pressure changes relative to the local inertia (dynamic head). The local pressure coefficient for a more meaningful comparison is defined as:

$$C_{p,local} = \frac{P_s - P_{baseline}}{P_{0,rel} - P_s} \tag{5.9}$$

where P_s is the local static pressure, $P_{baseline}$ is the local reference pressure taken from a uniform flow case solution. $P_{0,rel}$ is the local relative total pressure. For each mesh point, this is taken from the rotor inlet total pressure profile (Figure 5.24) at the same spanwise location.

The C_p contours are plotted in Figure 5.27. For the straight case there is a high localised pressure at the rotor midspan region, which effectively results in a pressure gradient acting towards either the hub or tip. This is detrimental as the hot fluid that

naturally travels in the midspan (for a hot streak inlet) is now shifted towards the rotor tip. This is in comparison to the leaned case, where the highly loaded endwalls generate an endwall-to-midspan pressure gradient. On the other hand, it should be mentioned that for the suction surface, the C_p contours (not presented) indicate very little change. This is simply because of the relatively much larger local dynamic head on the suction surface.

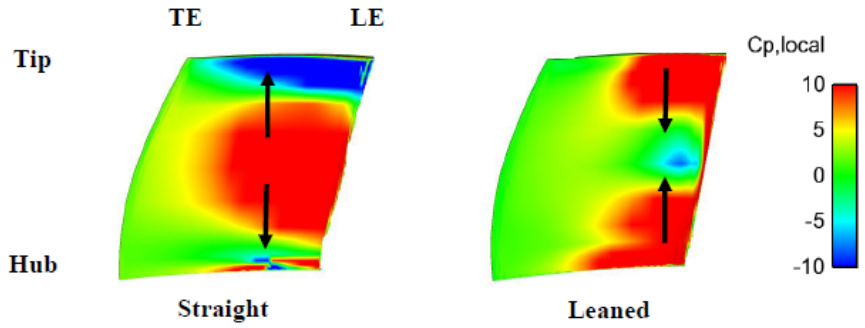


Fig. 5.27 Pressure differences on rotor pressure surface, normalized by the local relative dynamic head (Equation 5.8). Arrows indicate pressure gradient directions

Heat flux plots in the tip region are presented in Figure 5.27 and Figure 5.28 for the uniform and hot streak cases respectively. Under uniform conditions, the leaned case shows regions of higher heating when compared with the straight. However, an opposite trend is observed once the hot streak is introduced; there is now a significant reduction in heat flux, resulting in a cooler tip region over the majority of the section.

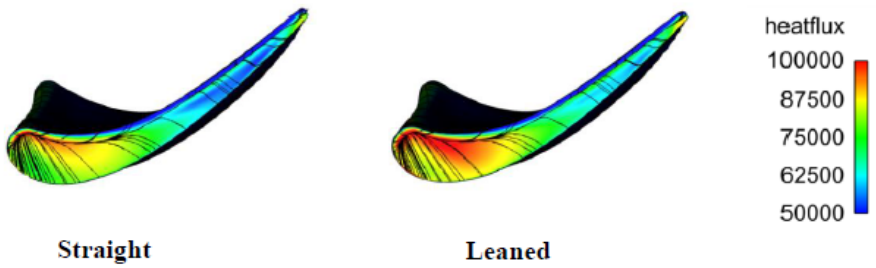


Fig. 5.28 Heat flux (W m^{-2}) on rotor tip (uniform inlet)

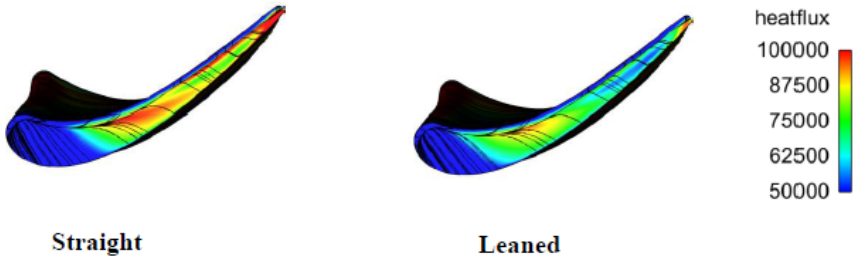


Fig. 5.29 Heat flux (W m^{-2}) on rotor tip (hot streak inlet)

To aid in the understanding of the rotor characteristics, it is useful to separate the contributions towards heat transfer into the surface HTC and those due to the local fluid driving temperature (which can be represented by T_{aw}). The time-averaged HTC and T_{aw} on the rotor pressure surface is shown in Figure 5.30. For the uniform inlet, the HTC is higher for the leaned case compared with the straight. Since the fluid driving temperature remains largely uniform at the rotor inlet (as seen by the T_{aw} images in Figure 5.30 and as a radial temperature plot in Figure 5.31), the result is a higher heat flux for the leaned case. Once the hot streak is introduced, the HTC is again higher for the leaned case than for the straight case; however, there is now a significant decrease in the fluid driving temperature at the rotor tip region (circled in Figure 5.30) due to the inlet profile (Figure 5.31). For the straight case there is a tendency for the hot fluid at the midspan to migrate towards the tip due to the diverging streamtraces on the pressure surface. Conversely, for the leaned case, this is prevented by the radial pressure gradient on the pressure surface (Figure 5.24), which blocks the hot gas movement towards the tip. This results in a cooler blade pressure surface near the casing for the leaned case over the straight case. Therefore, it is the ability of the leaned blade to control hot fluid migration (through a radial loading redistribution) that yields a beneficial outcome.

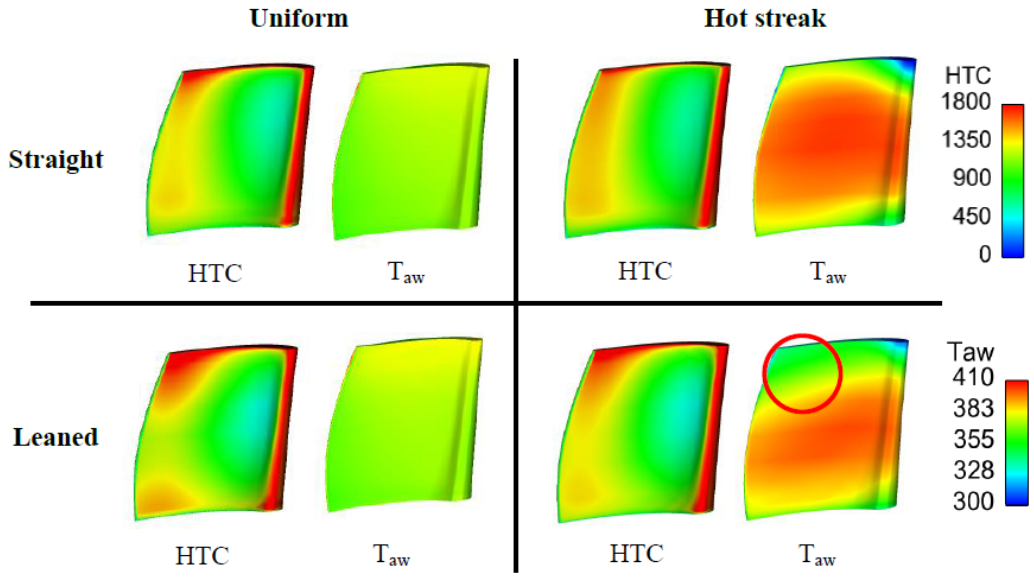


Fig. 5.30 HTC (W m^{-2} K^{-1}) and T_{aw} (K) (time-averaged) on rotor pressure surface

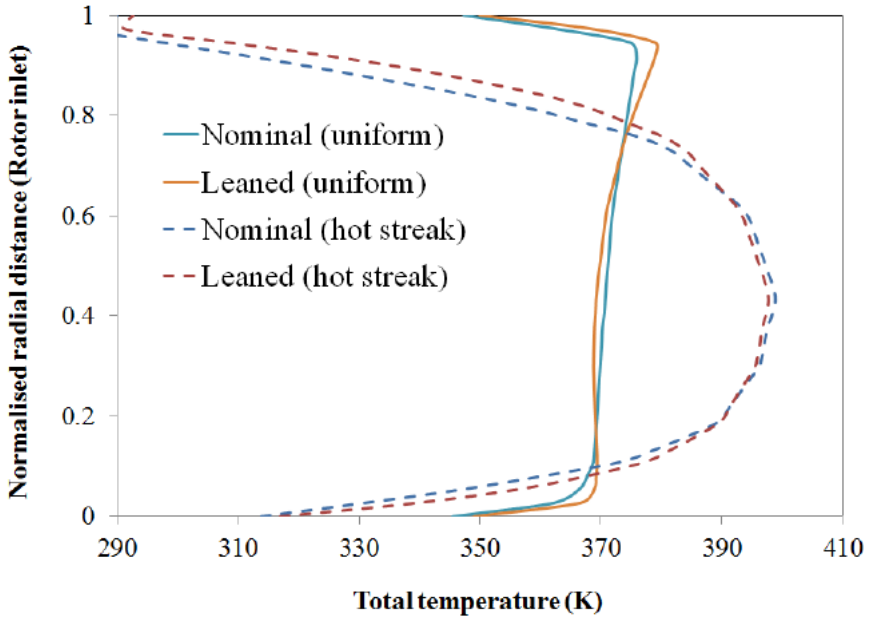


Fig. 5.31 Radial variations of pitch-averaged relative total temperature (K) at the rotor inlet

5.5 Overall Heat Transfer and Stage Performance

5.5.1 Stage Heat Transfer Results

Table 5.1 and Table 5.2 show the integrated heat flux component breakdown for the vane passage (hub, casing, and vanes) and the rotor passage (hub, casing, rotor blade) respectively. The area of the straight vanes is 120.4 cm^2, and for the leaned vanes is 126.6 cm^2. For the uniform inlet, the heat flux for both passages is consistently higher for the leaned case, resulting in an overall increase of 2.5% over the straight case. When the hot streak is present, an opposite trend is observed compared to the uniform inlet cases, with the leaned case showing lower integrated heat flux values in both rows and around 2% lower overall than the straight case. Once the hot streak is introduced, the values for both configurations are significantly lower by approximately 30% compared with the uniform inlet. This observation is similar to that made by Salvadori et al. (2012), and is primarily due to cooler regions on the hub and casing when the hot streak is introduced.

Table 5.1 Integrated Heat Flux (NGV)

Inlet temperature profile	**Case**	**NGV, W/(kg/s)**			**Total**
		Hub	Casing	Vanes	
Uniform inlet	Straight	874	1069	2232	4175
	Leaned	849	1082	2344	4275
Hot Streak	Straight	391	146	2345	2882
	Leaned	386	160	2316	2862

Table 5.2 Integrated Heat Flux (Rotor)

Inlet temperature profile	**Case**	**Rotor, W/(kg/s)**			**Total**
		Hub	Casing	Blade	
Uniform inlet	Straight	489	820	1123	2432
	Leaned	494	848	1157	2499
Hot Streak	Straight	452	192	1151	1795
	Leaned	414	201	1111	1726

5.5.2 Stage Efficacy Results

The non-adiabatic efficacy (defined earlier in the chapter) is shown in Table 5.3. For the uniform inlet, the straight case shows a slight increase over the leaned case (0.05%). The trend, however, is not maintained for the hot streak inlet, with the leaned case showing a 0.2% increase over the straight configuration. Further, it is noted that the ranking for the straight configuration under the two inlet conditions is reversed when compared with the adiabatic efficiency values.

Table 5.3 Non-adiabatic efficacy calculations

Inlet profile	**Case**	**Mass flow (kg s^{-1})**	$\frac{P_{03}}{P_{01}}$	$\frac{T_{03}}{T_{01}}$	$\eta(\%)$
Uniform inlet	Straight	17.42	0.353	0.752	90.41
	Leaned	17.50	0.353	0.752	90.36
Hot Streak	Straight	17.43	0.353	0.756	90.70
	Leaned	17.55	0.354	0.756	90.88

5.6 Summary of Chapter

An unsteady CFD study of the effect of NGV lean on stage aerothermal performance under two inlet conditions (uniform and hot streak) has been carried out. The mechanisms present in the NGV passage were investigated and discussed to understand its potential effect on the downstream rotor row. It is found that although the NGV compound lean offloads the endwalls and uploads the midspan as has been observed previously, another major effect on the rotor mechanisms is associated with the mass flow uploading to the casing/tip regions. The interplay between offloading in rotor inflow angle and uploading in rotor inflow head results in opposing trends for the vane lean with and without the hot streak.

The aerodynamics on the rotor blade pressure side is markedly altered by the compound lean. The streamlines are diverted away from the casing towards the midspan. The surface pressure variations, when normalised by the local dynamic head, show a clear trend of a local gradient from endwall to the midspan for the lean case, whilst there is a pressure gradient in the opposite direction for the straight case.

For the uniform inlet, the blade pressure surface experiences a lower heat flux towards the tip for the straight NGV. The leaned case gives a higher HTC, and given the largely uniform driving temperature, the high HTC results in the increase in rotor heat load, particularly in the tip region near the trailing edge, where the blade is more difficult to cool. Hence, the compound lean is shown to have a negative effect on rotor tip heat transfer.

However, when the hot streak is introduced, the trailing edge hot spot on the pressure surface for the compound lean configuration is markedly reduced. A favourable, cooler tip heat flux distribution is observed, compared with the straight configuration. Again, the leaned case had the higher HTC, but the roles of the HTC and fluid driving

temperature are completely changed. The change (reduction at endwalls) in driving temperature is seen to be the determining factor. The radial pressure gradient for the leaned case blocks the hot fluid at the midspan from reaching the tip.

A performance parameter (similar to that of the adiabatic efficiency) is used to evaluate the stage performance with heat transfer. It consistently shows that NGV lean has a beneficial impact when the stage is subject to a hot streak inlet, although the difference in the stage efficiency appears to be small when compared with the clearly contrasting rotor heat transfer characteristics.

Overall, the present results highlight the importance of inflow temperature profile when HP turbine blade shape design optimisation is considered. The findings also indicate the usefulness of including rotor heat transfer and coolability considerations during NGV aerodynamic shape design.

Having observed significant gains in performance through NGV lean under rich burn non-uniformities (hot streak inlet), Chapter 6 will seek to address the behaviour of compound lean under lean burn non-uniformities (combined hot streak and swirl). It is expected that further changes in heat transfer and flow physics will be observed in the rotor passage.

Chapter 6

Effect of NGV Shaping Under Combined Hot Streak and Swirling Flow

6.1 Introduction

The background and literature review (Chapters 1 and 2 respectively) have highlighted the need to understand the heat load characteristics for the rotor blade in general and in particular the tip region under lean burn combustor representative hot streak and swirl conditions. These components are a key consideration in HP turbine aerothermal design. An understanding of the complex environment would also allow better choice of objective functions and design parameters in order to assist with HP turbine optimisation.

In this chapter, a computational study is carried out on the aerothermal performance of a HP turbine stage under non-uniform temperature and velocity inlet profiles. The analyses are primarily conducted for two combined hot streak and swirl inlets,

with opposite swirl directions. The effects of three NGV shape configurations are investigated: straight, compound lean (CL) and reverse compound lean (RCL). In addition, comparisons are made against the results from Chapter 5, i.e. a hot-streak only case and a uniform inlet. It is of interest to compare and contrast the roles played by HTC and T_{aw} in a lean burn environment compared to the rich burn counterpart. A further question to be addressed is the extent, if any, to which the NGV shaping has in controlling these non-uniform inlet conditions (the positive impact of compound lean has already been identified for the hot streak only case). The chapter will commence with a mention of the computational setup and grid dependence study, before analysing the aerothermal characteristics through the NGV passage, and its effect on the rotor inlet and subsequent passage. Finally, heat transfer and stage performance calculations are presented in order to quantify the results.

6.2 Computational Setup

6.2.1 CFD Solver

The complex transport and interactions can only be expected to be captured through NGV-rotor coupled analysis; an unsteady method is thus required. The Rolls-Royce CFD suite HYDRA together with the pre-processing software PADRAM has been implemented on the unshrouded MT1 HP turbine geometry; full details of the solver and unsteady setup can be found in the CFD validation section in Chapter 3. For this work, one modification has been made; the $k-\omega$ SST turbulence model has been used in order to provide higher fidelity that may be required due to swirling flow effects.

6.2.2 Geometry and mesh

The baseline MT1 geometry as well as the surface mesh distribution is shown in Figure 6.1 for the NGV hub and blades. For the leaned configurations, the displacement of the NGV midspan section is approximately 17% of the radial height, in order to remain consistent with the results from Chapter 5. The Rolls-Royce CFD pre-processor PADRAM was used for the geometry and mesh creation and to generate the lean configuration. For the NGV, 70 radial grid points were used to ensure reliable aerodynamic and heat transfer results (see Section 6.2.3). The mesh density of the NGV passage was 1.44 x 10^6 nodes with 70 nodes radially and the rotor passage had a total of 1.60 x 10^6 with 80 nodes radially. To achieve a valid comparison, the total mass flow capacity for all configurations was matched to within 0.5% of the baseline straight NGV case. This was accomplished by applying a bulk skew to the leaned vanes during the mixing plane simulation (initialisation for unsteady method).

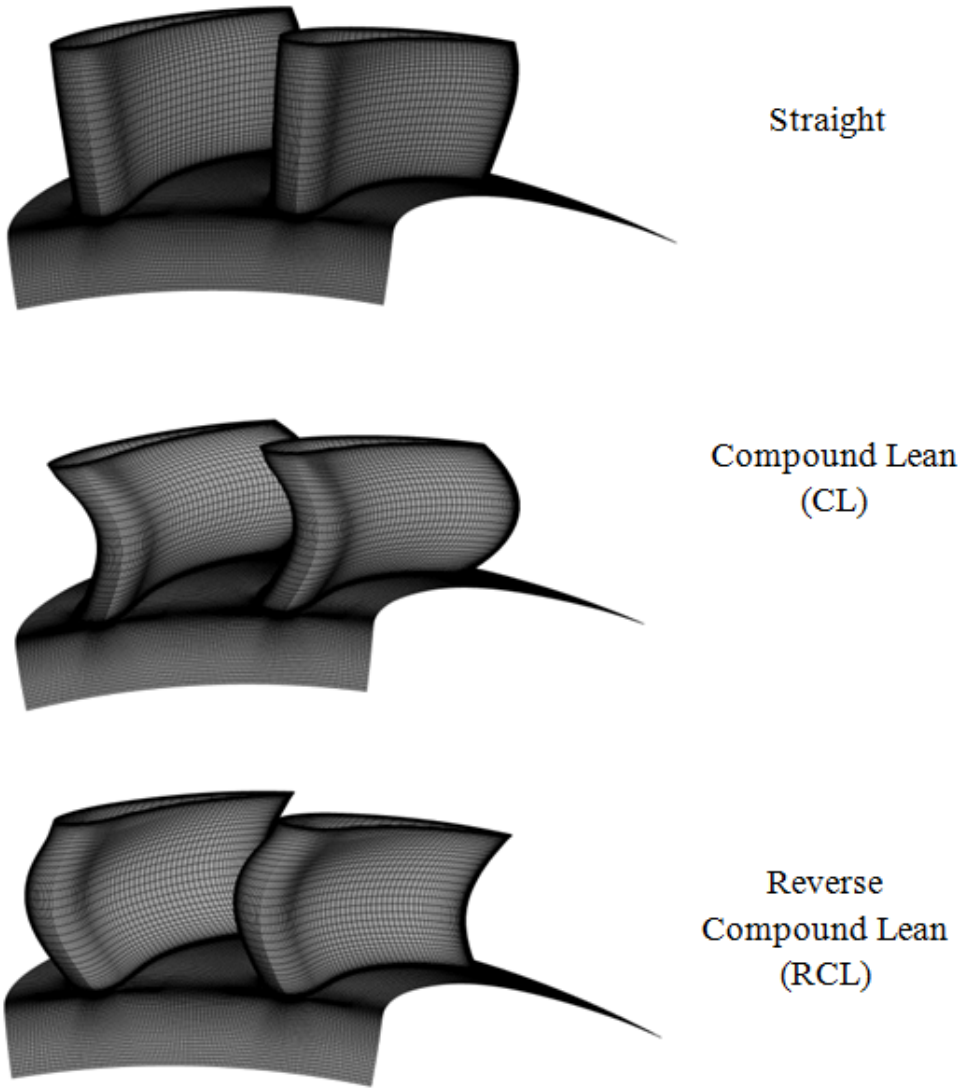


Fig. 6.1 Computational mesh for different vane arrangements

6.2.3 Mesh sensitivity analysis

Two grid dependency studies, similar to those performed in Chapter 3 and Chapter 5, were performed for the combined hot streak and swirl inlet. First, the number of radial grid points on a leaned NGV was varied with 30, 50, 70 and 100 radial points. The corresponding sectional plots at 10%, 50% and 90% span for isentropic Mach number and Nusselt number and shown in Figure 6.2 and Figure 6.3 respectively. With

respect to Mach number, good agreement is seen for 50% and 90% span but there are discrepancies at the suction side trailing edge for 10% span, with 70 and 100 radial points yielding almost the same solution. For Nusselt number, 30 and 50 radial points do not produce a reliable distribution (low Nu on suction side for 10% and 50% span), with 70 and 100 radial points again giving a similar solution. Therefore, in line with previous inlet cases, 70 radial points are selected.

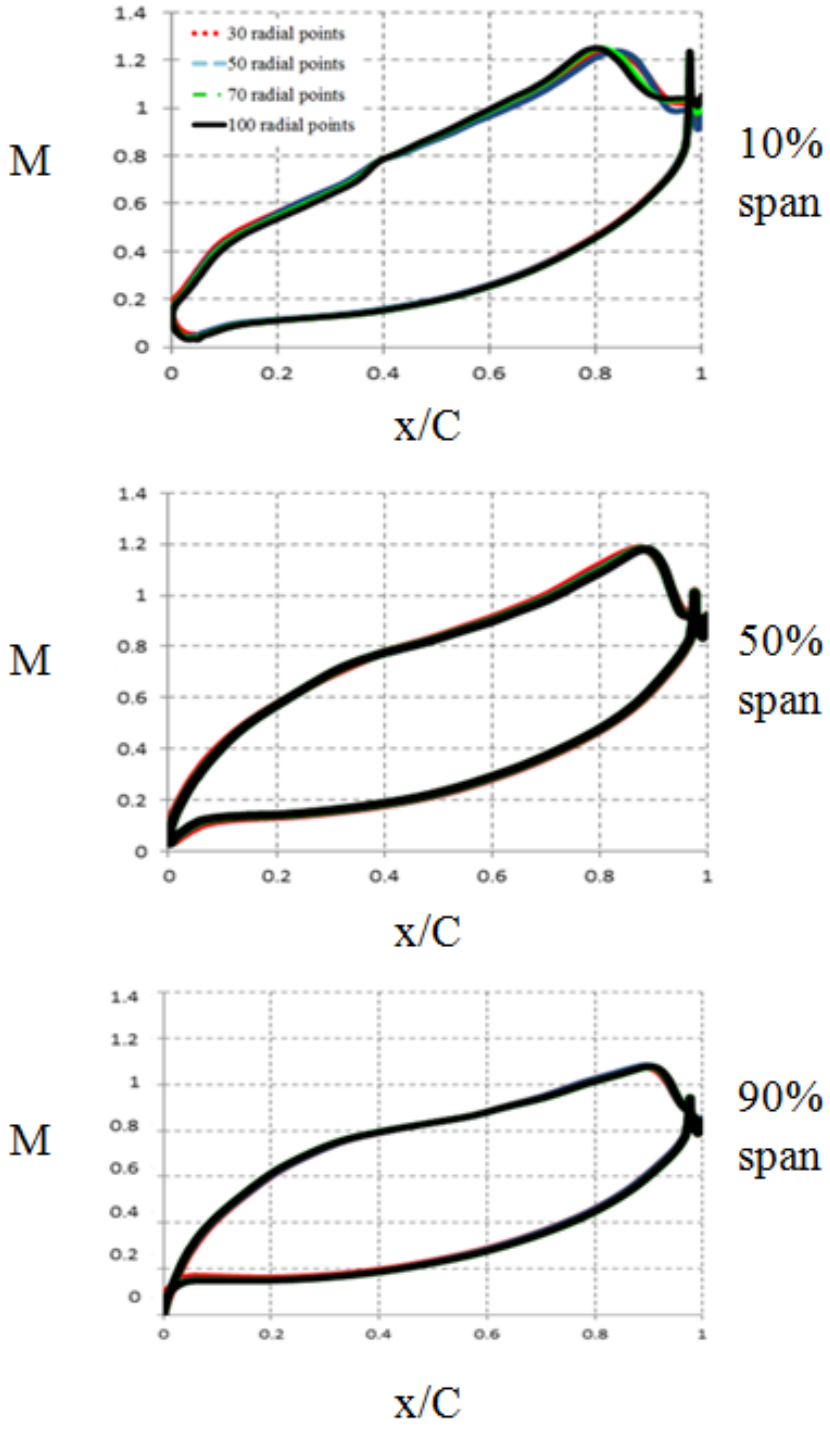


Fig. 6.2 Mesh dependency check for different NGV radial mesh points for isentropic Mach number at 10%, 50%, and 90% span

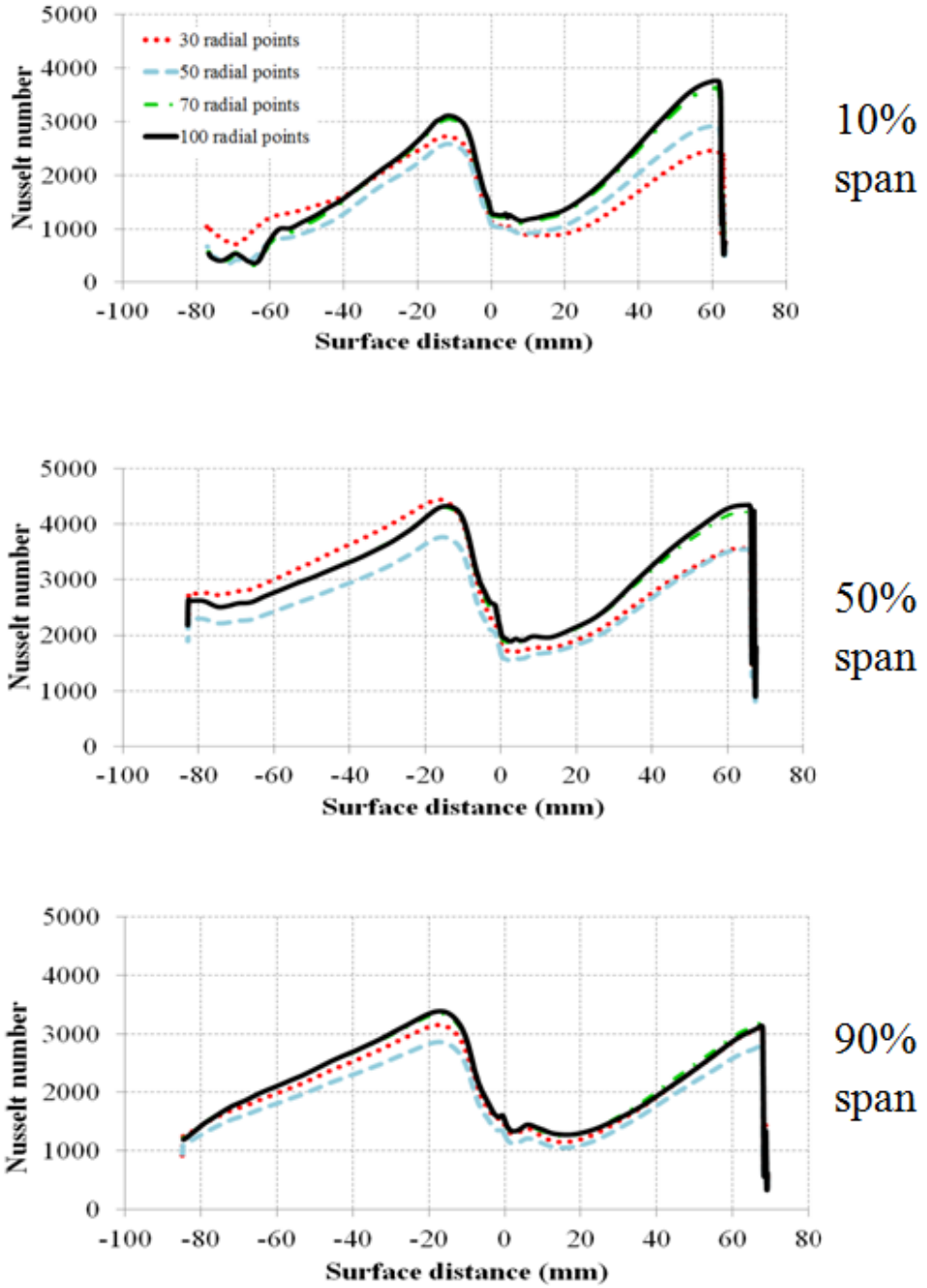


Fig. 6.3 Mesh dependency check for different NGV radial mesh points for Nusselt number at 10%, 50%, and 90% span

The second sensitivity analysis was carried out to ensure there were sufficient grid points in the rotor tip gap mesh. This is particularly important for the present study, in which the rotor tip surface will be analysed extensively in terms of heat transfer. The

rotor tip is tested for 10, 20 and 50 points, and the corresponding sectional data (10%, 50% and 90%) and circumferentially averaged data for Mach number and Nusselt number can be found in Figure 6.4 to Figure 6.7. From the graphs, it can clearly be seen that 10 points are insufficient in order to model the tip mesh to a good degree of accuracy, particularly for heat transfer, which is greatly underpredicted. The acceptable compromise is seen to be 20 points, which provides very good results over the front half of the tip, and reasonable accuracy over the rear of the chord (less than approximately 5% difference compared with 50 points).

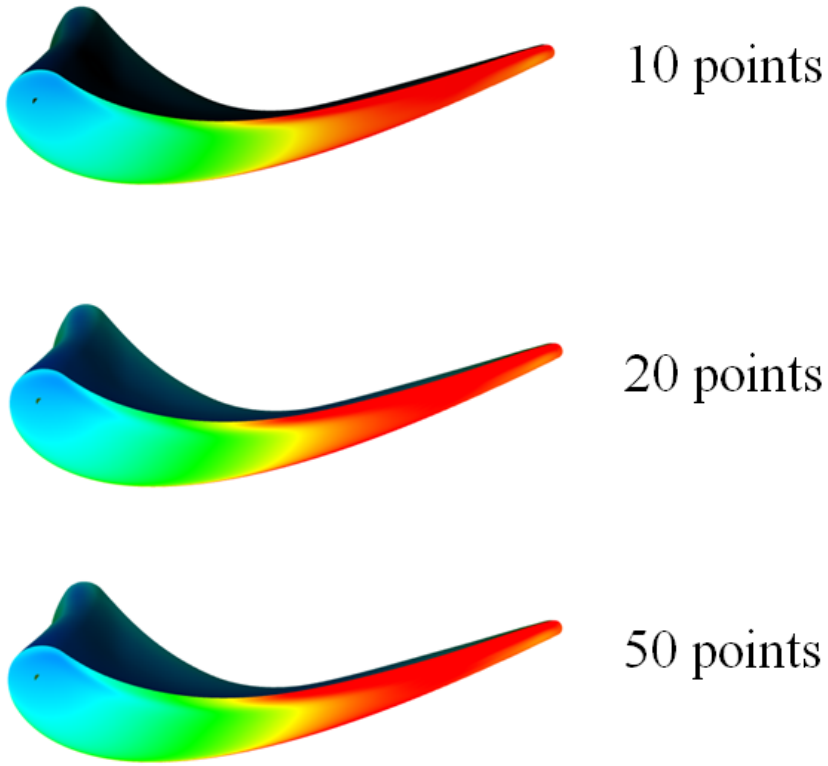


Fig. 6.4 Isentropic Mach number on rotor tip surface for varying number of grid points in the tip gap

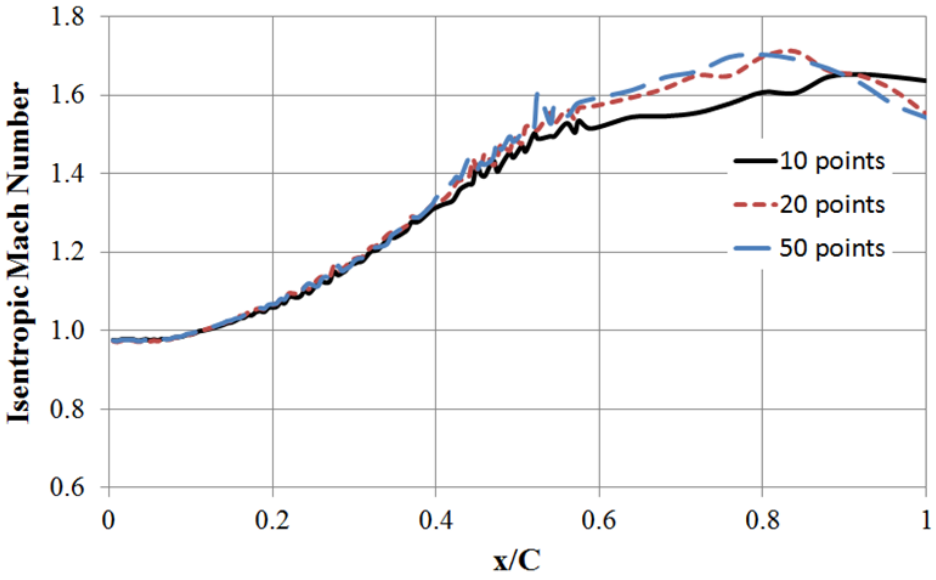


Fig. 6.5 Isentropic Mach number (pitch-averaged across tip surface) versus axial position on rotor tip surface for varying number of grid points in the tip gap

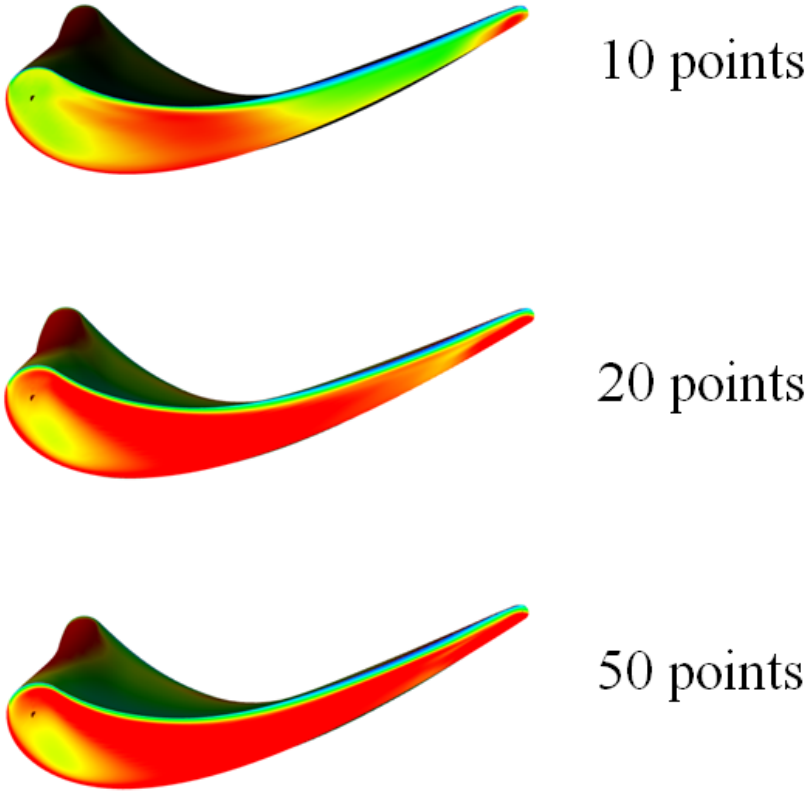


Fig. 6.6 Heat flux on rotor tip surface for varying number of grid points in the tip gap

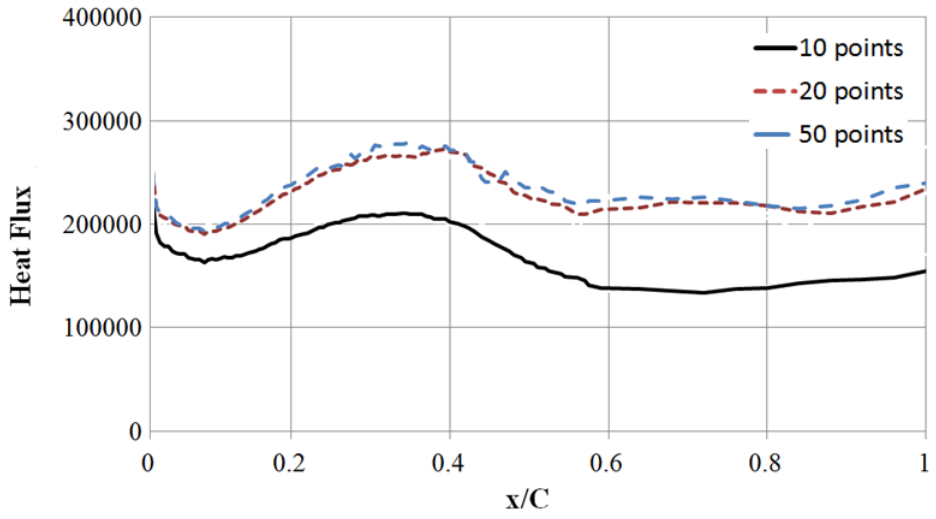
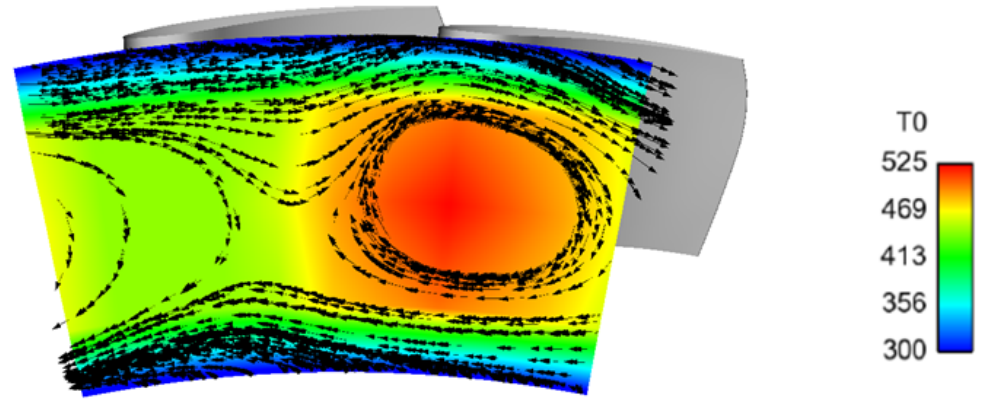


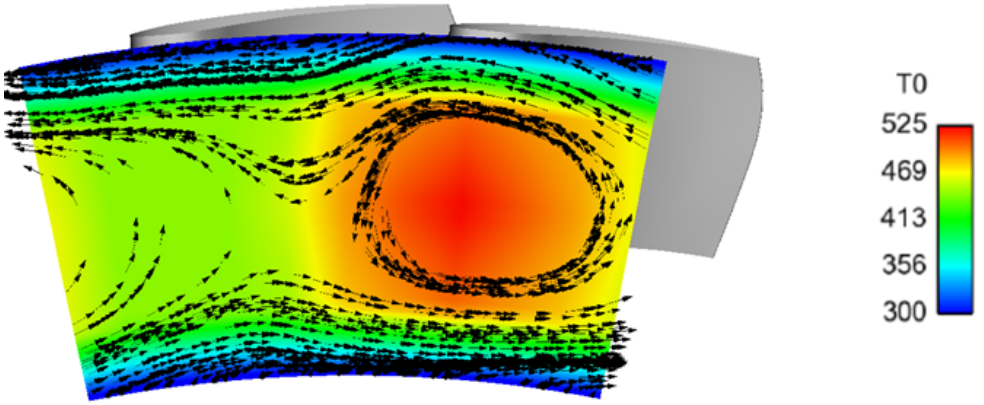
Fig. 6.7 Heat flux (W m^{-2}) (pitch-averaged across tip surface) versus axial position on rotor tip surface for varying number of grid points in the tip gap

6.2.4 Inflow temperature and velocity profile

The hot streak arrangement is the same as that used in the previous chapter; it is based on a practical combustor-NGV count ratio of 16:32 with a mass averaged temperature of 432 K. The hot-streak profile has a peak of 525 K, which is located at the blade mid-height, with the minimum of 290 K near the endwalls and the max-to-min temperature ratio is approximately 1.81. The combined hot streak and swirl profile for both swirl directions is shown graphically in Figure 6.8. The ratio of the inlet mass averaged temperature to the isothermal solid wall surfaces is 1.5. The swirling profile is based on the experimental study carried out by Qureshi et al. (2011). The pitch averaged T_0 profile at the NGV inlet is given in Figure 6.10. This chapter also includes comparisons of the combined hot streak and swirl inlet to the hot streak only case, which was reported on in Chapter 5. The hot streak profile used in this study differs marginally from the previous study, with a more realistic (hotter) profile being implemented. However, it is expected that all qualitative comparisons will still be valid.



(a) Hot streak and positive swirl

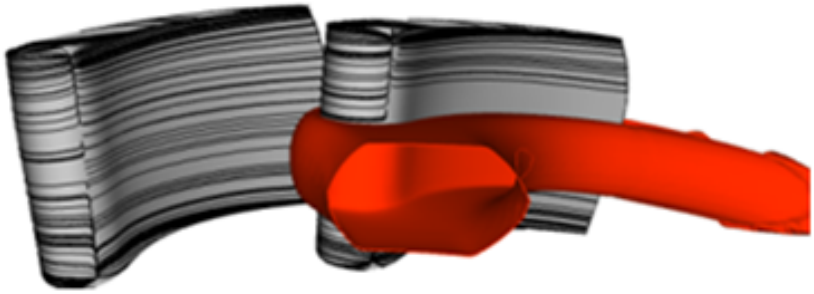


(b) Hot streak and negative swirl

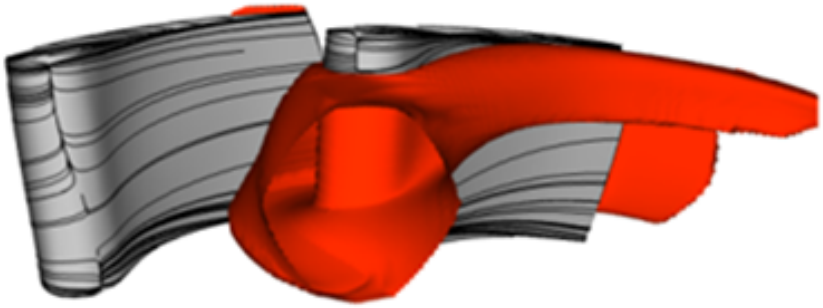
Fig. 6.8 Combined hot streak and swirl profiles at turbine inlet (T_0 units: K)

6.3 NGV Passage Analysis

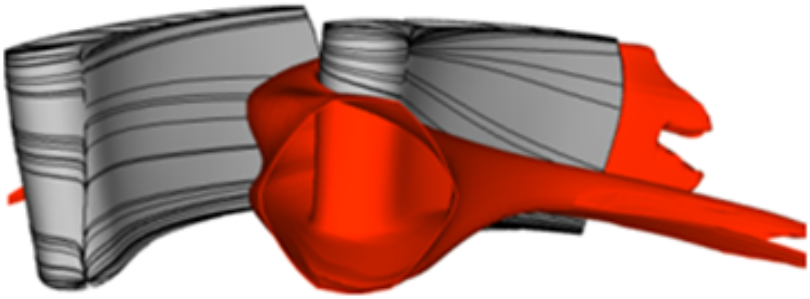
The migration of the hot streak through the NGV passage is illustrated in Figure 6.9 from an upstream view for three cases: the hot streak combined with positive swirl, negative swirl and a case without swirl is plotted for reference. The hot streak core is visualised through an iso-surface of the total temperature at 495 K, which is plotted from the NGV inlet to the NGV exit. It can be seen that for the hot-streak only case the hot core passes undisturbed through the vane passage, confirmed by the streamline pattern on the vanes (Figure 6.9).



(a) Hot streak only (rich burn)
(passively convective in NGV)



(b) Positive Swirl and Hot streak
(aerodynamically offload tip; thermally upload tip)



(c) Negative Swirl and Hot streak
(aerodynamically upload tip; thermally offload tip)

Fig. 6.9 Hot streak iso-surface visualisation (T_0 = 495 K) with and without swirl through NGV passage as viewed from upstream

In comparison, once the swirl is introduced, the hot core is redistributed significantly; for a positive swirling direction, hot fluid is pushed to the casing on the pressure

side and to the hub on the suction side. For a negative swirl, the opposite is observed. This was caused by a splitting of the swirling inlet vortex as it impinges the vane leading edge, causing a pair of counter rotating vortices to be formed, as explained by Khanal et al. (2013).

A simple but important marker of the aerothermal impact of the combined hot streak and swirl on the NGV passage and HP turbine stage as a whole is the NGV exit temperature profile. A reference point is taken using the hot streak only case, as presented in Chapter 5. It was shown that for a hot streak only at the inlet, the total temperature profile is almost fully preserved through the NGV passage (see Figure 5.31). As such there is no noticeable difference in the spanwise temperature profiles between NGV inlet and exit, another manifestation of the Munk and Prim principle (Munk and Prim (1947)). However, once the combined hot streak and swirl case is considered, this is no longer the case. Figure 6.10 shows the absolute total temperature radial profile at the NGV exit (circumferentially averaged) for the baseline straight NGVs. It can be seen that the combined effect of the hot streak and swirl results in a much flatter temperature profile at the NGV exit. This is perhaps to be expected given the strong radial migration as indicated in Figure 6.9. The flatter temperature profiles would generally be expected to lead to higher tip and hub heating.

A further comparison of the NGV exit temperature profiles suggests a trend that a positive swirl gives a hotter tip region (15% higher T_0 at the casing) than a negative swirl. This may be caused by the different fluid velocities which the split vortical fluid migrations are subjected to. A positive swirl splits around the NGV leading edge so that the pressure surface leg is radially migrated towards the casing, whilst the suction side leg is migrated towards the hub (Figure 6.9). A negative swirl does the opposite to migrate radially downwards on the pressure surface side, and upwards on the suction side. The radial migration can be viewed as a secondary flow, and its ability

to influence the overall flow pattern is related to its strength relative to that of the primary flow. It is thus clear that radial migration on the suction side is more difficult than on the pressure side, given the difference in inertia between the two primary flows. Hence a thermally uploaded rotor tip would be expected for a positive swirling flow. Interestingly, this should also be compared to the basic aerodynamic intent of adopting a positive swirl; to off-load the tip region as it gives a negative incidence on the NGV near the casing. Near the hub region, the profiles of the two swirl directions do not give a very clear contrast, however, a relatively higher temperature for negative swirl at around 10%-30% span seems to be in line with the present reasoning.

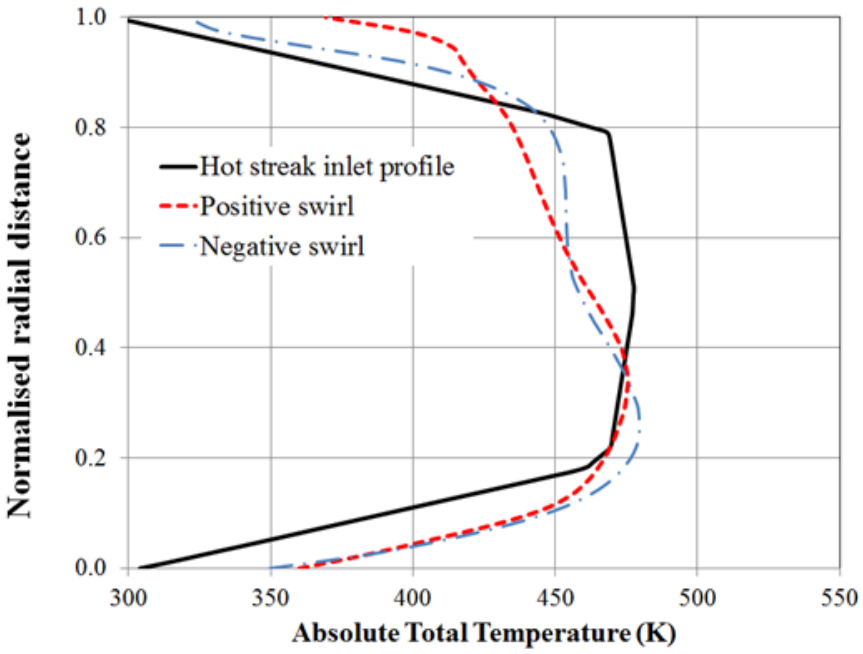


Fig. 6.10 Absolute total temperature (K) at vane exit for straight vane arrangement for positive and negative swirl directions, as well as a reference inlet hot streak case

The effect of NGV shaping is now examined. The NGV exit total temperature profiles are plotted for the combined hot streak and swirl cases (Figure 6.11 for the positive swirl and Figure 6.12 for the negative swirl). The hot streak inlet profile is also plotted for reference to observe any effects caused in the NGV passage. For the

negative swirl cases (Figure 6.12), the vane shaping seems to have a relatively small effect on the temperature profiles. More pronounced changes are observed for the positive swirl cases (Figure 6.11). There is a clear temperature reduction of 5% at 90% span for the reverse compound lean (RCL) compared with the straight vanes. The compound lean seems to be doing the opposite locally, causing an increase of 5% in temperature. The higher sensitivity of the temperature distribution for the NGV outer region is consistent with the higher primary flow velocity on the suction surface side, thus more amenable to local blade shape changes.

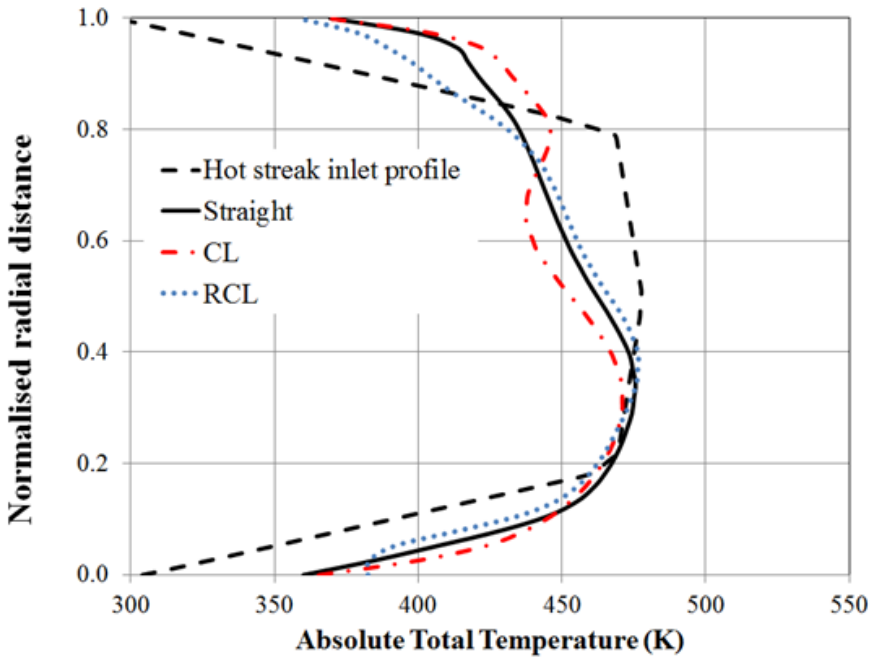


Fig. 6.11 Absolute total temperature (K) at vane exit (hot streak and positive swirl)

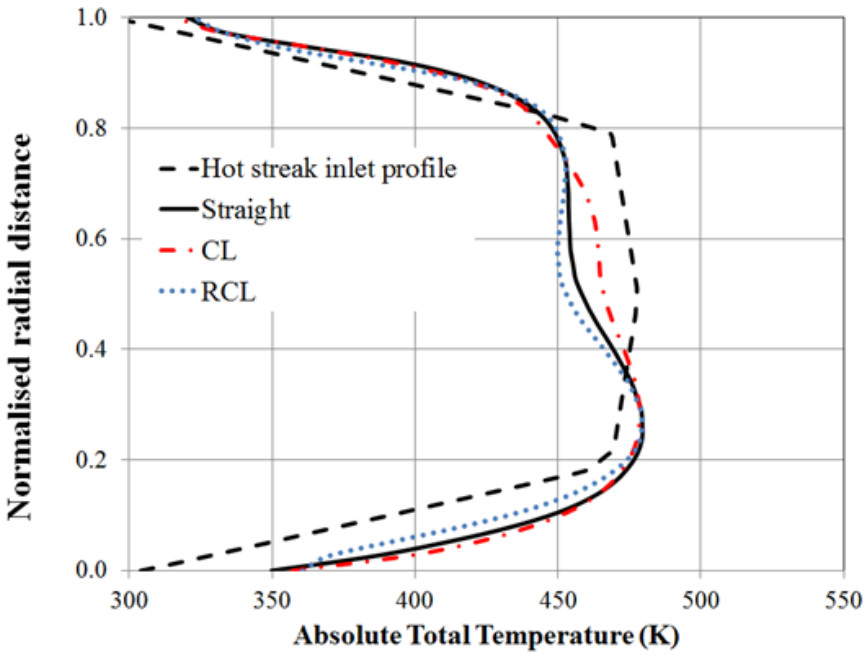


Fig. 6.12 Absolute total temperature (K) at vane exit (hot streak and negative swirl)

6.4 Rotor Blade and Tip Analysis

As introduced earlier, the effect of the combustor exit non-uniformities may be better understood and more useful for turbine design if blade aerothermal characteristics under different inlet conditions are directly compared. For this reason, the hot streak only (rich burn representative) case is first compared to a uniform inlet case as a brief recap, as this has already been discussed in Chapter 5 in detail. This baseline comparison should provide a useful reference point for when the combined hot streak and swirl (lean burn) cases are presented and discussed.

6.4.1 Uniform inlet versus hot-streak only inlet

For a uniform inflow it was seen that the HTC is dominant over the driver temperature for the heat flux distribution on the rotor pressure surface (see Chapter 5). As shown in

Figure 6.13, this trend is also observed over the rotor tip for both NGV designs (T_{aw} distributions are essentially the same due to uniform nature of the inlet).

Once the hot streak is introduced, the roles played by HTC and T_{aw} are reversed; the driver temperature is now the dominant parameter. This is due to the change in driver temperature (i.e. hot streak profile) which now determines the heat flux on the rotor pressure surface and over the rotor tip, as shown in Figure 6.14. Despite having a higher HTC over the tip, the compound lean NGV leads to a cooler heat flux distribution on the rotor tip caused by the lower T_{aw}, compared with the straight vane case. This reduction in T_{aw} is due to the local pressure gradient formed on the rotor pressure surface (which is a downstream effect of the NGV lean), which blocks the hot gas from reaching the rotor tip. This is the opposite result to that for the uniform inlet.

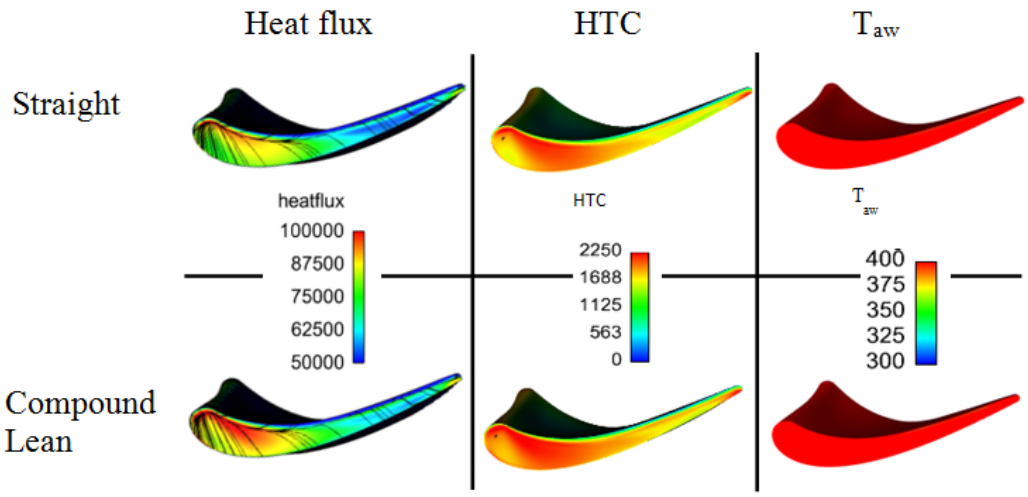


Fig. 6.13 Tip heat flux (W m^{-2}), HTC (W m^{-2} K^{-1}) and T_{aw} (K) for straight and compound lean vanes *(uniform inflow)*

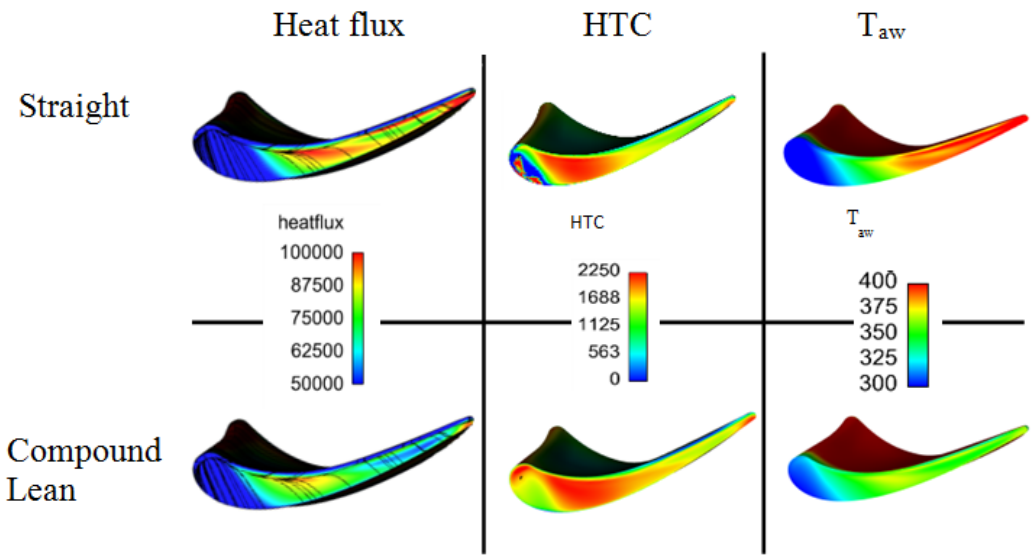


Fig. 6.14 Tip heat flux (W m^{-2}), HTC (W m^{-2} K^{-1}) and T_{aw} (K) for straight and compound lean vanes *(hot streak only)*

The aerothermal behaviour of the rotor blade with the combined hot streak and swirl is now considered, and specifically to address the following question: can the hot streak only results seen in the previous section be applied to the present case i.e. whether the HTC or T_{aw} the dominant factor in determining heat transfer when swirling flow is present. Figure 6.15 presents the heat flux with the HTC and T_{aw} (driver temperature) breakdown for the three vane configurations on the rotor pressure surface, for a hot streak and positive swirl inlet. The streamtraces on the surface are also plotted and superimposed on the heat flux images.

A closer look at the streamtraces shows the compound lean (CL) case diverts flow away from the tip, which has previously been seen in (Chapter 5) as a beneficial flow pattern attributable to a local pressure gradient caused by the NGV blade lean. In contrast, the reverse compound lean shows strong divergence from the midspan towards the tip, caused by the nature of the lean combining with the positive outward swirl pressure gradient; this would represent a detrimental flow pattern based on the

reasoning for the rich burn case, as it would promote the migration of mid-span hot fluid to the tip region.

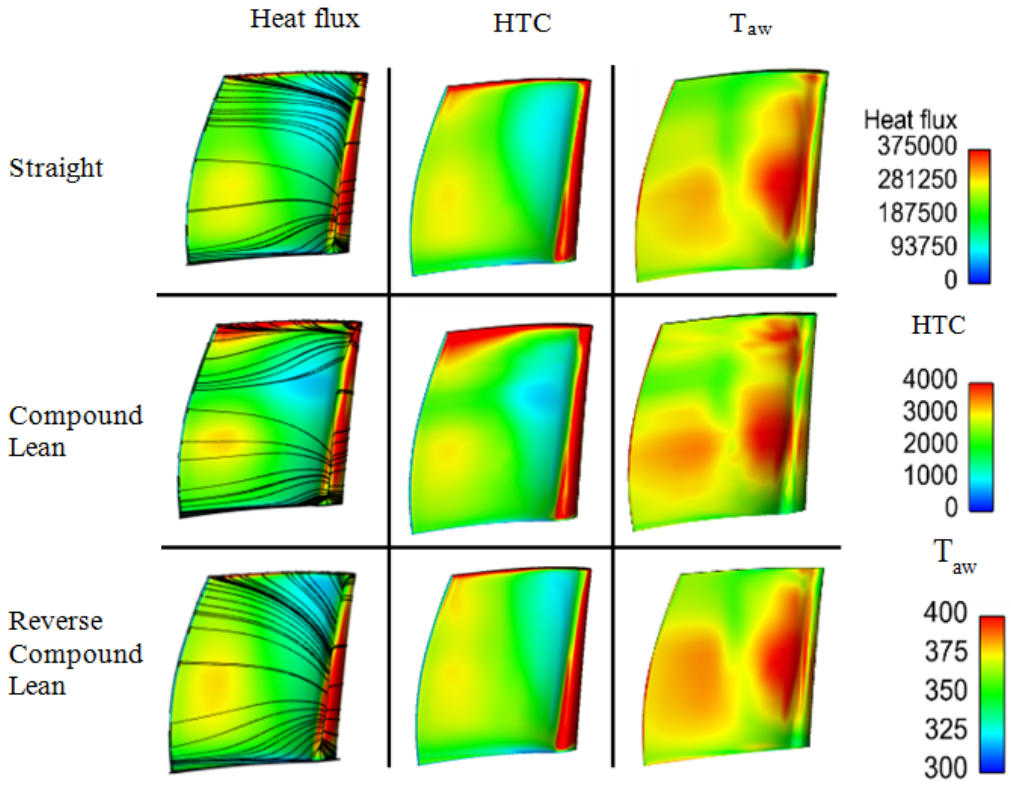


Fig. 6.15 Heat flux (W m^{-2}), HTC (W m^{-2} K^{-1}) and T_{aw} (K) on rotor pressure surface for different vane shapes *(hot streak and positive swirl)*

However, in terms of heat flux, it can be seen that the reverse compound lean and straight vane cases give favourable distributions with low heating close to the tip compared with the compound lean case. Further, by examining the HTC and T_{aw} plots it is observed that the driver temperature plots are largely the same for all vane cases, but the HTC ones differ in accordance to the heat flux plots. Therefore, in contrast to the hot streak only inlet, the HTC now appears to be dominant in determining the heat flux for the combined hot streak and swirl inlet. For the hot streak only cases, the compound lean had been shown to be effective as it could block the hot gas at midspan

from reaching close to the casing. However, once the swirl is introduced, the process governing the heat flux movement is no longer convective, and is now determined by the HTC subject to more complex aerodynamic interactions.

In order to quantify and confirm these observations, the HTC and T_{aw} surfaces are now processed as differences relative to a baseline case. The baseline in this instance is taken to be an average of the three configurations. The greater the deviations from the baseline case (higher or lower), the more it can be seen to contribute to the given parameter. The two 'differential' parameters are computed as:

$$\frac{\delta HTC}{HTC_{\text{baseline}}} = \frac{[HTC - HTC_{\text{baseline}}]}{HTC_{\text{baseline}}} \tag{6.1}$$

and:

$$\frac{\delta T_{aw}}{T_{\text{aw, baseline}}} = \frac{[T_{aw} - T_{\text{aw, baseline}}]}{T_{\text{aw, baseline}}} \tag{6.2}$$

Where $\text{HTC}_{\text{baseline}}$ and $T_{aw,baseline}$ indicate the baseline cases. The plots of these parameters are shown in Figure 6.16. It can be seen that in the region close to the tip, the percentage changes for HTC are noticeably higher than that of the T_{aw} equivalents. For example, for the compound lean case, the HTC close to the tip is approximately 40% higher than the average, whereas for the T_{aw} in the same region is only 3% of the average. This confirms that the HTC is more influential in yielding the heat flux patterns observed in Figure 6.15.

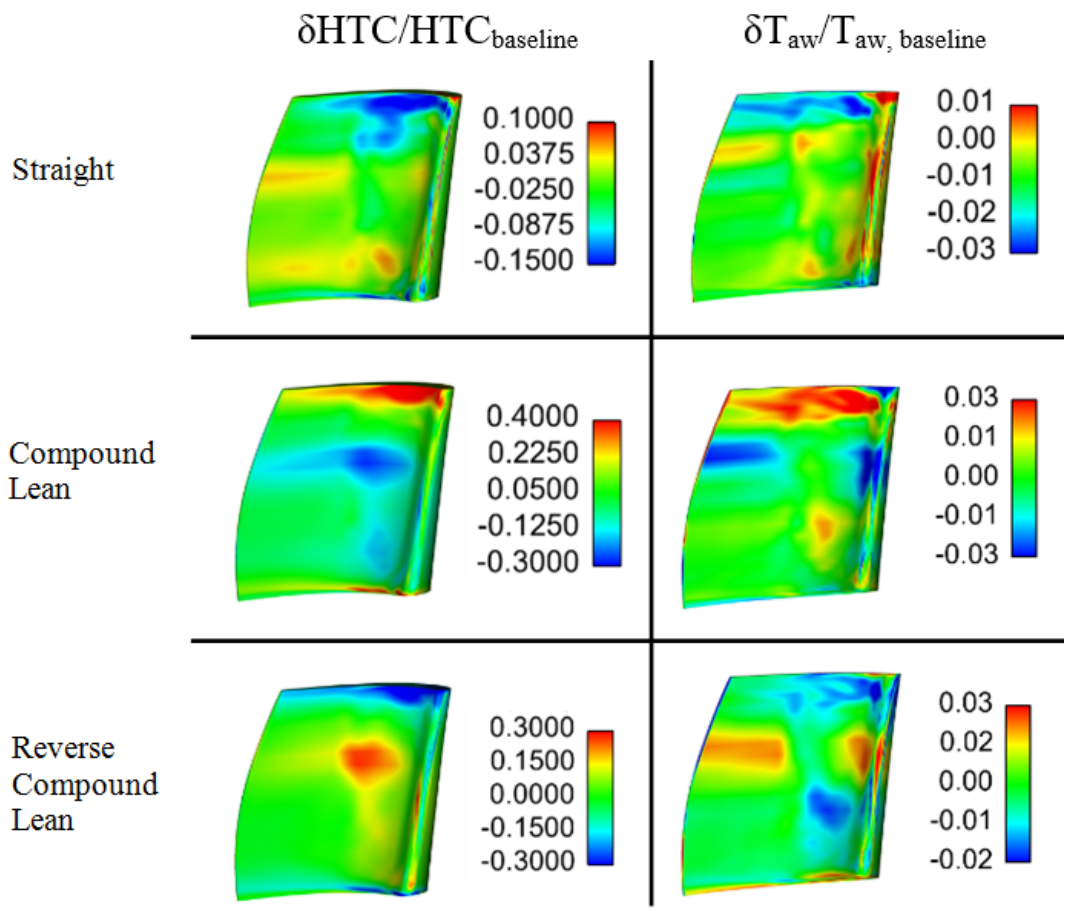


Fig. 6.16 δHTC and δT_{aw} plots on rotor pressure surface *(hot streak and positive swirl)*

The combined hot streak and negative swirl heat flux distributions on the rotor pressure surface are plotted in Figure 6.17 for the three vane cases, along with the HTC and T_{aw}. The streamtraces differ from those seen for the positive swirl, as the negative swirl creates a local pressure gradient from the tip to the hub; this is similar to the hot streak only case (Chapter 5). This effect causes a downward streamline pattern that strengthens the compound lean movement away from the tip, and weakens the sharp divergence of streamlines as seen for the reverse compound lean with the positive swirl (Figure 6.15).

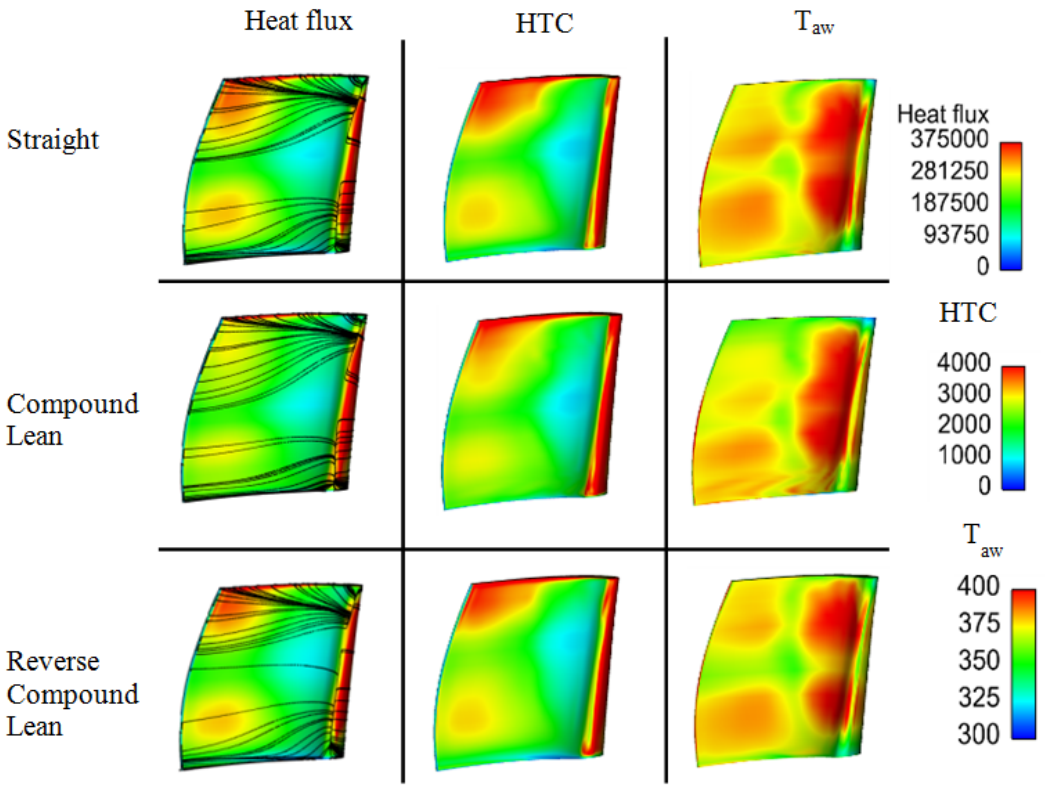


Fig. 6.17 Heat flux (W m^{-2}), HTC (W m^{-2} K^{-1}) and T_{aw} (K) on rotor pressure surface for different vane shapes *(hot streak and negative swirl)*

For the negative swirl cases, the heat flux is lowest for the compound lean case; this is in contrast to positive swirl, in which it displays the least favourable heat transfer characteristics. A further analysis of HTC and T_{aw} breakdowns (Figure 6.18) confirms again that the HTC is more dominant over the driver temperature in determining the heat flux. This illustrates that the significant rise of the role played by HTC is qualitatively independent of the swirling flow direction, and is more generally caused by an aerodynamic change due to the strong aerodynamic interactions in a swirl flow.

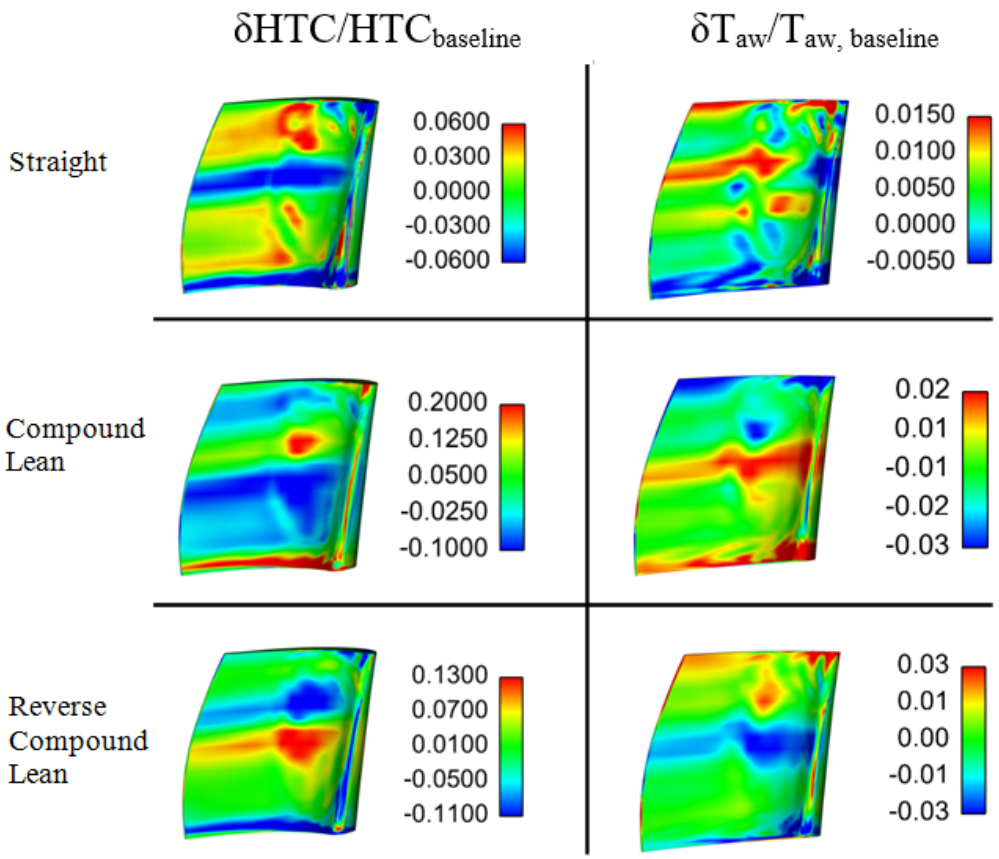


Fig. 6.18 δHTC and δT_{aw} plots on rotor pressure surface *(hot streak and negative swirl)*

6.4.2 Rotor tip heat transfer for combined hot streak and swirl

It is reminded that for a hot streak only case as discussed in Section 6.4.1, the fluid driving temperature is the dominant factor (over the HTC) in finding the heat flux distribution. The rotor tip will now be analysed for the different vane shapes to assess whether this is true for the combined hot streak and swirl, or whether the tip follows the same behaviour as the rotor pressure surface (i.e. HTC dominating for swirl) as discussed in 6.4.2. Figure 6.19 illustrates the tip heat flux with their respective HTC and T_{aw} plots. The compound lean exhibits high heating across most of the tip, whereas the reverse compound lean case shows the coolest tip.

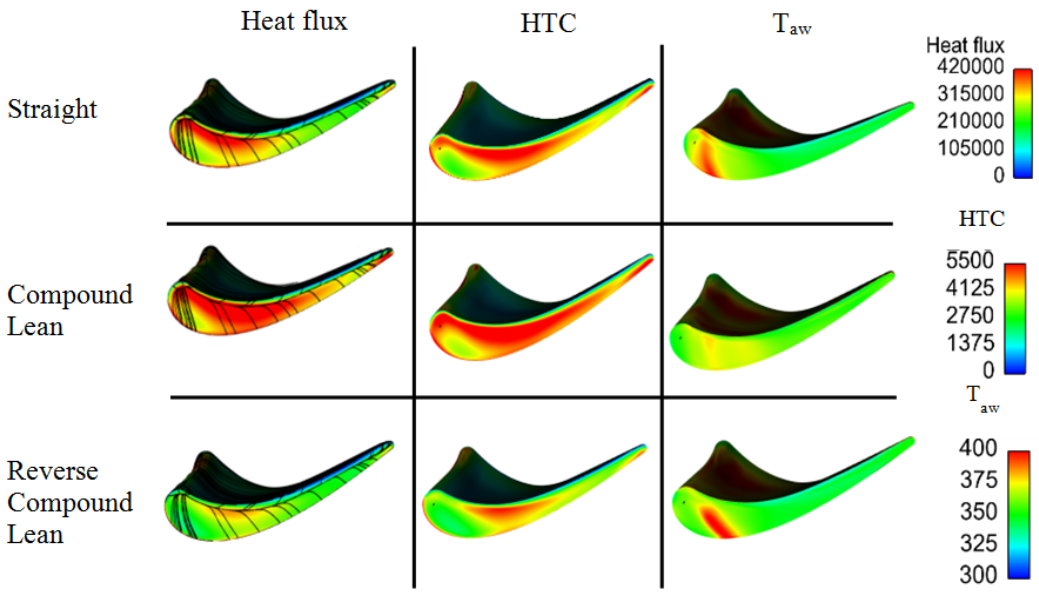


Fig. 6.19 Tip heat flux (W m^{-2}), HTC (W m^{-2} K^{-1}) and T_{aw} (K) for straight, CL and RCL shapes *(hot streak and positive swirl)*

To quantify the tip distributions, the heat flux is circumferentially area-averaged and plotted along the axial direction. The circumferentially averaged heat flux plot for the positive swirl case is shown in Figure 6.20. The cool rotor tip observed for the reverse compound lean (RCL) case in Figure 6.19 is confirmed by the plot, which shows the lowest heat flux along the entire axial chord. Towards the leading edge, the greatest difference can be seen, with an approximate 30% cooler region. The HTC and T_{aw} plots in Figure 6.19 again suggest that the HTC is more influential in determining heat flux, and this is confirmed by their equivalent contributions terms, with higher ranges being observed for HTC in all cases (Figure 6.21).

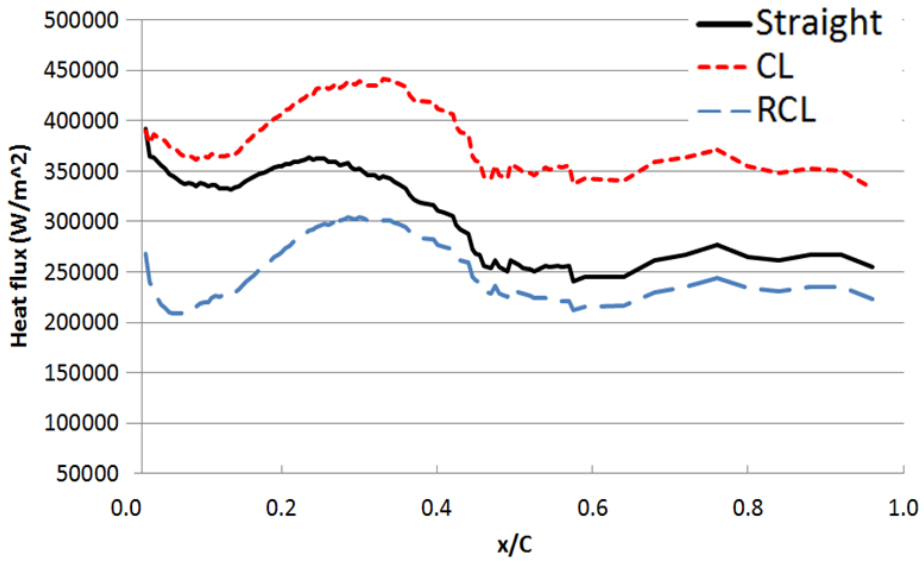


Fig. 6.20 Tip pitch-averaged heat flux (W m^{-2}) for the three NGV shapes *(hot streak and positive swirl)*

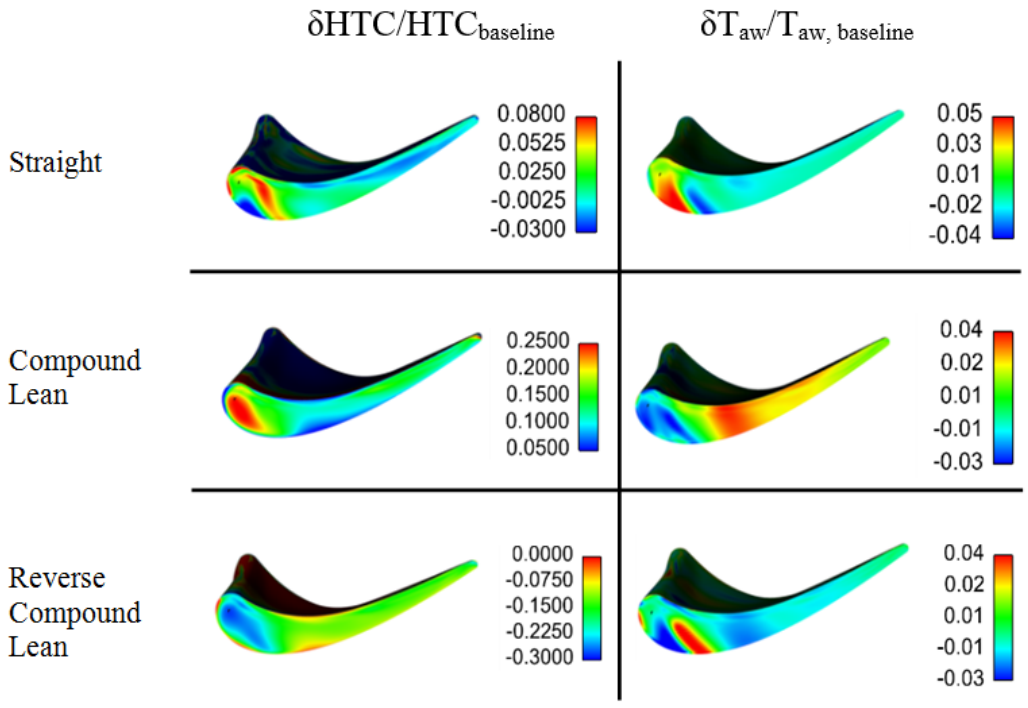


Fig. 6.21 δHTC and δT_{aw} plots on rotor tip surface for the three NGV shapes *(hot streak and positive swirl)*

The tip heat flux with HTC and T_{aw} breakdown for the combined hot streak and negative swirl is shown in Figure 6.22. It can now be seen that the compound lean case gives the coolest distribution, which is supported by the circumferentially averaged plot in Figure 6.23. It can also be seen that the heat flux values are approximately 25% lower than the positive swirl equivalents, which can be explained through the lower total temperature observed close to the casing for the negative swirl (Figure 6.12); this is mainly as a consequence of the differential inertia of the primary flow between the suction and pressure surfaces as discussed in Section 6.3. Further, Figure 6.22 suggests that the HTC is dominant for determining the heat flux distributions, and this is confirmed by the breakdown of HTC and T_{aw} changes (Figure 6.24).

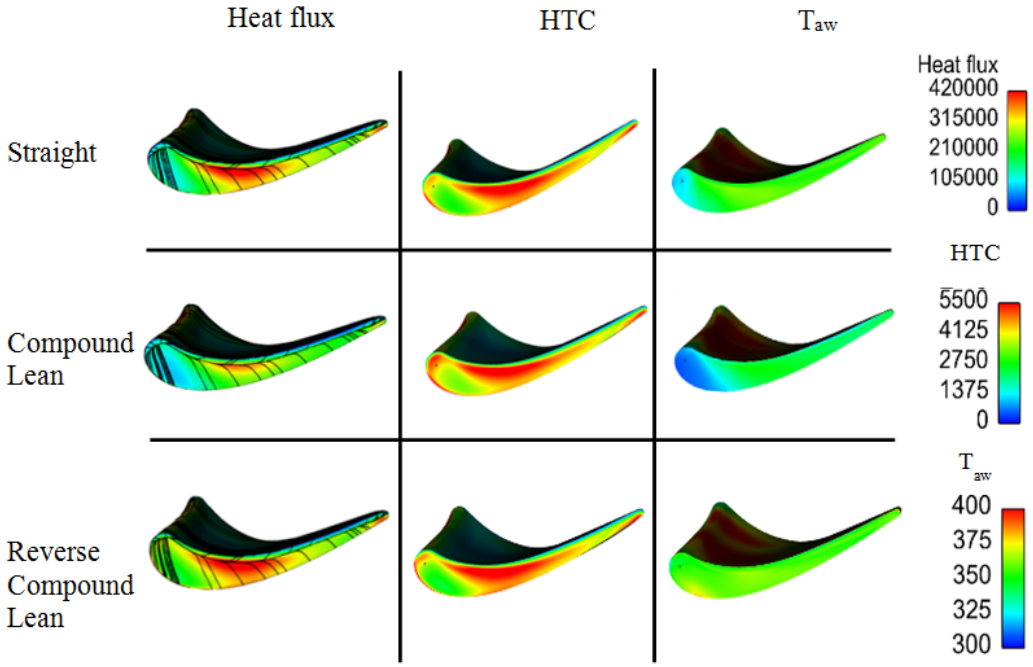


Fig. 6.22 Tip heat flux (W m^{-2}), HTC (W m^{-2} K^{-1}) and T_{aw} (K) for straight, CL and RCL shapes *(hot streak and negative swirl)*

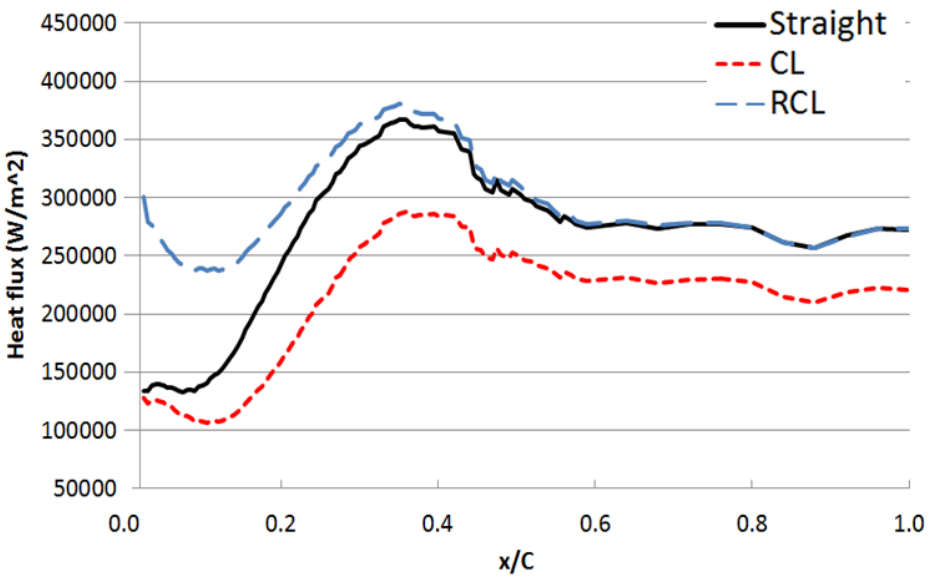


Fig. 6.23 Tip pitch-averaged heat flux (W m^{-2}) for the three NGV shapes *(hot streak and negative swirl)*

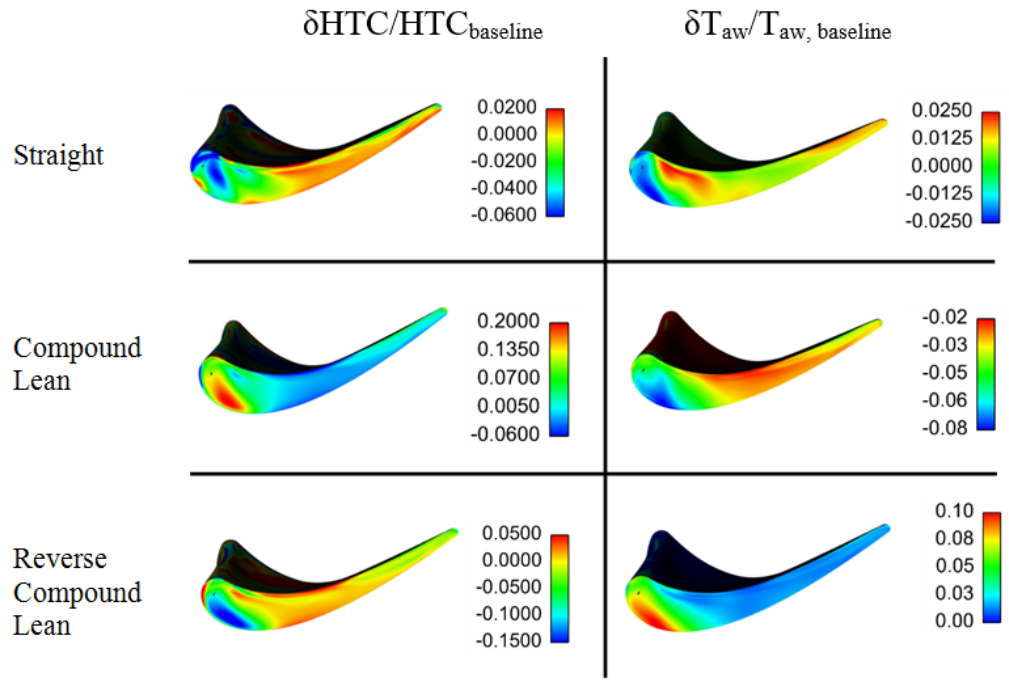


Fig. 6.24 δHTC and δT_{aw} plots on rotor tip surface for the three NGV shapes *(hot streak and negative swirl)*

6.5 Heat Transfer and Stage Efficacy

Although the main emphasis of the present work is on the rotor blade and tip heat transfer, it is also useful to consider the overall aerothermal performance of the HP turbine stage. Table 6.1 to Table 6.4 presents the integrated heat flux values for the NGV and rotor passages for both swirl directions.

For the NGV passage, for both swirl directions, the reverse compound lean case results in the highest overall heating for the NGV passage by approximately 6%. The component breakdown shows that the majority of the increase comes from a higher heat flux on the vanes.

Table 6.1 NGV heat flux breakdown for the three vane shapes (hot streak and positive swirl)

Case	**NGV, W/(kg/s)**			**Total**	$\Delta(\%)$
	Hub	Casing	Vanes		
Straight	403	389	2750	3542	-
CL	454	474	2625	3554	0.34
RCL	454	320	2969	3743	5.69

Table 6.2 NGV heat flux breakdown for the three vane shapes (hot streak and negative swirl)

Case	**NGV, W/(kg/s)**			**Total**	$\Delta(\%)$
	Hub	Casing	Vanes		
Straight	355	189	2839	3383	-
CL	381	235	2802	3418	1.03
RCL	410	178	2993	3581	5.83

In terms of rotor heat load (Table 6.3 and Table 6.4), the casing values for the two swirling directions vary significantly, with a higher value observed for the positive swirl cases. This is due to the radial hot fluid transport in the NGV passage to the casing for positive swirl resulting in a higher total temperature at the rotor inlet. Similarly, this hot fluid transport results in lower heating of the rotor casing for the negative swirl cases, which affects the total passage value considerably.

Furthermore, for the positive swirl cases, the NGV shaping has little effect on the rotor heat load. However, for the negative swirl, marked effects on rotor heating are observed. The most striking difference in the rotor heat transfer is between the two compound lean cases with opposite swirl directions. The compound lean with a negative swirl is nearly 22% lower in rotor heat load than its positive swirl counterpart.

Within the negative swirl cases, the compound lean NGV yields 9% lower rotor heat load than that for the straight NGV case. In contrast, the reverse compound lean appears to be detrimental; the RCL case for the negative swirl has a higher heat load than the straight vane case (over 10% higher), although it is still lower than the straight vane case for the positive swirl.

Table 6.3 Rotor heat flux breakdown for the three vane shapes (hot streak and positive swirl)

Case	**Rotor, W/(kg/s)**			**Total**	$\Delta(\%)$
	Hub	Casing	Blade		
Straight	698	1104	1971	3774	-
CL	600	1203	2040	3844	1.85
RCL	797	877	1995	3669	-2.78

Table 6.4 Rotor heat flux breakdown for the three vane shapes (hot streak and negative swirl)

Case	**Rotor, W/(kg/s)**			**Total**	$\Delta(\%)$
	Hub	Casing	Blade		
Straight	718	552	2039	3309	-
CL	634	404	1970	3008	-9.09
RCL	775	842	2078	3696	11.68

The normalized differences in the stage efficacy for all the cases are shown in the final column of Table 6.5. The efficacy changes for the negative swirl cases generally tend to be greater than those for the positive swirl ones, illustrating again the considerable impact of the swirl direction of combustor exit flow on HP turbine aerothermal performance.

Table 6.5 Stage performance calculations for all six cases

Swirl Direction	**Case**	$\frac{\eta_{non-ad}-\eta_{non-ad,avg}}{\eta_{non-ad}}(\%)$
Positive	Straight	-0.24
	CL	-0.33
	RCL	-0.01
Negative	Straight	0.37
	CL	0.30
	RCL	-0.10

6.6 Summary of Chapter

The previous chapter focussed on an investigation to assess the aerothermal impact of vane shaping subjected to a hot streak inlet. The present chapter has built on this foundation to present a non-linear unsteady time-domain analyses of a transonic HP turbine stage to understand the aerothermal effects of a combined inlet hot streak and swirl, a topic that has rarely been studied before, as noted in Chapter 2. Presently, the influences of the swirling flow direction and three NGV shapes are examined. The following observations can be made.

The lean burn conditions (with swirl) is seen to cause a marked radial redistribution of the hot fluid within the NGV passage in contrast to the rich burn inlet. This radial transport results in a much flatter spanwise temperature profile at the NGV exit, compared to the rich burn counterpart where the NGV transport of the hot fluid is predominantly a passive convection.

The swirl direction is shown to affect the NGV exit temperature distribution in a very distinctive manner. A positive swirl, seemingly offloading NGV aerodynamically in the casing region, is shown to thermally upload the casing with a higher local temperature at the NGV exit. A negative swirl, uploading the NGV near casing region aerodynamically, is shown to offload the casing region thermally. This opposing aerothermal behaviour may simply be attributed to the differential primary flow inertias on the suction and pressure surfaces when the swirling flow is transported through the NGV passage after being split at the vane leading edge.

The swirl direction is shown to affect the NGV exit temperature distribution in a very distinctive manner. A positive swirl, seemingly offloading NGV aerodynamically in the casing region, is shown to thermally upload the casing with a higher local temperature at the NGV exit. A negative swirl, uploading the NGV near casing region

aerodynamically, is shown to offload the casing region thermally. This opposing aerothermal behaviour may simply be attributed to the differential primary flow inertias on the suction and pressure surfaces when the swirling flow is transported through the NGV passage after being split at the vane leading edge.

Correspondingly, the rotor heat transfer characteristics in the combined hot streak and swirl cases are shown to be dependent on the NGV shaping but in a very different manner compared to those for the hot streak only case. For the rotor tip region in particular, the differences in heat load for different swirl directions and NGV shapes can be up to 30-40%, although the corresponding variations in integrated performance parameters (total heat load and stage aerothermal efficacy) are much smaller. This indicates the potential for combined aerodynamic and heat transfer optimisation procedures with the inclusion of the lean parameter as a key design variable. This is especially relevant where the coolability and durability of rotating parts are very important; lean burn combustor exit conditions will be further treated in Chapter 7, in which novel design concepts and a numerical optimisation are explored in order to realise the true optimum shape.

Chapter 7

NGV Design Optimisation for Lean Burn Combustion

7.1 Introduction

In the present chapter, a novel design methodology for the NGV row is presented in order to manage the inflow temperature and velocity conditions due to lean burn combustion. An example test shape is proposed that shows promising results. In order to further improve on this, in an aerothermal sense, an optimisation routine is carried out. Two optimisation strategies are presented, which have been designed in order to cope with the large changes in capacity across the design space. Building on the work from Chapter 6, the lean parameter is used as the design variable. Results are shown and analysed, with modest performance improvements being achieved.

7.2 NGV Design Concept

7.2.1 Current State of Art

As has been discussed previously, HPT blades operate in an environment that is subject to spatial temperature and velocity variations originating from combustor fuel injectors. Current CFD design practice is to model the turbine inlet as having uniform total temperature and velocity profiles; as has been seen in Chapter 5 and Chapter 6, this is very different from the rich and lean burn combustion cases.

It is well known that the circumferential non-uniform temperature distribution can affect the heat load on the blades in both the first row of nozzle guide vanes (NGVs or 'vanes') and the following rotor blade row. In particular, as seen in Chapter 5, the pressure surface of a rotor blade can be subject to a high heat load due to "positive jetting" (increased cross-passage movement from the suction surface to the pressure surface). This heat load build up can be countered by the influence of a 'negative jet' associated with a vane blade wake which causes a pressure-to-suction surface movement in a rotor passage. The negative jet phenomenon is achieved through impinging the hot streak onto the NGV leading edge. One consequence of this, however, is for the impinged vane to be subject to a higher heat load compared with the unimpinged vane.

One option for managing non-uniform heat load on the NGVs is to have different cooling arrangements for the NGVs, so that NGVs exposed to higher heat loads are subject to additional cooling. However, the non-equal cooling for the two NGVs introduces a non-equal aerodynamic flow field, which may prove to be detrimental to aerothermal performance. Another option is to shorten the chord length of some NGVs and position these NGVs so that their leading edges are further downstream than the other NGVs. The shortened NGVs can thus effectively be thermally shielded

by the adjacent longer NGVs. However, the long and short NGV arrangement can also produce flow non-uniformity which may be detrimental to aerodynamic performance.

These detrimental effects can be exacerbated when there is a strong aerodynamic non-uniformity at the NGV inlet, such as a swirling flow and a non-uniform turbulence intensity, with peak turbulence typically at hot streak centres.

7.2.2 Proposed Design Methodology and Analysis

Currently, the vane rows for a turbine stage are designed such that each vane is identical for the entire annulus configuration, as shown in Figure 7.1. However, as discussed earlier, it is not valid to assume a uniform inlet temperature variation, and hence a uniform, periodic vane arrangement. It would be desirable to provide a stator vane arrangement which facilitates an alternative approach to heat load and flow management. A potential option to manage this is to design the vanes in pairs. Advantageously, the non-uniformity in the pair of vanes can accommodate non-uniformity in the working gas arriving at the vanes, and thereby can help to enhance aerothermal performance, e.g. by lowering losses and cooling air requirements. For a common injector-NGV count ratio of 1:2, this may result in the vanes being shaped independently of one another within a pair.

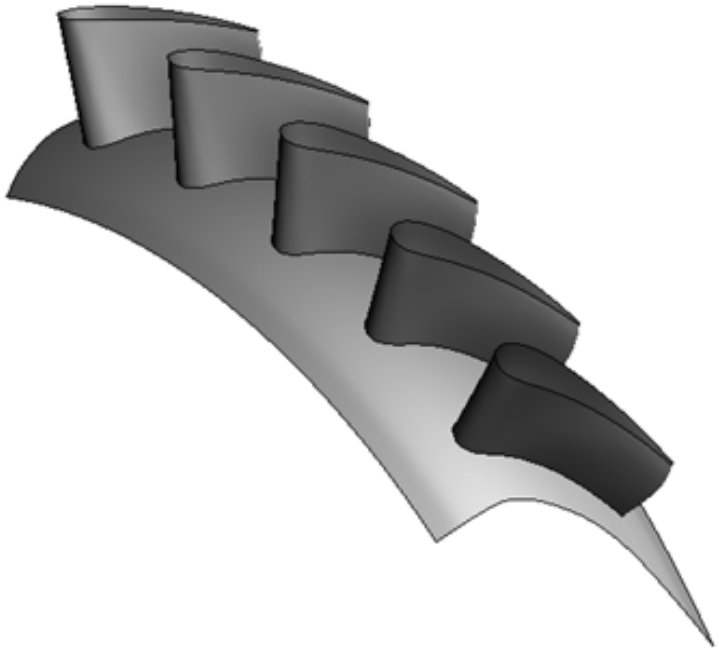


Fig. 7.1 Portion of an annular NGV cascade, with a conventional periodic blading arrangement

This non-equal blade shaping will ensure that for a given inlet non-uniform velocity and temperature condition, an improved combined heat transfer and aerodynamic performance can be gained from the design, which would be otherwise unachievable in the conventional designs of identical blade shape. The concept proposed in this research is for non-equal shaping from one blade passage to another; however, this may be extended to include a passage-to-passage variation of the casing and/or hub surfaces.

Consider a pair of conventional identical neighbouring NGVs subject to distorted temperature and velocity profiles. A possible non-equal geometrical shaping for the NGVs to mitigate the profiles can be achieved by tangentially leaning the two NGVs in opposite directions independently of one another, as illustrated in Figure 7.2. In more explicit terms, one of the vanes is reverse compound leaned, and the other is

compound leaned in a positive manner. The intent for tangential lean is to manipulate the NGV loading redistribution, and potentially create a constrained flow path for the hot streak and swirling flow that minimises the cooling required and heat load on blade components.

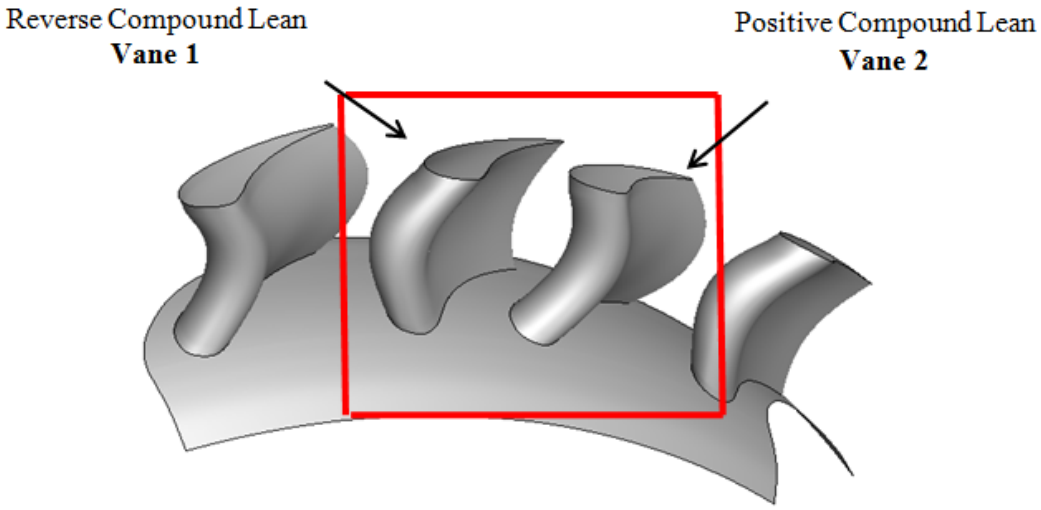


Fig. 7.2 A pair of unequally designed NGVs within a vane row

The rationale behind the design proposed will now be explained. With relation to a combined hot streak and swirl inflow, two design aspects should be considered. First, as mentioned earlier, there is a requirement for the thermal core (hot streak) to impinge on the leading edge of one of the NGVs. This is in order to utilise the negative jet effect of the vane wake and suppress the positive jet effect of hot gas migration from the rotor blade suction surface side to the pressure surface (and consequently secondary flow radial migration of hot gas to the rotor tip). Secondly, it is desirable for the core associated with a swirling flow to be placed in a low loading region to reduce further mixing loss generation.

In order to satisfy both of these aspects, a RCL vane is required to be impinged, since it is able to reduce loading at the midspan, which is the core of the high gradient

swirling flow, and have the effect of confining the hot streak to the midspan, which in turn would reduce the dispersal of the hot streak to the hub and casing platforms which are difficult to cool. Additionally, the other blade of the pair is compound leaned, which causes a reduction in loading at the endwalls (but an increase at midspan) which would reduce hub/casing endwall secondary flow losses and provide a more uniform loading distribution at the vane exit.

The unequal NGV shape shown in Figure 7.2 is now compared with the conventional straight vane case. Pitchwise averaged plots (across two stator pitches) of absolute total temperature and pressure loss are presented in Figure 7.3 for both NGV shapes. It can be seen that the uniformity in the temperature distribution of the fluid for the baseline case has been markedly changed by the unequal shaping from around 20% span to the casing. There is a slight reduction (approximately 5%) in temperature very close to the casing (95% upwards) due to the unequal shape. In Chapter 6, it was noted that the thermal loading due to the lean burn inlet was driven by the pressure leg of the NGV; for a positive swirl, this resulted in a thermal uploading at the casing. This mechanism appears to be slightly offset by the introduction of RCL. As was seen in Chapter 5, for a CL vane, the loading from the endwalls to the midspan was a local observation on the suction side, whilst a divergence was in fact dominant in the entire passage. Similarly, for an impinged RCL, a convergent streamline pattern would expect to be seen from the pressure side of the NGV and propagated into the passage. This convergent nature would therefore prevent some of the hot fluid from reaching the casing, and the result is an increase in temperature just above midspan, between 65% and 90% span.

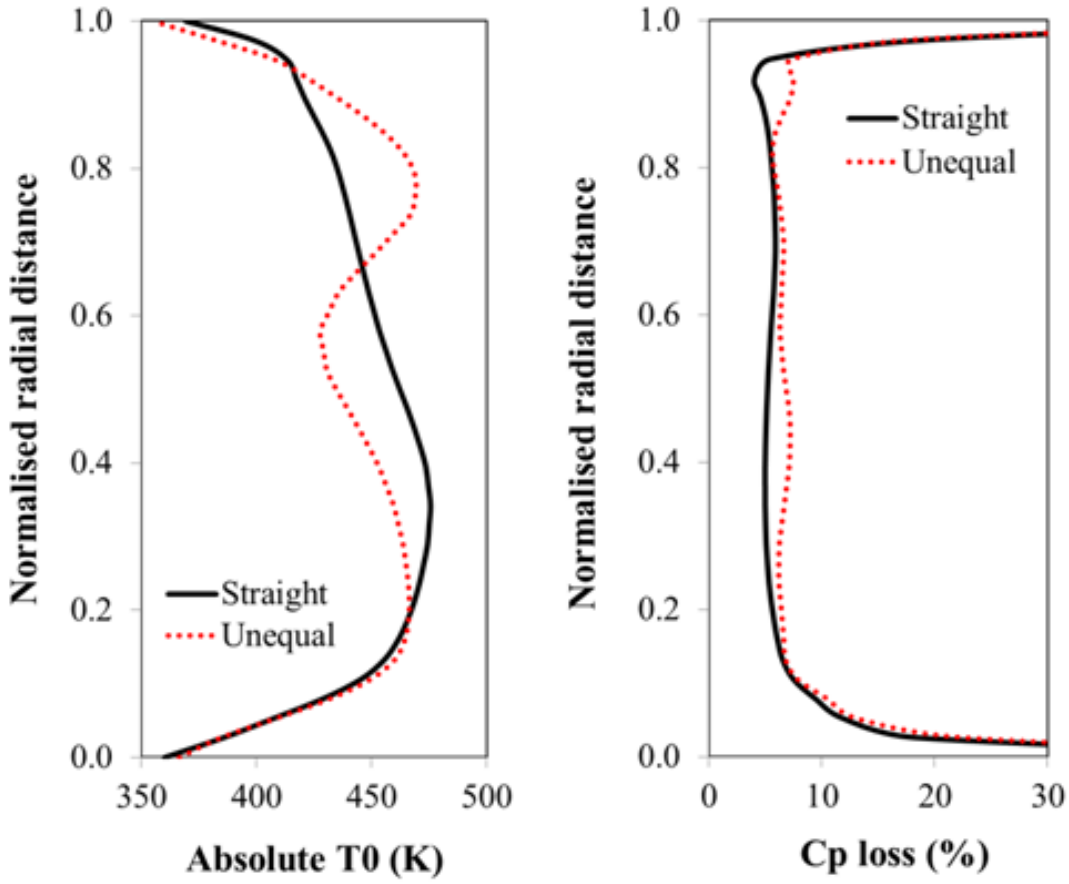


Fig. 7.3 Comparison between baseline (straight) and unequal cases at NGV exit for absolute total temperature (K) and pressure loss coefficient (pitch averaged)

The radial distribution of total pressure loss coefficient is also shown in Figure 7.3. It would be expected that the effects of the loading redistributions due to CL and RCL would cancel each other out i.e. the loading at the midspan due to CL would be cancelled out by the offloading due to RCL. However, a slight increase in loss due to the unequal shaping can be seen at midspan (3% increase) and towards the casing (4%).

The heat flux on the rotor pressure and suction sides, as well as on the tip is shown in Figure 7.4 and Figure 7.5 respectively. The distribution on the pressure surface appears to follow the trend of the NGV exit temperature profile. The unequal NGV

design results in a cooler midspan towards the leading edge compared with the baseline, but a higher heating towards the trailing edge near the casing. However, over the tip, there is a noticeable reduction in heat load at the leading edge for the unequal shape, corresponding to the lower total temperature in Figure 7.3.

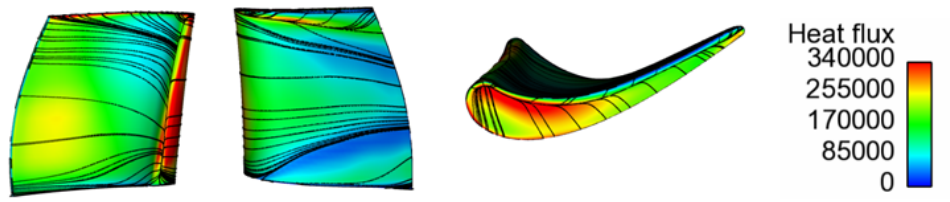


Fig. 7.4 Rotor heat flux (W m^{-2}) on (left to right) on pressure and suction surfaces, as well as tip (straight vane case)

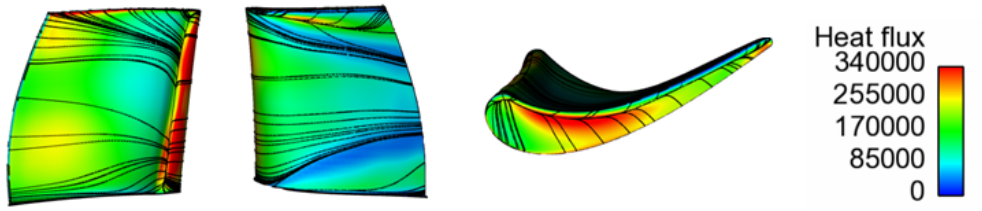


Fig. 7.5 Rotor heat flux (W m^{-2}) on (left to right) on pressure and suction surfaces, as well as tip (unequal vane case)

The effect of the unequal shaping on stage aerothermal performance is summarised in Table 7.1. A slight increase in heat load in the NGV passage and decrease in the rotor passage is observed. The stage efficacy shows a significant improvement of 0.51% over the baseline. The effect of shaping with a negative swirl orientation gives approximately a 15% lower heat load compared to the positive swirl baseline, and a 3% decrease compared with the negative swirl baseline. Interestingly, the unequal shape yields the highest efficacy, 1.8% greater than the positive swirl baseline, and 1.3% higher than the negative swirl baseline. This further demonstrates the effectiveness of the non-periodic design methodology for negative swirl cases.

Table 7.1 Percentage changes in heat load and efficacy relative to baseline (straight NGVs, positive swirl)

Swirl Direction	**Case**	Δ_{ngv} **heat load(%)**	Δ_{rotor} **heat load(%)**	$\Delta\eta_{non-ad}$ **(%)**
Positive	Straight	-	-	-
	Unequal	3.0	-3.0	0.51
Negative	Straight	-4.5	-12.3	0.54
	Unequal	-0.6	-15.0	1.80

It can be seen that the non-periodic design methodology has expanded the design space to deal with inflow non-uniformities, in which there are numerous variables that may be explored in order to achieve a design that maximises efficiency. In this section, the leaning of the vanes has been discussed; the hot streak clocking position and restaggering are two other such design parameters. For example, the hot streak could possibly be clocked onto the pressure surface of the impinged RCL vane. This would allow cooling air to be added more efficiently with reduced mixing loss from a pressure surface of a vane as opposed to a suction surface (injecting coolant into a lower speed flow would result in a lower loss than injecting into a higher speed flow).

Furthermore, the axial gap between the vane and blade row may also differ for a vane pair. The relative motion between the rotor and stator leads to unsteadiness, and this is affected by the size of the axial gap. Reducing the blade row interaction with the upstream vane wake would improve the aerodynamic performance.

In the above analysis, the precise degree of lean required on both NGVs in order to obtain the most favourable aerothermal results is unknown. The design proposed is based on the assumption that the hot streak and swirl core is most effectively dealt with by impinging on the RCL vane. Whether there are other arrangements that produce better results is yet to be seen. An aerothermal optimisation based on this design concept will now be investigated in an attempt to clarify this question.

7.3 Design Optimisation Problem and Setup

7.3.1 Problem Definition

This section provides details of the sampling and predictive modelling setup for the NGV lean optimisation subject to a hot streak and positive swirling flow at the turbine inlet. The subsequent two sections will present results based on this setup, for two clocking inlet positions; impinging and passage aligned hot streak and swirl.

One of the main challenges in rotor design is to minimise the heat load experienced by the tip, as described in Chapter 6. Thus the optimisation in this chapter will aim to optimise for rotor tip heat flux. However, in order to wholly define the problem, some important considerations must first be discussed. These will now be presented.

7.3.2 Steady Versus Unsteady CFD

Before determining the appropriate objective or target function (i.e. the quantity to be minimised/maximised), it is necessary to identify the limitations of the surrogate model optimisation method. Although the models (discussed in Section 4.4) will be constructed using a reduced initial batch of high fidelity CFD simulations, the number of CFD runs is still considered to be fairly high. In this analysis, 120 sample CFD runs will be required, from which the predictive models will be trained. This therefore means that unsteady CFD simulations cannot be employed, due to a prohibitive computational cost. Therefore, in order to optimise for stage efficiency, the question arises as to whether steady CFD simulations are capable of capturing aerothermal interactions between the stator and rotor for the combined hot streak and swirl inlet. This is explored through a comparison of five different NGV design test shapes for different performance parameters as shown in Table 7.2, Table 7.3, Table 7.4; non-adiabatic

efficacy, adiabatic efficiency and rotor heat load respectively. It can clearly be seen that, for all parameters, the ranking order is not maintained. For example, the best efficacy shapes for the steady simulations are shape 1 and shape 4, whereas the unsteady CFD reveals that this is no longer the case; case 5 now shows the most beneficial shape. It is thus apparent that the non-uniformity from the NGV passage gets mixed out with the steady CFD. Therefore, in order to save on computational time but still capture the correct behaviour, it was decided to identify an optimisation objective function at the NGV exit that is representative of the rotor tip heat flux (since this can not be measured directly). This will be discussed next.

Table 7.2 Steady versus unsteady CFD for non-adiabatic efficacy

Case	η_{non-ad} **(%)**	
	Steady	Unsteady
1	89.60	88.38
2	89.56	88.29
3	89.18	88.58
4	89.60	88.46
5	89.28	88.89

Table 7.3 Steady versus unsteady CFD for rotor heat load

Case	**Rotor heat load W/(kg/s)**	
	Steady	Unsteady
1	3376	3374
2	3347	3844
3	3443	3669
4	3399	4066
5	3335	3650

Table 7.4 Steady versus unsteady CFD adiabatic efficacy

Case	$\eta_{adiabatic}$ **(%)**	
	Steady	Unsteady
1	95.65	94.74
2	95.62	94.72
3	95.49	95.04
4	95.87	95.27
5	95.42	95.24

7.3.3 Objective Function

Following on from the previous section, a potential marker of rotor tip heat load, for the combined hot streak and swirl case, is the NGV exit total temperature profile. As presented in Chapter 6, the redistribution of hot fluid at the vane exit due to positive swirl was seen to generate very different tip heat fluxes for the different NGV lean

shapes, as shown in Figure 7.6. Specifically, significant changes in total temperature for 80% to 100% span height at the vane exit (Figure 7.6 (a)) were observed, with the RCL vane shape showing the lowest temperature profile, which translated into the lowest tip heat flux distribution (Figure 7.6 (b)). As discussed in Chapter 6, this was driven by aerodynamic mechanisms, as indicated by the contribution of HTC to the tip heat flux. Therefore, in order to represent this as a design optimisation objective function, the NGV exit was sliced on a radial line from 80% NGV spanwise height to the casing, and mass averaged over the slice.

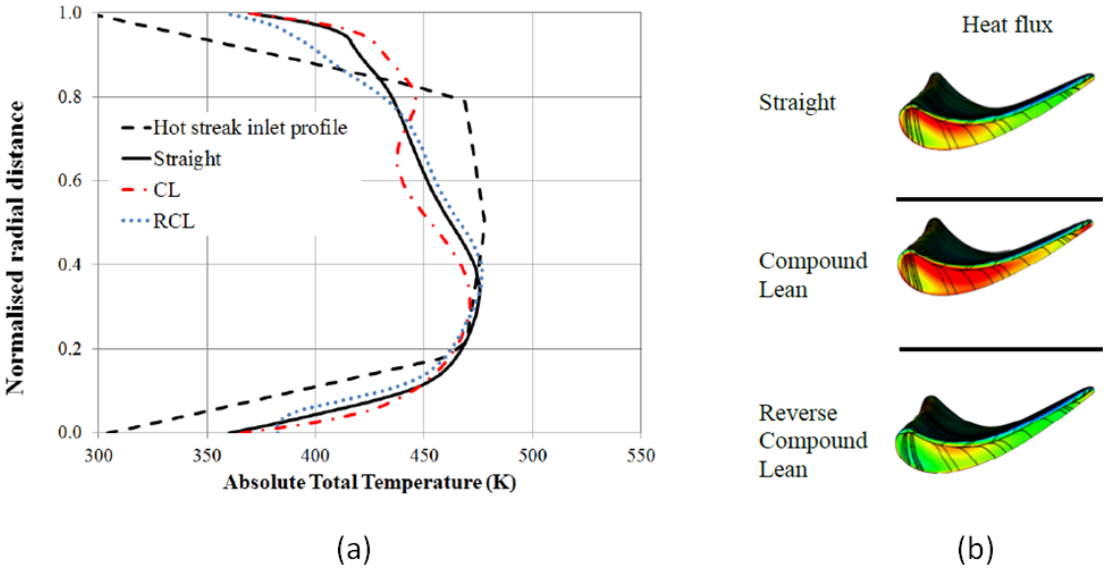


Fig. 7.6 (a) Total temperature pitch averaged profile at NGV exit, and (b) corresponding rotor tip heat flux

7.3.4 Design Variable Definition

In this optimisation, four control points or design variables will be implemented. These sections will be permitted to move tangentially, i.e. all control points will be subjected to the lean parameter, as shown in Figure 7.7. The hot streak and swirl impinged vane, denoted vane 1 (right), will have two control points, at the hub and casing of the vane.

Vane 2 will also have two control points at the hub and casing. This therefore ensures that the two NGVs may be shaped independently of one another. The design range for each of the four design variables will range between +/- 2° (approximately 18% of span height) from the NGV centre of rotation, as shown in Table 7.5. These bounds were selected in order to account for potential mechanical or structural issues that could be associated with manufacturing vanes with high degrees of lean. Further, if the bounds were increased, there would have an added difficulty in ensuring matching the inlet mass flow with the baseline case.

Table 7.5 Design variable specification

Design variable	**Lower Bound** (°)	**Upper Bound** (°)
Vane 1 - Hub	-2	2
Vane 1 - Casing	-2	2
Vane 2 - Hub	-2	2
Vane 2 - Casing	-2	2

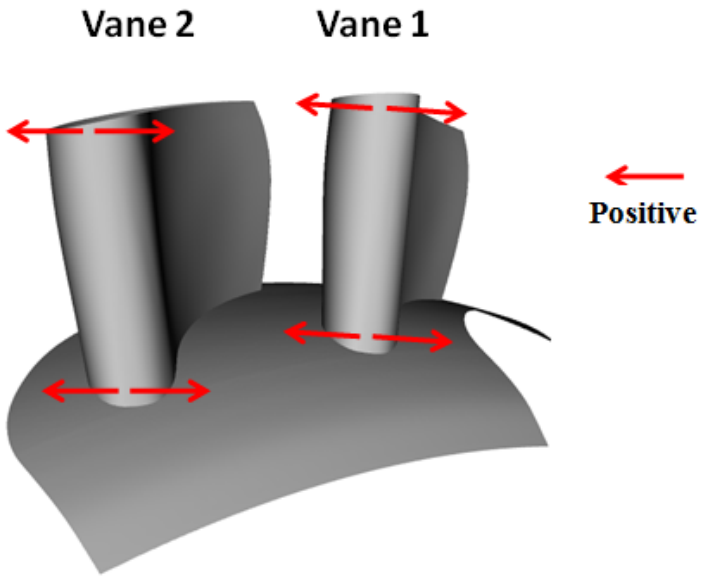


Fig. 7.7 Design variable specification on nozzle guide vanes. The right vane is denoted as 'Vane 1' as viewed from upstream

7.3.5 DOE Sampling for CFD Simulations

In order to build a predictive model, a training CFD dataset is required. Given the design variable definition in the previous section (four dimensional problem), the Latin Hypercube sampling method will be used to randomly generate NGV shapes across the four control points. In the current optimisation, 100 NGV shapes (representing the DOE samples) will be run using CFD and the objective function (mass averaged total temperature at NGV exit for upper 20%) for each shape will be extracted using the method described in Section 4.3.3. A transformation is required in order to plot and visualise the sample design space in two dimensions (since each shape is represented by a four dimensional design vector). This can be achieved through the dimensionality reduction technique known as t-distributed stochastic neighbour embedding (t-SNE), which was developed by van der Maaten and Hinton (2008). Given a set of N high

dimensional objects $x_1, ...x_N$, t-SNE first computes the similarities, p_{ij}, between two objects x_i and x_j:

$$p_{ij} = \frac{p_{j|i} + p_{i|j}}{2N} \tag{7.1}$$

where:

$$p_{j|i} = \frac{\exp(-\|x_i - x_j\|^2/2\sigma_i^2)}{\sum_{k\neq i}\exp(-\|x_i - x_k\|^2\ 2\sigma_i^2)} \tag{7.2}$$

where σ is the variance of the Gaussian that is centred on x_i. The t-SNE algorithm computes a two-dimensional representation or map with points $y_1, ..., y_N$ that reflects the similarities p_{ij} as best as possible. q_{ij} measures the similarities between two points y_i and y_j in this map, and is defined as:

$$q_{ij} = \frac{(1 + \|y_i - y_j\|^2)^{-1}}{\sum_{k\neq i}(1 + \|y_k - y_i\|^2)^{-1}} \tag{7.3}$$

The points $\mathbf{y}$ in the two dimensional map are obtained through the minimisation, using gradient descent, of the Kullback-Leibler divergence:

$$\sum_{i\neq j} p_{ij} \log \frac{p_{ij}}{q_{ij}} \tag{7.4}$$

In terms of the CFD setup, the combustor-to-NGV count ratio is set as 1:2. The combined hot streak and positive swirl boundary conditions for temperature and velocity respectively has been defined in Chapter 6. The mass averaged temperature is $432K$, with the peak and minimum being $525K$ and $290K$ respectively. The yaw and pitch angles for the swirl profile varies between +/- 40°. Since only the NGV passage domain is being considered, the exit static pressure radial distribution was specified

using the solution from a baseline (two straight NGVs) mixing plane case. In order to ensure that the samples obtained are valid, it is necessary to ensure that the mass flow was designed to be within 0.2% of the baseline, straight configuration. A bulk skew is applied to one of the NGVs in order to achieve this. The amount of skew is specified by a linear interpolation of two CFD solutions around the mass flow design point.

7.3.6 Model Setup

A surrogate model approach requires the training of a prediction model in order to be passed to the optimiser. In this study, four prediction models are to be tested, as defined in Table 7.6 and the most accurate model will be used for the optimisation procedure. Model accuracy will be determined through an evaluation of the mean squared error (average of the squared difference between the actual response and the prediction of the response) and R^2, which is defined as:

$$R^2 = \frac{TSS - RSS}{TSS} = 1 - \frac{RSS}{TSS} \tag{7.5}$$

where $RSS = \sum_{i-1}^{N}(y_i - \hat{y}_i)^2$ and $TSS = \sum_{i-1}^{N}(y_i - \overline{y})^2$. R^2 measures the proportion of the variability in the response that can be explained by the inputs.

Table 7.6 Prediction models to be investigated, with hyperparameters to be tuned

Model	**Hyperparameter(s)**
Linear SVR	C
Polynomial SVR	C, d
Radial Basis SVR	C, γ
Random Forest	number of trees, min samples at leaf node

Table 7.6 also indicates the parameters of each learning algorithm, known as hyperparameters, that require separate tuning in order to be optimised for model performance. This is achieved through the technique known as grid search, which will find the optimal combination of hyperparameter values. Grid search is an exhaustive technique; the user specifies a list of discrete values for each hyperparameter, which are then evaluated, and the optimal set of parameters that yields the best k-fold cross-validation accuracy is returned. The reader is referred to Chapter 4, Section 4.3, for further details of k-fold cross-validation. For the grid search, 10 folds were used. The list of hyperparameter values specified is shown in Table 7.7.

Table 7.7 Hyperparameter values specified for grid search

Hyperparameter	**List of values**
C	[0.001,0.01,0.1,1,10,100,1000]
γ	[0.001,0.01,0.1,1,10,100,1000]
d	[2,3,4]
number of trees	[1000,2000,5000,10000]
min samples at leaf node	[1,2,3]

7.4 Case 1: Design Optimisation with Impinging Hot Streak and Swirl

7.4.1 Model Performance

The resulting plot of the 100 DOE sample points (representing a four dimensional space) projected into two dimensions is shown in Figure 7.8. Good coverage of the

design space can be seen. Although some of the boundaries of the design space do not appear to be represented, the author does not expect any extreme changes in the gradient of the objective function in these areas that would affect the model predictions.

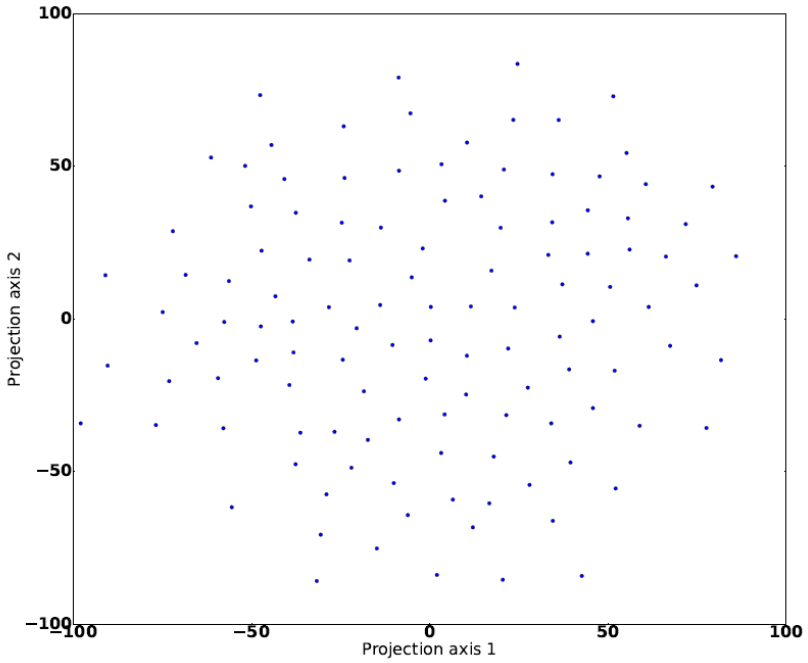


Fig. 7.8 t-SNE two dimensional representation of feature design space

The 100 DOE sample points requiring CFD simulations for the NGV domain were computed on a high performance computing Dell Sandybridge cluster. 32 cores (2 nodes*16 processors per node) of 2.0GHz Xeon SandyBridge were used. The samples were then processed to compute the objective function. Thereafter, prediction models were coded and built using Python's scikit-learn library. The models were trained on 85% of the DOE samples (selected at random), with 15% being held out as a test set in order to score the models for assessment and comparison. The test set is used for model evaluation in order to avoid potentially misleading training MSEs, due to possible overfitting. The best model that resulted in the lowest test MSE was the linear model, with a score of 2.825, as shown in Table 7.8. The table shows the MSE and R^2 for the training and test sets. The optimum value of the parameter C, as computed by

the grid search technique, was 100, which produced the highest cross-validated score of 0.938.

Table 7.8 Performance metrics for the best model

Model	**MSE train**	**MSE test**	R^2 **train**	R^2 **test**
Linear SVR	2.860	2.825	0.954	0.963

A plot of the linear model residuals (difference between the actual and predicted values) versus the predicted values for the training and test data points is shown below in Figure 7.9. Residual plots are used to identify potential nonlinearity, and to ensure that the errors are randomly distributed. The latter point is important, as correlated residuals could indicate that the model is failing to capture some explanatory information. It can be seen that the residuals are randomly scattered around the zero centreline, indicating that they are uncorrelated.

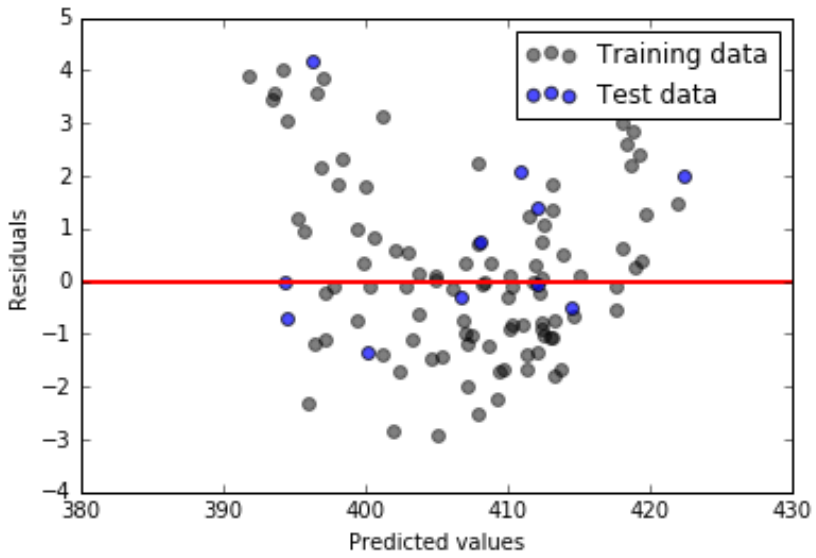


Fig. 7.9 Residual plot for SVR linear model

7.4.2 Feature Importance

Four design variables or features have been used in order to build machine learning models through an estimation of weighting parameters or feature coefficients that can be used to predict the objective function or target. As well as having the task of prediction, interpretability is also necessary in order to understand which features are the most important. The Lasso regularization technique was used in order to understand feature importance of the NGV lean control parameters. In comparison to a linear regression least squares approach (where the RSS is minimised in order to find the optimal β coefficients), the Lasso coefficients minimise the following quantity:

$$\sum_{i=1}^{n}(y_i - \beta_0 - \sum_{j=1}^{p}\beta_j x_{ij})^2 + \lambda \sum_{j=1}^{p}|\beta_j| = RSS + \lambda \sum_{j=1}^{p}|\beta_j| \tag{7.6}$$

Where $\lambda \geq 0$ is a tuning parameter that is determined separately. The second term on the right hand side represents a shrinkage penalty; as $\lambda \to \infty$, the impact of the penalty increases and the lasso coefficients will tend towards zero. One property of the penalty term is that it is able to force some of the coefficient estimates to zero if λ is sufficiently large. Therefore, it is possible to identify those coefficients that are still present in the model even when the regularization parameter is large, thus representing the main or important features. The Lasso model was trained on the DOE sample dataset, and plotted against different values of λ as shown in Figure 7.10. It can be see that the hub features for both vanes approach zero first, followed by the casing lean on vane 2 (unimpinged vane), with the casing lean coefficient on vane 1 (impinged vane) eventually shrinking to zero at a higher value of λ. Therefore, the 'Vane 1 - Casing' design variable was the most important in predicting the mass averaged total temperature at the vane exit for the top 20% of span height (i.e. the objective or target function). This implies that the redistribution and minimisation of hot fluid towards

the NGV casing is mostly dependent on the local casing lean shaping parameter of the impinged vane, followed by the casing lean of the unimpinged vane.

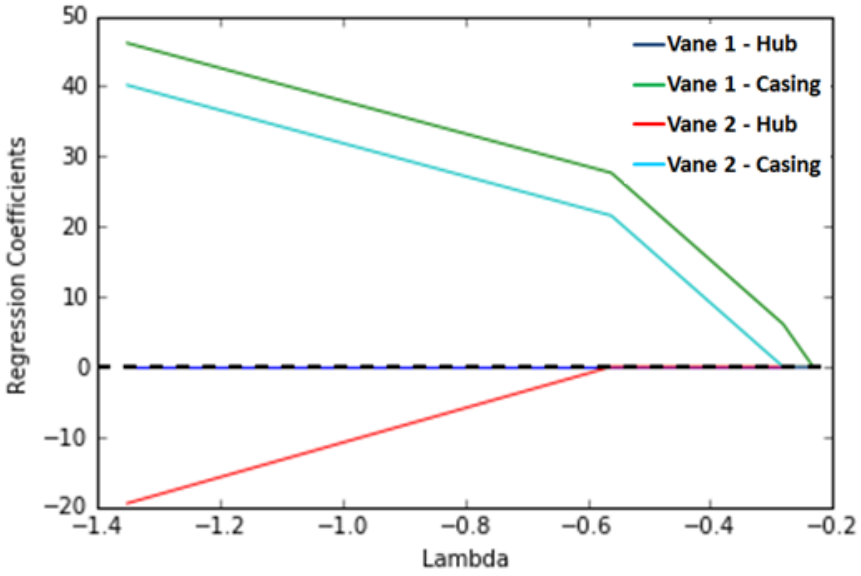


Fig. 7.10 Lasso coefficients versus regularization parameter

7.4.3 Optimised NGV Geometry

As discussed above, the best performing prediction model was the SVR model with a linear kernel. This surrogate model was combined with a Genetic Algorithm optimiser in order to find the minimum predicted objective function within the design space. For the optimisation, each generation consisted of a population of 200 individuals. The rest of the GA specifics are the same as those used in the optimisation validation presented in Chapter 4. After 62 iterations, the algorithm was terminated using the tolerance stopping criteria; the optimisation history showing the best and mean individual fitness is shown in Figure 7.11. The individual with the best performance is found within 10 iterations/generations, and the mean fitness within the population reaches this value in 30 iterations.

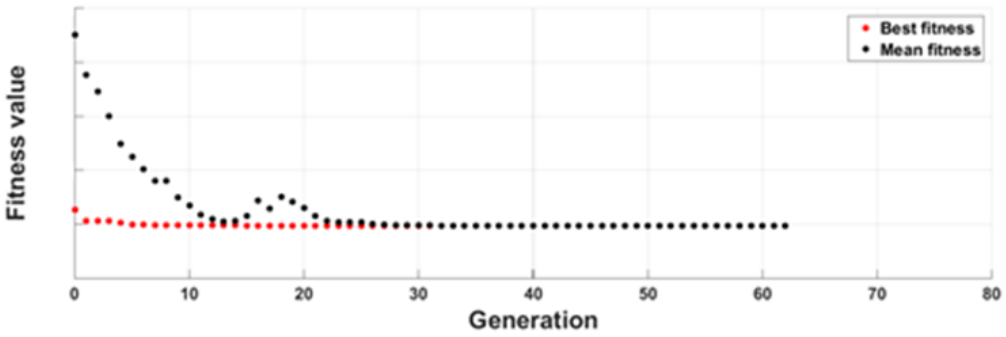


Fig. 7.11 Optimisation history using GA, indicating best and mean fitness per generation

The corresponding NGV shape for the best fitness function was run using CFD; the results are presented in Table 7.9, with the difference between the model and actual value being 1.23%. This was deemed to be within an acceptable limit.

Table 7.9 Objective function for Linear SVR (predicted and actual CFD)

Objective Function	**Linear SVR**	**CFD**	**Δ (Linear SVR - CFD)**
OF	388.38	383.65	1.23%

Table 7.10 shows the objective function for both the baseline and optimised cases. The mass flow at the NGV inlet for the Linear SVR case was constrained to within 0.5% of the baseline. An improvement (decrease) of 6.03% was observed in the objective function with the optimised shape.

Table 7.10 Objective function comparison for baseline and optimised geometries

Case	**Inlet mass flow (kg s^{-1})**	*OF*
Baseline	17.22	408.29
Optimised	17.30	383.65

The optimised NGV lean parameter values are shown in Table 7.11; it can be seen that the best shape is found on the design space boundary, with an unequal shaping design obtained. A comparison of the geometry is illustrated in Figure 7.12. The impinged vane is reverse compound leaned, and the unimpinged vane is negatively leaned at the casing, and positively leaned at the hub.

Table 7.11 NGV optimum design variables

Model	**Vane 1 Hub**(°)	**Vane 1 Casing**(°)	**Vane 2 Hub**(°)	**Vane 2 Casing**(°)
Linear SVR	-2	-2	2	-2

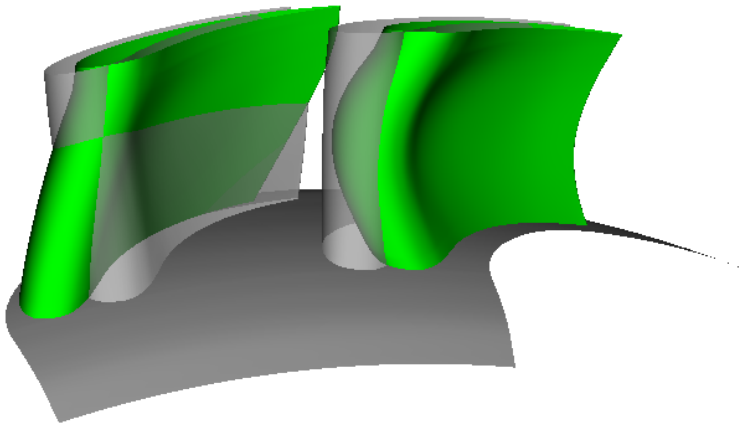


Fig. 7.12 Optimum and baseline NGV geometry comparison. Baseline geometry in grey; optimum geometry in green

7.5 Case 1: Analysis and Discussion

The optimised NGV geometry (using the design parameters from the previous section) was generated and meshed using PADRAM. The HP turbine stage was run using the HYDRA unsteady CFD solver, in order to capture and compare the rotor aerothermal characteristics. The optimised geometry will now be compared to the baseline case

(two straight vanes) for the NGV and rotor passages. All results presented are time averaged.

7.5.1 NGV Analysis

Figure 7.13 and Figure 7.14 shows the loading (static pressure normalised by the stage inlet total pressure) for the baseline and optimum cases, for the impinged and unimpinged vanes respectively, at 10%, 50% and 90% spanwise sections. The optimised impinged vane shows the characteristics expected for a reverse compound leaned vane; there is a marked increase in loading at the hub and casing sections, and a slight decrease at midspan. For the unimpinged optimised vane (reverse lean at casing; positive lean at hub), there is an increase in loading at the casing, and a decrease at the hub section.

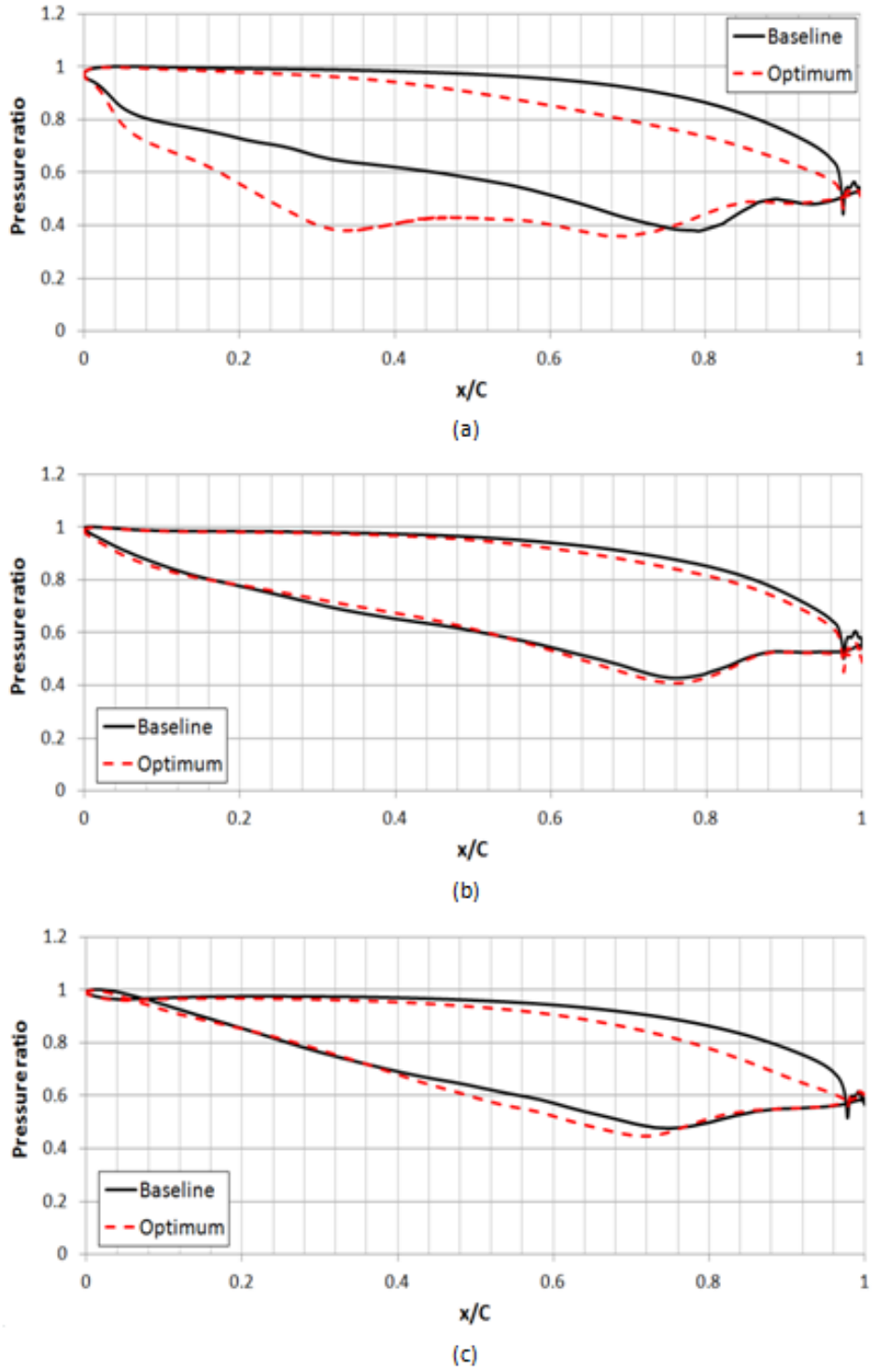


Fig. 7.13 NGV static pressure distributions on impinged vane at (a) 10%, (b) 50% and (c) 90% spanwise sections

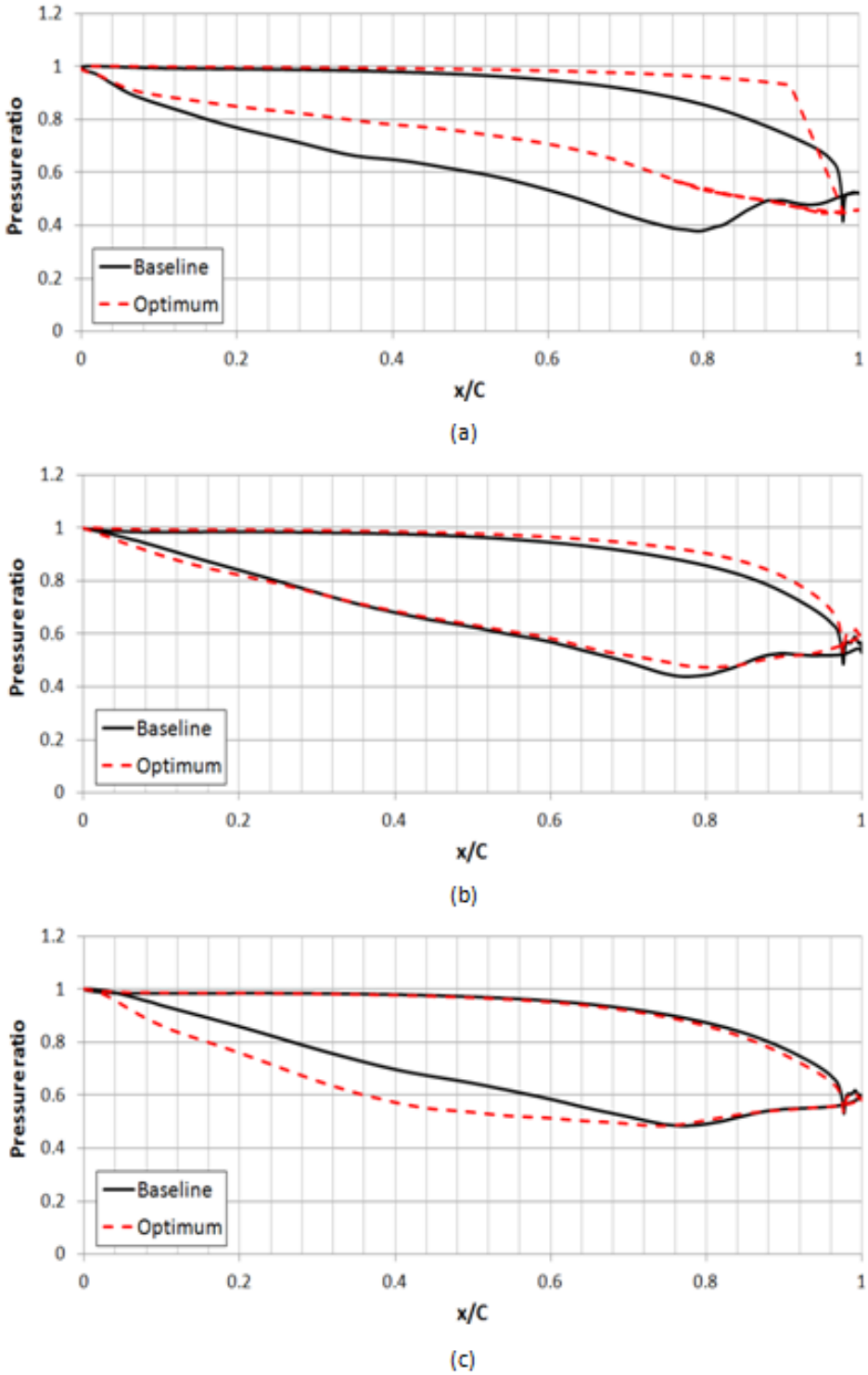


Fig. 7.14 NGV static pressure distributions on unimpinged vane at (a) 10%, (b) 50% and (c) 90% spanwise sections

The radial (pitchwise averaged) distributions of axial and tangential velocity components at the NGV exit plane are plotted in Figure 7.15. The radial flow distribution has now been altered by the optimisation. The axial velocity has increased by almost 30% near the hub, and decreased by a similar amount near the casing. The increase in axial velocity is possibly due to a thinning of the boundary layer wake for the optimum over the baseline case, as shown in Figure 7.16. The tangential velocity component indicates a more uniform distribution for the optimised case.

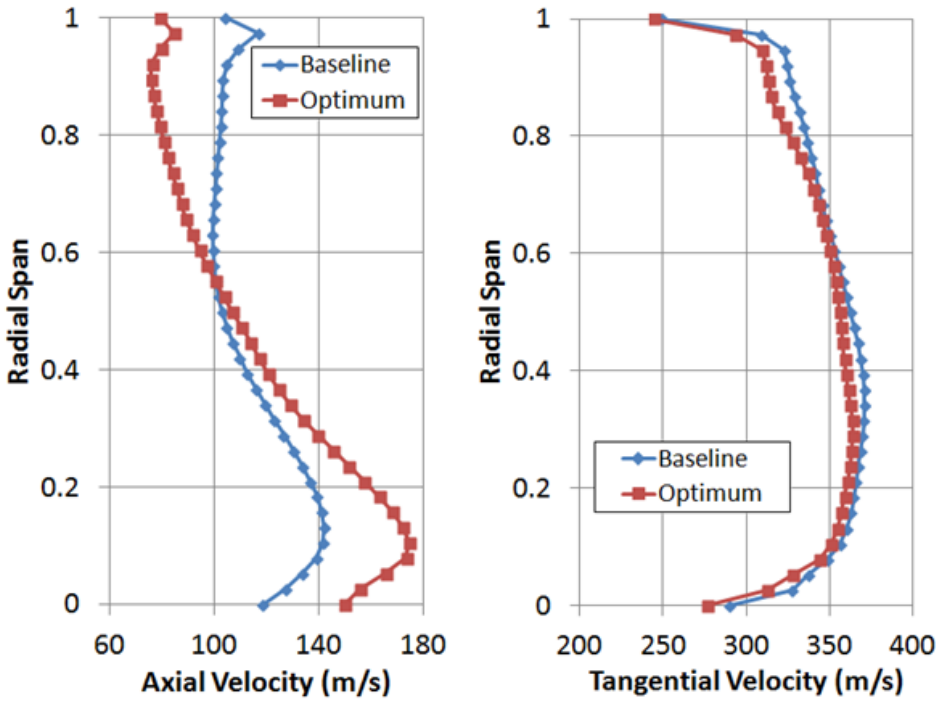


Fig. 7.15 Pitch averaged axial (left) and tangential (right) velocities (m s^{-1}) at the NGV exit plane for baseline and optimum case

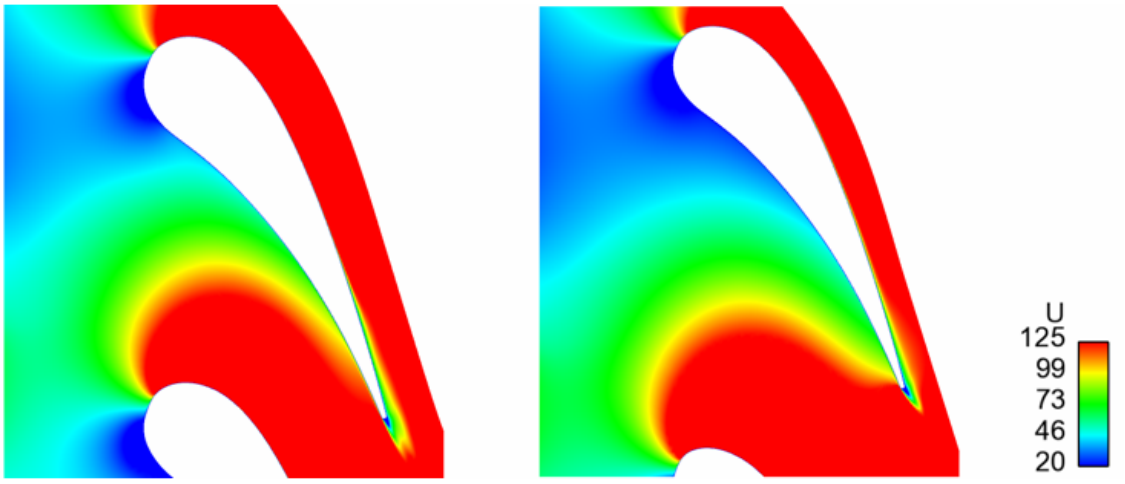


Fig. 7.16 Axial velocity (m s^{-1}) contours near NGV hub for baseline and optimum cases

The loss coefficients at the NGV exit plane are compared for the two cases. The pressure loss coefficient for each case is calculated using the following relation:

$$C_{P,Loss} = \frac{P_{01} - P_{02}}{P_{ref}} \tag{7.7}$$

where, P_{01} = inlet total pressure, P_{02} = NGV exit total pressure (time-mean value) and P_{ref} is taken to be the average dynamic pressure (time-mean value) at the mid-span of the exit plane in the uniform inlet case. In order to examine the differences between the cases, a $\Delta C_{P,Loss}$ quantity was plotted, which is an element wise subtraction of the baseline pressure loss field from the optimised field. This is shown in Figure 7.17. There is an overall reduction in pressure loss in the near hub region for the optimised shape over the baseline. Further, close to the mid span line, there appears to be a reduction in pressure loss for the optimised case.

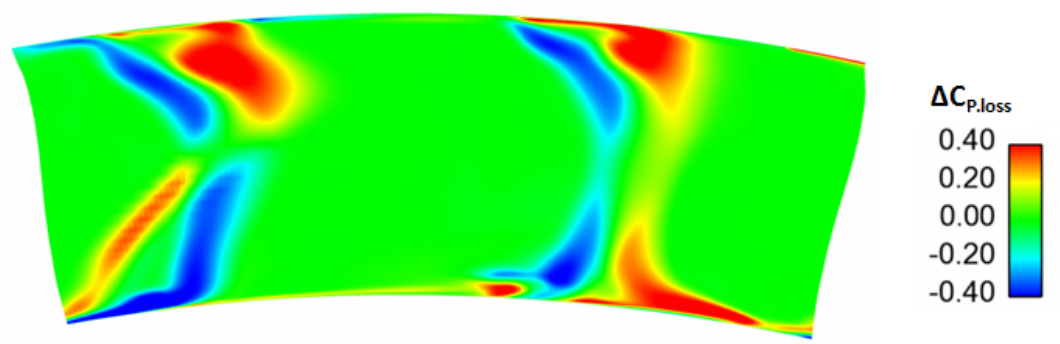


Fig. 7.17 Pressure loss coefficient difference (optimum - baseline)

7.5.2 Rotor Analysis

As has been seen in this investigation, the optimisation routine was successful in minimising the objective function; the mass averaged total temperature on the NGV exit plane from 80% radial span to the casing. As mentioned in Section 7.3.3, this was seen to be representative or influential on the rotor tip heat flux patterns. The resulting total temperature profile for the baseline and optimised NGV shapes on the NGV exit plane are shown in Figure 7.18. It can be seen that the optimised geometry causes a redistribution in T_0, with a lower temperature from 60% span to the casing, and a higher temperature near the hub (although not to the same degree as the casing temperature decrease) compared with the baseline.

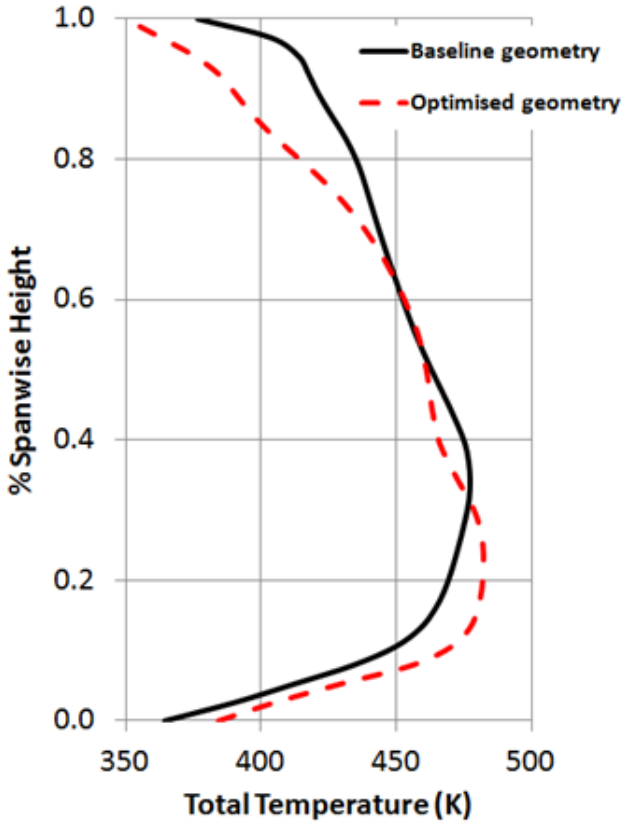


Fig. 7.18 Radial distribution of total temperature (K) at NGV exit plane

The unsteady rotor CFD results will now be presented. All results are time averaged plots. The rotor blade surface heat flux distributions are shown for the baseline and optimised geometries in Figure 7.19 and Figure 7.20 respectively. Considering the pressure surface in the first instance, it can be observed that the optimised shape yields a cooler rotor leading edge for the upper 50% radial span, when compared with the baseline. Additionally, the distribution of heat flux along the leading edge (in a spanwise sense) appears to follow the same radial pattern as the NGV exit T_0 distribution, Figure 7.18.

Furthermore, the surface streamlines (superimposed onto the rotor heat flux figures) that direct flow over the tip region from the (pressure surface to the suction surface) exhibit differences for the two geometries. For the baseline case, the streamlines from

80% span to the casing pass over the tip region. This is in contrast to the optimised shape, where the upper 50% of streamlines transport flow from the pressure surface to the suction surface. As mentioned above, since the leading edge for the optimum shape is cooler, it would be expected that this lower temperature fluid would result in a lower tip heat flux distribution compared with the baseline (as will be seen shortly). Finally, a hotter region of heat flux is observed close to the hub trailing edge for the optimised shape over the baseline.

Considering the rotor suction surface, the optimised shape yields a cooler upper third heat flux pattern, with a hot, narrow region close to the leading edge near-casing being noticeably reduced; this can be attributed to the transportation of cooler fluid from the pressure surface.

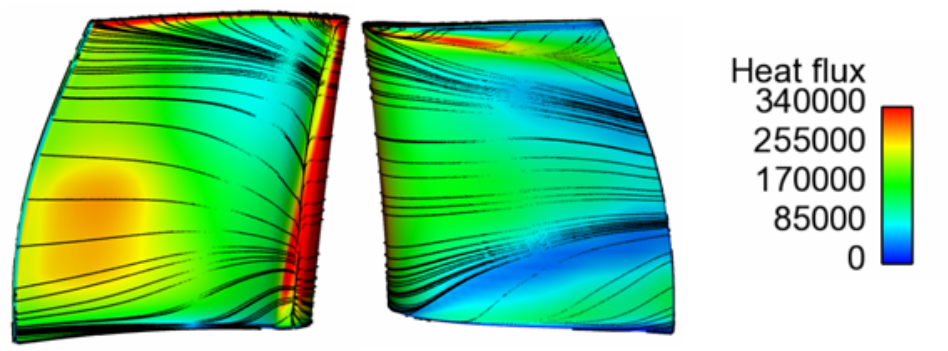


Fig. 7.19 Rotor surface heat flux (W m^{-2}) distributions for baseline geometry on pressure surface (left) and suction surface (right)

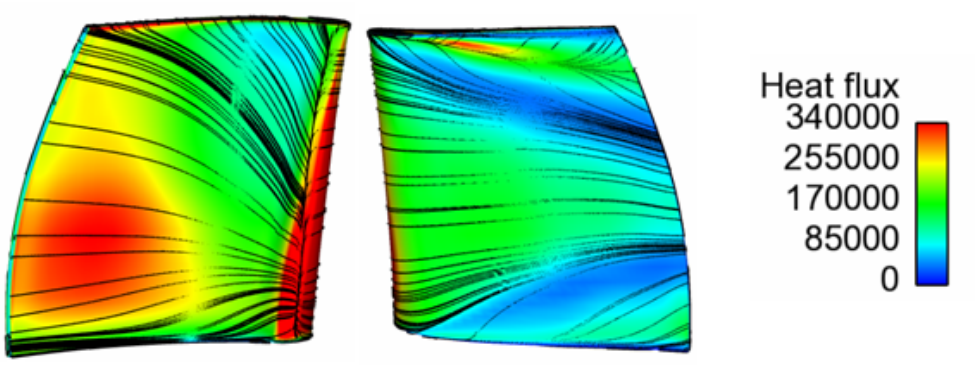


Fig. 7.20 Rotor surface heat flux (W m^{-2}) distributions for optimum geometry on pressure surface (left) and suction surface (right)

The rotor tip heat flux distributions for the two cases is shown in Figure 7.21. The optimised case has resulted in a much cooler pattern over almost the entire tip. This is especially prominent for the first 50% of the rotor axial chord. It also confirms streamline migration of hot fluid from the rotor leading edge on the pressure surface, to the suction surface.

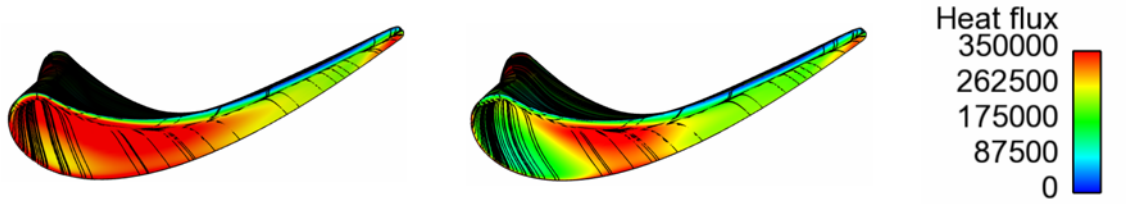


Fig. 7.21 Rotor tip heat flux (W m^{-2}) distributions for the baseline (left) and optimised (right) NGV geometries

Figure 7.22 shows the loading at 10%, 50% and 90% radial height. For the 10% and 50% plots, the pressure difference between the pressure and suction side, between the leading edge and mid chord, is greater for the optimum case over the baseline. At 90% span, the lower pressure difference for the optimum case acts to reduce the leakage vortex intensity.

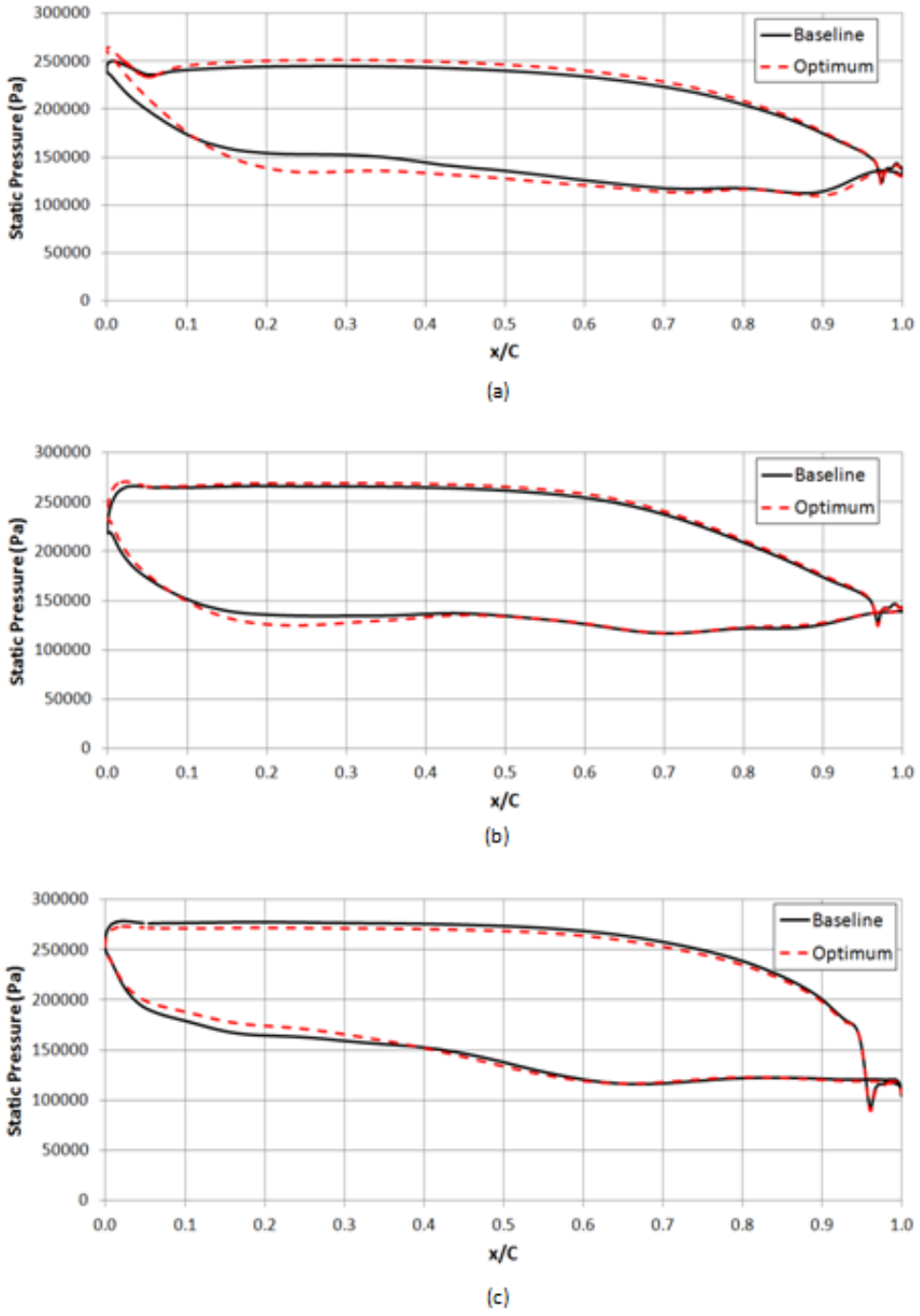


Fig. 7.22 Rotor static pressure (Pa) distributions at (a) 10%, (b) 50% and (c) 90% spanwise sections for the baseline and optimum NGV configurations

7.5.3 Integrated Results and Stage Efficacy

The integrated heat flux values and overall aerothermal performance for both cases are now presented. Table 7.12 and Table 7.13 shows the component breakdown of integrated heat flux for the NGV and rotor stages. For the NGV passage, the optimised case resulted in a 0.82% increase in heat flux across all components, however a reduction by almost 38% for the casing component. This is in line with the T_0 radial plot shown earlier, in which a redistribution of the hot fluid resulted in a cooler upper region at the NGV exit plane.

The rotor component breakdown indicates a decrease in integrated heat flux by 1.16% for the optimum shape over the baseline, with a 25% reduction at the casing. This is consistent with the tip heat flux distributions shown earlier.

Table 7.12 NGV heat flux component breakdown for baseline and optimum NGV cases

Case	**NGV, W/(kg/s)**			**Total**	$\Delta(\%)$
	Hub	Casing	Vanes		
Baseline	400	395	2762	3557	-
Optimum	415	246	2925	3586	0.82

Table 7.13 Rotor heat flux component breakdown for baseline and optimum NGV cases

Case	**Rotor, W/(kg/s)**			**Total**	$\Delta(\%)$
	Hub	Casing	Blade		
Baseline	707	1112	1982	3801	-
Optimum	842	830	2085	3757	-1.16

Finally, the stage non-adiabatic efficiency was also computed for both cases. It was ensured that the mass flow of the optimised geometry was within 0.5% of the baseline. The baseline geometry had an efficiency of 88.4%, and the optimum case yielded an efficiency of 90.1%. The optimum case therefore showed a considerable improvement in overall efficiency of approximately 1.7% over the baseline.

7.6 Case 2: Design Optimisation with Passage Hot Streak and Swirl

7.6.1 Model Performance

100 DOE sample points were generated for the four features/design variables. This has been projected into two dimensions using the t-SNE method (see Section 7.3.5), and is illustrated in Figure 7.23. Good coverage of the design space can be seen.

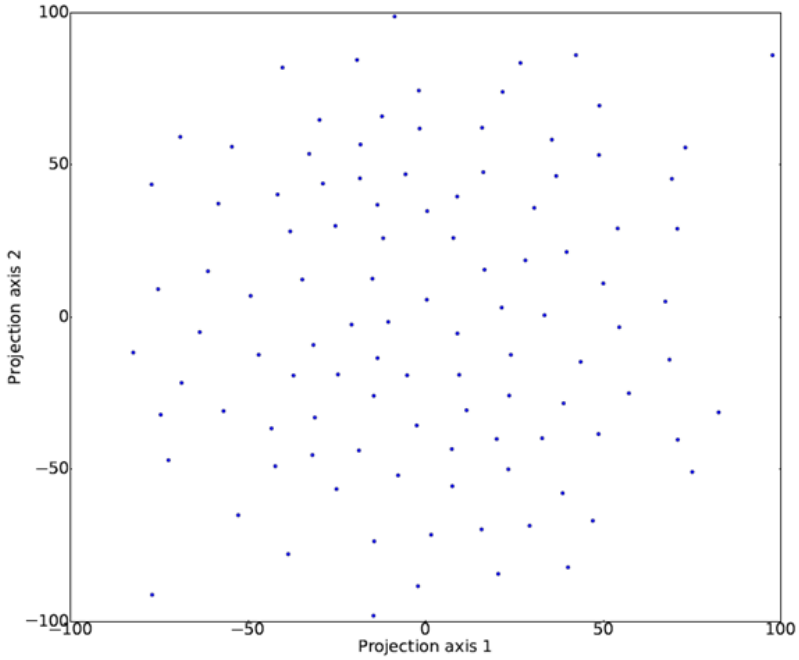


Fig. 7.23 t-SNE two dimensional representation of feature design space

As with case 1, the 100 DOE sample points requiring CFD simulations for the NGV domain were computed on a high performance computing Dell Sandybridge cluster. 32 cores (2 nodes*16 processors per node) of 2.0GHz Xeon SandyBridge were used. The samples were then processed to compute the objective function. Thereafter, prediction models were coded and built using Python's scikit-learn library. The models were trained on 85% of the DOE samples (selected at random), with 15% being held out as a test set in order to score the models for assessment and comparison. The best model that resulted in the lowest test MSE was the linear model, with a score of 1.870, as shown in Table 7.14. The table shows the MSE and R^2 for the training and test sets. The optimum value of the parameter C, as computed by the grid search technique, was 10, which produced the highest cross-validated score of 0.902.

Table 7.14 Performance metrics for the best model

Model	**MSE train**	**MSE test**	R^2 **train**	R^2 **test**
Linear SVR	1.880	1.870	0.954	0.958

A plot of the linear model residuals is shown below in Figure 7.24. Residual plots are used to identify potential nonlinearity, and to ensure that the errors are randomly distributed. It can be seen that the residuals are randomly scattered around the zero centreline, indicating that they are uncorrelated.

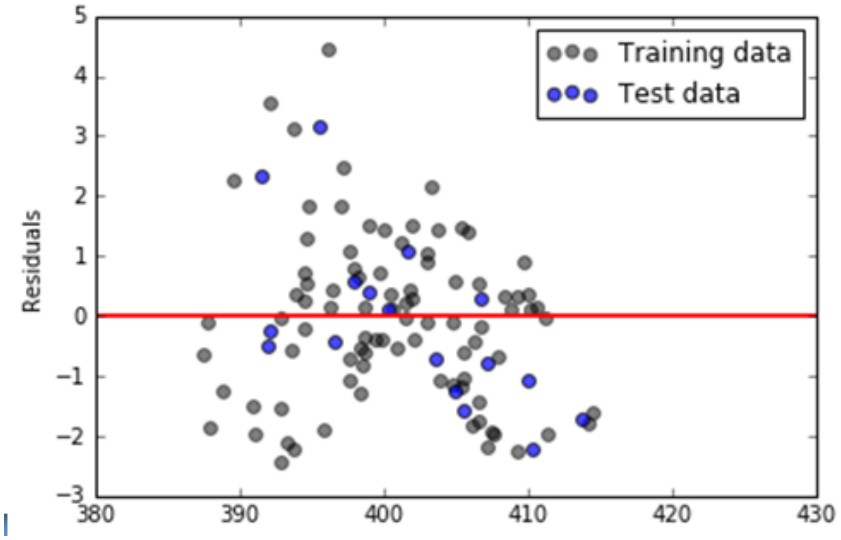


Fig. 7.24 Residual plot for SVR linear model

7.6.2 Feature Importance

The Lasso regularization technique was again used in order to understand feature importance of the NGV lean control parameters. The Lasso model was trained on the DOE sample dataset, and plotted against different values of λ as shown in Figure 7.25. Contrary to the impinging case, it can be see that the vane 1 features approach zero first (as opposed to both hub features for case 1), followed by the hub lean and finally casing lean on vane 2. Therefore, the 'Vane 2 - Casing' design variable was the most important in predicting the mass averaged total temperature at the vane exit for the top 20% of span height (i.e. the objective or target function).

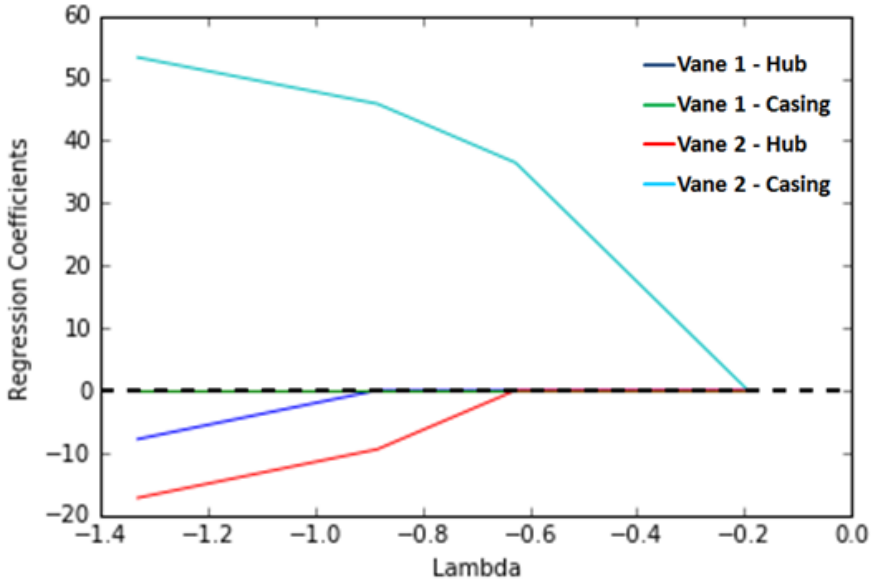


Fig. 7.25 Lasso coefficients versus regularization parameter

7.6.3 Optimised NGV Geometry

The best performing prediction model was the SVR model with a linear kernel. This surrogate model was combined with a Genetic Algorithm optimiser in order to find the minimum predicted objective function within the design space. For the optimisation, each generation consisted of a population of 200 individuals. The rest of the GA specifics are the same as those used in the optimisation validation presented in Chapter 4. After 45 iterations, the algorithm was terminated using the tolerance stopping criteria. The corresponding NGV shape for the best fitness function was run using CFD; the results are presented in Table 7.15, with the difference between the model and actual value being 0.28%. This was deemed to be within an acceptable limit.

Table 7.15 Objective function for Linear SVR (predicted and actual CFD)

Objective Function	**Linear SVR**	**CFD**	**Δ (Linear SVR - CFD)**
OF	385.09	386.17	-0.28%

Table 7.16 shows the objective function for both the baseline and optimised cases. The mass flow at the NGV inlet for the Linear SVR case was constrained to within 0.5% of the baseline. An improvement (decrease) of 3.75% was observed in the objective function with the optimised shape.

Table 7.16 Objective function comparison for baseline and optimised geometries

Case	**Inlet mass flow (kg s^{-1})**	*OF*
Baseline	17.16	401.23
Optimised	17.16	386.17

The optimised NGV lean parameter values are shown in Table 7.17; it can be seen that the best shape is again found on the design space boundary, with an unequal shaping design obtained. A comparison of the geometry is illustrated in Figure 7.26. Vane 1 is positive compound leaned, and the Vane 2 is negatively leaned at the casing, and positively leaned at the hub. In comparison with the impinging hot streak and swirl optimum geometry (case 1), Vane 1 has been leaned in the opposite direction, while Vane 2 has remained the same.

Table 7.17 NGV optimum design variables

Model	**Vane 1 - Hub**(°)	**Vane 1 - Casing**(°)	**Vane 2 - Hub**(°)	**Vane 2 - Casing**(°)
Linear SVR	2	2	2	-2

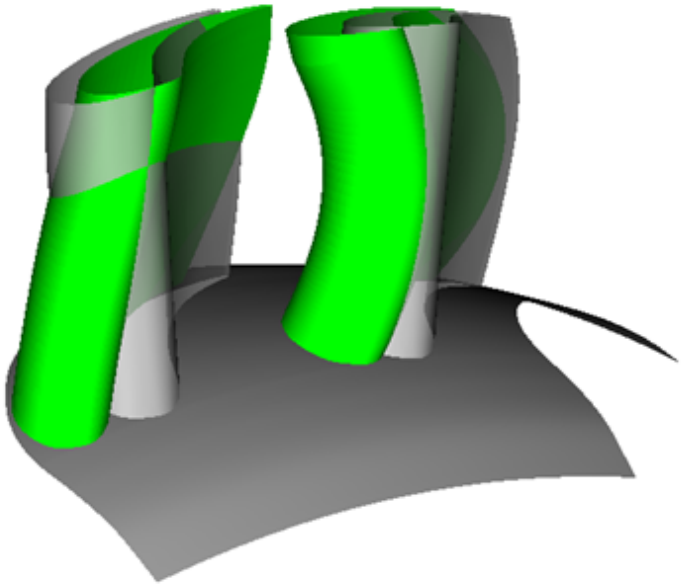


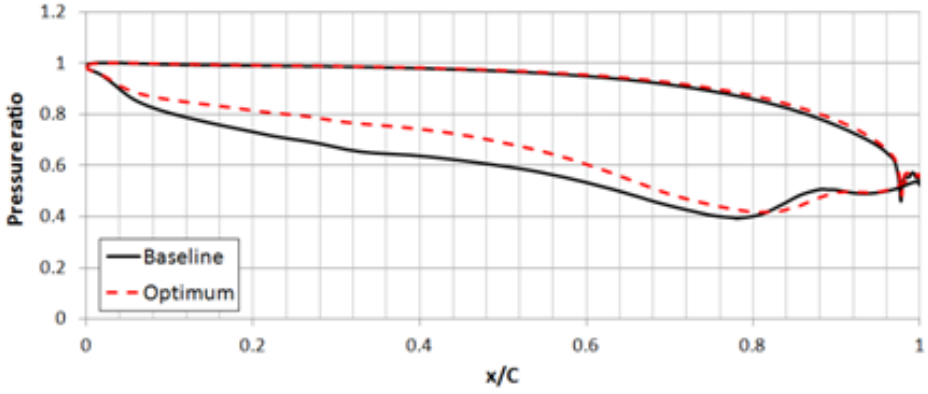
Fig. 7.26 Optimum and baseline NGV geometry comparison. Baseline geometry in grey; optimum geometry in green

7.7 Case 2: Analysis and Discussion

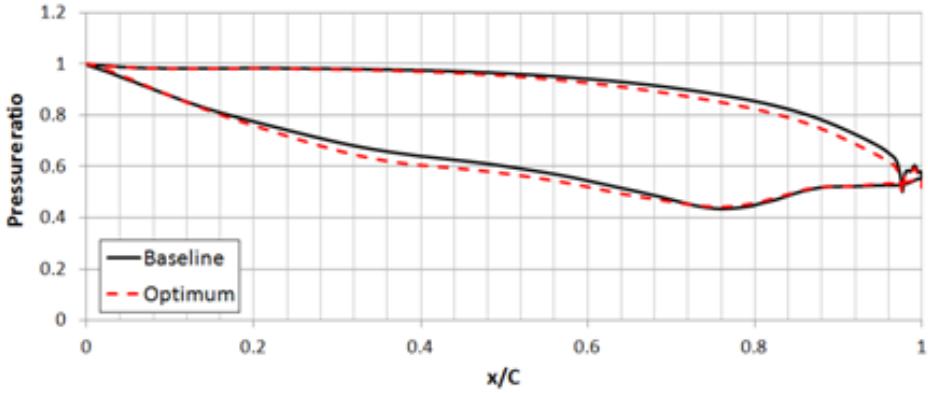
As with Case 1, the optimised NGV geometry (using the design parameters from the previous section) was generated and meshed using PADRAM. The HP turbine stage was run using the HYDRA unsteady CFD solver, in order to capture and compare the rotor aerothermal characteristics. The optimised geometry will now be compared to the baseline case (two straight vanes) for the NGV and rotor passages. All results presented are time averaged.

7.7.1 NGV Analysis

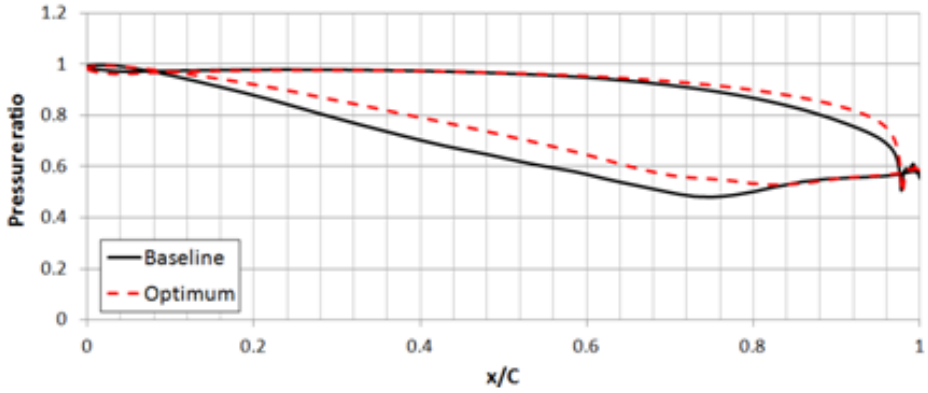
Figure 7.27 and Figure 7.28 shows the loading (static pressure normalised by the stage inlet total pressure) for the baseline and optimum cases, for vanes 1 and 2 respectively, at 10%, 50% and 90% spanwise sections. The optimised vane 1 shows the characteristics expected for a positive compound leaned vane; there is an increase in loading at the midspan section, with marked decreases in loading at the hub and casing sections. For the vane 2 (reverse lean at casing; positive lean at hub), there is a large increase in loading at the casing, and a decrease at the hub section.



(a)



(b)



(c)

Fig. 7.27 NGV static pressure distributions on vane 1 at (a) 10%, (b) 50% and (c) 90% spanwise sections

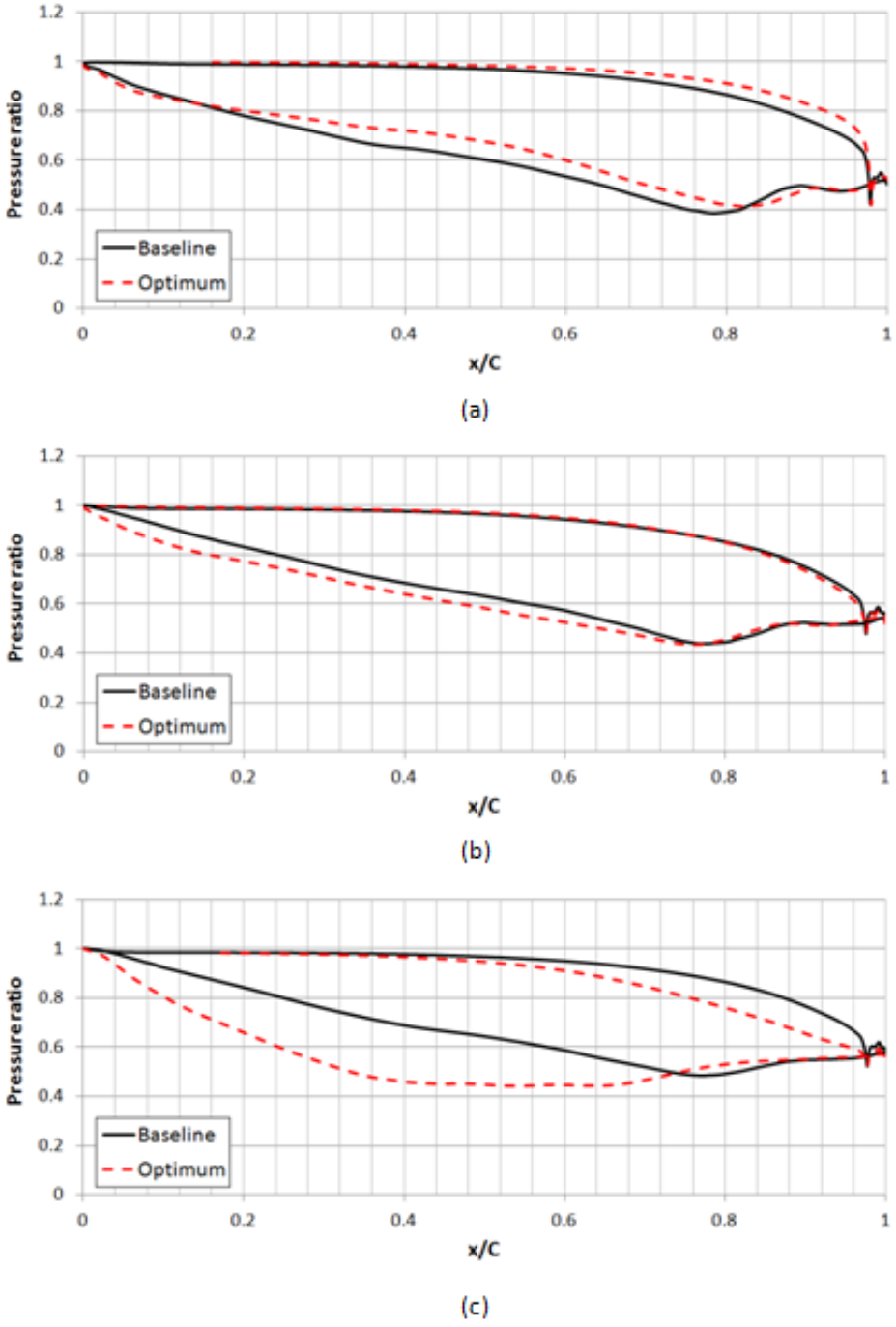


Fig. 7.28 NGV static pressure distributions on vane 2 at (a) 10%, (b) 50% and (c) 90% spanwise sections

The radial (pitchwise averaged) distributions of axial and tangential velocity components at the NGV exit plane are plotted in Figure 7.29. Similar to the first

optimisation, the axial velocity has increased by almost 30% near the hub. However, at the casing, the optimum and baseline axial velocities are approximately matched. This will result in a closer yaw angle for the two cases compared with the impinging case. The increase in hub axial velocity is possibly due to a thinner boundary layer wake for the optimum over the baseline case, as shown in Figure 7.30. The tangential velocity component indicates a less uniform distribution for the optimised case, but this effect appears to be marginal.

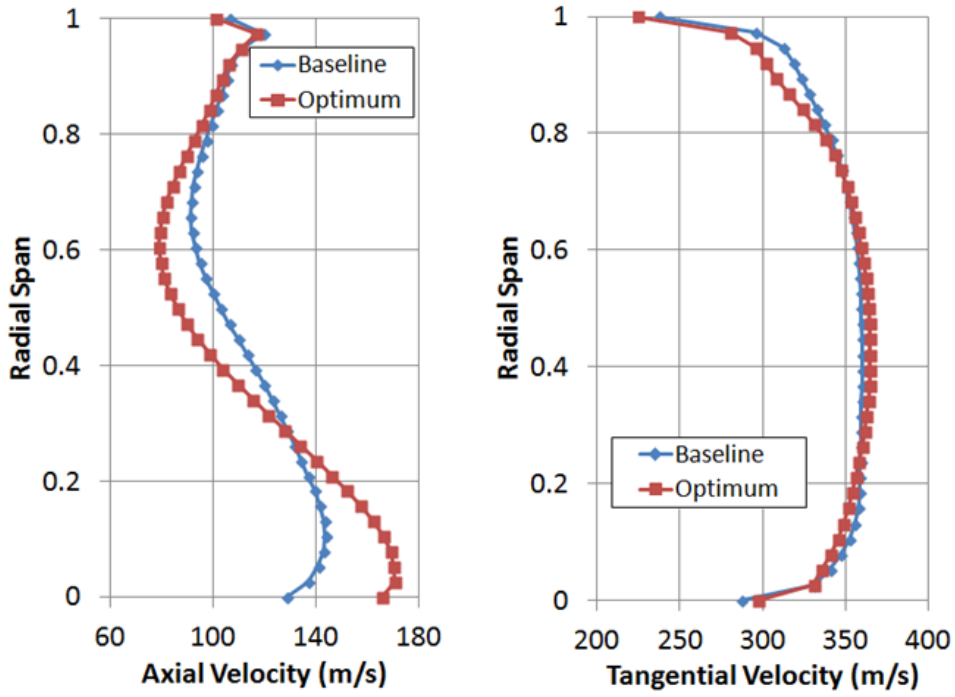


Fig. 7.29 Pitch averaged axial (left) and tangential (right) velocities (m s^{-1}) at the NGV exit plane for baseline and optimum case

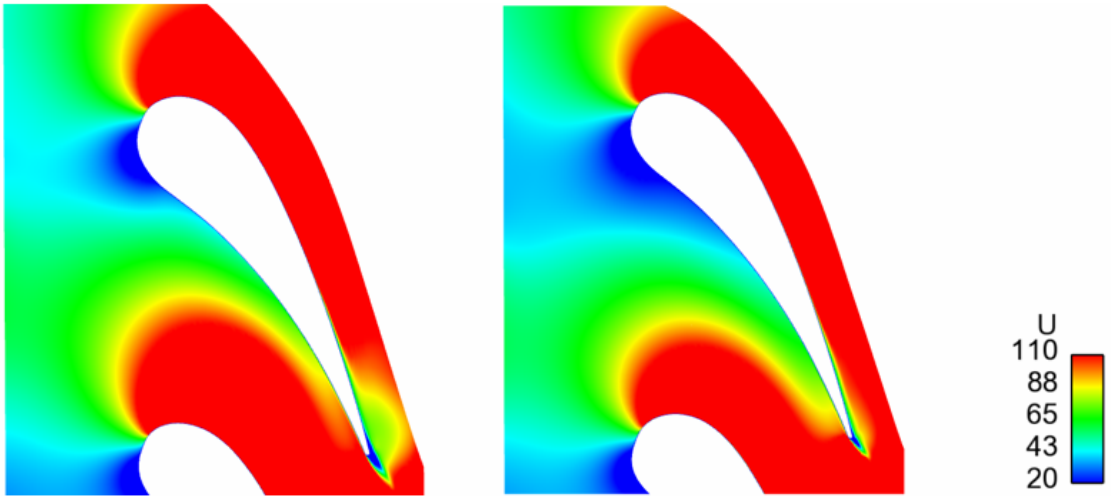


Fig. 7.30 Axial velocity (m s^{-1}) contours near NGV hub for baseline and optimum cases

The loss coefficients at the NGV exit plane are compared for the two cases, as shown in Figure 7.31. There is noticeable overall reduction in pressure loss in the near hub region for the optimised shape over the baseline. This is as expected due to the local positive lean on both optimised vanes. Towards the casing, there is a greater pressure loss region for the optimum case, due to the local reverse lean on vane 2.

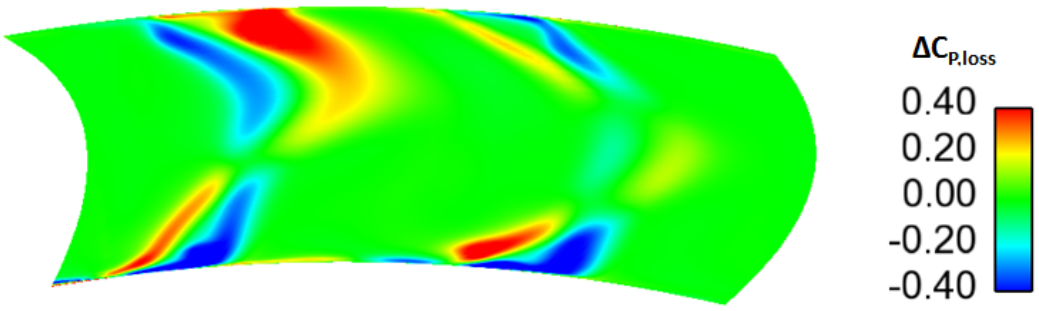


Fig. 7.31 Pressure loss coefficient difference (optimum - baseline)

7.7.2 Rotor Analysis

The resulting total temperature profile for the baseline and optimised NGV shapes on the NGV exit plane are shown in Figure 7.32. It can be seen that the optimised

geometry causes a redistribution in T_0, although not to the same extent in terms of quantitative value or radially as the impinging vane optimisation. The geometry shows a lower temperature from 80% span to the casing, and a temperature closely matched to the baseline near the hub. Overall, the effect is less pronounced than the case 1 optimisation. This logically suggests that the hot streak and swirling flow passes through more undisturbed compared with the impinging case.

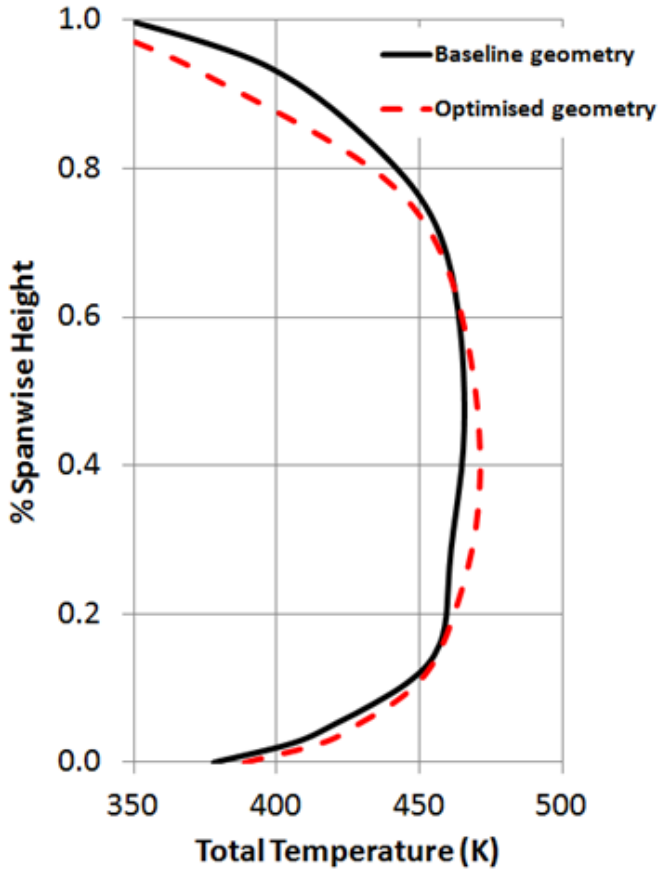


Fig. 7.32 Radial distribution of total temperature (K) at NGV exit plane

The unsteady rotor CFD results are now presented. Again, all results are time averaged plots. The rotor blade surface heat flux distributions are shown for the baseline and optimised geometries in Figure 7.33 and Figure 7.34 respectively. Considering the pressure surface, it can be observed that both configurations exhibit similar character-

istics over most of the span. However, the top 10-15% of the spans are significantly different. The optimised shape yields a cooler rotor leading edge (also cooler across the entire chord) close to the casing. As seen with the case 1 optimisation, the distribution of heat flux along the leading edge (in a spanwise sense) appears to follow the same radial pattern as the NGV exit T_0 distribution, Figure 7.32.

Furthermore, whereas for the optimised geometry for the impinging clocking case the streamlines were drastically changed (leading to a beneficial heat flux distribution), this is no longer the case for the case 2 optimisation, where the streamlines are almost identical. This is most likely due to the reduced interaction of the hot streak and swirl with the vanes from upstream. However, this streamline pattern is still favourable for the optimum case, since it is able to transport the lower incoming temperature (governed by the T_0 radial distribution) close to the casing over the remaining span and tip.

Considering the rotor suction surface, the optimised shape yields a much cooler upper third heat flux pattern, with a hot, narrow region close to the leading edge no longer present; this can be attributed to the transportation of cooler fluid from the pressure surface.

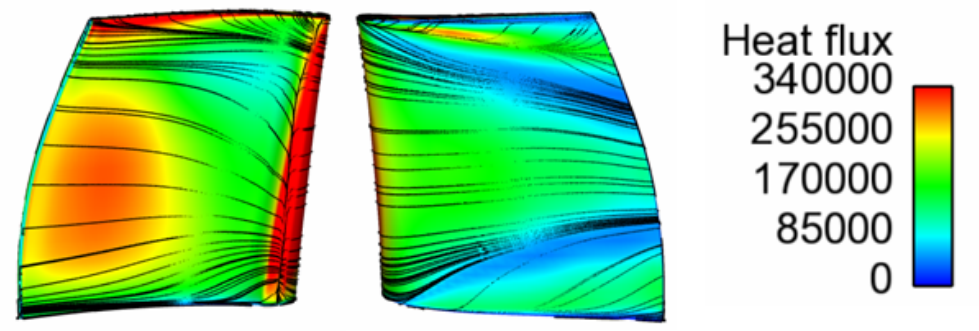


Fig. 7.33 Rotor surface heat flux (W m^{-2}) distributions for baseline geometry on pressure surface (left) and suction surface (right)

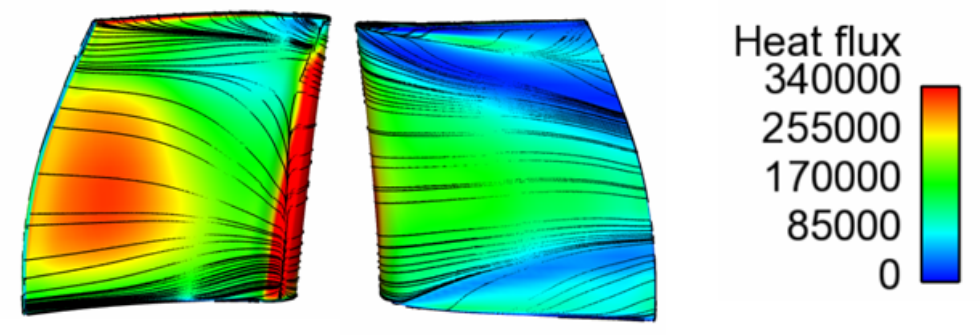


Fig. 7.34 Rotor surface heat flux (W m^{-2}) distributions for optimum geometry on pressure surface (left) and suction surface (right)

The rotor tip heat flux distributions for the two cases is shown in Figure 7.35. The optimised case has resulted in a much cooler pattern (almost 40% in some regions) over the entire tip. It also confirms streamline migration of hot fluid from the rotor leading edge on the pressure surface, to the suction surface.

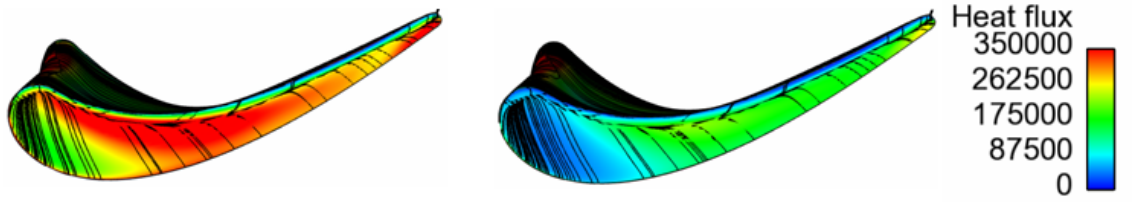


Fig. 7.35 Rotor tip heat flux (W m^{-2}) distributions for the baseline (left) and optimised (right) NGV geometries

Figure 7.36 shows the loading at 10%, 50% and 90% radial height. For the 10% plot, there is a drop in suction side pressure between 15-40% axial chord. For the 50% and 90% plots, the baseline and optimum configurations are largely matched.

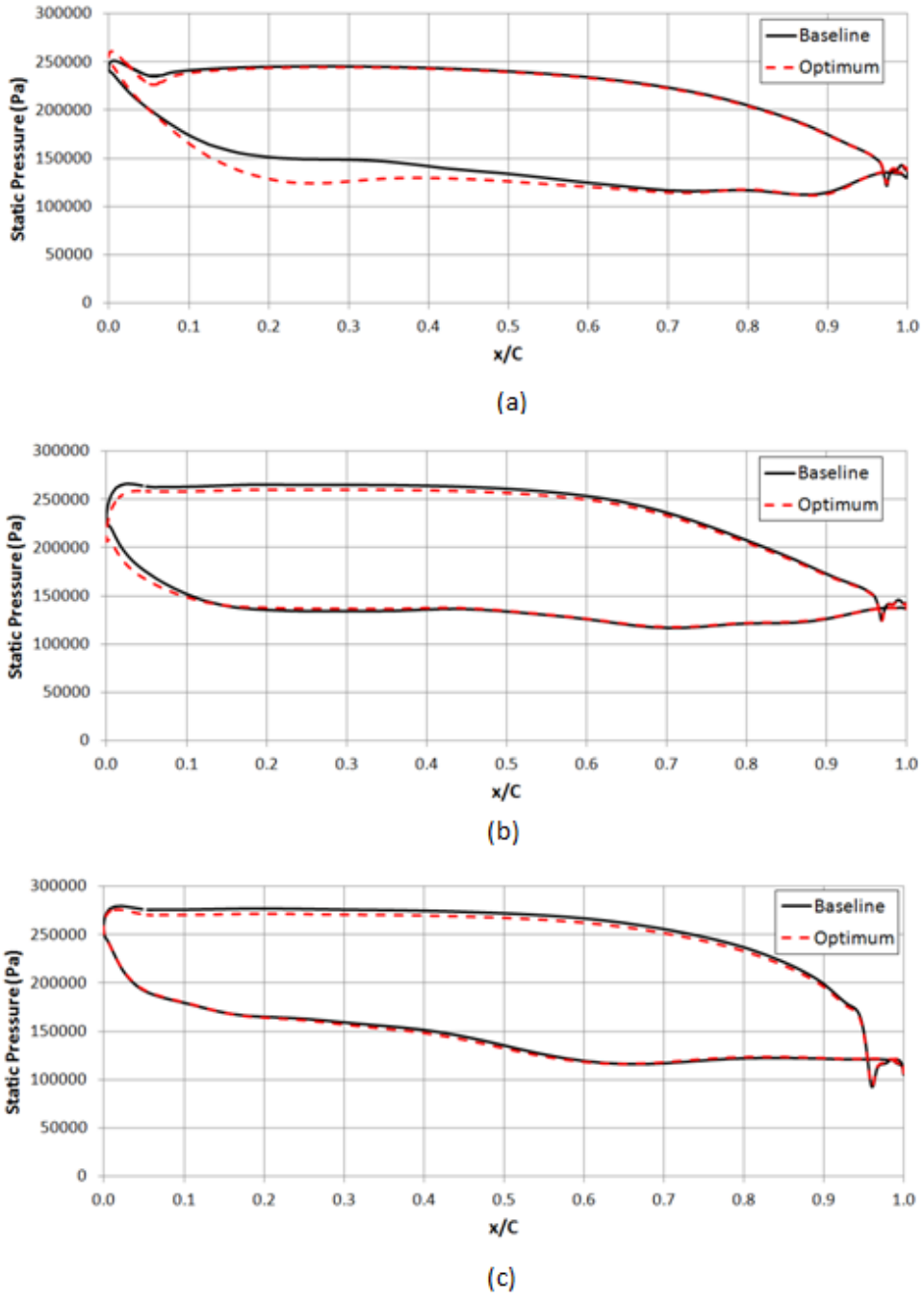


Fig. 7.36 Rotor static pressure (Pa) distributions at (a) 10%, (b) 50% and (c) 90% spanwise sections for the baseline and optimum NGV configurations

7.7.3 Integrated Results and Stage Efficacy

The integrated heat flux values and overall aerothermal performance for both cases are now presented. Table 7.18 and Table 7.19 shows the component breakdown of integrated heat flux for the NGV and rotor stages. For the NGV passage, the optimised case resulted in a 8.87% increase in heat flux across all components, however a reduction by almost 14% for the casing component. This is in line with the T_0 radial plot shown earlier, in which a redistribution of the hot fluid resulted in a cooler upper region at the NGV exit plane.

The rotor component breakdown indicates a decrease in integrated heat flux by almost 20% for the optimum shape over the baseline, with a 55% reduction at the casing. This is consistent with the tip heat flux distributions shown earlier.

Table 7.18 NGV heat flux component breakdown for baseline and optimum NGV cases

Case	**NGV, W/(kg/s)**			**Total**	$\Delta(\%)$
	Hub	Casing	Vanes		
Baseline	609	418	2761	3788	-
Optimum	659	360	3105	4124	8.87

Table 7.19 Rotor heat flux component breakdown for baseline and optimum NGV cases

Case	**Rotor, W/(kg/s)**			**Total**	$\Delta(\%)$
	Hub	Casing	Blade		
Baseline	723	903	2200	3826	-
Optimum	627	408	2028	3063	-19.94

The stage non-adiabatic efficiency was also computed for both cases. It was ensured that the mass flow of the optimised geometry was within 0.5% of the baseline. The baseline geometry had an efficiency of 87.80%, and the optimum case yielded an efficiency of 88.59%. The optimum case therefore showed a good improvement in overall efficiency of approximately 0.8% over the baseline. It is noted that this is lower than the optimised shape for the impinging case, suggesting that the interaction of hot streak and swirl with the NGVs can be manipulated to achieve large gains.

7.8 Summary of Chapter

This chapter commenced with a novel approach to NGV design. In order to accommodate combined hot streak and swirling flow at the turbine inlet, a non-equal NGV pair design methodology was proposed and demonstrated. This approach effectively opened the design space in terms of design parameters and shapes to explore for an optimisation procedure.

Two optimisations were subsequently carried out for two hot streak and swirl clocking positions; impinging and passage aligned. The objective was to reduce the rotor tip heat flux without running unsteady (time costly) CFD simulations. This was achieved through the selection of the total temperature at the NGV exit plane, from 80% to the casing. The lean parameter was used as the design variable and allowed to vary independently with respect to its neighbour.

For the impinging optimisation case, the optimum shape redistributed the T_0 at the NGV exit, lowering it towards the casing, whilst increasing it near the hub. The flow angles were also redistributed, with a higher axial velocity close to the vane hub. The aerodynamics in the rotor passage were altered, with divergent streamlines transporting the cooler leading edge flow over the tip.

The passage aligned optimisation did not result in any change to the rotor streamlines, however a lowering of T_0 at the vane exit very close to the casing resulted in a significantly cooler tip heat flux distribution (40% in some regions) as well as a 0.8% increase in efficiency over the baseline.

The optimised shape for the passage case resulted in the lowest tip heat flux distribution, however the optimum shape for the impinging case led to the highest gain in stage efficiency. This therefore suggests that the clocking position should be a consideration for future optimisation and design of the HP stage.

Finally, the linearity in the design space was highlighted, since the linear SVR gave the best model performance of all the ones tested. This therefore yielded optimum shapes at the design bounds.

Chapter 8

Conclusions and Future Work

8.1 Introduction

This chapter presents the main conclusions and findings based on the author's work shown in this thesis. This will be followed by recommendations and suggestions for future work that the author feels would enhance and progress the current work.

8.2 Conclusions

The main conclusions arising from this thesis are:

(a) The compound lean NGV parameter has been investigated extensively by turbine designers in an effort to realise a gain in aerodynamic stage performance. However, to the author's knowledge, there is no published work that seeks to understand its aerodynamics-heat transfer impact under rich burn (hot streak only) and lean burn (combined hot streak and aggressive swirl) combustion exit profiles on HPT stage performance. Additionally, the author has found no studies

that implement an NGV aerothermal design optimisation under these realistic inflow conditions. To this extent, the current work is the first of its kind.

(b) In the NGV passage, the vane lean is seen to mass upload the endwalls, whilst offloading them in an aerodynamic sense. This results in a higher head at the inflow near the rotor tip. These observations are independent of the turbine inflow conditions.

(c) The high rotor inlet head alters the streamlines on the rotor blade pressure surface, which are generally diverted away from the casing endwall. A result of this is a reduction in leakage of flow over the rotor tip (lower secondary flow region). This is also independent of the turbine inflow conditions.

(d) For the hot streak only inlet, the rotor blade, with the streamline diversion from the casing due to NGV lean, is able to effectively block the hottest portion of the hot fluid (found at the midspan for a hot streak profile) from reaching the tip. This results in a cooler rotor near tip pressure surface and over the tip itself.

(e) There is a reversal in the roles played by HTC and fluid driving temperature in determining heat flux; for a uniform inlet, the HTC is dominant, whereas the driving temperature (T_{aw}) is the primary factor for a hot streak only inlet.

(f) For lean burn combustor exit conditions (hot streak and swirl), the inlet swirl is seen to cause a significant redistribution of hot fluid through the vane passage, and is dependent on the swirl orientation. For a positive swirl, there is a thermal uploading in the near casing region (although offloading aerodynamically). The trend is reversed for negative swirl. The thermal behaviour is possibly governed by the difference in primary flow inertias on the suction and pressure surfaces after the swirl interacts with the vane leading edge.

(g) The thermal offloading (near casing) identified for negative swirl results in very different and more favourable rotor heat transfer characteristics compared with

positive swirl. Furthermore, for a positive swirl, RCL vanes gives a cooler rotor tip leading edge region (compared to the straight vane case), with a reduction of approximately 30%.

(h) The complex NGV aerodynamics due to lean burn leads to the HTC being more influential in determining rotor blade heat transfer. This is in contrast to the rich burn case, where a more convective mechanism was observed as a result of driver temperature variations.

(i) Two optimisation cases were carried out for two clocking positions; vane impinging and passage aligned combined hot streak and swirl. The NGV exit total temperature was used as the objective function, as it was seen as a marker of rotor tip heat flux distribution and stage efficiency. The vanes (using the lean parameter) were permitted to be shaped independently of each other.

(j) Unequal shaped NGV pairs were found to be the optimum in both cases. Although the passage aligned optimum resulted in a cooler rotor tip heat transfer distribution, the impinging case optimised geometry provided the best overall aerothermal performance, with an improvement in stage efficiency of almost 1.7% over the baseline. The importance of clocking position on stage performance has thus been demonstrated.

8.3 Recommendations for Future Work

The optimisations performed in this thesis are seen as the first iteration in understanding the effect of design variables on rotor heat flux and stage efficiency. In order to build on this work, more design variables should be added to the model, which requires more sample simulations (which grows by a power of two with the number of design variables). In order to account for aerothermal effects in an explicit manner, the author

would suggest a multi-objective optimisation approach, using a Pareto Front technique in order to find a compromised solution.

The model found to be the most accurate with the lean parameter in Chapter 7 was a linear SVR. This highlighted the strong linearity in the datasets explored. However, as the number of design variables grows, to include perhaps stagger and sweep, there could be a non-linear response. In order to account for this, an Artificial Neural Network model is recommended, which is capable of handling such scenarios.

As the author noted in Chapter 7, in order to optimise explicitly for stage efficiency, unsteady CFD simulations would be required. If this approach were to be adopted in the future, it would be of interest to see how the optimum shape compares with those found in Chapter 7. However, it is noted that this would require in excess of 100 unsteady simulations, which may not be suitable for commercial use.

Finally, experimental setups with combined hot streak and swirling flow at the turbine inlet are required. This is necessary in order to confirm the validity of the results presented in this thesis (currently validation against inlet swirl only), and also to further the aerothermal understanding on non-periodic shaping through an experimental optimisation.

References

F. E. Ames, C. Wang, and P. A. Barbot. Measurement and prediction of the influence of catalytic and dry low nox combustor turbulence on vane surface heat transfer. *ASME Journal of Turbomachinery*, 125:221–231, 2003.

ANSYS. *Fluent Theory Guide*. 2010.

M. Arabnia and W. Ghaly. On the use of blades stagger and stacking in turbine stage optimization. (ASME Paper GT2010-23399), 2010.

D. Bagshaw, G. Ingram, D. G. Gregory-Smith, and M. Stokes. An experimental study of reverse compound lean in a linear turbine cascade. *Journal of Power and Energy*, 219 (6)(Proceedings of IMechE, part A):443–449, 2005.

N. S. Bakhvalov. On the convergence of a relaxation method with natural constraints on the elliptic operator. *U.S.S.R Comp. Math. And Math. Phys*, 6:101–135, 1966.

R. H. Barnard and D. R. Philpot. *Aircraft flight: a description of physical principles of aircraft flight*. Pearson Prentice Hall, 2004.

P. F. Beard. *On Transient Turbine Efficiency Measurements with Engine Representative Inlet Flows*. PhD thesis, University of Oxford, Department of Engineering Science, 2010.

P. F. Beard, A. D. Smith, and T. Povey. Effect of combustor swirl on transonic high pressure turbine efficiency. *ASME Journal of Turbomachinery*, 136:011002, 2014.

M. W. Benner, S. A. Sjolander, and S. H. Moustapha. Influence of leading-edge geometry on profile losses in turbines at off-design incidence: Experimental results and an improved correlation. *ASME Journal of Turbomachinery*, 119:1039–1046, 1997.

J. Blazek. *Computational Fluid Dynamics: Principles and Applications*. Elsevier, 2001.

P. Boselli and M. Zangeneh. An inverse design based methodology for rapid 3d multi-objective/multidisciplinary optimization of axial turbines. (ASME Paper GT2011-46729), 2011.

T. L. Butler, O. P. Sharma, H. D. Jopslyn, and R. P. Dring. Redistribution of inlet temperature distortion in an axial flow turbine stage. *AIAA Journal of Propulsion and Power*, pages 64–71, 1989.

L. Cambier and M. Gazaix. elsa : An efficient object-oriented solution to cfd complexity. *40th AIAA Aerospace Sciences Meeting Exhibit*, 2002.

K. S. Chana. Heat transfer and aerodynamics of a high rim speed turbine nozzle guide vane with profile endwalls. (ASME Paper No. 92-GT-243), 1992.

K. S. Chana and T. V. Jones. An investigation on turbine tip and shroud heat transfer. (ASME Paper No. GT2002-30554), 2002.

K. S. Chana, T. Patel, and A. H. Mole. A summary of the measurements with a non-uniform inlet temperature profile from the mt1 single stage hp turbine. *Technical Report, Report DERA/AS/PPD/CR010116, Qinetiq*, 2001.

K. S. Chana, J. R. Hurrion, and T. V. Jones. The design, development and testing of a non-uniform inlet temperature generator for the qinetiq transient turbine research facility. (ASME Paper No. GT2003-38469), 2003.

N. X. Chen, H. W. Zhang, and Q. Hu. Application of simple gradient-based method and multi-section blade parameterization technique to aerodynamics design optmization of a 3d transonic single rotor compressor. (ASME Paper GT2009-59734), 2009.

D. Corriveau and S. A. Sjolander. Influence of loading distribution on the performance of transonic high pressure turbine blades. *ASME Journal of Turbomachinery*, 126: 288–296, 2004.

A. Datta and S. K. Som. Combustions and emissions characteristics in a gas turbine combustor at different pressure and swirl conditions. *Journal of Applied Thermal Engineering*, (19):949–967, 1999.

J. Denton and U. K. Singh. Time marching methods for turbomachinery flow calculations. *VKI Lecture Series*, 1979.

J. Denton and L. Xu. The exploitation of three-dimensional flow in turbomachinery design. *Journal of Mechanical Engineering Science*, 213 (2)(Proceedings of IMechE, part C):125–137, 1999.

J. D. Denton. Loss mechanisms in turbomachines. *ASME Journal of Turbomachinery*, 115(4), 1993.

D. J. Dorney and K. L. Gundy-Burlet. Hot streak clocking effects in a 1-1/2 stage turbine. *AIAA Journal of Propulsion and Power*, 12:619–620, 1996.

D. J. Dorney, R. L. Davis, D. E. Edwards, and N. K. Madavan. Unsteady analysis of hot-streak migration in a turbine stage. *AIAA Journal of Propulsion and Power*, 8: 520–529, 1992.

R. P. Fedorenko. A relaxation method for solving elliptic difference equations. *U.S.S.R Comp. Math. And Math. Phys*, 1:1092–1096, 1962.

A. I. J. Forrester, N. W. Bressloff, and A. J. Keane. Optimization using surrogate models and partially converged computational fluid dynamics simulations. *Proceedings of the Royal Society A: Mathematical, Physical and Engineering Sciences*, 462: 2177–2204, 2006.

R. J. Goldstein, K. Y. Lau, and C. C. Leung. Velocity and turbulence measurements in combustion systems. *Experiments in Fluids*, 1:93–99, 1983.

D. G. Gregory-Smith, C. P. Graves, and J. A. Walsh. Growth of secondary losses and vorticity in an axial turbine cascade. *ASME Journal of Turbomachinery*, 110:1–8, 1988.

D. G. Gregory-Smith, D. Bagshaw, G. Ingram, and M. Stokes. Using profiled endwalls, blade lean and leading edge extensions to minimise secondary flow. (ASME Paper No. GT2008-50811), 2008.

S. R. Gunn. Support vector machines for classification and regression. *Technical Report, University of Southampton*, 1998.

A. K. Gupta, M. J. Lewis, and M. Daurer. Swirl effects on combustion characteristics of premixed flames. *ASME Journal of Engineering for Gas Turbines and Power*, 120(3):619–626, 2001.

S. Harrison. The influence of blade lean on turbine losses. *ASME Journal of Turbomachinery*, 114:184–190, 1992.

N. W. Harvey, M. G. Rose, M. D. Taylor, S. Shahpar, J. Hartland, and D. G. Gregory-Smith. Nonaxisymmetric turbine end wall design: Part i - three-dimensional linear design system. *ASME Journal of Turbomachinery*, 122:278, 2000.

W. R. Hawthorne. Rotational flow through cascades, part i: The components of vorticity. *Journal of Mechanics and Applied Mathematics*, 8:266–279, 1955-a.

L. He. An euler solution for unsteady flows around oscillating blades. *ASME Journal of Turbomachinery*, 112:714–722, 1990.

L. He. Fourier methods for turbomachinery applications. *Progress in Aerospace Sciences*, 46:329–341, 2010.

L. He and M. L. G. Oldfield. Unsteady conjugate heat transfer modeling. *ASME Journal of Turbomachinery*, 133:031022, 2011.

L. He, V. Menchikova, and B. R. Haller. Effect of hot-streak counts on turbine blade heat load and forcing. *AIAA Journal of Propulsion and Power*, 23:1235–1241, 2007.

H. P. Hodson. Boundary-layer transition and separation near the leading edge of a high-speed turbine blade. *ASME Journal of Engineering for Gas Turbines and Power*, 107:127–134, 1985.

H. P. Hodson and R. G. Dominy. Three-dimensional flow in a low pressure turbine cascade at design condition. *ASME Journal of Turbomachinery*, 109:177, 1987.

J. H. Horlock. Recent developments in secondary flow. *Proceedings of the AGARD Conference, Seconary Flows in Turbomachines*, (Paper No. AGARD CP-214), 1977.

J. Houmouziadis and N. Hubner. Three-dimensional design of turbine airfoils. (ASME Paper No. 85-GT-188), 1985.

F. W. Huber, R. J. Rowey, and R. Ni. Application of 3d computations to gas turbine aerodynamic design. (AIAA Paper No. 85-1216), 1985.

G. James, D. Witten, T. Hastie, and R. Tibshirani. *An Introduction to Statistical Learning with Applications in R*. Springer, 2015.

A. Jameson. Time-dependent calculations using multi-grid, with applications to unsteady flows past airfoils and wings. (AIAA Paper No. 91-1596), 1991.

M. Joly, G. Paniagua, and T. Verstraete. Attenuation of vane distortion in a transonic turbine using optimization strategies. part 2 - optimization. (ASME Paper GT2010-22371), 2010.

D. B. M. Jouini, S. A. Sjolander, and S .H. Moustapha. Aerodynamic performance of a transonic turbine cascade at off-design conditions. *ASME Journal of Turbomachinery*, 123:510–518, 2001.

J. L. Kerrebrock and A. A. Mikolajczak. Intra-stator transport of rotor wakes and its effect on compressor performance. *ASME Journal of Engineering for Gas Turbines and Power*, pages 359–370, 1970.

A. Keskin, M. Swoboda, and P. M. Flassig. Accelerated industrial blade design based on multi-objective optimization using surrogate model methodology. (ASME Paper GT2008-50506), 2008.

B. Khanal, L. He, J. D. Northall, and P. Adami. Unsteady aero thermal behaviour of hp turbine stage under combustor hot streak and swirl. *13th International Symposium on Unsteady Aerodynamics Aero-Elasticity and Aero-Acoustics of Turbomachines*, (ISUAAT13-S8-1), 2012.

B. Khanal, L. He, J. D. Northall, and P. Adami. Analysis of radial migration of hot streak in swirling flow through high-pressure turbine stage. *ASME Journal of Turbomachinery*, 135:041005, 2013.

J. R. Koehler and A. B. Owen. Computer experiments. *Handbook of Statistics*, pages 261–308, 1996.

B. Krouthen and M. B. Giles. Numerical investigation of hot-streaks in a turbine stage. *AIAA Journal of Propulsion and Power*, 6(6):769–776, 1990.

B. Lakshminarayana. *Fluid Dynamics and Heat Transfer in Turbomachinery*. John Wiley and Sons, 1st edition, 1996.

L. S. Langston. Crossflows in a turbine cascade passage. *ASME Journal of Engineering for Power*, 102:866–874, 1980.

L. S. Langston. Secondary flows in axial turbines - a review. *Annals of the New York Academy of Sciences*, 934, 2001.

L. S. Langston, M. L. Nice, and R. M. Hooper. Three-dimensional flow within a turbine cascade passage. *ASME Journal of Engineering for Power*, 99:21–28, 1977.

C. D. Maesschalck, S. Lavagnoli, and G. Paniagua. Blade tip shape optimization for enhanced turbine aerothermal performance. *ASME Journal of Turbomachinery*, 136: 041016, 2013.

R. Mafulli and L. He. Wall temperature effects on heat transfer coefficient for high-pressure turbines. *AIAA Journal of Propulsion of Power*, 30(4):1080–1090, 2014-a.

R. Mafulli and L. He. Dependence of external heat transfer heat coefficient and aerodynamics on wall temperature for 3-d turbine blade passage. (ASME Paper GT2014-26763), 2014-b.

S. R. Manwaring and K. L. Kirkengr. Forced response vibrations of a low pressure turbine due to circumferential temperature distortions. *Proceedings of 8th Internation Symposium on Unsteady Aerodynamics and Aeroelasticity of Turbomachines*, 1997.

F. Martelli, P. Adami, S. Salvadori, K.S. Chana, and L. Castillon. Aero-thermal study of the unsteady flow field in a transonic gas turbine with inlet temperature distortions. (ASME Paper No. GT2008-50628), 2008.

J. J. McGuirk. The aerodynamic challenges of aeroengine gas-turbine combustion systems. *The Aeronautical Journal*, 118:557–599, 2014.

M. D. McKay, R. J. Beckman, and W. J. Conover. A comparison of three methods for selecting values of input variables in the analysis of output from a computer code. *Technometrics*, 21(2):239–245, 1979.

T. Mengistu, W. Ghaly, and T. Mansour. Aerodynamic shape optimization of turbine blades using design-parameter-based shape representation. (ASME Paper GT2007-28041), 2007.

A. Milli and S. Shahpar. Full-parametric design system to improve the stage efficiency of a high-fidelity hp turbine configuration. (ASME Paper GT2008-51348), 2008.

G. Modgil, A. W. Crossley, and D. Xiu. Design optimization of a high-pressure turbine blade using generalized polynomial chaos (gpc). *10th World Congress on Structural and Multidisciplinary Optimization, Orlando, Florida, U.S.A.*, 2013.

P. Moinier. *Algorithm Developments for an Unstructured Viscous Flow Solver*. PhD thesis, University of Oxford, Department of Engineering Science, 1999.

M. Munk and R. C. Prim. On the multiplicity of steady gas flows having the same streamwise pattern. *Proceedings of the National Academy of Science, U.S.A.*, 33: 137–141, 1947.

S. Nasir, J. S. Carullo, W. Ng, K. A. Thole, H. Wu, L. J. Zhang, and H. K. Moon. Effects of large scale high freestream turbulence and exit reynolds number on turbine vane heat transfer in a transonic cascade. *ASME Journal of Turbomachinery*, 131: 021021, 2009.

O. Oksuz and I. S. Akmandor. Axial turbine blade aerodynamic optimization using a novel multi-level genetic algorithm. *ASME Journal of Turbomachinery*, 132:041009, 2010.

J. Periaux and T. Verstraete. *Introduction to optimization and multidisciplinary design in aeronautics and turbomachinery*. von Karman Institute for Fluid Dynamics, 2010.

T. Povey and I. Qureshi. Development in hot-streak simulators for turbine testing. *ASME Journal of Turbomachinery*, 131:031009, 2009.

R. Puente, G. Paniagua, and T. Verstraete. Aerodynamic characterization of transonic turbine vanes optimized to attenuate rotor forcing. (ASME Paper GT2011-46553), 2011.

G. Pullan. Secondary flows and loss caused by blade row interaction in a turbine stage. *ASME Journal of Turbomachinery*, 128:484, 2006.

I. Qureshi, A. Beretta, and T. Povey. Effect of simulated combustor temperature nonuniformity on hp vane and end wall heat transfer. *ASME Journal of Engineering for Gas Turbines and Power*, 133:031901, 2010.

I. Qureshi, A. D. Smith, and K. S. Chana. Effect of temperature nonuniformity on heat transfer in an unshrouded transonic hp turbine: An experimental and computational investigation. *ASME Journal of Turbomachinery*, 134:011005, 2011-a.

I. Qureshi, A. D. Smith, and T. Povey. Hp vane aerodynamics and heat transfer in the presence of aggressive inlet swirl. (ASME Paper GT2011-46037), 2011-b.

I. Qureshi, A. Beretta, K. S. Chana, and T. Povey. Effect of aggressive inlet swirl on heat transfer and aerodynamics in an unshrouded transonic hp turbine. (ASME Paper GT2011-46038), 2011-c.

R. W. Radomsky and K. A. Thole. Detailed boundary layer measurements on a turbine stator vane at elevated freestream turbulence levels. *ASME Journal of Turbomachinery*, 124:107–118, 2002.

M. M. Rai and R. P. Dring. Navier-stokes analysis of the redistribution of inlet temperature distortions in a turbine. *AIAA Journal of Propulsion and Power*, 6: 276–282, 1990.

S. Raschka. *Python Machine Learning*. Packt Publishing, 2015.

R. J. Roback and R. P. Dring. Hot streaks and phantom cooling in a turbine rotor passage: Part 1 - separate effects. *ASME Journal of Turbomachinery*, 115:657–666, 1993.

P. L. Roe. Approximate riemann solvers, parameter vectors and difference schemes. *Journal of Computational Physics*, 43:357–372, 1981.

Rolls-Royce. *The Jet Engine*. Wiley-Blackwell, 5th edition, 2005.

Rolls-Royce. *PADRAM User Guide*. 2006.

B. Rosic and L. Xu. Blade lean and shroud leakage flows in low aspect ratio turbines. *ASME Journal of Turbomachinery*, 134:031003, 2012.

S. Salvadori, F. Montomoli, F. Martelli, K. S. Chana, I. Qureshi, and T. Povey. Analysis of the effect of a non-uniform inlet temperature profile on the heat transfer and fluid flow in turbine stages. *ASME Journal of Turbomachinery*, 134:011012, 2012.

Z. Schabowski, H. Hodson, D. Giacche, B. Power, and M. R. Stokes. Aeromechanical optimization of a winglet-squealer tip for an axial turbine. *ASME Journal of Turbomachinery*, 136:071004, 2014.

G. Schmid, A. Krichbaum, H. Werschnik, and H. Schiffer. The impact of realistic inlet swirl in a 1 1/2 stage axial turbine. (ASME Paper GT2014-26716), 2014.

S. Shahpar and S. Caloni. Aerodynamic optimisation of high pressure turbines for lean-burn combustion system. (ASME Paper GT2012-69228), 2012.

T. Shang. *Influence of Inlet Temperature Distortion on Turbine Heat Transfer*. PhD thesis, Massachusetts Institute of Technology, Department of Aeronautics and Astronautics, 1995.

T. Shang and A. H. Epstein. Analysis of hot-streak effects on turbine rotor heat load. *ASME Journal of Turbomachinery*, 119:544–553, 1997.

O. Sharma, F. Kopper, G. Stetson, S. Magge, F. Price, and R. Ni. A perspective on the use of physical and numerical experiements in the advancement of design technology for axial flow turbines. *International Symposium on Air Breathing Engines*, (Paper AIAA-2003-1035), 2003.

O. P. Sharma and T. L. Butler. Predictions of endwall losses and secondary flows in axial flow turbine cascades. *ASME Journal of Turbomachinery*, 109:229–236, 1987.

O. P. Sharma, T. L. Renaud, T. L. Butler, and K. Milsaps. Rotor-stator interaction in multi-stage axial-flow turbines. (AIAA Paper No. 88-3013), 1988.

C. H. Sieverding. Recent progress in the understanding of basic aspects of secondary flows in turbine blade passages. *ASME Journal of Engineering for Gas Turbines and Power*, 107:248–252, 1985.

C. H. Sieverding and P. Van den Bossche. The use of colored smoke to visualize secondary flows in a turbine-blade cascade. *Journal of Fluid Mechanics*, 134:85–89, 1983.

T. W. Simpson. *A concept exploration method for product family design*. PhD thesis, Georgia Institute of Technology, 1998.

S. N. Sivanandam and S. N. Deepa. *Introduction to Genetic Algorithms*. Springer Publishing Company, 2007.

D. L. Sondak, V. Gupta, P. D. Orkwis, and D. J. Dorney. Effects of blade count on linearized and nonlinear hot streak clocking simulations. *AIAA Journal of Propulsion and Power*, 18:1273–1279, 2002.

P.R. Spalart and S.R. Allmaras. A one-equation turbulence model for aerodynamic flows. *AIAA Aerospace Sciences Meeting and Exhibit*, (Paper AIAA-1992-0439), 1992.

H. B. Squire and K. G. Winter. The secondary flow in a cascade of airfoils in a nonuniform stream. *Journal of Aerospace Science and Technology*, 18:271–277, 1951.

R. Storn and K. Price. Differential evolution - a simple and efficient adaptive scheme for global optimization over continuous spaces. (Tech. Rep. TR-95-012, ICSI, UC Berkeley), 1997.

R. K. Takahashi, R. H. Ni, O. P. Sharma, and J. B. Staubach. Effects of hot-streak and indexing on a 1-1/2 stage turbine. (AIAA Paper 96-2796), 1996.

C. Tan, A. Yamamoto, and H. Chen. Influences of blade bowing on flowfields of turbine stator cascades. *AIAA Journal*, 41:1967–1972, 2003.

L.J.P. van der Maaten and G.E. Hinton. Visualizing high-dimensional data using t-sne. *Journal of Machine Learning Research*, pages 2579–2605, 2008.

P. J. Walker. *Blade Lean in Axial Turbines: Model Turbine Measurements and Simulation by a Novel Numerical Method*. PhD thesis, Cambridge University, Department of Engineering, 1987.

D. X. Wang and L. He. Adjoint aerodynamics design optimization for blades in multi-stage turbomachines: Part i - methodology and verification. *ASME Journal of Turbomachinery*, 132:021011, 2010-a.

D. X. Wang, L. He, Y. S. Li, T. Chen, and R. G. Wells. Adjoint aerodynamics design optimization for blades in multi-stage turbomachines: Part ii - verification and application. *ASME Journal of Turbomachinery*, 132:021012, 2010-b.

Z. Wang, W. Han, and W. Shu. An experimental investigation into the influence of diameter blade height ratios on secondary flow losses in annular cascades with leaned blades. (ASME Paper No. 87-GT-131), 1987.

A. P. S. Wheeler, N. R. Atkins, and L. He. Turbine blade tip heat transfer in low speed and high speed flows. *ASME Journal of Turbomachinery*, 133:041025, 2011.

A. Yamamoto. Endwall flow/loss mechanisms in a linear cascade with blade tip clearance. *ASME Journal of Turbomachinery*, 111:264, 1989.

Q. Zhang and L. He. Impact of wall temperature on turbine blade tip aerothermal performance. *ASME Journal of Engineering for Gas Turbines and Power*, 136: 052602, 2013.

Z. Zhong and T. R. Carr. Application of mixed kernels function (mkf) based support vector regression model (svr) for co2 reservoir oil minimum miscibility pressure prediction. *Fuel*, 184:590–603, 2016.